



University of Fort Hare

Together in Excellence

**A STUDY OF THE GEOLOGY OF THE VAALBANK AND LADY FRERE AREAS
IN THE KAROO BASIN OF SOUTH AFRICA USING GRAVITY, MAGNETIC
AND GAMMA-RAY SPECTROMETRY DATA: IMPLICATIONS OF
GROUNDWATER POTENTIAL**

A dissertation submitted in fulfilment of the requirements for the degree of

MASTER OF SCIENCE IN GEOLOGY

KHALIMASHE SINESIHLE (201202283)

In the
Department of Geology
Faculty of Science and Agriculture
University of Fort Hare, South Africa

Supervisor: Prof O Gwavava
Co- Supervisor: Ms M Havenga

2020

DECLARATION

I, Sinesihle Khalimashe, hereby declare that this dissertation entitled “*A study of the geology of the Vaalbank and Lady Frere areas in the Karoo Basin of South Africa using gravity, magnetic and gamma-ray spectrometry data*” is my own work except where proper referencing and acknowledgement has been made. It is being submitted for the degree of Master of Science at the University of Fort Hare, Alice, and it has never been submitted before, for the purpose of any degree or examination at any other institution

Signature 

Date: 13-05-2020.....



University of Fort Hare
Together in Excellence

ABSTRACT

The Vaalbank and Lady Frere areas belong to the Elliot, Molteno and Burgersdorp Formations, that are part of the sedimentary succession of the Beaufort Group in the Karoo Basin of South Africa. There is Quaternary alluvium covering the mudstone, sandstone and shale rocks of the Beaufort Group. Dolerite and gabbro sills of the Karoo age have intruded the whole area.

A number of investigations were carried out for the study namely field observations, petrographic, X-ray diffraction, airborne gamma-ray spectrometry, aeromagnetic and gravity analyses.

Twenty four rock samples were collected in the field from fresh outcrops of the Karoo dolerites, Burgersdorp and Molteno formations. The measured densities and porosities show that the Karoo dolerite suite has the highest average dry density of 2.771 g/cm^3 and the lowest average porosity of 3%. The Burgersdorp Formation has an intermediate average density of 2.458 g/cm^3 and an intermediate average porosity of 5.4%. The Molteno Formation has the lowest average density of 2.190 g/cm^3 and the highest average porosity of 14.5%.

Petrographic and geochemical investigations were carried on 19 rocks samples collected in the field to determine the mineralogy character using microscopic and XRD analyses. Both petrographic and X-ray diffraction analyses revealed that the sandstones of the study area are composed of quartz as their primary mineral and feldspars as the secondary mineral. The dolerite consists of euhedral structured minerals such as magnetite, pyroxene, plagioclase and amphibole.

The gamma ray maps show high spectrometric values are associated with the Burgersdorp Formation, alluvium cover and dolerite dykes. The low spectrometric values are associated with dolerite sills and ring complexes. The boundaries of the sill/ring complexes are clearly delineated by the K/U ratio and ternary maps.

The magnetic maps show ring like patterns of magnetic high anomalies that are due to the sills/ring complexes whilst the numerous, narrow, linear magnetic highs are due to faults and dolerite dyke swarms. The majority of the dykes trend in a NW-SE direction and a few dykes are in a NE-SE direction. The magnetic power spectrum indicates four depths of the magnetic sources at average depths of 0.13 km, 1.60 km, 2.83 km and 12.40 km. The magnetic depth

slices maps show that both the circular/ring like and linear anomalies extend from shallow to deeper depth of 12.4 km.

The gravity map is dominated by a long wavelength gravity anomaly that increases from about -120 mGals in the northwestern corner of the study area to -110 mGals in the southeastern corner of the study area. Results from 2½D gravity modelling show that this long wavelength anomaly is due to a horizontal Moho at a depth of 47 km in the study area, which shallows outside the study area near the coast. Superimposed on it are short wavelength gravity anomalies due to low density sediments and high density dolerite intrusions. The simple 2½D models generated from five profiles traversing the study area reveal that the sediments of the Karoo Supergroup extend from the surface down to a depth 5 km below sea level attaining a maximum thickness of about 6½ km. These sediments are dykes, sills and ring complexes.

The dykes and sills/ring complexes identified from gamma ray spectrometry, magnetic and gravity data results are likely to be associated with fractures, joints, cracks and fissures in the host rocks, which form preferential pathways for groundwater transmission. Hence, they could be suitable targets for groundwater.

Keywords: Magnetic, gamma-ray spectrometry, gravity, X-ray diffraction, thin sections, 2½D gravity modelling, Karoo Basin



University of Fort Hare
Together in Excellence

DEDICATION

This research work is dedicated to God Almighty (giver of life and wisdom) and dedicated to my son Khazimla and my parents Mrs and Mr Khalimashe.



University of Fort Hare
Together in Excellence

ACKNOWLEDGEMENTS

This research was funded by the Council for Geoscience, Govan Mbeki Research and Development Centre (GMRDC) for the fee waiver, National Research Fund and the Geology Department at University of Fort Hare. I am highly grateful to all for their financial support towards the successful completion of this work.

I offer my sincerest gratitude to my supervisor, Prof O Gwavava for his guidance, motivation suggestions and constructive criticism throughout the project. I would not have completed this project without his advice. I would also thank Ms Marinda Havenga and Mpumi Dube from Council for Geoscience for their guidance.

I would like to acknowledge Prof K Liu for sharing his knowledge in the field of mineralogy in thin sections analysis. I am grateful to Geosoft for providing the “Extended GM-SYS” license (free of charge) for the period of my research which made it possible to generate gravity models.

I would like to express my gratitude to Ms Nontobeko Scheppers from Council for Geoscience for assistance throughout the course of this research.

I would like to express my appreciation to Christopher Baiyegunhi for his time and patience in assisting me in gravity modelling and taking me to the field for sample collection. I appreciate the assistance and support I got from Zandile Ndlazi and Puseletso Takalimane when I was collecting my rock samples.

I would like to thank my fellow graduate students, Mimi Mokoele, Asanda Ntunja, and Nomveliso Caku for their support.

Lastly, my heartfelt indebted gratitude goes to my family, especially my mother for prayers, support, and encouragement throughout my career.

Table of Contents

DECLARATION	i
ABSTRACT	ii
DEDICATION	iv
ACKNOWLEDGEMENTS	v
LIST OF FIGURES	xi
LIST OF TABLES	xv
CHAPTER 1: INTRODUCTION	1
1.1 Background	1
1.2 Location of the study area	2
1.3 Climatology	4
1.4 Problem statement	5
1.5 Aim and objectives	6
1.6 Research questions	7
1.7 Rationale of the study	7
1.8 Delineation and limitation	7
1.9 Structure of dissertation	7
CHAPTER 2: LITERATURE REVIEW	9
2.1 Geology	9
2.1.1 Introduction	9
2.1.2 Kaapvaal Craton	9
2.2 Stratigraphy of the Karoo Supergroup	10
2.2.1 Dwyka Group	13
2.2.2 Eccra Group	14
2.2.3 Beaufort Group	15
2.2.4 Stomberg Group	16
2.2.5 Drakensberg Group	17

2.2.6 Karoo dolerite suite	17
2.3 Geology of the study area.....	21
2.4. Significance of dolerite sill and ring structures on groundwater occurrence	22
CHAPTER 3: RESEARCH MATERIALS AND METHODOLOGY	25
3.1 Introduction	25
3.2 Desktop study.....	25
3.3 Research instruments.....	25
3.4 The software packages	25
3.5 Geophysical data	26
3.6 Samples collected.....	26
3.7 Laboratory studies	26
3.7.1 Density measurements of rocks samples	26
3.7.2 Field observation and petrographic analysis	31
3.7.3 X-ray diffraction analysis (XRD)	44
3.8 Conclusion.....	47
CHAPTER 4: GAMMA RAY SPECTROMETRY METHOD	48
4.1 Gamma ray spectrometry background	48
4.2 Airborne radiometric data acquisition.....	50
4.3 Data enhancement	50
4.4 Radiometric results and interpretation	51
4.4.1 K channel map.....	52
4.4.2 Th channel map	53
4.4.3 Total counts channel map	55
4.4.4 K-U ratio map.....	56
4.4.5 K-Th ratio map	57
4.4.6 U-Th ratio map	58
4.4.7 Ternary map.....	59

4.5 Discussion and summary of the gamma ray spectrometry results	60
4.6 Conclusion.....	61
CHAPTER 5: MAGNETIC METHOD	62
5.1 Magnetic method theory.....	62
5.1.1 Magnetic units	62
5.1.2 Geomagnetic field.....	62
5.1.3 Remanent and induced magnetization	64
5.1.4 Magnetic inclination and declination	65
5.1.5. Temporal variations of the Earth's magnetic field	66
5.1.6 Magnetic instruments	69
5.2 Data acquisition and data processing	70
5.3 Data reduction	70
5.4 Magnetic data enhancement.....	71
5.5 Data presentation and interpretation.....	71
5.5.1 Geology map.....	72
5.5.2 Reduced to pole map	73
5.5.3 Vertical derivative magnetic map.....	75
5.5.4 Total horizontal derivative magnetic map	76
5.5.5 Analytical signal magnetic map	76
5.5.6 Radially averaged power spectrum and depth slicing	77
5.5.7 Depth slicing.....	78
5.6 Discussion and summary of magnetic results	79
5.7 Conclusion.....	80
CHAPTER 6: GRAVITY METHOD	81
6.1 Introduction	81
6.1.1 Units for gravity	82
6.2 Gravity instrumentation.....	82

6.3 Data acquisition and processing	83
6.4 Data presentation and interpretation	83
6.4.1 Bouguer gravity map	84
6.4.3 Gravity power spectrum	86
6.4.4 Gravity slice maps	87
6.5 Discussion of the gravity results	87
6.6 Conclusion.....	88
CHAPTER 7: 2 ½D GRAVITY MODELLING.....	89
7.1 Introduction to gravity modelling	89
7.1.1. Gravity profile modelling	89
7.2 Gravity modelling results	92
7.2.1 Modelling results for Profile A-A'	92
7.2.2 Modelling results for Profile B-B'	95
7.2.3 Modelling results for Profile C-C'	96
7.2.4 Modelling results for Profile D-D'	98
7.2.5 Modelling results for Profile E-E'	99
7.3 Discussion of the gravity models	100
7.4 Conclusion.....	102
CHAPTER 8: SUMMARY OF FINDINGS, CONCLUSIONS AND RECOMMENDATIONS.....	103
8.1 Summary of findings	103
8.2 Conclusions	104
8.2.1 Petrographic and geochemical investigations (XRD)	104
8.2.2 Density and porosity investigations.....	105
8.2.3 Geophysical investigations	105
8.2.4 2 ½ D gravity modelling.....	106
8.3 Previous work done	106

8.4 Contribution of the study.....	107
8.5 Recommendations	107
REFERENCES.....	108
APPENDIX A	119
APPENDIX B:	129
APPENDIX C	135
APPENDIX D	138
APPENDIX E	142



University of Fort Hare
Together in Excellence

LIST OF FIGURES

Figure 1. 1: Google Earth view map of the study area [Google Earth, accessed on 02-03-2017].
3

Figure 1. 2: The geological map of South Africa [Council for Geoscience,].The rectangle indicates the study area. 4

Figure 1. 3: Digital Terrain map showing topographic highs and lows of the study area 5

Figure 2. 1: Stratigraphic subdivision of the Karoo Supergroup in the main Karoo Basin of South Africa [Modified after Johnson et al., 1997].
11

Figure 2. 2: Geographical distribution/widespread of the dolerite intrusions throughout the Karoo Basin of South Africa (<http://karoospace.co.za/dolerite-karoo-fracking-game-changer>).
18

Figure 2. 3: Schematic SW-NE cross section of the Karoo Basin showing dolerite sills and dykes as roots and feeders of the Drakensberg [After Chevallier *et al.*, 2001] 19

Figure 2. 4: Dolerite dykes of the main Karoo Basin. Insert in a simplified structural map showing three structural domains [After Woodford and Chevallier, 2002] 20

Figure 2. 5: Simplified geological map showing formations of the study area [From Council for Geoscience]. 22

Figure 3. 1: Photograph showing the procedure and equipment used in the laboratory for measuring rock densities using Archimedes' principle. 27

Figure 3. 2: Bar chart for average dry, particle and wet density of the study area geologic formations. 29

Figure 3. 3: Bar chart showing porosity of the study area geologic formations. 30

Figure 3. 4: Photograph showing the study area where samples were collected. 31

Figure 3. 5: Photograph displaying an outcrop of the Burgersdorp Formation consisting of dolerite dyke, fault, red mudstone and the sandstone. GPS coordinates: S 31° 33' 21.5" E 26° 57' 11.0". 32

Figure 3. 6: Picture displaying two outcrops of the Burgersdorp Formation. One outcrop is red mudstone and the second outcrop being sandstone and the fault that occurred on the sandstone. GPS coordinate: S 31° 38' 42.8" E 27° 01' 17.1". 33

Figure 3. 7: Picture of an outcrop of the Molteno Formation having weathered sandstone. 34

Figure 3. 8: Picture displaying a dolerite dyke at the study area. GPS coordinate: S 31° 44' 11.9" E 26° 57' 17.9".	35
Figure 3. 9: Photomicrograph displaying moderate sorted sandstone of the Burgersdorp Formation.	36
Figure 3. 10: Photomicrograph displaying a fine grained weathered siltstone of the Burgersdorp Formation.	37
Figure 3. 11: Photomicrograph displaying moderate sandstone of the Burgersdorp Formation.	38
Figure 3. 12: Photomicrograph displaying a medium to coarse grain sandstone of the Burgersdorp Formation.	39
Figure 3. 13: Photomicrograph displaying medium sandstone of the Burgersdorp Formation.	40
Figure 3. 14: Photomicrograph displaying a coarse grain sandstone from Molteno Formation.	41
Figure 3. 15: Photomicrograph displaying moderate grain sandstone from Molteno Formation.	42
Figure 3. 16: Photomicrograph displaying medium grain sandstone from Molteno Formation.	43
Figure 3. 17: Photomicrograph displaying a dolerite of the Karoo dolerite suite.	44
Figure 3.18: Figure A. 1: XRD pattern for sandstone of the Burgersdorp Formation	48
Figure 4. 1: Interaction of gamma rays with matter [Killeen, 1979].	49
Figure 4. 2: K-channel map overlain with the geology of the study area.	52
Figure 4. 4: U channel map overlain with the geology of the study area	54
Figure 4. 5: Total counts channel map overlain with the geology of the study area	55
Figure 4. 6: <i>KU</i> ratio map overlain with the geology of the study area	56
Figure 4. 7: <i>KTh</i> ratio map overlain with the geology of the study area.	57
Figure 4. 8: <i>UTh</i> ratio map overlain with the geology of the study area.	58
Figure 4. 9: Ternary map overlaid with geology of the study area	59
Figure 5. 1: The Earth's dipolar magnetic field. Note that the geomagnetic South Pole is a magnetic north pole and the geomagnetic North Pole is a magnetic south pole [Reeves, 2005].	63

Figure 5. 2: The field due to an inclined geocentric dipole and the field lines [Reeves, 2005].	64
Figure 5. 3: The vector total magnetic field [Reeves, 2005].	66
Figure 5. 4: The solar wind distorts the outer reached of the Earth's magnetic field [Reeves, 2005].	67
Figure 5. 5: Micropulsations recorded at stations few tens of kilometres apart [Reeves, 2005].	68
Figure 5. 6: A typical magnetic storm, as observed at a time of high solar activity [Reeves, 2005].	68
Figure 5. 7: Formations, simplified geology map of the study area from (Council for Geoscience, geology database accessed on 04/2017)	72
Figure 5. 8: Reduced to pole magnetic map overlain with the geology of the study area. The warm colours (red to purple) on the map represent high magnetic values whilst the cold colours (blue to deep blue) represent low magnetic values.	73
Figure 5. 9: Vertical derivative magnetic map superimposed geological features of the study area.	75
Figure 5. 10: Total horizontal derivative magnetic map superimposed geological features of the study area	76
Figure 5. 11: Analytical signal magnetic map superimposed on geological features of the study area.	77
Figure 5. 12: Radially averaged power spectrum of magnetic data.	78
Figure 5. 13: Depth slice maps of the magnetic data showing changes in the magnetic anomalies with depth.	79
Figure 6. 1: Bouguer gravity map overlain with the geology. <i>Note: 1mGal= 10.g.u.</i> Pink-Yellow areas high gravity values while deep blue areas have low gravity values.	84
Figure 6. 2: Trended gravity map overlain with the geology of the study area	85
Figure 6. 3: Gravity radially averaged power spectrum	86
Figure 6. 4: Gravity slice maps of the study area at different depths.	87
Figure 7. 1: Geology map of the study area with profile lines A-E	90
Figure 7. 2: A starting geological subsurface model for A-A'. <i>Note: The Moho varied within a depth range of 45-47 km. Note that the model block extends far away from the ends of the profile, i.e. to ± 550 km, vertical exaggeration (VE) =9.760 and RMS= 17.217</i>	93

Figure 7. 3: A geological subsurface model for profile A-A'. VE = 0.76 , Initial RMS =1.627 and final RMS=0.602. Note: The Moho is horizontal and at a depth of 47 km. 94

Figure 7. 4: A geological subsurface model along profile B-B'.VE = 0.98, initial RMS error = 3.889and final = 0.329 96

Figure 7. 5: A geological subsurface model along profile C-C'. VE = 0.59, Initial RMS error = 6.07 and final = 0.704. 97

Figure 7. 6: A geological subsurface model along profile D-D'. VE = 0.63, Initial RMS error =8.925 and final = 0.399. 99

Figure 7. 7: A geological subsurface model along profile E-E'. VE = 0.68, Initial RMS error = 11.956 and final = 0.882 100

Figure A. 1: XRD pattern for Burgersdorp Formation sandstone 120

Figure A. 2. XRD pattern for Burgersdorp Formation sandstone..... 121

Figure A. 3 XRD pattern for Burgersdorp Formation sandstone..... 122

Figure A. 4: XRD pattern for Burgersdorp Formation sandstone 123

Figure A. 5: XRD pattern for Dolerite of the Karoo Suite 124

Figure A. 6: XRD pattern for Sandstone of the Molteno Formation 125

Figure A. 7: XRD pattern for Sandstone of the Molteno Formation 126

Figure A. 8: XRD pattern for Sandstone of the Molteno Formation 127

Figure A. 9: XRD pattern for Molteno Formation sandstone..... 128

Figure E. 1: Profile A-A' gravity model for minimum density values. 142

Figure E. 2: Profile B-B' gravity models for minimum density values 143

Figure E. 3: Profile C-C' gravity model for minimum density values 144

Figure E. 4: Profile D-D' gravity model for minimum density values 145

Figure E. 5: Profile E-E' gravity model for minimum density values. 146

Figure E. 6: Profile A-A' gravity model for maximum density values..... 147

Figure E. 7: Profile B-B' gravity model for maximum density values. 148

Figure E. 8: Profile C-C' gravity model for maximum density values. 149

Figure E. 9: Profile D-D' gravity model for maximum density values..... 150

Figure E. 10: Profile E-E' gravity model for maximum density values..... 151

LIST OF TABLES

Table 2. 1: Lithostratigraphy of the Karoo Supergroup in the Eastern Cape Province compiled by the Council for Geoscience [Johnson <i>et al.</i> , 2006]	12
Table 3. 1: Formulae for calculating dry and particle, wet densities and porosity of rock samples.....	28
Table 3. 2: Dry, particle and wet densities, and porosity	28
Table 4. 1: Radioelement concentrations in different rock types [Killeen, 1979].....	50
Table 7. 1 Rock density values used for gravity profile modelling. Units are in g/cm ³	91
Table 7. 1 Rock density values used for gravity profile modelling. Units are in g/cm ³	91
Table 7. 2: Minimum thicknesses of the Karoo Supergroup sediments along different profiles.	101
Table 7. 3: Maximum thicknesses of the Karoo Supergroup sediments along different profiles.	101



University of Fort Hare
Together in Excellence

CHAPTER 1: INTRODUCTION

1.1 Background

The Karoo Basin is an extensive, dry, relatively flat area at high altitude that covers 700,000km² of South Africa, which mostly is the internal part of South Africa [Catuneanu *et al.*, 1998; Johnson *et al.*, 1996]. According to Catuneanu *et al.* [1998], the Karoo Supergroup is believed to have developed from the Gondwana Supercontinent. The Karoo Basin sediments were deposited from the late Carboniferous (300 Ma) to the middle Jurassic (180 Ma) and these attain a total cumulative thickness of ~12 km in the southeastern portion of the Main Karoo Basin towards the eastern end of the Karoo Trough (a linear east-west zone of maximum subsidence along the southern basin edge) [Johnson *et al.*, 1996]. The Karoo Basin sediments were later intruded by dolerite dykes and sills during a magmatic activity that took place on the whole Southern Africa subcontinent during the breakup of Gondwanaland [Johnson *et al.*, 1996].

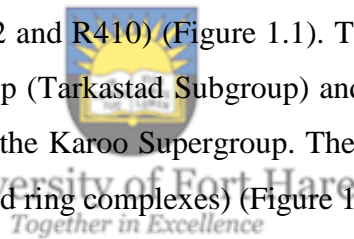
These intrusives represent roots and feeders of the extrusive Drakensberg basalt and one of the biggest flood basalt in the world [Duncan *et al.*, 1997; Fitch and Miller, 1984; Richardson, 1984]. The dolerite intrusions comprise of an intense network of dykes and sills with many sills bodies being saucer-shaped [Chevallier *et al.*, 2001; Malthe-Sørensen *et al.*, 2004; Polteau *et al.*, 2008]. Most of the igneous bodies are emplaced at the contact between the Dwyka and Ecca and between the upper Ecca and lower Ecca and lower Beaufort Group [Chevallier and Woodford, 1999]. The dolerites are important for groundwater retention and exploration since Karoo sedimentary rocks such as mudstones have low permeability [Nhleko, 2008]. Karoo fractured aquifers are associated with dolerite intrusions as they store groundwater in interconnected fractures that have formed in the sediments. Good water yielding capacity has been associated with the Karoo dykes [Chevallier and Woodford, 2002,] and fractured sediments above the sills [Botha *et al.*, 1998; Burger *et al.*, 1981]. The dolerite intrusions and surrounding geology can be mapped using airborne magnetic, gamma-ray spectrometry and gravity methods.

Airborne magnetic and gravity methods are geophysical tools that are capable of delineating the subsurface geology in terms of its lithology, structures (fractures, shear zones, folds, veins, sills, dykes and faults) and hydrothermally altered zones [Akulga, 2013]. These methods are reliable in mapping dolerite intrusions.

Radiometric or gamma-ray spectrometry method is used to characterize the regolith of up to 40 cm below the Earth's surface [Cooke *et al.*, 1996]. Mineralogical and geochemical studies of rocks and soils play a fundamental role in corroborating the interpretation of gamma ray spectrometry surveys, as they provide insight in the mode of occurrence of the radioelements and their petrogenetic or pedogenetic associations [IAEA, 2013]. Sedimentary environments can be distinguished from igneous or metamorphic environments through the use of radiometric data. Further, any near surface igneous intrusions in the sediments such as in the study area can be mapped using the gamma ray technique.

1.2 Location of the study area

The study area is located in the Eastern Cape Province of South Africa and covers two 1: 50 000 scale map sheets namely 3126DB Vaalbank and 3127CA Lady Frere. Geographically, the study area lies within the latitudes 31°30'S and 31°45' and longitudes 26° 45'E and 27°15' E. The study area has villages (e.g. Matyantya and Agnes), one town (Lady Frere) and three major accessible roads (R344, R392 and R410) (Figure 1.1). The geology of the study area belongs to the upper Beaufort Group (Tarkastad Subgroup) and the lower Stomberg Group (Molteno and Elliot formations) of the Karoo Supergroup. The Karoo sediments have been intruded by dolerites (dykes, sills and ring complexes) (Figure 1.2).



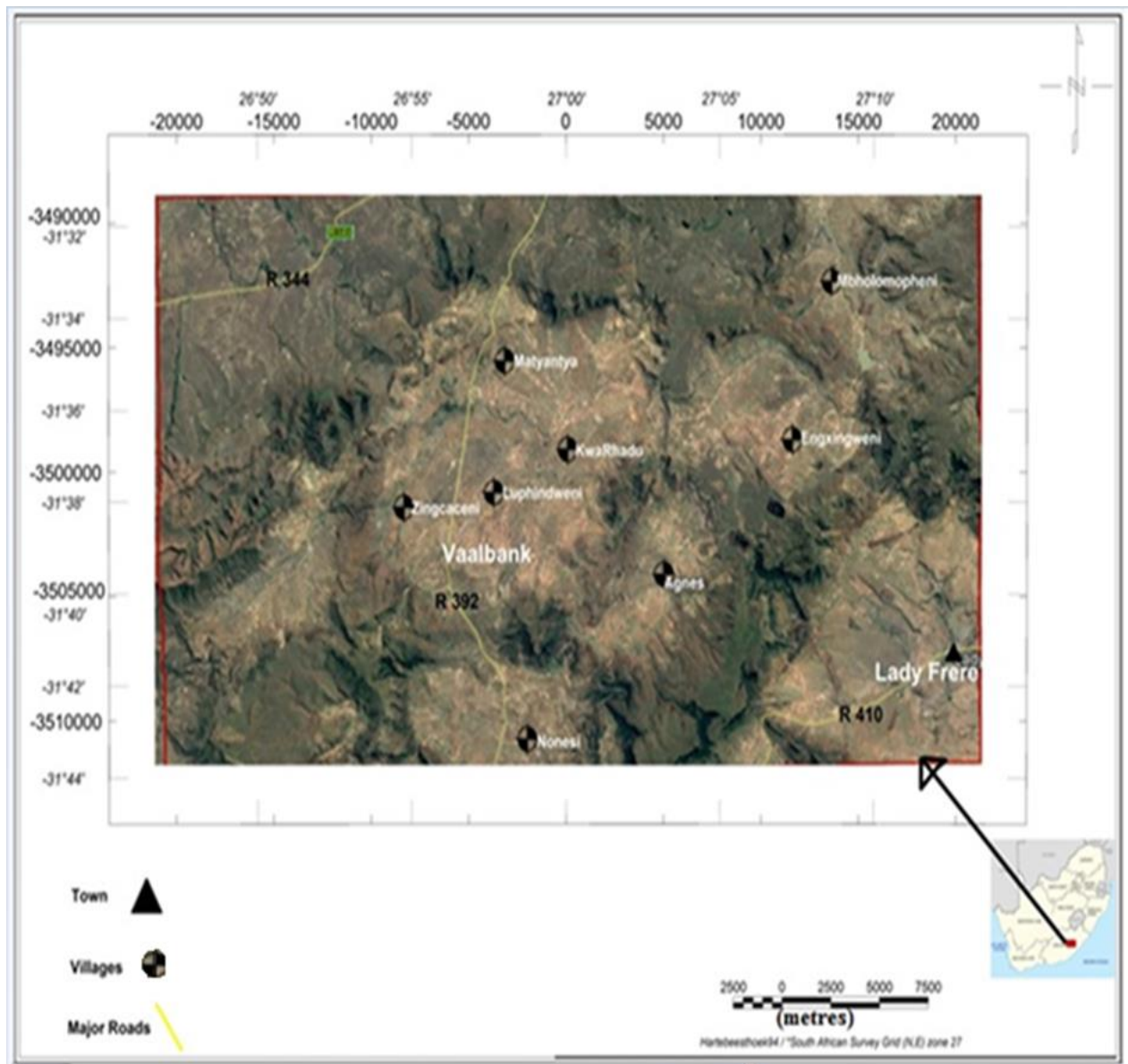


Figure 1. 1: Google Earth view map of the study area [Google Earth, accessed on 02-03-2017].

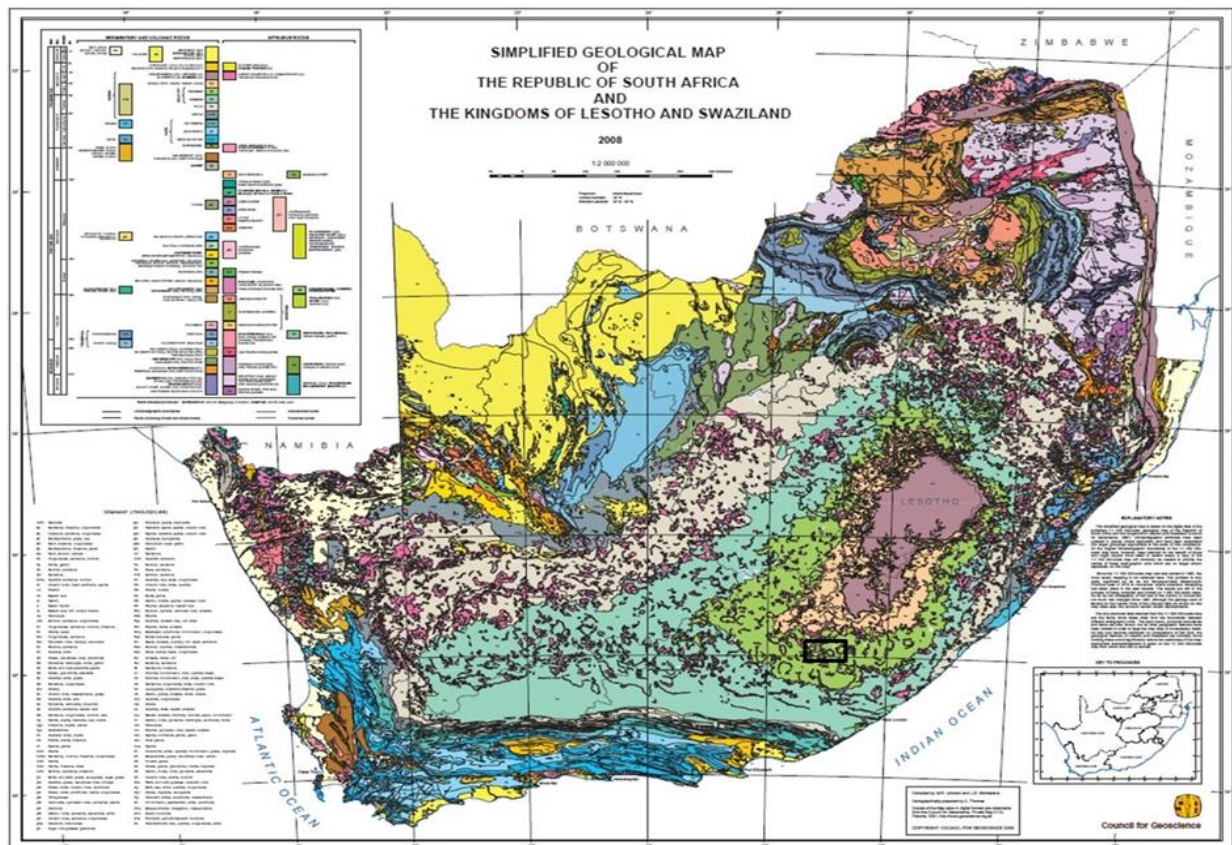


Figure 1. 2: The geological map of South Africa [Council for Geoscience]. The rectangle indicates the study area.


 University of Fort Hare
Together in Excellence

1.3 Climatology

The Karoo is classified as a semi-desert region that receives rainfall as little as 400 - 800 mm during the summer season with the exception of the south eastern region, which receives rainfall throughout the year [Low and Rebelo, 1996] in [Nxantsiya, 2017]. In general, the Karoo region is an arid, windy region with average temperatures rising as high as 43° C in the summer season and it becomes extremely cold during winter months (5° C). The western and eastern Karoo regions have mean annual precipitation ranges from 300 mm to more than 1000 mm.

There is a direct correlation between elevation above sea-level and rainfall; the higher elevation areas receive more rain [Smart, 1998] in [Nhleko, 2008]. The topography of the study area ranges from 977 m to 2063 m as shown the digital terrain map (Figure 1.3). The dolerite rings may be large scale features forming topographic highs, and controlling

morphology. These topographic highs receive more rainfall than the flatter inner part of the ring system (topographic lows). This means that the study area receives orographic rainfall and the areas away farther from the dolerite rings receive normal rainfall.

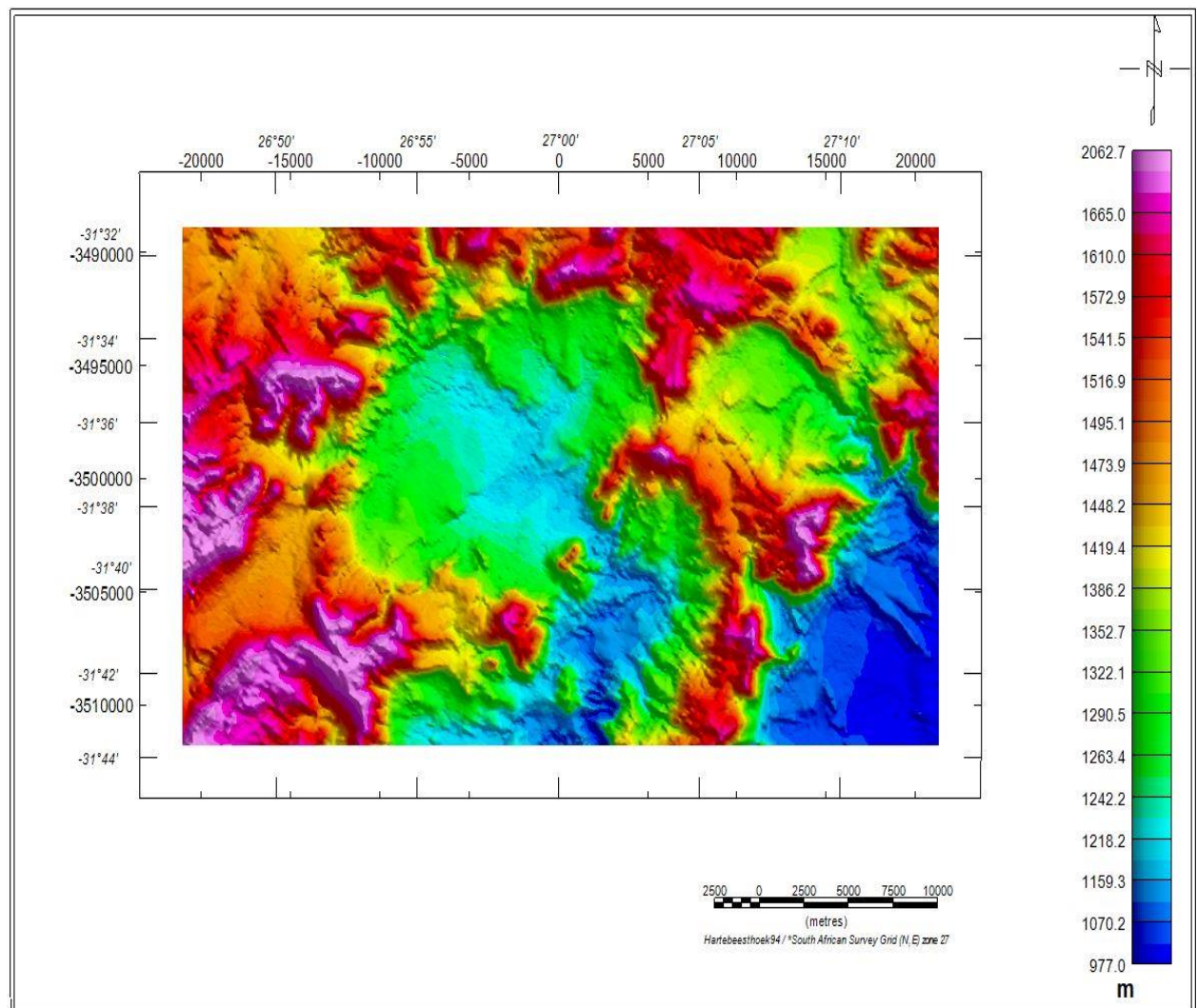


Figure 1. 3: Digital terrain map showing topographic highs and lows of the study area [Council for Geoscience].

1.4 Problem statement

South Africa has been experiencing serious drought since 2015, with associated crop losses, water restrictions, and impacts on food and water security [DEA, accessed on October 2018]. This also led to water shortages in a number of public water supply schemes/dams. Groundwater is much slower to be affected by drought than surface water and this groundwater is a good buffer against drought conditions worldwide. The geology of the study

area which includes 3126DB Vaalbank and 3127CA Lady Frere is quite complex considering the fact that the area was intruded by multiple dolerite sills and dykes at about 183 Ma [Chevallier and Woodford, 1999; Svensen *et al.*, 2007]. Several groundwater investigations have been carried out on the dolerite intrusions in the Karoo in the past. These intrusions are associated with high yields and sustainable groundwater potential shown by exploration drillings [Smart, 1998]. Generally, in the Beaufort Group, the sills form nested saucer-shaped intrusions with a thickness of about 100 m [Woodford and Chevallier, 2002]. The sills are less common in the uppermost part of the Karoo Basin (Stormberg Group) when compared to the dykes that form about 120-180 km long lineaments (i.e. the 100-200 m wide gap dykes) [Johnson *et al.*, 1996; Catuneanu *et al.*, 2005].

Despite the fact that published data give a vast amount of information on the geology, stratigraphy and lithostratigraphy of the Beaufort and Stormberg Groups, there is still insufficient information available to review the network of dolerites in the study area. Also, the identified dolerites in the area have not been thoroughly mapped or modelled in order to unravel the basin architecture, which will provide a reference for future groundwater exploration projects in the area. Hence, there is an urgent need to use geophysical techniques to investigate the geology of the study area in order to reveal the extensive network of dolerites that are known to be good groundwater targets.



University of Fort Hare
Together in Excellence

1.5 Aim and objectives

The aim of the research is to use geophysics to map the subsurface geology such as sediments, basement, intrusions and faults.

In order to achieve this, the following objectives were considered;

- i. To use existing gravity, magnetic and gamma-ray spectrometry data to generate geophysical maps in order to reveal sub-surface geologic structures of interest such as dolerite intrusions in the study area; use the power spectra of gravity and magnetic data to estimate average depths of the sources.
- ii. Measure the densities (dry, wet and particle or grain) of rocks using Archimede's principle as well as calculate the porosity of the rocks.
- iii. To elucidate the formations of the Beaufort and Stormberg Groups in the Vaalbank and Lady Frere areas by building simple models using forward modelling of gravity data along a number of profiles traversing the study area; hence establish the

orientation of and relationships between geological structures (interconnectivity of dolerite intrusions) at depth.

- iv. To identify the mineral composition of the rocks outcropping in the study area using petrography and XRD analyses.

1.6 Research questions

Below are the research questions;

- i. Which geophysical data can be used to generate maps that reveal the subsurface geologic structures?
- ii. How to obtain densities of rocks as well as to calculate their porosity?
- iii. How to explain the formations of the Beaufort Group and Stomberg Group; in terms of the orientation of the rocks and relationships between geological structures?
- iv. How to identify the mineral composition of the rocks of the study area?

1.7 Rationale of the study



Knowledge of the location of the geological structures and their configuration in depth is crucial information needed for groundwater exploration. Hence the need for field observations, collection of rock samples for density and porosity determination, petrographic and XRD analyses, the use of air airborne gamma-ray spectrometry, aeromagnetic and gravity data to map the surface and subsurface geology.

1.8 Delineation and limitation

The study will use geophysical data to map the geology and locate geological structures that are likely to be targeted for groundwater, by generating maps and creating gravity models. The mineralogy of the rocks will also be determined to aid the geophysical interpretation.

1.9 Structure of dissertation

This dissertation is divided into eight chapters. A summary of the five chapters and an overview of the scope of the study are provided in this section.

Chapter 1 provides the research and geological background of the study, the geographic location of the study area and the climate of the study area is explained in this chapter. The aim and objectives and problem statement of the research are presented in this chapter.

Chapter 2 is a synthesis of the relevant literature on the regional geology of the Karoo Supergroup with also literature on the local geology of the, Burgersdorp, Molteno, and Elliot Formations, and the Karoo dolerite which intrudes these formations.

Chapter 3 presents the methodologies and materials used in the research to achieve the research aim. These methods include the desktop studies, data collection and laboratory studies (i.e. density and porosity, petrographic and XRD analyses), the instruments and the software used in the research.

Chapter 4 presents the gamma-ray spectrometry method. This chapter comprises of the introduction of the method, data acquisition and processing, data enhancement done on the radiometric grid data, data presentation and interpretation, discussion and the conclusion.

Chapter 5 presents the magnetic method. This chapter comprises of the introduction of the method, data acquisition and processing, data reduction, data enhancement done on the magnetic grid data, data presentation and interpretation, discussion and the conclusion.

Chapter 6 presents the gravity method. This chapter comprises of the introduction of the method and processing and data reduction, data enhancement done on the gravity grid data, data presentation and interpretation, discussion and the conclusion.

Chapter 7 discusses the generation of models using gravity data, elevation data, and rock densities to create simple gravity models of the geology, presentation and interpretation of models and conclusions.

Chapter 8 includes a summary of findings, discussions, conclusions and recommendations. This is where the major contributions of the research are presented. It also compares the results obtained from the research with other previous work and how it links with geology.

CHAPTER 2: LITERATURE REVIEW

2.1 Geology

2.1.1 Introduction

The study area belongs to the Karoo Supergroup where the word “Karoo” comes from the Main Karoo Basin of South Africa which describes the sedimentary fill of all other basins of similar age across Gondwana. The Karoo Basin is a retro-arc foreland basin developed in front of the Cape Fold Belt in relation to subduction of the Paleo-Pacific plate beneath the Gondwana plate [Lock, 1978; 1980; Winter, 1984; Johnson, 1991]. The Karoo-aged basins formed during a first order cycle of supercontinent assembly and breakup when Pangaea was under the influence of two different tectonic regimes sourced from the convergent (southern) and divergent (northern) margins of Gondwana [Rust, 1975; Bumby and Guiraud, 2005; Catuneanu et al., 2005]. The Karoo Supergroup is a thick succession of sedimentary rocks that accumulated a basin in southwestern Gondwana [Smith, 1995]. Accumulation of Karoo aged successions in Africa is related to the Pangea first-order phase of supercontinent assembly and breakup.



University of Fort Hare
Together in Excellence

2.1.2 Kaapvaal Craton

The Kaapvaal Craton is an ancient segment of continental crust which formed in southern Africa during the Archaean Eon about 3.7 Ga to 2.7 Ga [Robb and Meyer, 1995]. The craton has not altered for 3000 Ma from when it was formed and is buried beneath younger rocks [MacDonald *et al.*, 2005]. The formation of the craton is by an extensive granitoid basement and amalgamation with arc-like oceanic terranes and associated igneous intrusions around its margin [de Witt *et al.*, 1992; McCarthy and Rubidge, 2005].

The craton is bordered on the north by the high-grade Limpopo Mobile Belt, initially formed when the Kaapvaal and Zimbabwe cratons collided 2.6 billion years ago [Robb and Meyer, 1995]. On its southern and western margins, the craton is bordered by the Namaqua-Natal Proterozoic orogens, and it is overlapped on the east by the Lebombo sequence Jurassic rocks recording the breaking Gondwana. The collision between the two cratons not only saw the formation of the Limpopo Belt but also formed the Witwatersrand Supergroup (2.97-285 Ga) [Robb and Meyer, 1995]. The Kaapvaal Craton contains two basins of vast enrichment which

are of economic importance in South Africa, the basins known as the Witwatersrand and the Karoo basins. The craton is composed of granitoids, granites, gneisses and greenstones.

2.2 Stratigraphy of the Karoo Supergroup

The main Karoo Basin is formed on the ancient Kaapvaal Craton and forms the thickest and most complete stratigraphic sequence of be approximately 110 Ma from Late Carboniferous - (~300 Ma) to Mid-Jurassic (~180Ma). This 12 km thick succession of sediments comprises of rocks which were deposited successively in glacial, deep marine (including turbidite), shallow marine, deltaic, fluvial, lacustrine and aeolian environments [Johnson *et al.*, 1996]. The Karoo Supergroup is subdivided stratigraphically into five main major groups with subgroups, formations and members within the major groups (see Figure 2.1 and Table 2.1). The Karoo Basin fill started with the deposition of the Late Carboniferous glacial sediments of the Dwyka Group with a thickness of approximately 600 m - 700 m [Johnson *et al.*, 2006]. This formation is overlain by the postglacial Permian marine shale, mudrock, sandstone and rhythmite units of Eccu Group (Prince Albert, Whitehill, Collingham, Ripon, Fort Brown and the Waterford Formations) [Smith *et al.*, 1993]. Following the Eccu Group the Late Permian - Early Triassic Beaufort Group was emplaced on fluvial environment (Koonap, Middleton, Balfour, Katberg and Burgersdorp Formations). The group above the Beaufort Group is the Middle Triassic age Stormberg Group (Molteno, Elliot and Clarens Formations). The youngest group consists of basalt and pyroclastic deposits of the Drakensberg Group, which is the last set of rocks to be deposited in the Karoo Supergroup.

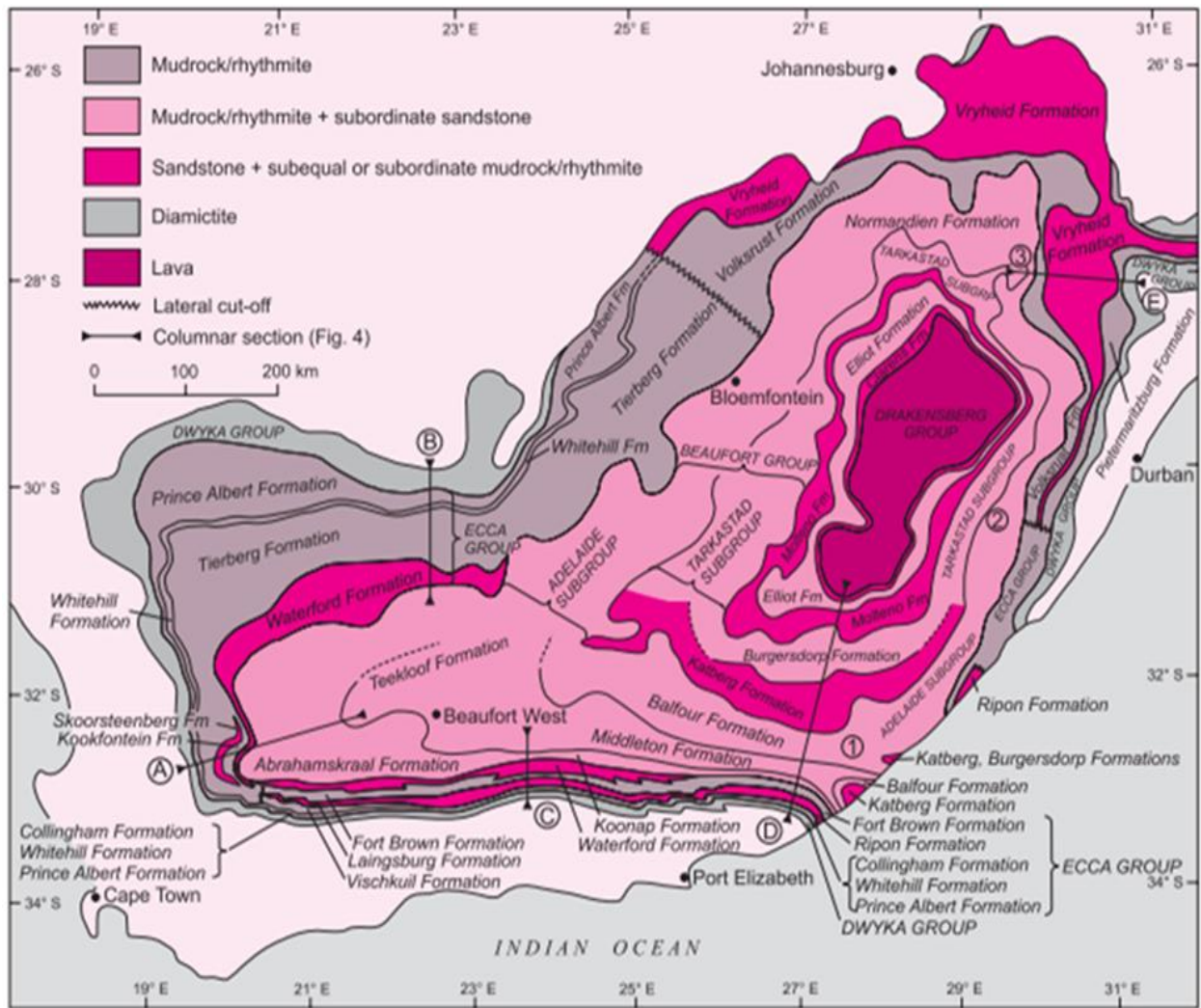


Figure 2. 1: Stratigraphic subdivision of the Karoo Supergroup in the main Karoo Basin of South Africa [Modified after Johnson et al., 1996].

Table 2. 1: Lithostratigraphy of the Karoo Supergroup in the Eastern Cape Province compiled by the Council for Geoscience [Johnson *et al.*, 2006]

SUPERGROUP	GROUP	SUBGROUP	FORMATION	LITHOLOGY	MAXIMUM THICKNESS (m)
KAROO	STOMBERG		Drakensberg	Basalt Lava	1400
			Clarens	Sandstone	300
			Elliot	Red Mudstone Sandstone	500
			Molteno	Coarse Sandstone Grey & Khaki	450
		TARKASTAD	Burgersdorp	Red Mudstone Sandstone Light Grey Sandstone Grey Shale	1000
			Katberg	Light Grey Sandstone Red Mudstone	900
				Red Mudstone Light Grey	50
				Sandstone Siltstone	700
	BEAUFORT				

		ADELAIDE	Balfour	Light Grey Sandstone	100
				Grey Shale Sandstone Siltstone	1200
				Light Grey Sandstone Khaki Shale	100
			Middleton	Grey & Black shale	1500
				Light grey Sandstone	
				Red mudstone	
	ECCA	University of Fort Hare Together in Excellence	Koonap	Grey Sandstone Shale	1300
			Waterford	Sandstone	800
			Fort Brown	Shale	1500
			Ripon	Sandstone Shale	1000
			Collingham	Grey Shale Yellow	30
			Whitehill	Black Shale Chert	70
			Prince Albert	Khaki Shale	120
	Dwyka			Diamicite, Tillite, Shale	750

2.2.1 Dwyka Group

According to Linol *et al.* [2016] the Dwyka Group is the lower most units of the Karoo Supergroup that have been deposited between the mid Carboniferous to Early Permian. This unit consists predominantly of massive diamictite of glacial origin and subordinate varved deglaciation shale and sandstone units with a maximum thickness of 800 m [Toerien and Hill,

1989; Visser, 1989; Linol *et al.*, 2016]. The diamictites are thinly bedded to massive, and contain matrix-supported clasts of pebble to cobble-sized rocks. The clasts show a wide range of compositions and rock types such as vein quartz, quartzite, banded ironstone, dolomite, slate, granite, gneiss, and amygdaloidal lava in an argillaceous and arenaceous matrix [Smith *et al.*, 1993]. According to Catuneanu and Elango [2001], the deeper marine glacial facies of the Dwyka Group, including those of the early Eccca Group, accumulated during the under-filled phase of the fore-land basin. In the south, as Catuneanu *et al.* [1998] explained, the Dwyka succession has a uniform character with lateral continuity of layers suggesting that deposition from floating ice within a large marine basin was the dominant process. Bamford [2004] also agrees and explained that the tillites are uniform and laterally extensive, having formed in a glacial marine environment with deposition from both grounded and floating ice.

2.2.2 Eccca Group

The Eccca Group is a sequence that accumulated between the Late Carboniferous Dwyka Group and the late Permian–Middle Triassic Beaufort Group, occupying most of the Permian time of the Karoo Supergroup [Catuneanu *et al.*, 2005]. The Eccca represents the final deglaciation of Gondwana. This sequence is marked by mostly black, organic rich shales directly above the Dwyka Group. The Eccca Group consists of deep-water and coastal sediments that were deposited in a closed interior water body [McCarthy and Rubidge, 2005]. The sediments of the Eccca Group comprise of mudstones, siltstones, sandstones, minor conglomerates and coal. The lower Eccca Group is made up of inter-bedded mudstone and sandstone that represent turbidite deposits accumulated within a shallow inland sea (Eccca Sea). The Eccca sea was saturated by glacial meltwater, and its southern margin began to prograde northeast following the deglaciation of Gondwana [Johnson *et al.*, 2006]. Progradation occurred as large deltas built out across the coastline, resulting in thick deposits that overlie the Dwyka turbidite sequences. This transgression is also revealed by the distribution of the turbidities, which show deposition in increasingly shallow environments over time [Johnson *et al.*, 2006]. Deltaic and coastal plain deposition eventually filled enough of the basin to end an Eccca sea, and the dominant depositional setting became broad alluvial flood plains. The Eccca Group consists of six formations, namely, the Prince Albert Formation, Whitehill Formation, Collingham Formation, Ripon Formation, Fort Brown Formation and the Waterford Formation.

2.2.3 Beaufort Group

The Beaufort Group is the first fully continental sequence in the Karoo Supergroup, and is divided into Permian Adelaide Subgroup (further separated into the Koonap, Middleton, and Balfour Formations) and the overlaying Triassic Tarkastad Subgroup (separated into the Katberg and Burgersdorp Formations) [Johnson *et al.*, 2006]. The western side of the Adelaide Subgroup is more divided into lower Abrahamskraal and Teekloof formation [Keyser and Smith, 1977/78]. According to Johnson *et al.* [1996] in the western part of the basin, the lower Abrahamskraal Formation attains a maximum thickness of about 2500 m while the upper Teekloof Formation attains a thickness of approximately 1400 m with its upper contact being eroded. Cole and Smith [2008] used the presence of chert beds with more abundant sandstone and a paucity of reddish-maroon mudrock to distinguish between the Abrahamskraal and Teekloof Formations. The Beaufort Group consists of mostly red and purple sandstone that are fining upwards into red-purple mudstone with inclusions of abundant vertebrate fossils, cracks and paleopedogenic carbonate nodule horizons [Smith *et al.*, 1993].



A. Katberg Formation

The Katberg Formation is the formation of the Tarkastad Subgroup and it consists of the lower 700 m thick sandstone-rich (>30 %) [Hancox, 1998]. The sandstone of the Katberg Formation are light brownish grey or greenish grey sandstones and are fine to medium grained, with scattered pebbles that are up to 15 cm in diameter that are usually present in coastal outcrops [Johnson *et al.*, 1996]. The sedimentary structures that are mostly seen on the sandstones of the Katberg Formation are horizontal lamination with parting lineation and cross-bedding (both trough and planar) [Johnson *et al.*, 2006].

B. Burgersdorp Formation

Above the Katberg Formation is the Burgersdorp Formation (mudstone-rich and sandstone rich) 700 m thick [Hancox, 1998]. The Burgersdorp Formation comprises of fine grained sandstones are light brownish grey or greenish grey in colour and show a distinct horizontal lamination, cross-bedding and ripple lamination [Johnson *et al.*, 2006].

2.2.4 Stormberg Group

According to South African Committee for Stratigraphy [SACS, 1980] there are no unifying lithological features in the various units of the Stormberg Group which makes them different from all the geological groups of the Karoo Basin. The committee also suggested to discontinue the use of “Stormberg” as a group title to formally describe the lithostratigraphy of Molteno, Elliot and Clarens Formations [Kent, 1980]. The Late Triassic-Early Jurassic age Stormberg Group in the southwestern region was deposited as a result of the final deformational phase in the Cape Fold Belt and subsidence of the southwestern Karoo Basin due to the compressive nature of tectonic regime of the Karoo Basin region was still active during the Late Triassic-Early Jurassic time [Hälbich, 1983]. The Stormberg Group is made up of the fluvial and aeolian-lacustrine successions of the Molteno, Elliot and Clarens Formations [Johnson *et al.*, 1996]. According to Cole [1992] in Catuneanu *et al.* [1998], the sandstone-rich Molteno Formation was deposited by low-meandering braided rivers, whilst the Elliot Formation was deposited by high- meandering (sinuosity) rivers.



A. Molteno Formation

The Triassic Molteno Formation in the main Karoo Basin, South Africa, forms a northerly thinning intracratonic clastic wedge deposited by sandy braided rivers of South Saskatchewan type [Turner, 1984]. The formation is dominated by horizontal tabular sheets of cross stratified medium- to coarse grained sandstone which were deposited by braided streams [Catuneanu *et al.*, 1998]. The Molteno Formation consists of the Bamboesberg Member, Indwe Member, Mayaputi Member, Qiba Member and Tsomo Member. According to Hancox [1998], the formation has a maximum thickness of 600 m in the southern outcrop and much thinner northward. Turner [1975] suggested that the deposition of the Molteno Formation was predominantly by bed-load dominated rivers flowing across extensive braid plains. Siltstone, mudstone and coal occur, but coal is far less abundant than the coal in Ecca Group, and these deposits are interpreted as the fills of abandoned channel tracts and within ponded bodies of water on the braid plain [Turner, 1975].

B. Elliot Formation

The Elliot Formation sequence highlights that depositional energy greatly reduced with time and that aeolian conditions prevailed towards the end of Elliot deposition [Visser and Botha, 1980]. The Elliot Formation comprises an alternating sequence of mudrock and subordinate fine to medium grained sandstone with a maximum thickness of about 500 m in the South fore deep area [Visser and Botha, 1980]. The Formation was deposited when the climate was changing to arid conditions hence the reddish mudstones. The top formation in the Stormberg Group is the Clarens Formation, which was deposited in a desert environment.

2.2.5 Drakensberg Group

There was a rapid change in environmental conditions in the Karoo Basin prior to the Middle Jurassic period associated with large movement of the Earth's mantle, the crust experienced a large scale lifting, and eruption of massive volumes of basaltic lava that make up the Drakensberg Group [Johnson *et al.*, 2006]. The basaltic lava spread across much of Gondwana about 180 million years ago indicating the start of Gondwana breakup. The magma penetrated and made its way to the surface along a complex system of fractures. The magma cooled and crystallised within fractures resulted in the dolerite sills and dykes (about 180 Ma). The Drakensberg lava that form the upper parts of the Drakensberg Mountain is made up of a thick succession of basalts that cap the Karoo sedimentary succession and covers some part of Lesotho, northern part of the Eastern Cape and mountain range along the western Kwazulu-Natal border.

2.2.6 Karoo dolerite suite

The Karoo basalts extruded at the top of the Karoo Supergroup sediments during the Mid-Jurassic (183 Ma) period of magmatic activity that took place during the breakup of Gondwana [Duncan *et al.*, 1997]. The magma extruded on the Southern African continent was estimated to the total volume of 10 million km³ [White, 1997]. The deeper portions of the intrusive system and the tectonic complexity that is not taken into consideration in other major continental systems in the world were revealed and exposed by larger scale erosion that took place in the main Karoo Basin (Figure 2.2).

Dolerite dykes, sills and rings of the Karoo represent the roots and the feeders of the Drakensberg volcanism (see Figure 2.3). These intrusions comprise of an intense network of dykes and sills, with many sill bodies being saucer shaped [Chevallier *et al.*, 2001; Malthe-Sørensen *et al.*, 2004; Polteau *et al.*, 2008]. The dykes, sills and rings form a complex, interconnected network that can possibly be attributed to one magmatic event [Chevallier and Woodford, 1999].

Flat lying dolerite sills (40 to 80 m thick) are well developed within the Ecca Group and at the base of the Beaufort Group, while saucer-shape dolerite rings are more common in the upper part of the succession i.e. Beaufort Group, Molteno and Elliot Formations [Chevallier *et al.*, 2001].

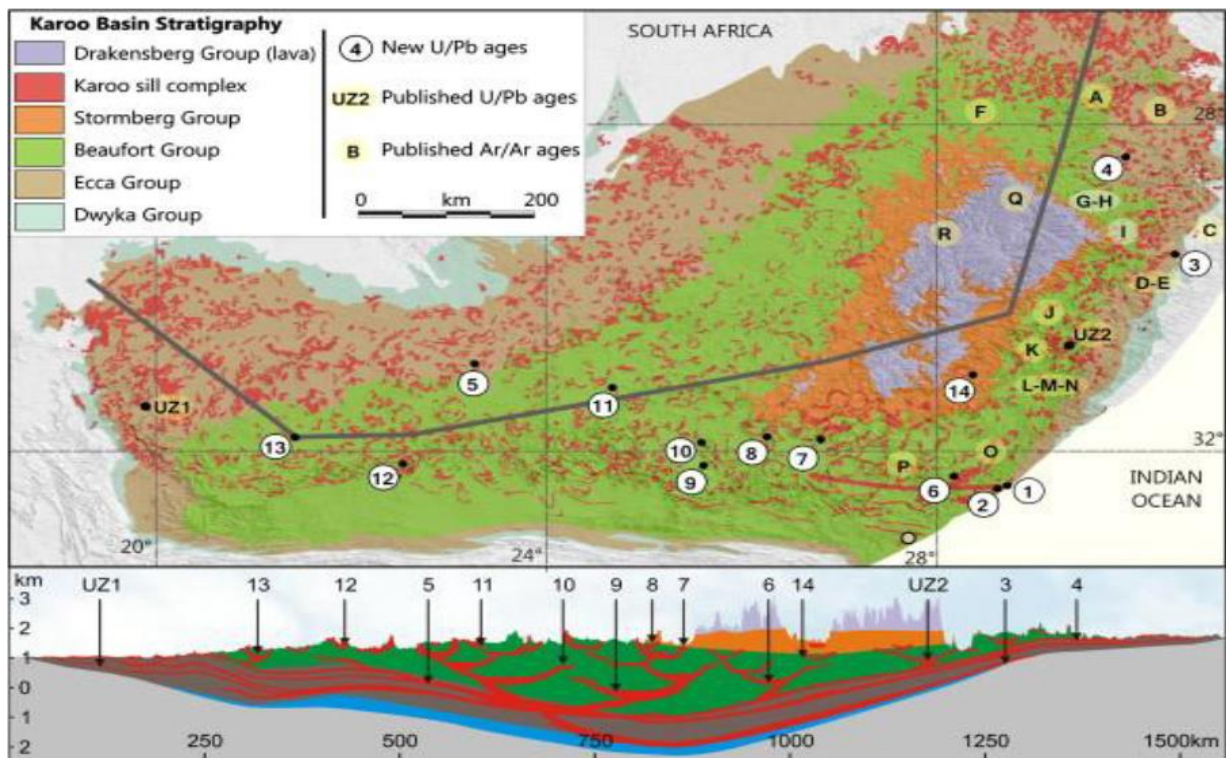


Figure 2. 2: Geographical distribution/widespread of the dolerite intrusions throughout the Karoo Basin of South Africa (<http://karoospace.co.za/dolerite-Karoo-fracking-game-changer>).

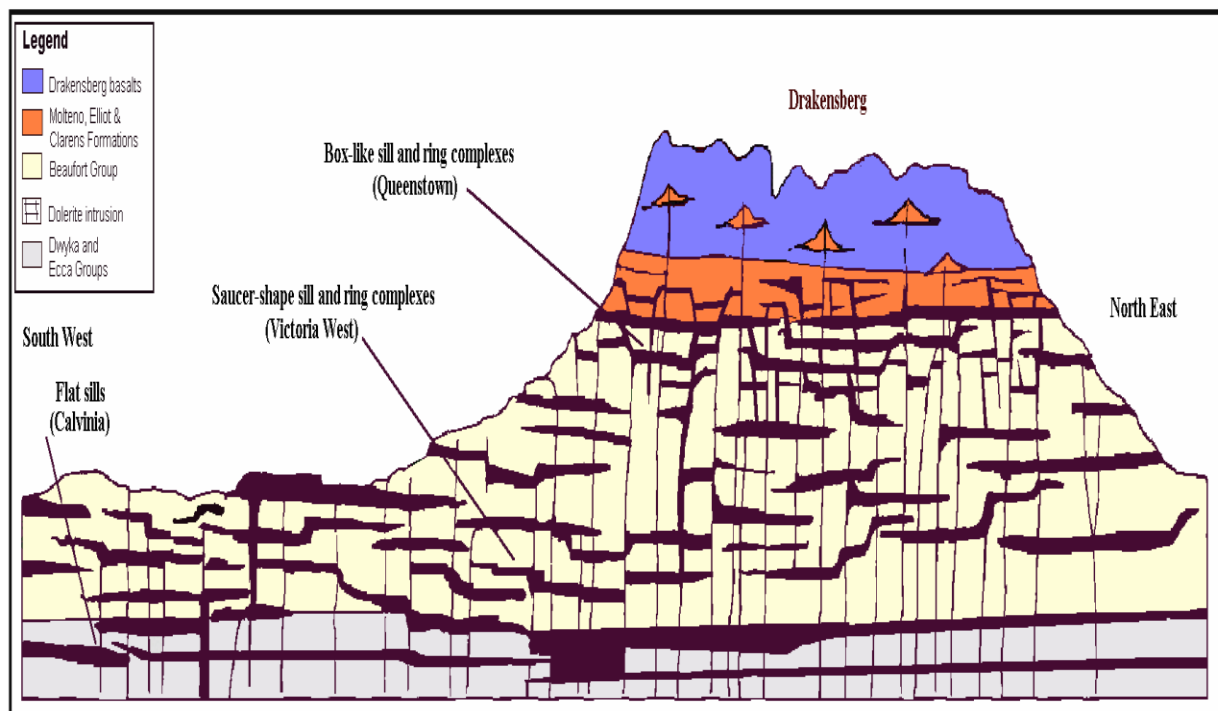


Figure 2. 3: Schematic SW-NE cross section of the Karoo Basin showing dolerite sills and dykes as roots and feeders of the Drakensberg [After Chevallier *et al.*, 2001]



University of Fort Hare
Together in Excellence

A. Dykes

A map of the Karoo dolerite dykes compiled from existing 1:250 000 scale geological maps, aerial photograph and satellite lineament interpretation reveals that there is an association between lithology and dolerite distribution [Chevallier and Woodford, 1999]. According to Chevallier *et al.* [2001], three major structural domains that are indicated by dyke distribution have been identified in the Main Karoo Basin (Figure 2.4). These domains are:

- i. The Western Karoo Domain: It extends from Calvinia to Middelburg and is characterised by two distinctive structural features; east west trending zone of long and thick dykes associated with right lateral shear deformation and north northwest striking dykes.
- ii. The Eastern Karoo Domain: It extends from Middelburg to East London and comprises two major dyke swarms, namely a major curvi-linear swarm of extensive and thick dykes diverging from a point offshore of East London and minor north northeast trending dykes.

- iii. The Transkei-Lesotho-Northern Karoo Domain: It consists of two swarms; northwest trending dykes in the Transkei region, curving to east-west in the Free State and northeast trending dykes mainly occurring within and alongside the Lesotho basalt.

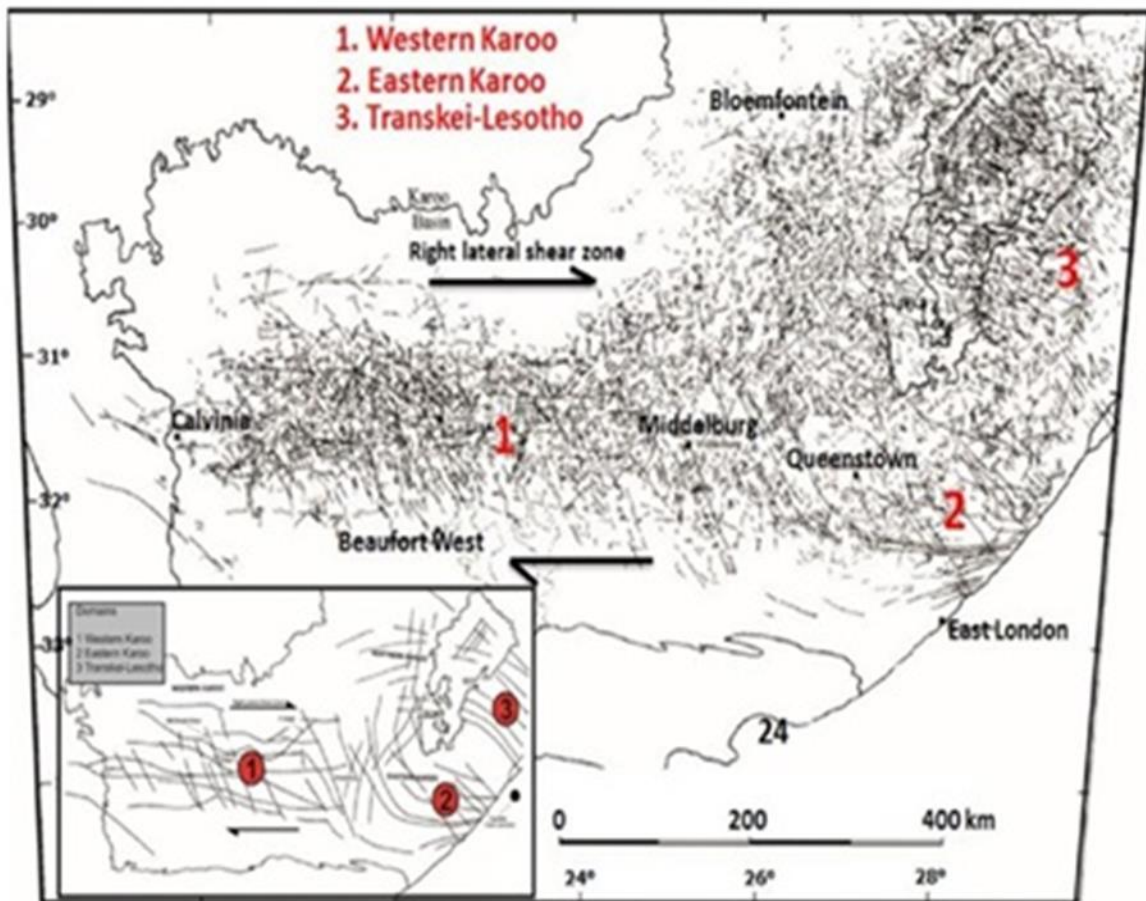


Figure 2. 4: Dolerite dykes of the main Karoo Basin. Insert in a simplified structural map showing three structural domains [After Woodford and Chevallier, 2002]

B. Sills and ring complexes

Du Toit [1905, 1920] in [Chevallier et al., 2002] described the sills and ring structures in the vicinity of Queenstown although structural interpretation of a three dimensional undulating sill producing a "basin and dome" or "egg-box" geometry is no longer valid. In the Beaufort Group, the sills form nested saucer-shaped intrusions with thickness of about 100 m. The sills are less common in the uppermost part of the Karoo Basin (Stormberg Group) when compared to the dykes that form about 120 -180 km long lineaments (e.g. the 100 - 200 m wide Gap dykes) [Johnson *et al.*, 1996; Catuneanu *et al.*, 2005; Svensen *et al.*, 2007]. Svensen *et al.*

[2007] suggested that the absence of sills in the Drakensberg Group lavas indicates that the sills were emplaced prior to the main phase of flood volcanism or that sill emplacement within the lava was prevented. Galerne *et al.* [2011] predicted that the Karoo sills are mostly tholeiitic basalts to basaltic andesite, however, some present-day sills evolved locally. One of the most noticeable features of the present Karoo landscape is the numerous dolerite sills and ring-complexes.

2.3 Geology of the study area

According to Cole and Cole [2003] the Vaalbank and Lady Frere are both underlain by rocks of the Beaufort Group formations (Katberg Formation which is very little exposed at these areas and Burgersdorp Formation), some of the Stomberg Group formations (Molteno and Elliot Formations) and also the Karoo dolerite suite which comprises of sills, dykes and ring complexes. On top of the Karoo Supergroup sediments there is Quaternary (alluvium) cover (Figure 2.5)



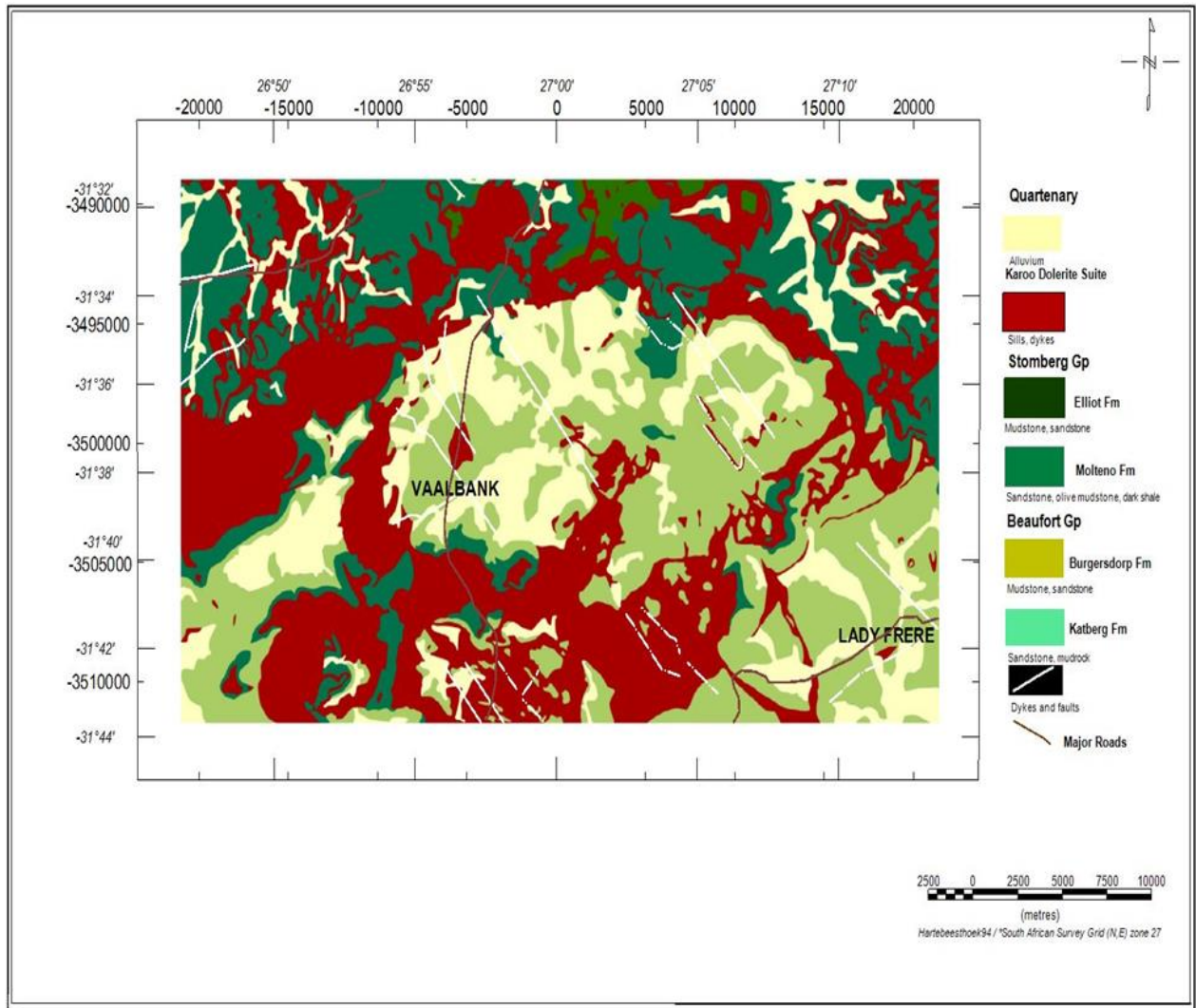


Figure 2. 5: Simplified geological map showing formations of the study area [From Council for Geoscience, created from geology database on -04/2017].

2.4. Significance of dolerite sill and ring structures on groundwater occurrence

There is a high density of dolerite intrusion in the Eastern Karoo [Woodford and Chevallier, 2002(b)]. These dolerite dykes and sills are important geological structures in the exploration of groundwater resources. As a dolerite intrudes into the Earth's crust, the heat (900-1200 °C) of the magma will cause a zone of contact metamorphism within the host rock, along the sides of the intruded body [Smart, 1998]. Joints and fractures occur in this zone of metamorphism as a result of cooling. A dolerite dyke or sill serves as a barrier for groundwater flow and water accumulates in this zone of contact metamorphism known as the baked zone, resulting in a possible good aquifer system [Smart, 1998].

According to Woodford and Chevallier [2002] dolerite dykes represent thin, linear zones of relatively higher permeability which act as conduits for groundwater flow within the aquifer. These dykes have always been the preferred drilling targets for ground water in the Karoo, away from the big valleys. Dyke contact aquifers are confined and yields around 2 to 3 l/s are common and enough for wind-pump supply. Transgressive oblique fractures extend tens of metres away from the dyke into the country rock. These transgressive fractures are related either to another dolerite sheet intrusion nearby or to late tectonic stress during the cooling and hydrothermal activity that followed the magmatic event. These fractures, together with other structural complication along the dykes (offshoots, en-echelon segmentation, change in dip, etc.), substantially improve the yield.

An exhaustive hydrogeological investigation of the lineaments, and specially dolerite dykes, was carried out for Victoria West sheet by Woodford and Chevallier [2001] and summarized by Woodford and Chevallier [1996] in Chevallier *et al.*, [2001]. Spatial analysis of the hydrocensus data shows a clear relation between borehole yields and lineaments. In area with high-density intrusives, a high percentage of boreholes with yield between 2 and 10 l/s are found, whereas in areas with the lower intrusives density lower yields (below 1.5 l/s) are encountered. Exploration drilling has also shown high success rates along dolerite dykes especially in structurally complex areas, with a high strike frequency and many yields above 3 l/s Woodford and Chevallier [2001] in Chevallier *et al.* [2001]. Dyke orientation also seems to play a role. Boreholes drilled into E-W trending regional intrusions showed the highest rate of success and shallow dipping, horizontally striking fractures cross cutting the dyke commonly deliver the highest yields Woodford and Chevallier [2001] in Chevallier *et al.* [2001].

On the Queenstown map sheet Vandoolaeghe [1980] and Smart [1998] in Chevallier *et al.* [2001] show that boreholes targeting dolerite are more successful than bore holes not - targeting dolerite, especially in the medium-range yields between 4 and 7 l/s. Boreholes along the Lehman's Drift dyke, west of Queenstown, once again show that transgressive cross-cutting oblique fractures play an important role on water occurrence and yields. Yields between 3 and 8 l/s were reported along the structure by Vandoolaeghe [1980] and Smart [1998] in Chevallier *et al.* [2001].

Dolerite sill and ring complexes have to a large extent been overlooked by hydrogeologists in the Karoo. However, Vandoolaeghe [1980] was the first to mention their ground water potential in the vicinity of Queenstown. He also stated that the presence of water bearing fractures near dolerite sheets is conditioned by three parameters: an optimal thickness of 30 to 50 m for the intrusion, the curvature in the sheet (from horizontal to inclined), and the relative position of the upper and lower sides of the sheet in respect of the regional piezometric head. From yield frequency histograms for the Queenstown area, Smart [1998] reports that "dykes appear to be more productive than dolerite sheets. However, in the same way that dolerite in general has not been adequately tested in this area, it is even more likely that dolerite sheets in particular have not been properly explored". Vandoolaeghe [1980] in Chevallier *et al.*, [2001] concludes that "exploration of these aquifers is not straightforward, even in the best cases" and that these aquifers do not stand out for their prolificacy, a blow yield of 10 l/s is considered to be good but 4 l/s is more near average.



CHAPTER 3: RESEARCH MATERIALS AND METHODOLOGY

3.1 Introduction

This chapter reveals an overview of the research methods and field equipment that have been used in this study to achieve its aims and objectives. These include geophysical and geological methods.

3.2 Desktop study

A desktop study was done throughout the project, which involves the consultation of online research published papers to give information about the study area and the geophysical methods used in the project. The geophysical data used in the project are mainly airborne gamma ray spectrometry, aeromagnetic and gravity data and these were analysed using Geosoft Oasis Montaj, Arc Map and GM-SYS packages.

3.3 Research instruments

- i. A Global Positioning System receiver
- ii. Hammer
- iii. Camera
- iv. Petrographic microscope
- v. Adam electronic weighing balance
- vi. Copper wire sample holder (loop)
- vii. Density bottle (100 ml)



3.4 The software packages

- i. Geosoft Oasis Montaj is a software package that was used to view, digitize existing and create maps, and generate gravity models.
- ii. Google Earth- used to view satellite image of the study area using the survey locality coordinates from the Council for Geoscience.

- iii. Arc Map10.4.2- an Arc GIS package that was used to extract the geology of the study area from a bigger map using its coordinates from the geology database and create a geology map of the study area.
- iv. GM-SYS- is a Geosoft package and this was used to create 2½ D gravity models. This was used to produce forward models from gravity profiles.

3.5 Geophysical data

Geophysics is the study of the physics of the solid Earth, its properties and how the Earth works. It is mainly used to get a better understanding of the subsurface and deeper parts of the Earth. Geophysical methods are widely used in ore, oil, gas and groundwater exploration. These methods map the physical changes of rocks to determine geological structures and lithology. There are a number of geophysical techniques and only the gamma ray spectrometry, magnetic and gravity methods will be presented in chapter 4 to 7.



3.6 Samples collected

A total of 24 rock samples were collected from the accessible formations in the study area. At least five fresh representative samples were collected along the road cuts outcrops from Molteno Formation, Burgersdorp Formation and Karoo dolerite suite.

3.7 Laboratory studies

The laboratory studies consisted of density and porosity measurements, analyses of thin sections and X-ray diffraction analyses.

3.7.1 Density measurements of rocks samples

Twenty-four rock samples were collected from three accessible Formations of the study area namely Burgersdorp Formation, Molteno Formation and the Karoo dolerite suite. The rock samples were dried in the sunlight for 2 days. Then the mass of each rock sample was weighed in air (M_d) and when immediately submerged (M_b) in water using an Adam PGW 4520e digital balance and an under hook sample holder (Figure 3.1). The rock samples were then

soaked in a water bath for at least 24 hours to allow the pore spaces to absorb and be saturated with water. The saturated samples were weighed still submerged in water to get a mass M_C .



Figure 3. 1: Photograph showing the procedure and equipment used in the laboratory for measuring rock densities using Archimedes' principle.

3.7.1.1 Density of water

The density of water was determined every 30 minutes during the mass measurements of the rock samples. A 100 ml density bottle was used to determine the density of water by measuring its mass when empty on the Adam PGW-3502e electronic weighing balance and measuring its mass when filled with water. The mass of the water was determined and the density was calculated. The obtained water density (ρ_w) was 1.015 g/cm^3 . The temperature was measured and it was constant at 21°C throughout the measuring period. The density of water was needed in the calculations of the three density types (refer to Table 3.1).

Table 3. 1: Formulae for calculating dry, particle and wet densities and porosity of rock samples.

TYPE OF DENSITY	FORMULA
Dry density	$\rho d = \left(\frac{Md}{Md - Mb} \right) \times \rho w$
Grain or particle density	$\rho g = \left(\frac{Md}{Md - Mc} \right) \times \rho w$
Porosity	$\phi = 1 - \left(\frac{Md - Mc}{Md - Mb} \right)$
Saturated or wet density	$\rho s = \rho d + \phi \rho w$

3.7.1.2 Density and porosity results

Table 3. 2: Dry, particle and wet densities, and porosity

Formation	Samples	Dry density (g/cm ³)	Particle density (g/cm ³)	Wet density (g/cm ³)	Fractional Porosity	Porosity (%)
Karoo dolerite						
	4A1	2.797	2.933	2.848	0.046	4.6
	4A2	2.941	2.965	2.951	0.008	0.8
	4C1	2.624	2.641	2.634	0.006	0.6
	5A	2.723	2.893	2.784	0.059	5.9
Average		2.771	2.858	2.804	0.030	3.0
Burgersdorp Fm						
	4B1	2.356	2.634	2.768	0.106	10.6
	4B2	2.587	2.623	2.597	0.014	1.4
	4B3	2.613	2.631	2.614	0.007	0.7
	4B4	2.642	2.659	2.643	0.006	0.6
	5B	2.654	2.802	2.705	0.053	5.3
	5C	2.192	2.386	2.273	0.081	8.1
	9A	2.471	2.540	2.502	0.027	2.7
	9B	2.418	2.563	2.434	0.057	5.7
	10A	2.567	2.629	2.628	0.024	2.4
	10B	2.315	2.543	2.335	0.090	9.0
	12A	2.460	2.623	2.521	0.062	6.2
	12B	2.207	2.580	2.339	0.145	14.5

	12C	2.469	2.559	2.509	0.035	3.5
Average		2.458	2.598	2.528	0.054	5.4
Molteno Fm						
	6A	2.548	2.638	2.893	0.034	3.4
	6B	1.557	2.545	1.953	0.388	38.8
	7A	2.329	2.614	2.441	0.109	10.9
	7B	2.567	2.587	2.577	0.008	0.8
	7C	1.827	2.643	2.121	0.309	30.9
	8A1	2.499	2.609	2.509	0.042	4.2
	8A2	2.006	2.289	2.138	0.124	12.4
Average		2.190	2.561	2.376	0.145	14.5

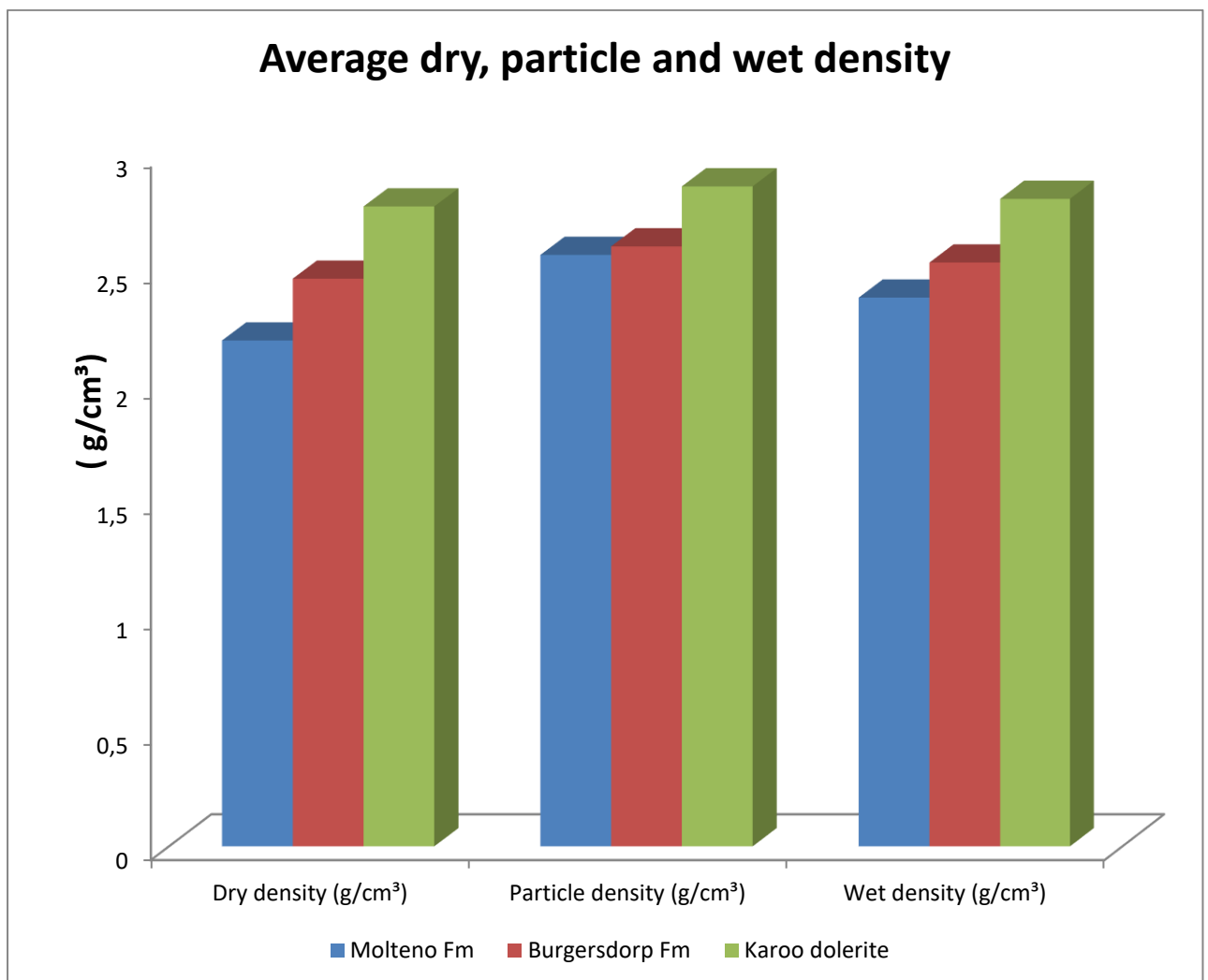


Figure 3. 2: Bar chart for average dry, particle and wet density of the study area geologic formations.

Figure 3.2 shows the average dry, particle and wet density of the rocks of the study area. The Karoo dolerite suite displays the highest densities for dry (2.624 -2.941 g/cm³), particle (2.641-2.965g/cm³) and wet/saturated densities (2.634-2.951 g/cm³). The Burgersdorp Formation which mostly has quartz rich sandstone displays the intermediate densities for dry (2.192-2.654 g/cm³), particle (2.386-2.802 g/cm³) and wet/saturated densities (2.273-2.768 g/cm³). The lowest densities for dry (1.557-2.567 g/cm³), particle (2.289- 2.643 g/cm³) and wet density (1.953 -2.893 g/cm³) are displayed by the Molteno Formation which consists of mostly weathered sandstone and mudstone.

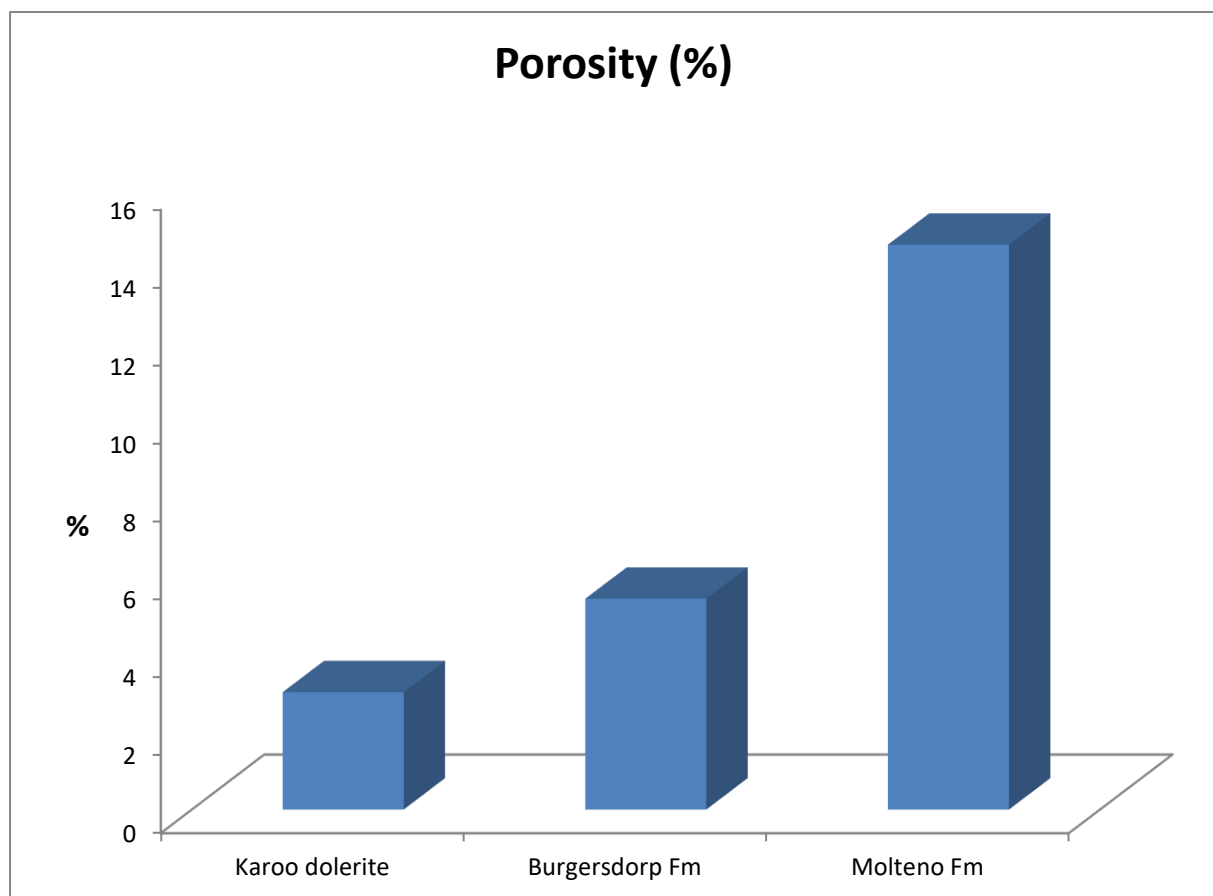


Figure 3. 3: Bar chart showing porosity of the study area geologic formations.

Figure 3.3 shows average porosity values calculated from the density measurements. High porosity values calculated are from the Molteno Formation with an average of 14.5 % which is mostly dominated by highly weathered sandstone. The Burgersdorp Formation has an intermediate average porosity of 5.4% and the Karoo dolerite suite has the lowest porosity of 3%.

3.7.2 Field observation and petrographic analysis

The rock samples that were collected from the study area along the road cuts were sent to CGS laboratory for thin sections preparation, for petrography study (in order to identify the mineralogical composition of rocks that may cause a high or low geophysical response, and porosity and grain maturity in the rock samples). The thin section were analysed using a petrographic optical microscope, Olympus CX 31, in the Department of Geology, University of Fort Hare.

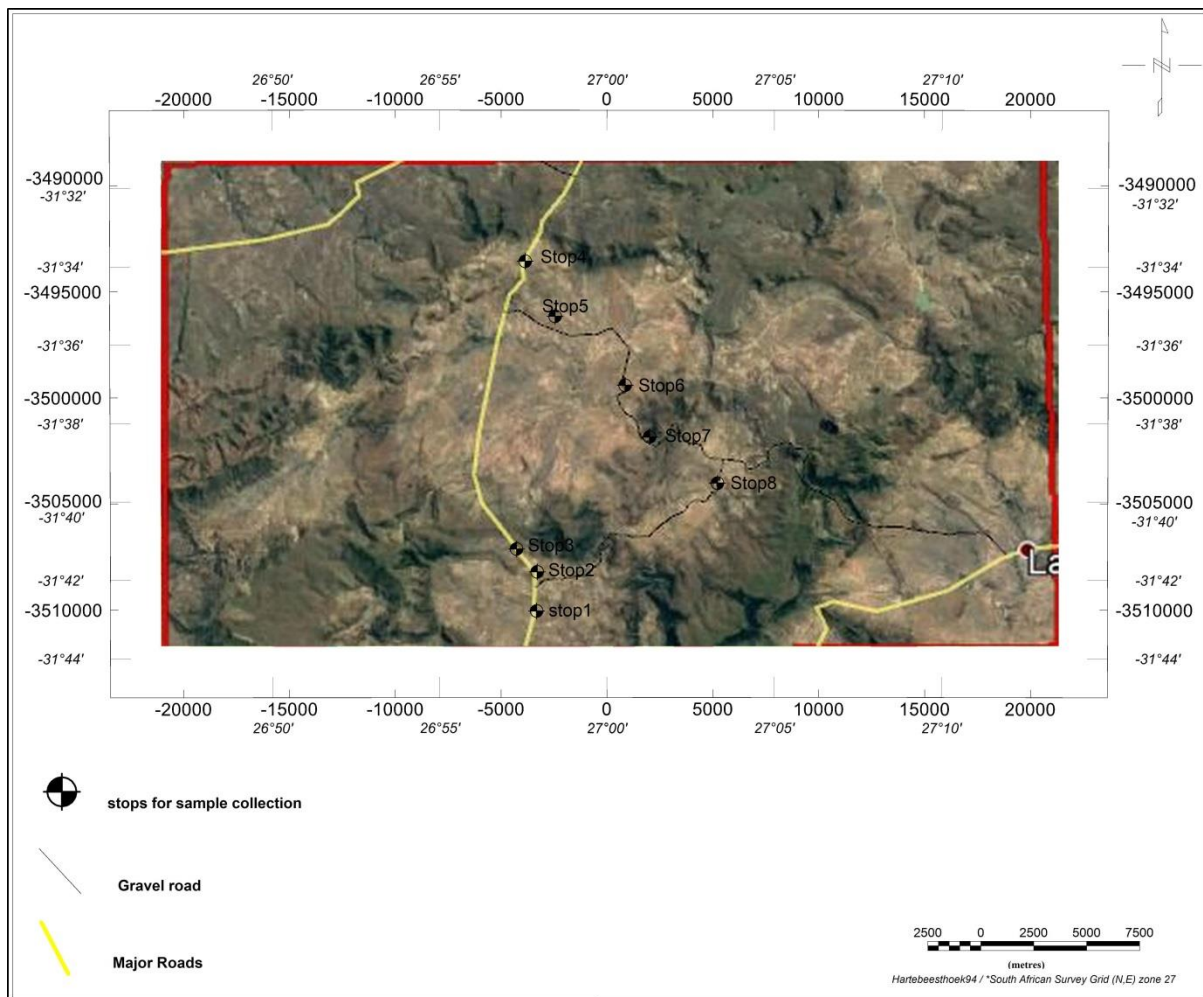


Figure 3. 4: Photograph showing the study area where samples were collected.

3.7.2.1 Field observation of the geology

A. Burgersdorp Formation

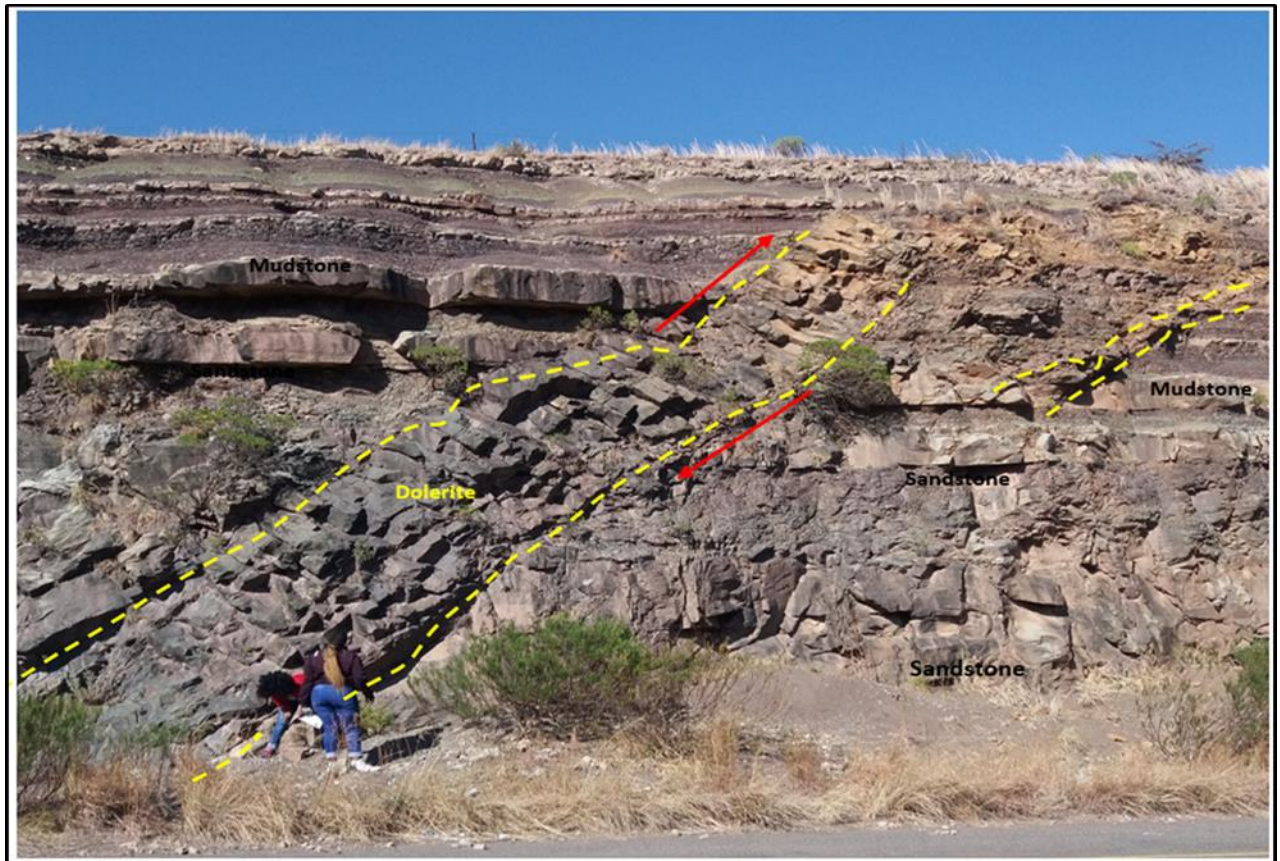


Figure 3. 5: Photograph displaying an outcrop of the Burgersdorp Formation consisting of dolerite dyke, fault, red mudstone and the sandstone. GPS coordinates: S 31° 33' 21.5" E 26° 57' 11.0".



Figure 3. 6: Picture displaying two outcrops of the Burgersdorp Formation. One outcrop is red mudstone and the second outcrop being sandstone and the fault that occurred on the sandstone. GPS coordinate: S 31° 38' 42.8" E 27° 01' 17.1".

Figures 3.5 and 3.6 display the Burgersdorp Formation, which is the youngest formation of the Beaufort Group. This outcrop of the Burgersdorp Formation displays light grey sandstone and red mudstone. These sediments are intruded by a dolerite dyke (Figure 3.6). The dolerite dyke resulted in a fault causing one block to move up and another block to move down on either side of the dyke

B. Molteno Formation



Figure 3. 7: Picture of an outcrop of the Molteno Formation having weathered sandstone.

GPS coordinate: S 31° 33' 21.5" E 26° 57' 11.0".

The Molteno Formation is the oldest formation of the Stormberg Group sitting on Burgersdorp Form. The outcrop of this formation displays khaki sandstone (Figure 3.7). These are coarse textured and mostly weathered sandstone.



Figure 3. 8: Picture displaying a dolerite dyke at the study area. GPS coordinate: S 31° 44' 11.9" E 26° 57' 17.9".



University of Fort Hare
Together in Excellence

3.7.2.2 Mineralogy

A. Burgersdorp Formation

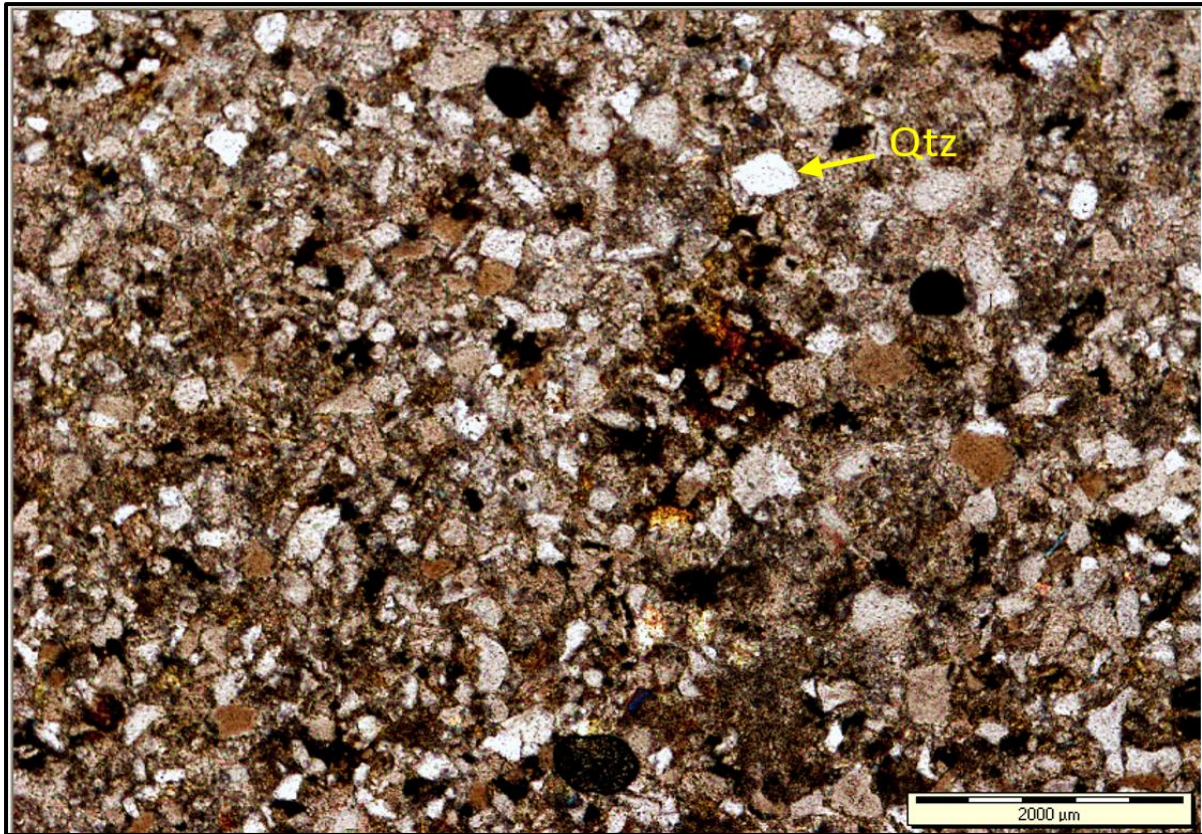


Figure 3. 9: Photomicrograph displaying moderate sorted sandstone of the Burgersdorp Formation.

The moderate sorted sandstone of the Burgersdorp Formation (Figure 3.9) consists of medium-coarse sized, sub-angular to sub-round shaped grains of quartz and clay minerals. The grains of this sandstone are cemented by clay matrix.

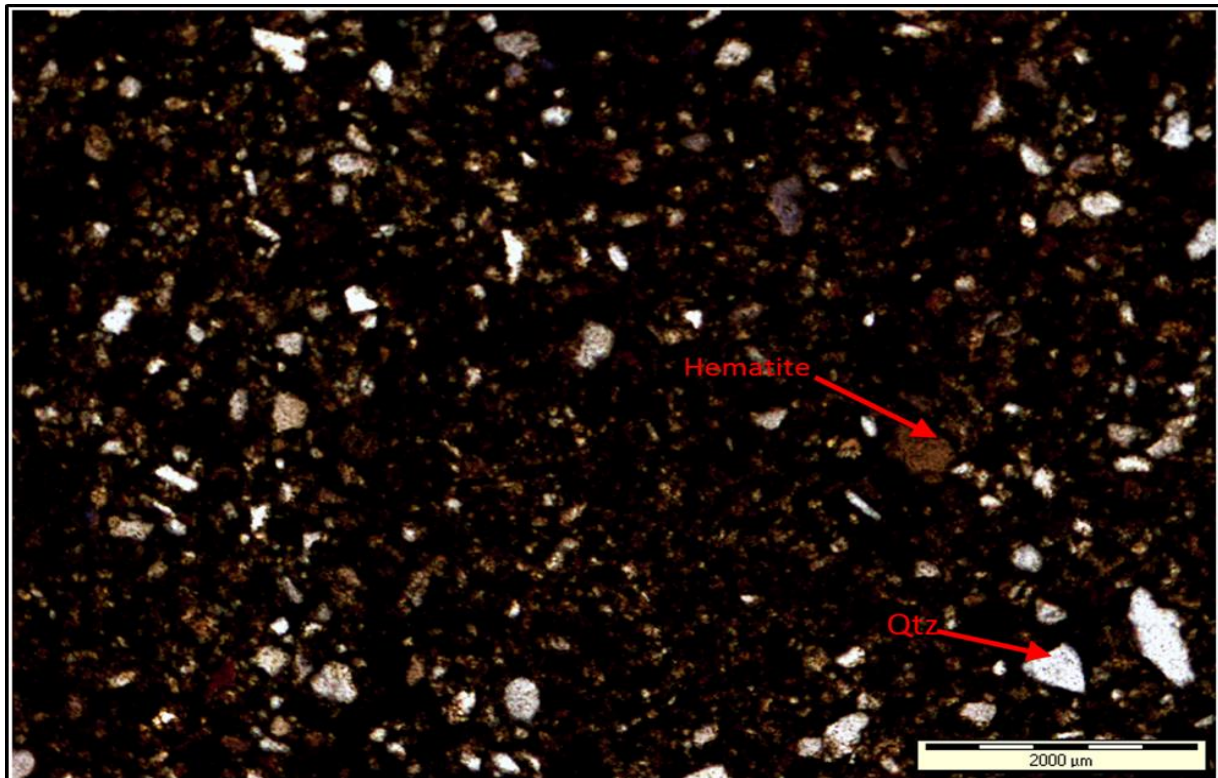


Figure 3. 10: Photomicrograph displaying a fine grained weathered siltstone of the Burgersdorp Formation.



The fine grain weathered siltstone of the Burgersdorp Formation (Figure 3.10) contains angular shaped, poorly sorted grains of quartz, feldspar and traces of metal mineral hematite silt. The grains are cemented by organic cement.

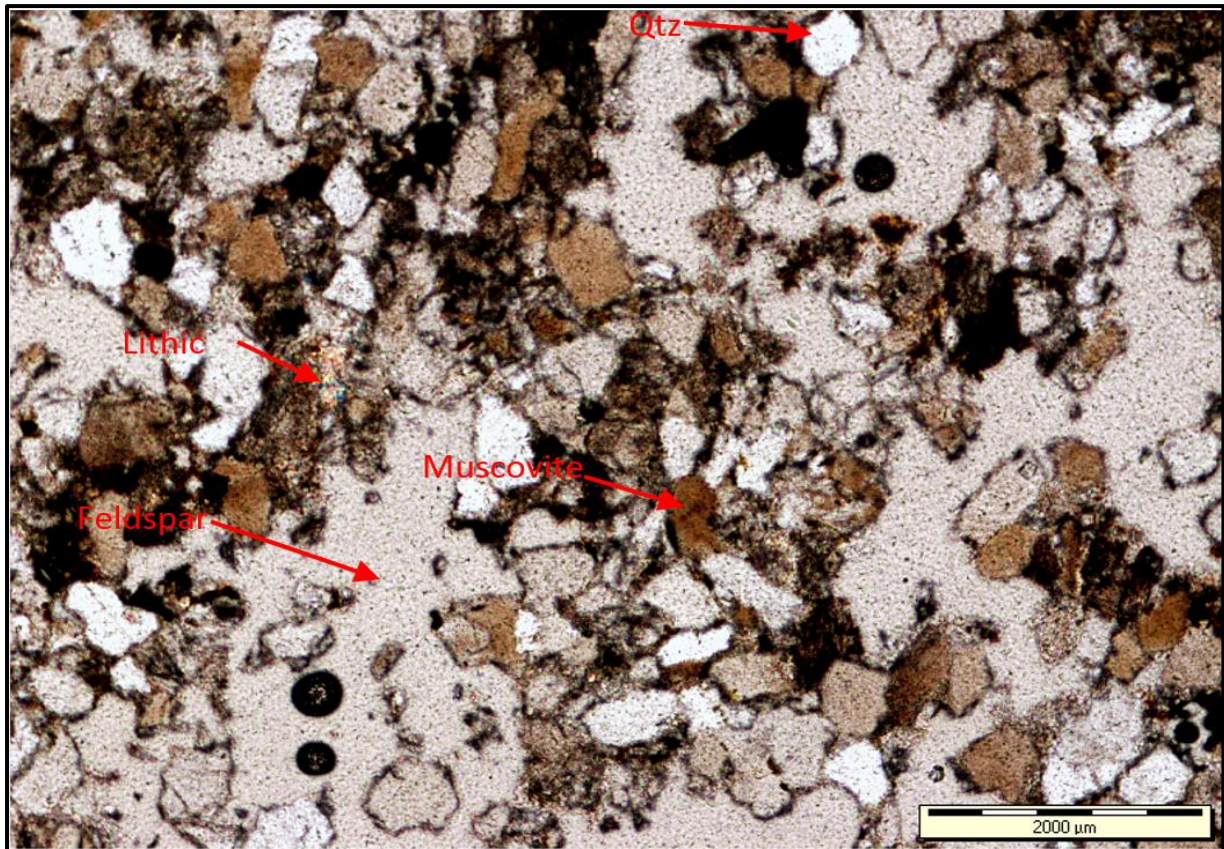


Figure 3. 11: Photomicrograph displaying moderate sandstone of the Burgersdorp Formation.

The sub arkose sandstone of the Burgersdorp Formation (Figure 3.11) composes of poorly sorted grains of feldspar that exceeds rock framework with traces of poorly sorted muscovite and quartz minerals. There are two types of cement matrix, the clay mineral cement and the quartz cement. The shape of the individual grain is sub-round to round.

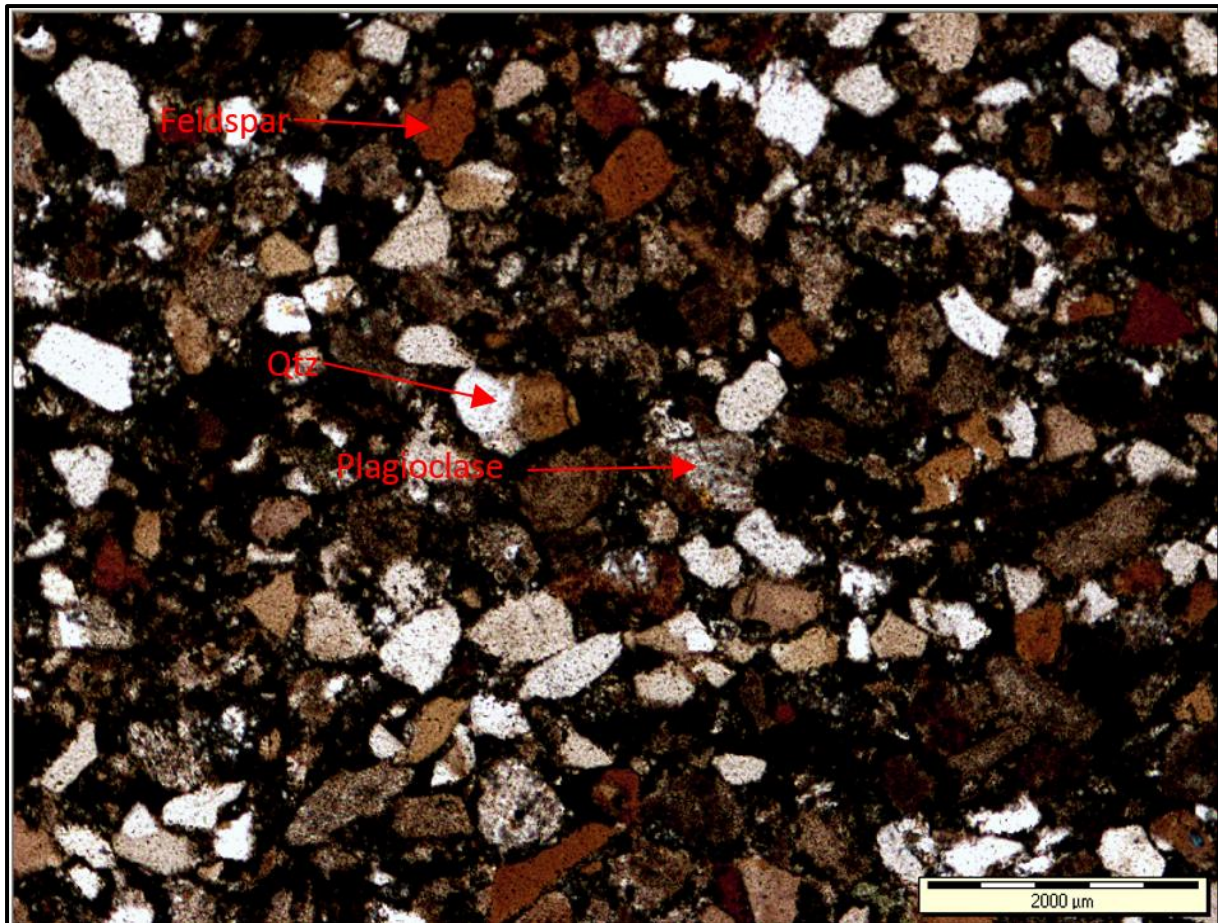


Figure 3. 12: Photomicrograph displaying a medium to coarse grain sandstone of the Burgersdorp Formation.

University of Fort Hare
Together in Excellence

This medium to coarse grain sandstone of the Burgersdorp Formation (Figure 3.12) is sub-angular to sub-round shape which indicates that the minerals were not transported for a long distance. It is composed of moderate sorted feldspars, quartz and plagioclase minerals with traces of detrital muscovite. The mineral grains are cemented by organic cement.

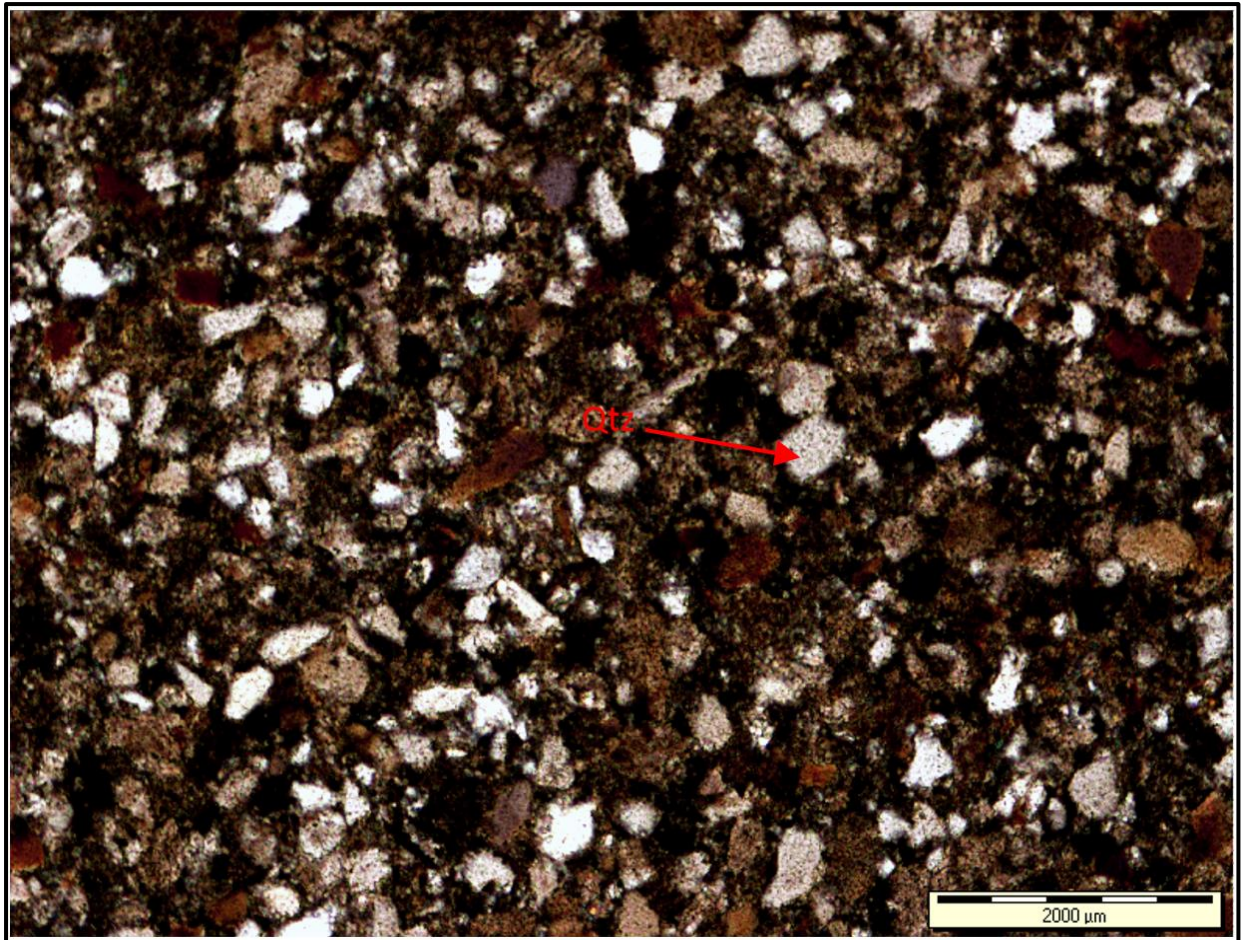


Figure 3. 13: Photomicrograph displaying medium sandstone of the Burgersdorp Formation.

The medium grain sized sandstone consists is dominated by quartz mineral (Figure 3.13). The grains of the specimen are cemented by quartz and organic cement. The shapes of individual grains are sub-round and these are moderately sorted.

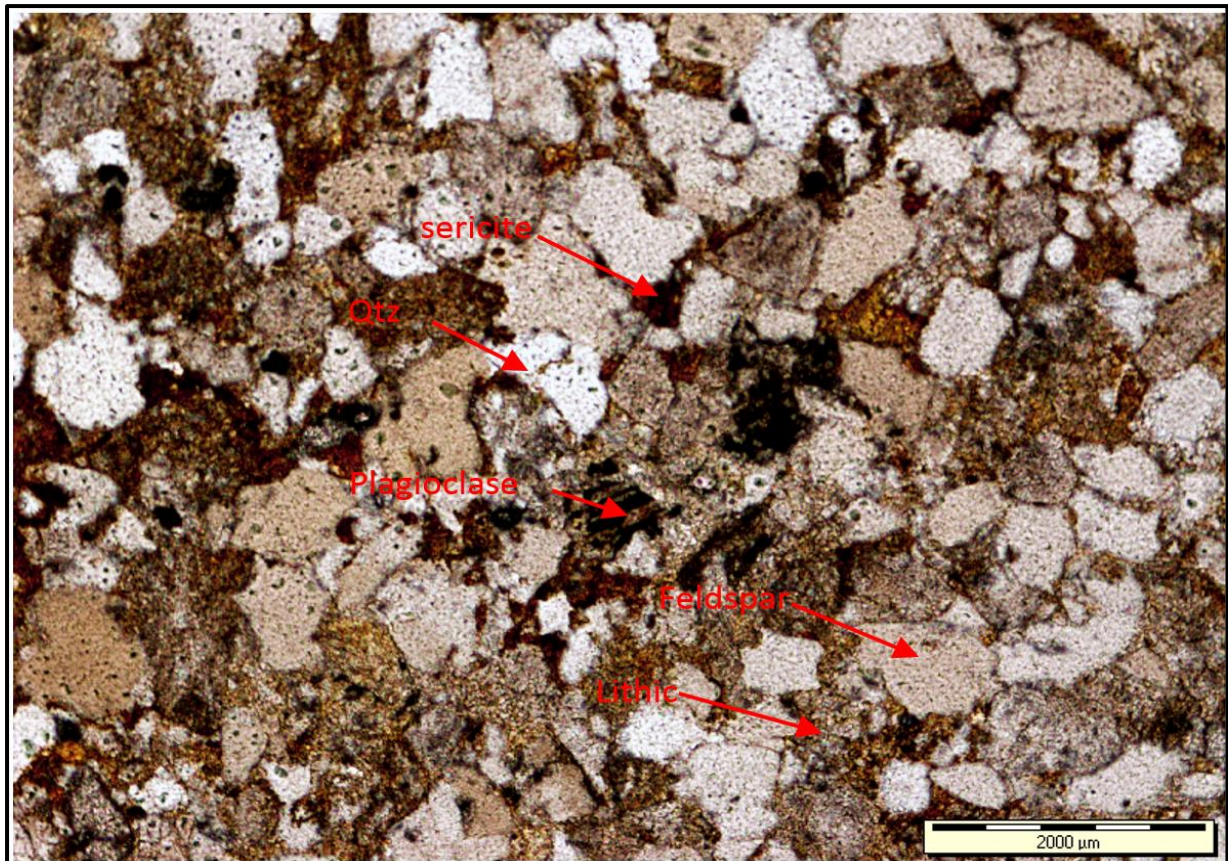


Figure 3. 14: Photomicrograph displaying a coarse grain sandstone from Molteno Formation.

The well sorted coarse grain sandstone of the Molteno Formation (Figure 3.14) which consists of about 15-20% clay minerals (the yellowish part) and grains that are cemented by clay matrix. This sandstone is composed of mostly feldspars, quartz, and plagioclase. There are metamorphic rock fragments within the specimen and these are lithics. The shape of the mineral grains is sub-round to sub-angular shape.

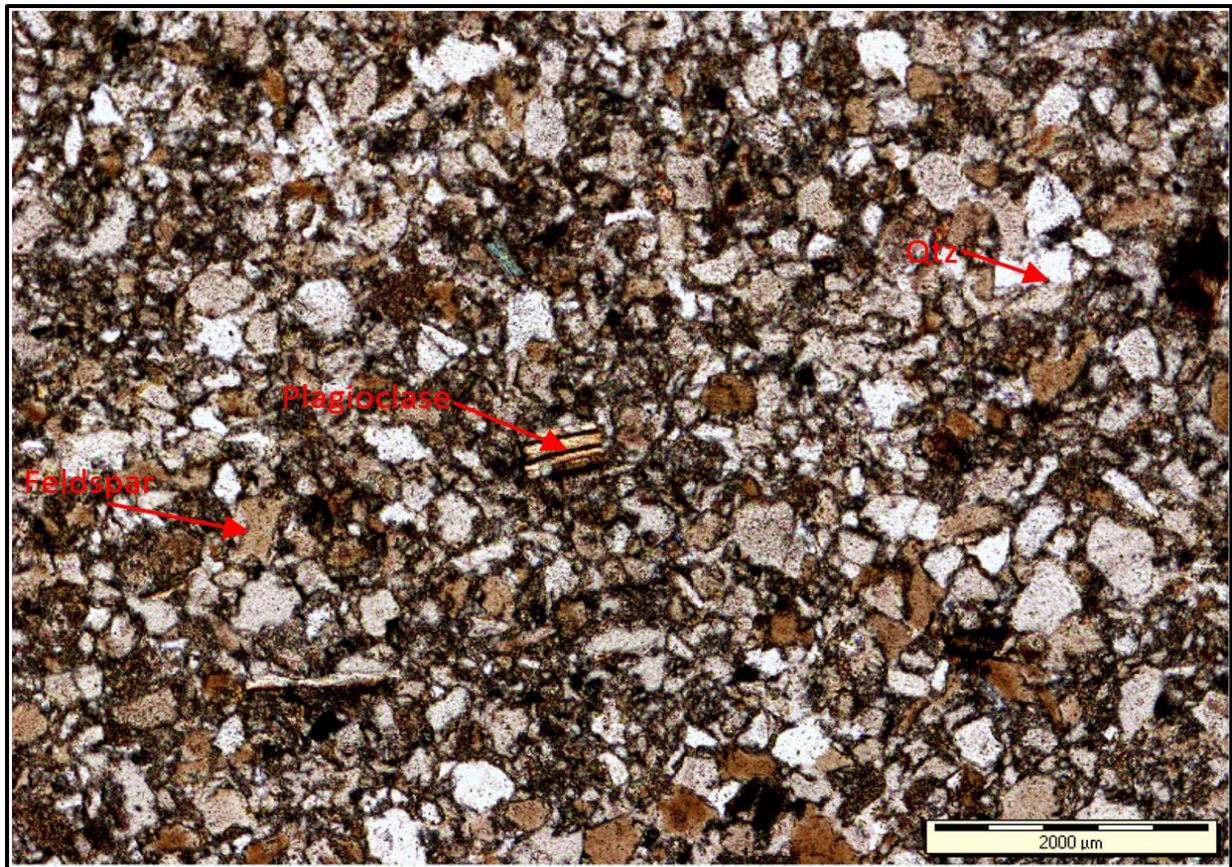


Figure 3. 15: Photomicrograph displaying moderate grain sandstone from Molteno Formation.

The moderate sorted sandstone of the Molteno Formation (Figure 3.15) is fine grain size sandstone and is composed of feldspars and quartz minerals. The shapes of the mineral grain are sub-round to sub-angular. The grains are cemented by clay matrix.

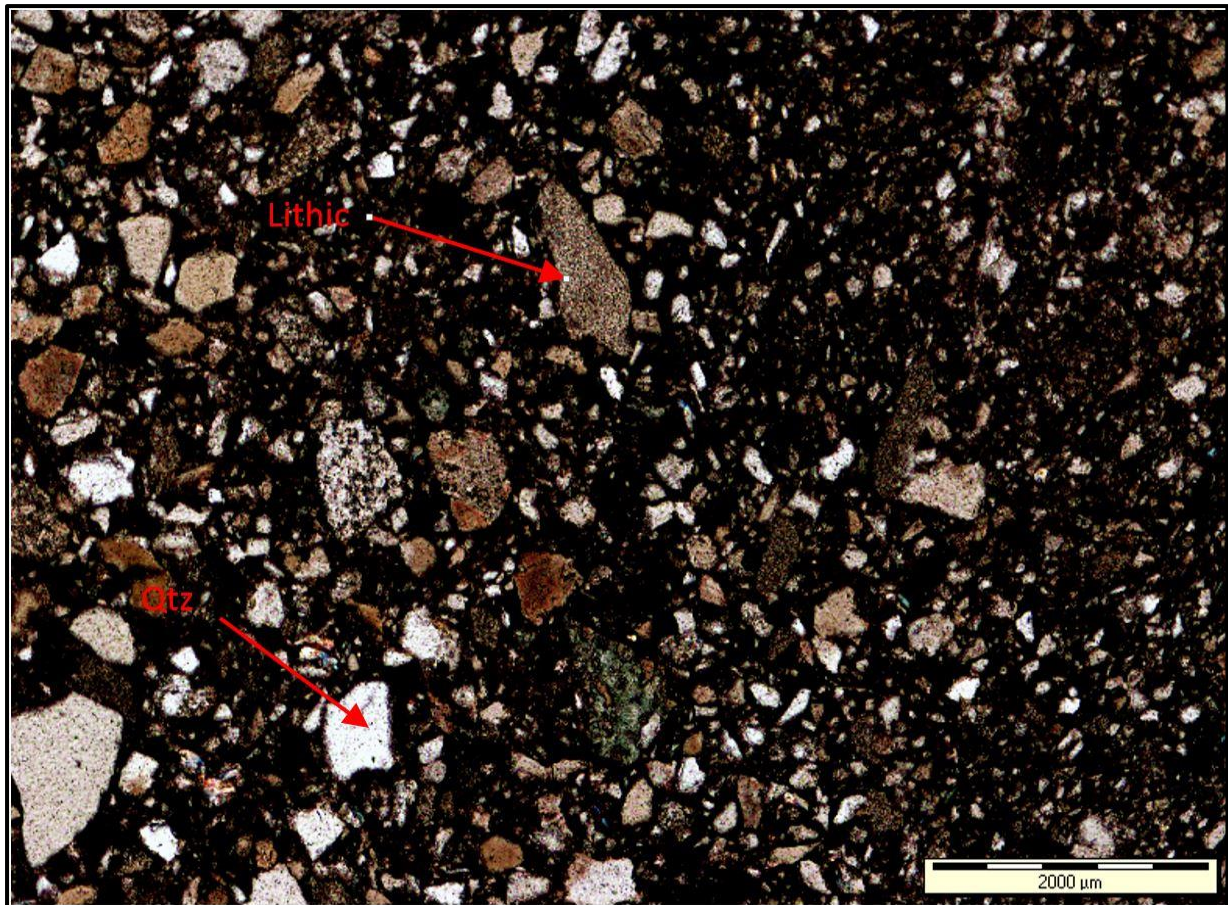


Figure 3. 16: Photomicrograph displaying medium grain sandstone from Molteno Formation.

University of Fort Hare
Together in Excellence

The fine-medium grain sandstone of the Molteno Formation (Figure 3.16) is poorly sorted to moderate sorted with grain shapes being sub-angular to sub-round. It is composed of quartz mineral. The grains are cemented by organic cement.

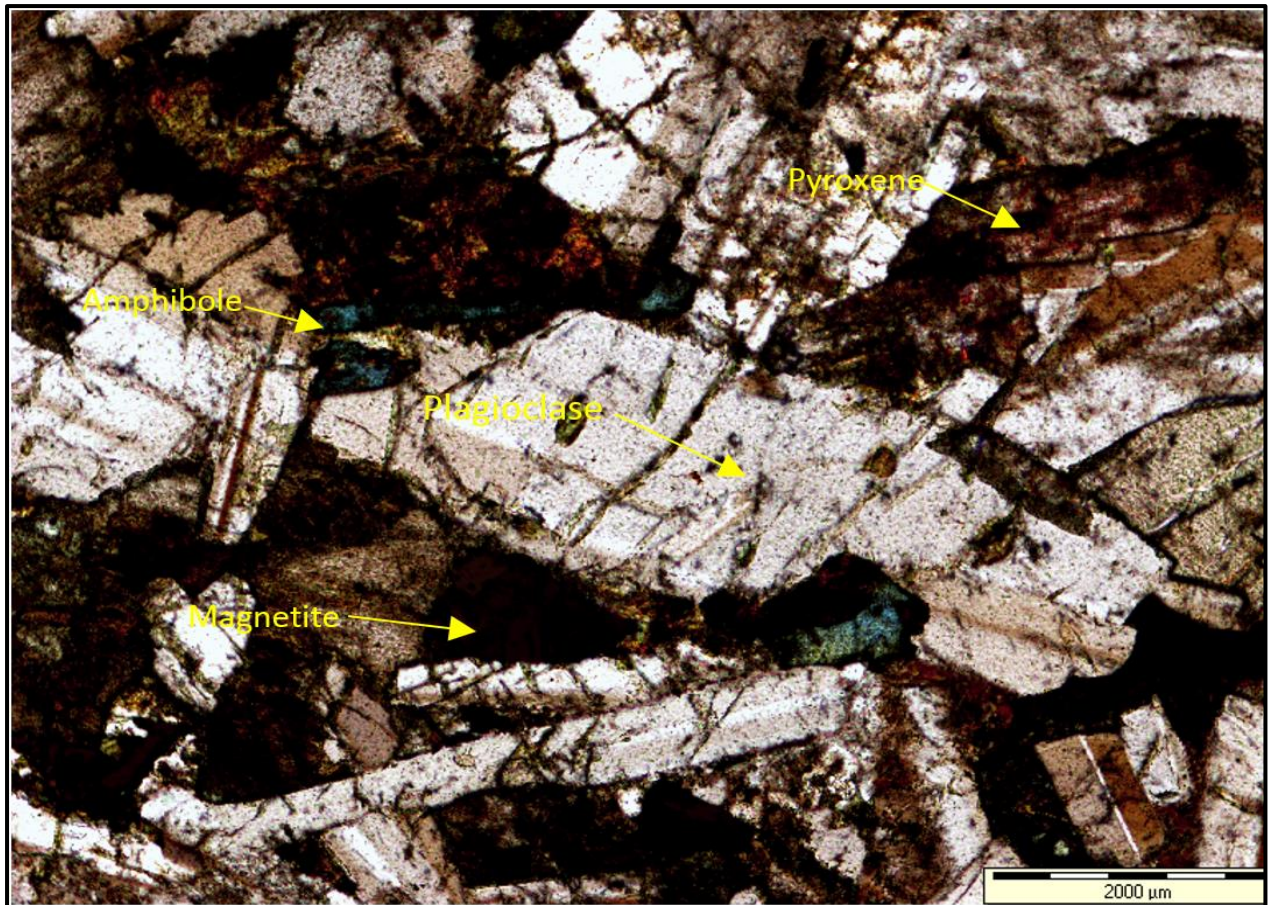


Figure 3. 17: Photomicrograph displaying a dolerite of the Karoo dolerite suite.

The Karoo dolerite (Figure 3.17) is composed of cleavage plagioclase, the amphibole and pyroxene minerals. This dolerite also has oxide mineral magnetite which is a dark mineral in the thin section. The Karoo dolerite has coarse grains and has interlock euhedral structure.

3.7.3 X-ray diffraction analysis (XRD)

Ten samples were sent for X-ray diffraction analysis (for mineral components, percentages and crystalline structure in minerals) to the CGS laboratory. X-ray diffraction analysis was conducted to verify the presence of minerals observed under petrographic microscope, to identify new and unrecognized minerals, and also the crystalline properties of a mineral, such as clay.

3.7.3.1 Procedure for XRD

According to CGS, selected rock samples were washed with distilled water to remove contaminants and dried in the oven. Only representative samples of the rocks were crushed

and milled to a fine powder of around 20 μm in size. The fine powdered samples were then spread on a glass slide and scanned at 22° to 70° 2θ at a speed of 0.02° 2θ steps size/0.5 s using Bruker XRD D8 Advance instrument with 2.2 kW Cu long fine focus tube ($\text{Cu K}\alpha$, $\lambda=1.54060 \text{ \AA}$) and 90 position sample at a room temperature of 25°C . A sub-sample is pressed into a shallow plastic sample holder against a rough filter paper in order to ensure random orientation. A beam of X-ray was directed on the powdered sample whose crystals are randomly arranged in every angle. The quality of minerals presents on the rock samples was determined by measuring the intensities of X-ray peaks for the minerals and compared them with calibrated standard [Brime, 1985]. The intensities of the outgoing diffracted beams were recorded by moving detector connected to a chart record. The LED green ready light was displayed and the XRD Commander program was performed. Minerals were searched manually by their names using the normal search processes in the data command panel

3.7.3.2 XRD results and interpretation

The results of the analysis identify quantitative weight percent of minerals in a rock. The results of XRD are presented in form of patterns called diffractograms and in a table (Appendix A)



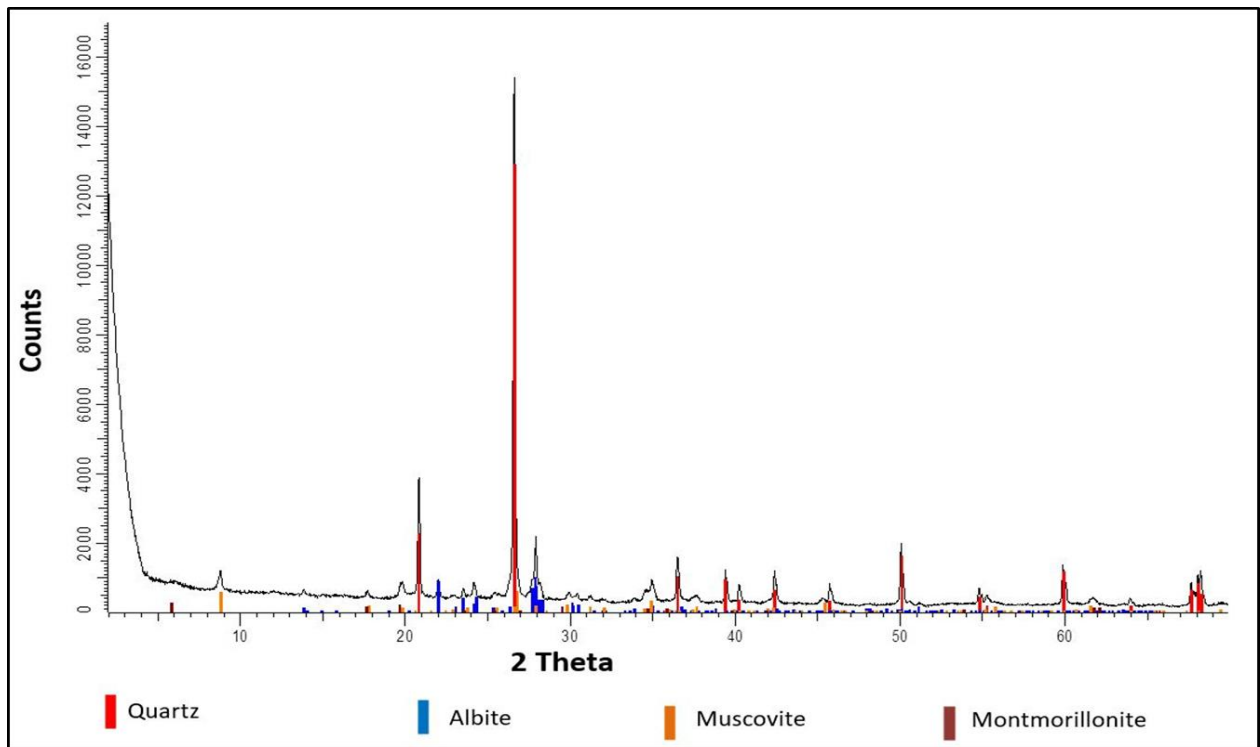


Figure 3.18 : XRD pattern for sandstone of the Burgersdorp Formation

Figure show the XRD patterns of the sandstone minerals of the Burgersdorp Formation. This patter is mostly dominated by quartz mineral with small counts of albite, muscovite and montmorillonite.

The results show that the study area is mostly dominated by sandstone. The sandstone of the Burgersdorp Formation contains about 51-70% of quartz, 9-35% of plagioclase and mica of about 4-18%. The Molteno Formation contains about 55-95% quartz, plagioclase of about 5-29% and mica of about 2%. The dolerites have about 5% of quartz, 53% of plagioclase, 25% of pyroxene and 9% of amphibole.

The diffractograms show that the sandstone of the study area is composed of quartz, albite, muscovite, montmorillonite and clinochlore minerals. The clay minerals in the sandstone and siltstone units are inferred to result from the weathering and alteration of silicate minerals such as feldspars and other minerals. The dolerite consists of albite, calcian, augite as revealed by the diffractograms.

3.8 Conclusion

The field observations, petrography and mineralogy of the study area reveal that the study area is dominated by sedimentary rocks (such as sandstone, siltstone).

The Burgersdorp Formation is composed of moderate to poorly sorted grains, with sub-angular to sub-round grain shape which could be due to low energy water during transportation of sediments and the sediments were transported for a short distance. The sandstone of the Molteno Formation composed of poorly to well sorted, sub-angular to sub-round mineral grains. These grains could be results of low water energy environment, transported for longer distance than those of the Burgersdorp Formation. Dolerite consists of very coarse grained minerals with euhedral structure (plagioclase and pyroxene).

The sandstones of the study area are mostly composed of quartz as the primary mineral which could be due to the nature of its crystal framework which makes it hard and resistant to weathering and erosion, thus it withstood the effect of chemical dissolution and physical abrasion during sediment transportation. Feldspar is the second dominant mineral among rocks of the study area which characterizes immature sandstones.



University of Fort Hare
Together in Excellence

CHAPTER 4: GAMMA RAY SPECTROMETRY METHOD

4.1 Gamma ray spectrometry background

Some isotopes are unstable due to having too many protons or neutrons and to achieve stability the nuclei decay or disintegrate. This nuclei transformation is called radioactivity and results in stable isotopes. This process is followed by emission of particles or energy release which is known as nuclear radiation [IAEA, 2013]. A material that is able to spontaneously release this kind of energy is radioactive. The disintegration does not depend on the physical and chemical conditions. There are natural and man-made radioactive sources. Potassium, uranium and thorium are naturally occurring radioactive elements found in abundance in the rocks all over the world [IAEA, 2013]. Three of the naturally occurring radioactive elements decay through chain/series and of these are uranium 238 (U^{238}), uranium 235 (U^{235}) and thorium 232 (Th^{232}). U^{235} exists in small amounts in rocks and its radioactivity is insignificant for exploration. Radioactive potassium 40 (K^{40}) has single stage decay and is only 0.012% of the naturally occurring potassium.



Man-made radioactive isotopes also emit radiation which can also be measured by radiometric survey. These man-made isotopes are produced by nuclear reactors or due to atomic weapon testing programmes [IAEA, 1991]. The radioactive elements achieve stability by the following: (a) if instability is due to too many nucleons, the excess nucleons are emitted in the form of an alpha particle i.e. two proton and two neutrons bound together (helium nucleus), (b) if there are more protons for stability, one of the spontaneously changes to a neutrons and a positron (beta plus particle) is rejected from the nucleus at a high speed, (c) if there are neutrons for stability, one of them transforms to a proton and an electron (beta minus particle) is ejected from the nucleus at high speed, or (d) a nucleus may capture one of the innermost orbital electrons, which combines with a proton (another form of beta decay) All these nuclear transformations are accompanied by emission of ionizing radiation (gamma ray) from the nucleus. The half-life of radioactive isotope is the amount of time needed for half the original parent atoms to decay. K^{40} decays to Ar^{40} while uranium and thorium are measured indirectly from emission peaks associated with Tl^{208} and Bi^{214} , respectively [Stevenson et al., 2004].

In exploration an instrument called gamma spectrometer is used to detect gamma radiation using four channels: U^{238} , Th^{232} , K^{40} and total count with energy windows centred 2.62 MeV for thorium, 1.76 MeV for uranium 1.46 MeV for potassium and the total count measures all

the energies (total radioactivity) [IAEA, 1991]. The difference in the radioactive elements concentration can be used to map and distinguish different lithologies (see Table 4.1) [Elawadi et al., 2004, Killeen, 1979].

Potassium has crustal abundance between 2.0-2.5% and occurs in many rock forming minerals such as k-feldspars, micas and clay minerals such as illite and is associated with sedimentary minerals and hydrothermal alteration in some uranium deposits [IAEA, 2013].

The measurements can be converted to concentration of the radioisotopes after calibration using known pure sources of radioactivity samples. According to Killeen [1979], the three main processes by which gamma rays interact with matter are photoelectric effect, Compton scattering and pair production (see Figure 4.1). It is photo electric effect that is used for the detection and measurement of radioactivity. In the thorium window gamma rays of high energy 2.6 MeV can be Compton scattered and end up being detected in the uranium and potassium windows. Similarly, gamma rays in the uranium window can undergo Compton scattering and can be detected in the potassium channel. Hence there is pollution of lower energy channels and this need to be corrected. The alpha and beta particles are completely absorbed by rocks and only the gamma rays emerge from beneath the surface. The spectrometer can be used to detect the gamma ray on the ground or airborne up to altitude of 100 m. Apart from radiation coming from the Earth, there is also background radiation in the atmosphere due to cosmic rays. This background radiation needs to be accounted for during a gamma ray survey and removed.

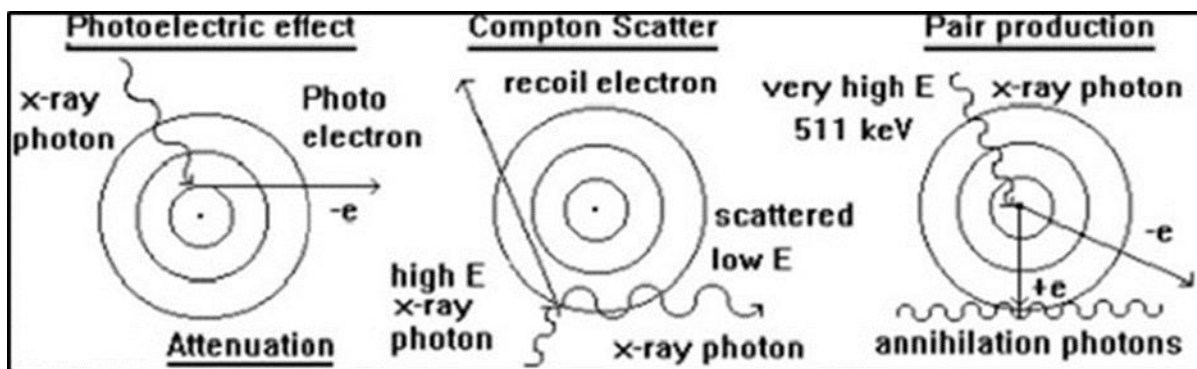


Figure 4. 1: Interaction of gamma rays with matter [Killeen, 1979].

Table 4. 1: Radioelement concentrations in different rock types [Killeen, 1979].

Rock type	K (%)	U (ppm)	Th (ppm)
Acidic	0.1-8	0.1-30	0.1-50
Basic	0.02-3	0.01-6	0.03-15
Ultrabasic	0-1	0-1.6	0-8
Sedimentary	0.01-10	0.1-80	0.2-350
Metamorphic	0.01-6	0.1-150	0.1-100

The unit for measuring gamma ray energy is electron-volt (eV) which is usually expressed in keV or MeV ($k = 10^3$; $M = 10^6$). The measurement of gamma rays of all energy is known as total count which is measured in counts per second (cps).

4.2 Airborne radiometric data acquisition

According to Cole and Cole [2003] the radiometric data was collected by an aircraft Cessna 206 using a spectrometer with two Bicro 41 NaI (TI) detectors with ancillary equipment. The system records 512 channels of data between 0 and 5.12 MeV. The survey includes basic mapping of photopeaks of K^{40} gamma rays at 1460 keV, Bi^{214} gamma rays at 1760 keV from the U^{238} to ^{226}Ra decay series, Tl^{208} gamma rays at 2615 keV from Th^{232} to Pb^{208} decay series and total counts channel for gamma rays in the energy window 410-2810 keV. In addition, a cosmic ray window that measures photo energies ≥ 3 MeV is used to monitor and correct for cosmic rays energy which increases exponentially with elevation. The corrected count rates were converted to concentrations in the ground for the radioisotopes K (%), U and Th in ppm. The sampling spacing was 50 m and the flying line direction was north- south. The ground speed of an aircraft was 200 km per hour.

4.3 Data enhancement

The following radiometric data enhancements were used in the study; The K-U ratio map, K-Th ratio and U- Th ratio map and ternary map.

4.4 Radiometric spectrometer processing

The airborne gamma ray spectrometry data were collected by CGS at the same time with magnetic data for four spectrometric channels. The supplied data was already corrected for;

- i. Livetime/ deadtime normalisation,
- ii. Energy calibration,
- iii. Cosmic correction,
- iv. Radon correction,
- v. Noise Adjusted Singular Value Decomposition (NASVD)
- vi. Windowing of 256 channel spectrum into K, Th, U and Total counts,
- vii. Compton stripping of K, Th, U channels,
- viii. Height attenuation correction,
- ix. Conversion to ground concentration,
- x. Levelling and Microlevelling of ground correction.

4.4 Radiometric results and interpretation



It is worthwhile to note that some of the reduced spectrometric values for the four channels have negative values. This could be due to some areas having count rates which were close to but lower than the background count rate used by CGS in the data reduction.

4.4.1 K channel map

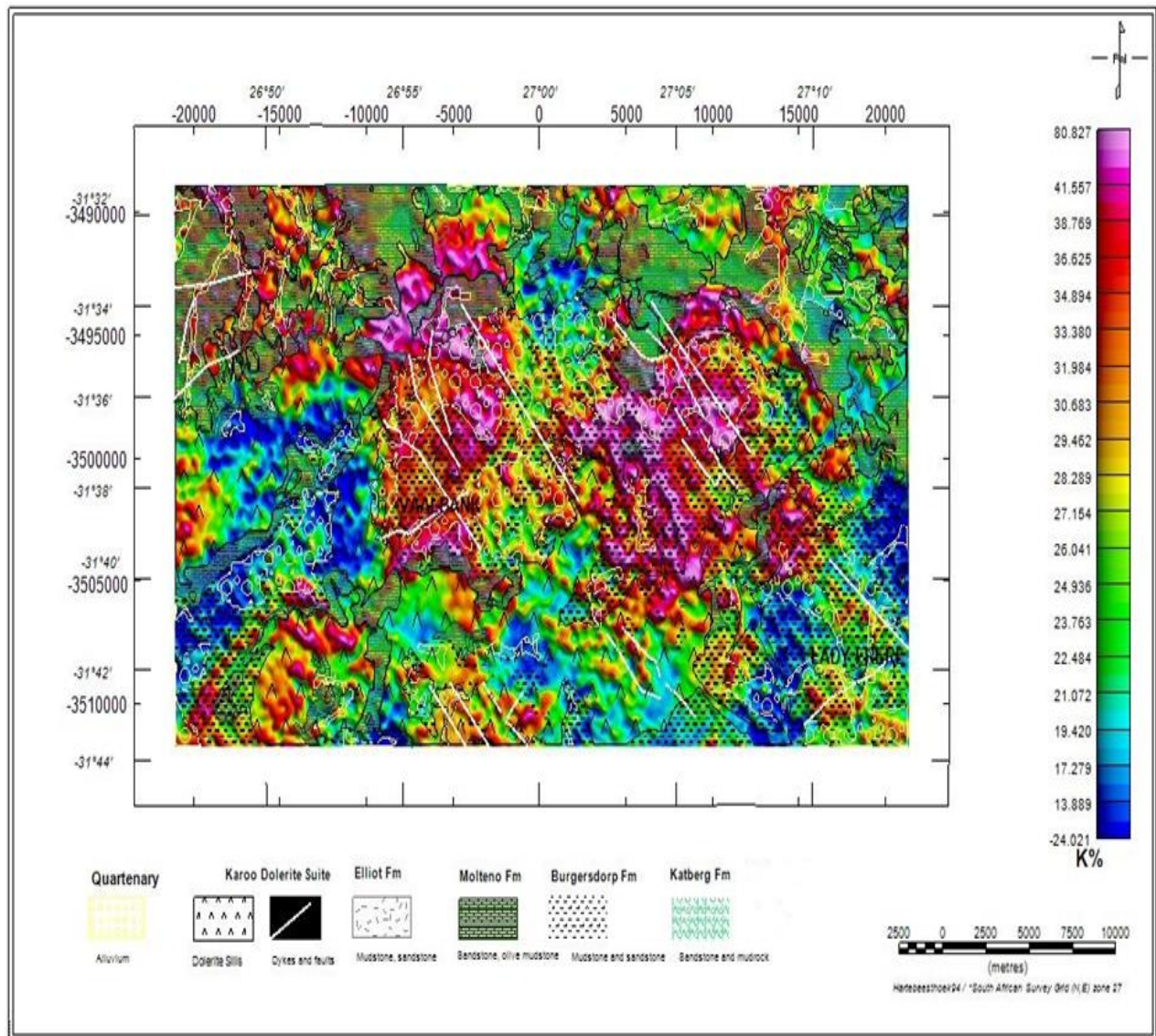


Figure 4. 2: K-channel map overlain with the geology of the study area.

The northwest corner of the map (Figure 4.2) has high concentrations of potassium correlating with the rocks of the Molteno Formation. In the central part of the map from the Vaalbank area to its north and to the far east of Vaalbank there are high concentrations of potassium-40. These high concentrations correlate with the Burgersdorp Formation and alluvium cover. In the western part of the map there are low concentrations of potassium 40 ranging from -24.021% to 80.827%. At Lady Frere and areas around it there are low potassium-40 concentrations. This area is covered by the rocks of the Burgersdorp Formation and alluvium cover. There are lineaments of high potassium-40 concentration trending NW-SE which are

due to the Karoo dykes swarms. On the contrary, the areas covered by Karoo sills and ring complexes have low potassium-40 concentrations.

4.4.2 Th channel map

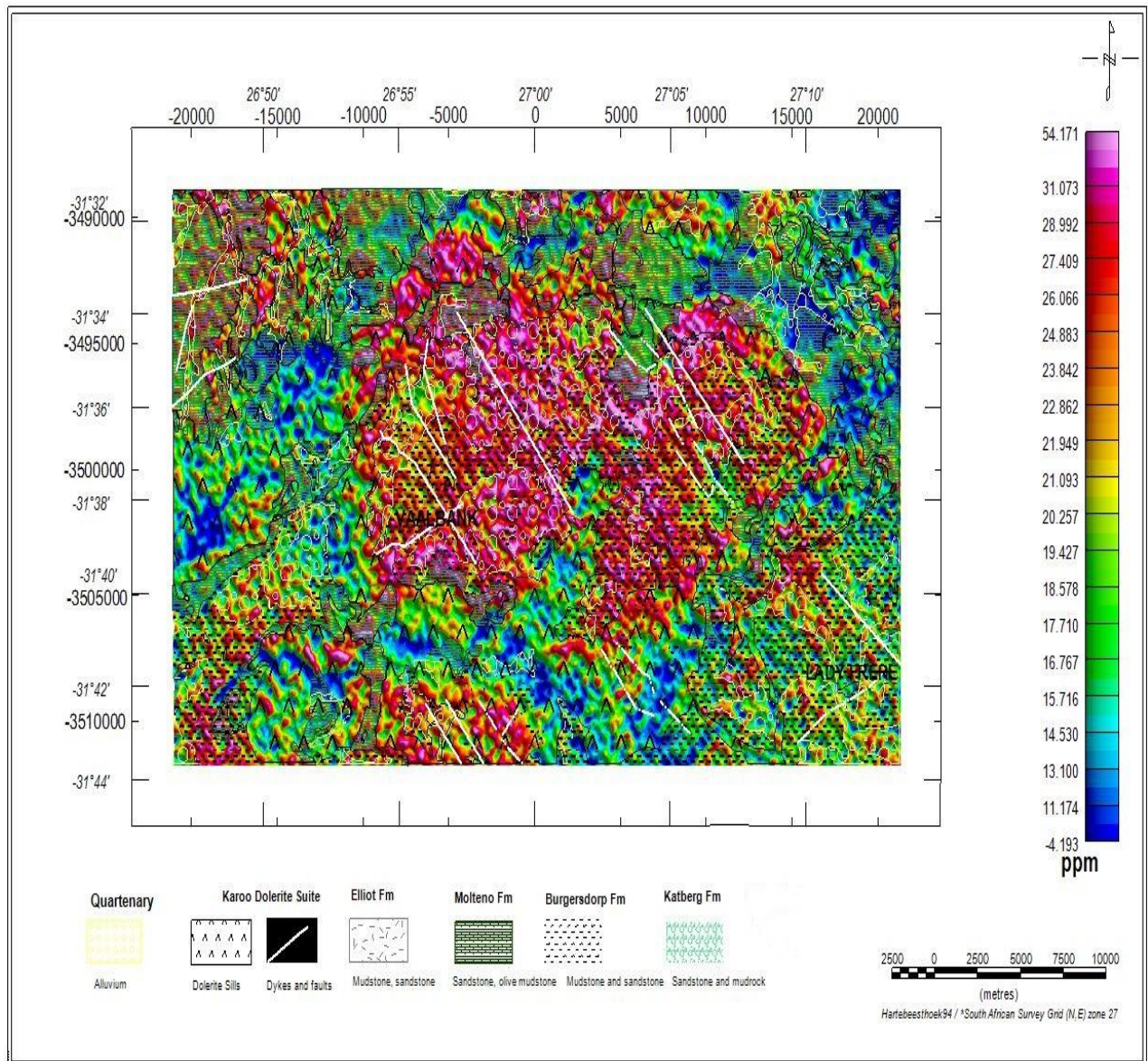


Figure 4. 3: Th-channel map overlain with the geology of the study area.

Figure 4.3 shows the thorium map which has similar spatial distribution to the K map. The highest thorium concentrations are up to 54.171 ppm and these occur at the central part of the map. In the NW corner of the study area there are high thorium concentrations and these correlate with the Molteno Formation. The NE corner of the map has a low spectral signal of gamma ray radiation from K^{40} . The areas covered by Karoo sills and ring complexes exhibit

low radiation counts from K^{40} . The signature of the dyke swarms is visible following a NW-SE trend.

4.4.3 U channel map

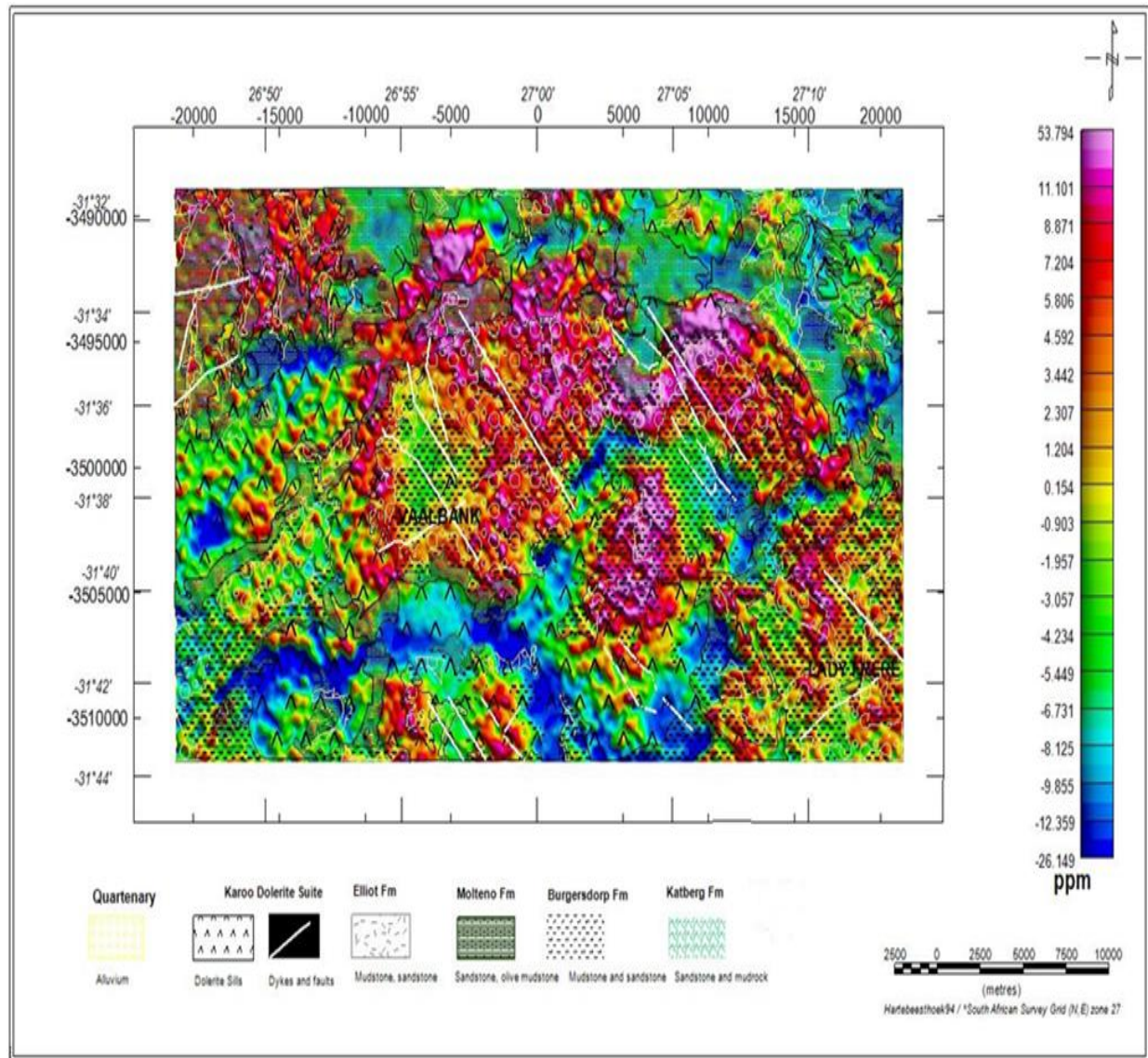


Figure 4. 4: U channel map overlain with the geology of the study area

The spatial distribution of U isotope is more or less similar to that of the K and the Th radioelements. In the north-west corner of the map there are high uranium concentrations that coincide with the sediments of the Molteno Formation. The central part of the map has uranium concentrations which decrease at the Vaalbank area. The high concentrations surrounding the Vaalbank area correlate with sediments of the Burgersdorp and alluvium cover. In the northwest corner of the map there are high uranium concentrations that coincide

with the sediments of the Molteno Formation, while the north-east side of the map there are low concentrations of uranium, this part of the map is covered by Karoo dolerite sills. There are low uranium concentrations that occur also in the southern part of the map and these correlate with dolerite sills and ring complexes.

4.4.3 Total counts channel map

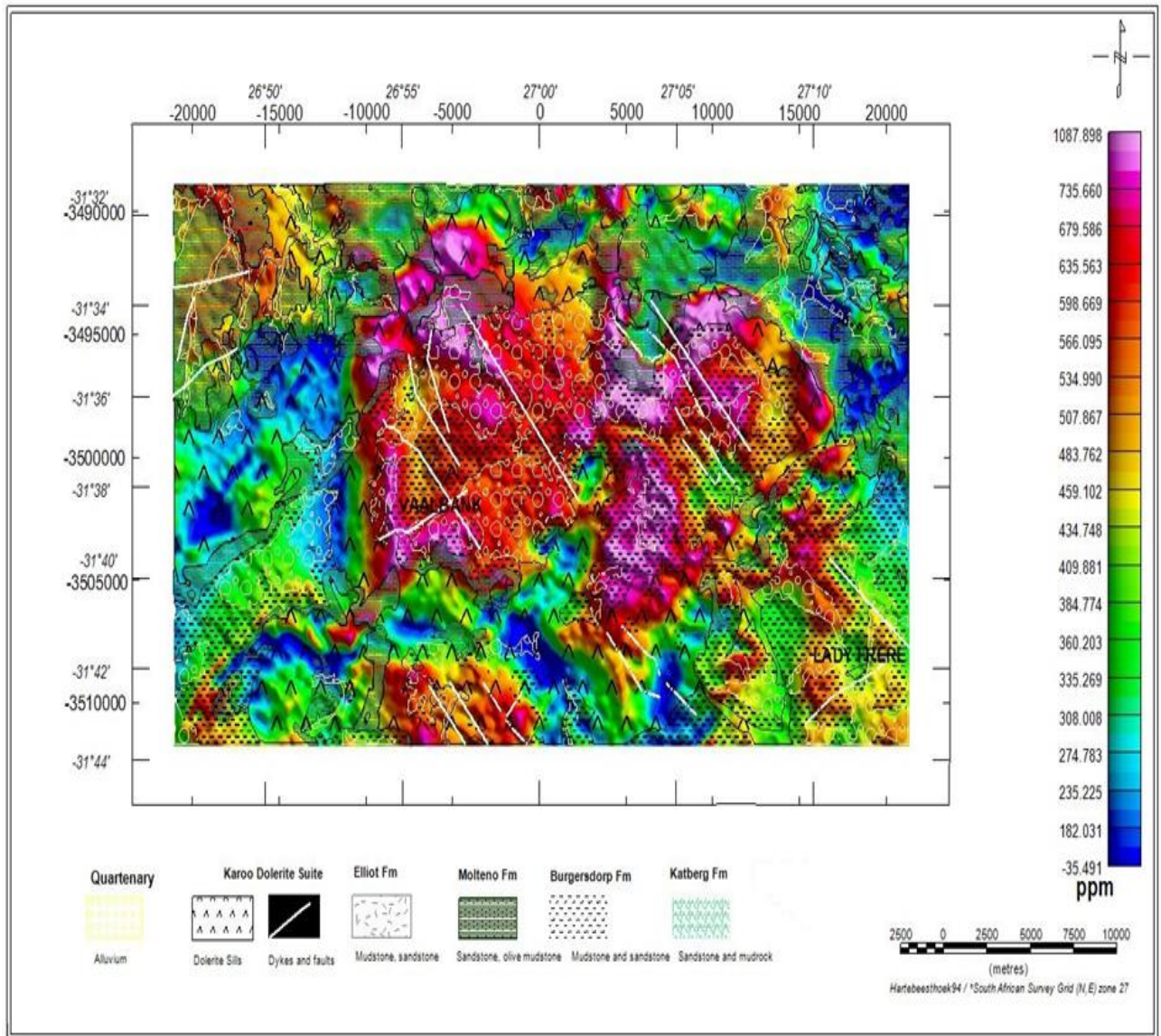


Figure 4. 5: Total counts channel map overlain with the geology of the study area

Figure 4.5 shows a remarkable high concentration of the radioelements in the central part of the map coinciding with the Burgersdorp Formation and alluvium cover. There are also high total counts far south of the Vaalbank area. The area covered by Karoo dolerite sills and ring

complexes has very low total counts which indicate low concentrations of the radioisotopes. However, the Karoo dykes that are seen trending NW-SE have higher concentrations of the radioelements compared to the sills and ring complexes.

4.4.4 K-U ratio map

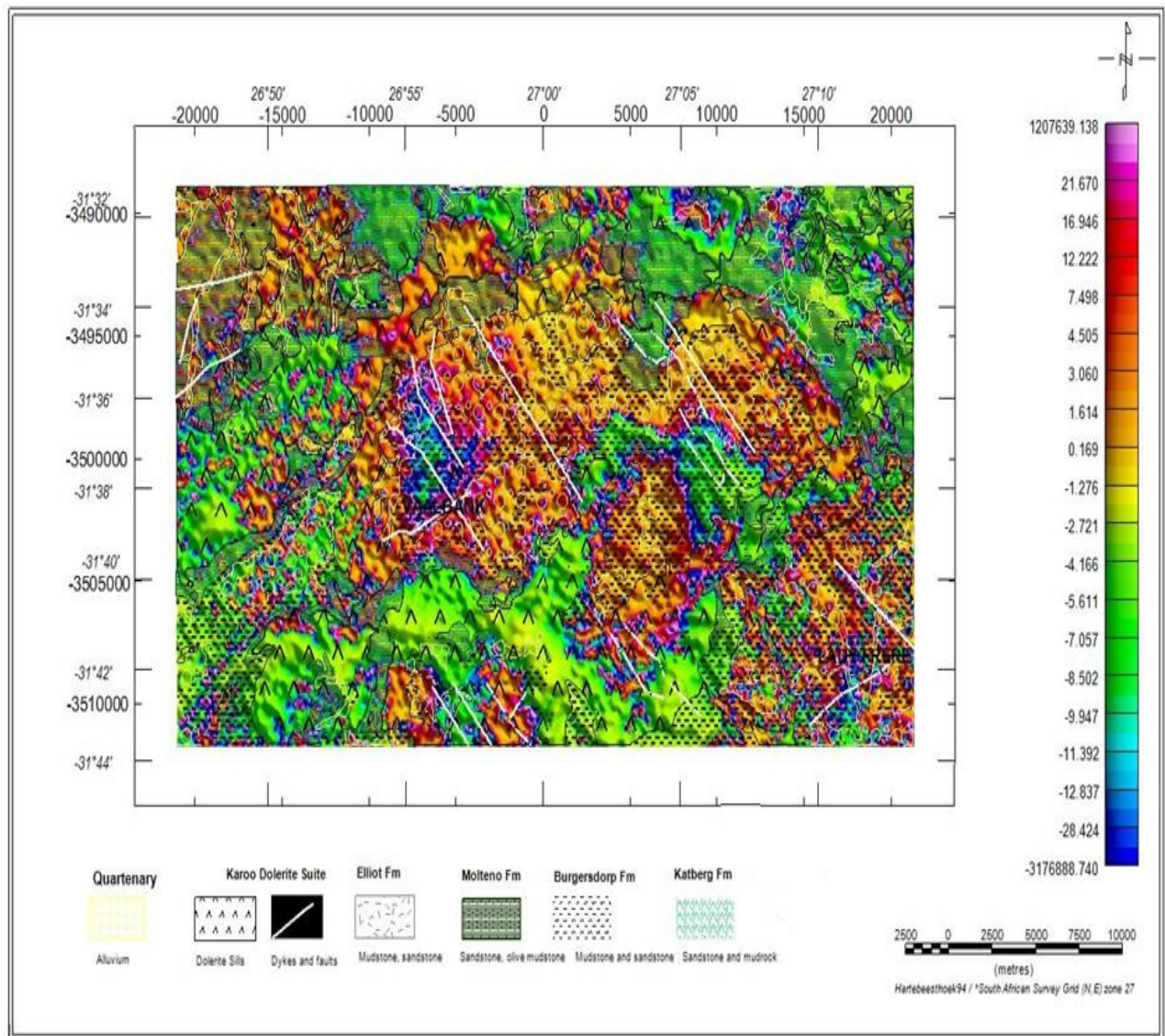


Figure 4. 6: K/U ratio map overlain with the geology of the study area

Figure 4.6 shows apparent potassium/uranium concentrations ratio map overlain with the geology of the area. The north-west corner of the map and at the central part of the map there are high ratios for K/U except at the Vaalbank area where the ratio is low and these low K/U ratio correlate with the dolerite sill at Vaalbank. The high K/U ratio at the central part of the

map coincides with the Burgersdorp Formation, while the high K/U ratio at the north-west corner is coinciding with the sediments of the Molteno Formation. The Lady Frere area has mainly high K/U ratios and these occur over the Burgersdorp Formation and alluvium cover. The low K/U ratios which are predominantly represented by negative values occur over the Karoo dolerite sills and ring complexes. Hence this map clearly maps the boundaries of the dolerite sills and ring complexes. The NW-SE dyke swarms still have medium K/U ratios that are shown as lineaments across the whole map.

4.4.5 K-Th ratio map

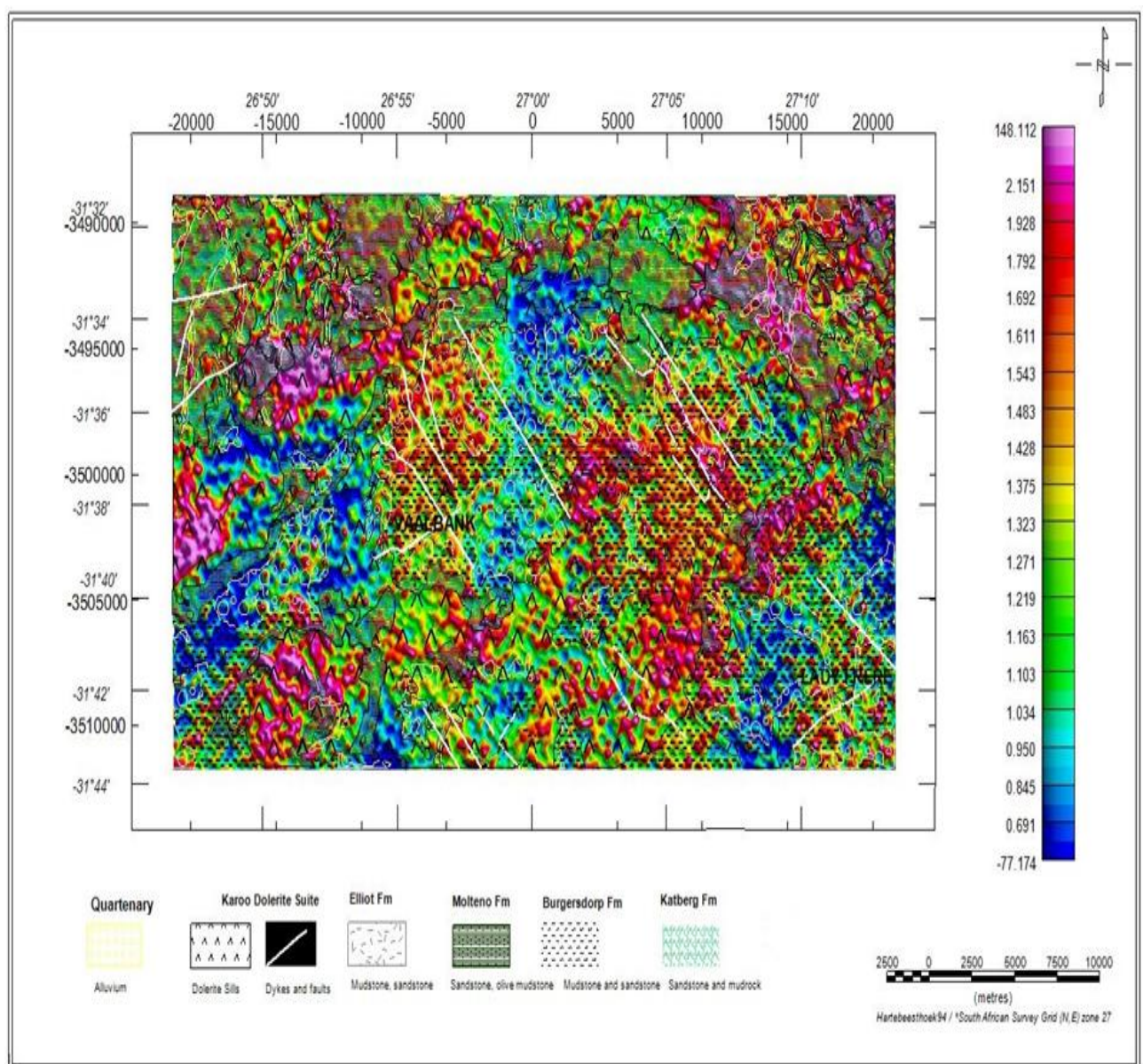


Figure 4. 7: K/Th ratio map overlain with the geology of the study area.

Figure 4.7 shows apparent K/Th concentration ratio map overlain with the geology of the study area. The K/Th ratios vary from -77.174 to 148.112. The most prominent features on this map are the high values of K/Th that occur as lineaments along NW-SE direction and where the lineaments are very close, they form broader high zones. These coincide with the dyke swarms. Low ratio values occur over the areas with sills and ring complexes.

4.4.6 U-Th ratio map

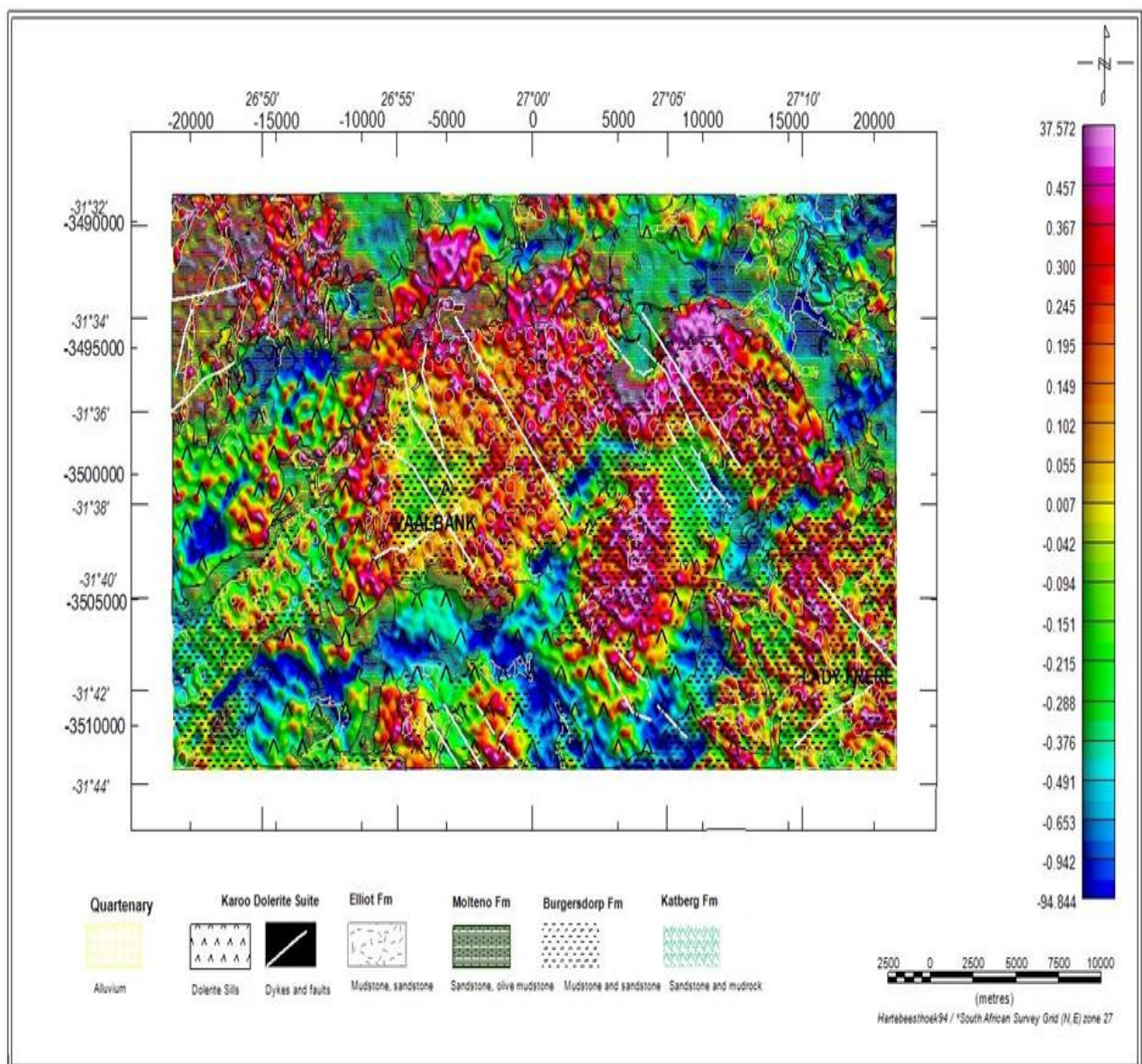


Figure 4. 8: U/Th ratio map overlain with the geology of the study area.

Figure 4.8 shows apparent U/Th concentration ratio map overlain by the geology of the study area. The U/Th ratio values are generally small ranging -94.844 - 0.007. In the north-west corner of the map, there are high U/Th ratio values from 0.367- 37.572 which correlate with Molteno Formation. There are high U/Th ratio values at the central part of the map except the Vaalbank area which coincides with the Burgersdorp Formation and alluvium cover. Low U/Th ratio values occur in the north-east corner and the southern part of the map which coincides with the dolerite sills and ring complexes. Some high U/Th values occur as lineaments trending in a NW-SE direction and these are inferred to be due to the Karoo dyke swarm.

4.4.7 Ternary map

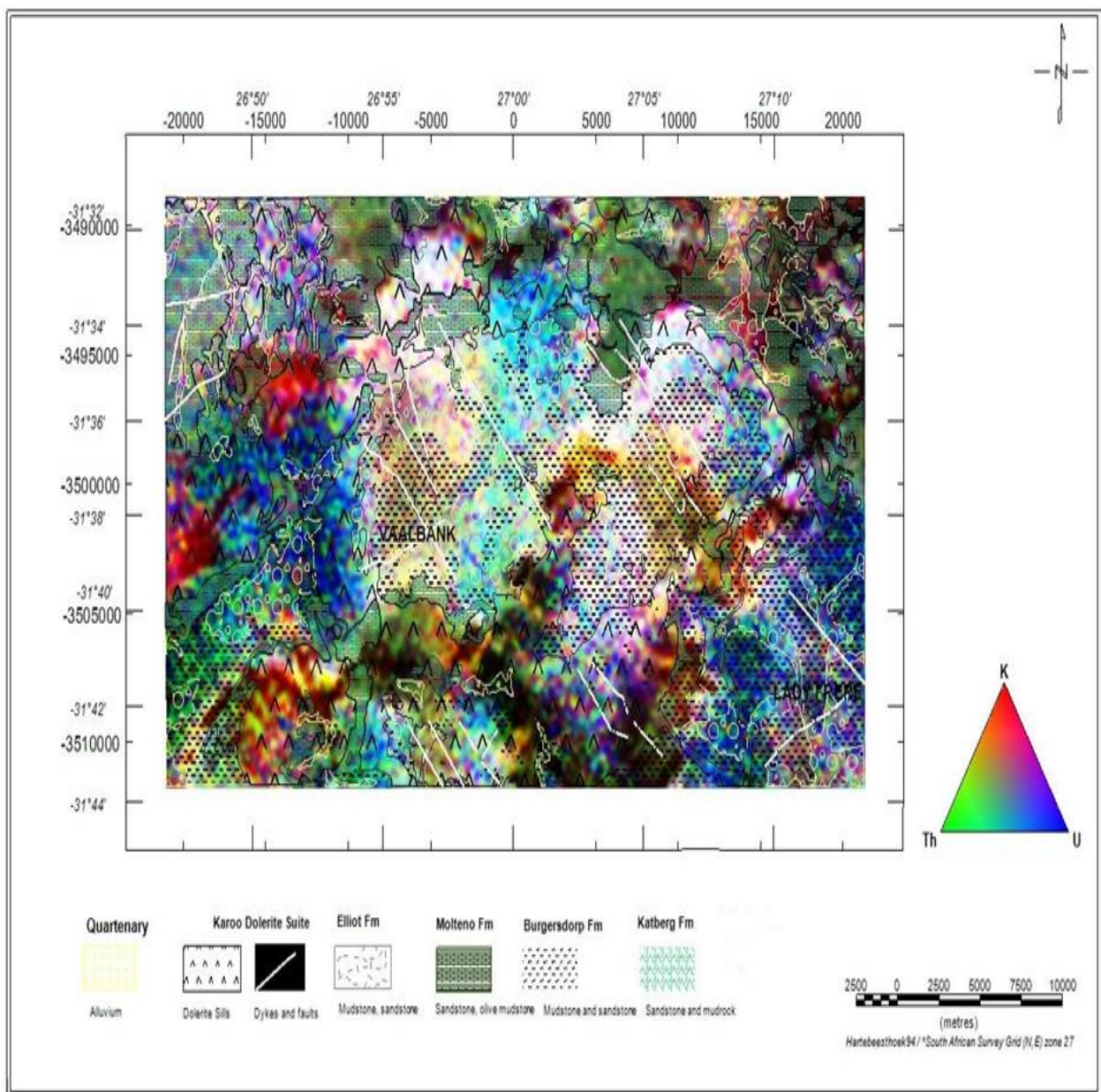
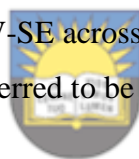


Figure 4. 9: Ternary map overlaid with geology of the study area

Figure 4.9 was generated by combining three radioactive channels namely the uranium, thorium and potassium channels. These three data channels were combined in Geosoft software and are displayed as a ternary map in order to make interpretation easier. The colour schemes of the ternary map are red-magenta for K, green to cyan for Th and blue to yellow for U. The ternary map shows distributions of uranium, thorium and potassium in the uppermost part of the bedrock and soil.

The spectrometric response has four distinct patterns as follows;

- a. Broad large circular whitish to pale bluish colour that coincides with the Molteno Formation in the north western corner of the map, the Burgersdorp Formation and alluvium cover in the south eastern part. These areas have high concentrations of three radioelements.
- b. The greenish to dark greenish colour resembling ring patterns which occur over the Karoo sills and ring complexes. These areas have low concentrations of K, U and Th.
- c. Isolated smaller patches of red to purple colour which are indicative of high K radioelement.
- d. Purplish linear zones trending NW-SE across the whole map. These have intermediate concentrations of K and U, are inferred to be due to the Karoo dolerite dykes swarms.



4.5 Discussion and summary of the gamma ray spectrometry results

The gamma ray spectrometry maps (Figures 4.2 - 4.9) are showing high concentrations of radioactive elements in the NW part of the map. These high concentrations correlate with the Molteno Formation. The central part of the maps also displays high radioelements concentrations and these coincide with the Burgersdorp Formation and the alluvium cover. In the western part of the maps, there are low radioelements concentrations and these correlate with the Karoo dolerite sills and ring complexes, while the dolerite dyke swarms have high radioelements concentrations.

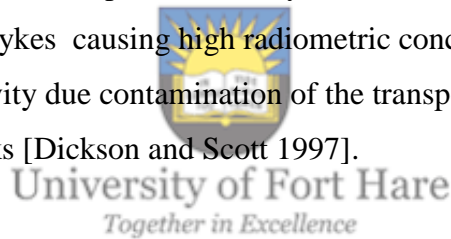
The gamma ray spectrometry technique maps geology that is shallow up to 40 cm soil and rocks. The dolerite dyke swarms of the study area have high radioelements concentrations probably due to weathered dykes. According to Wilford 1997 weathering modifies the distribution and concentrations of radioelements compared to the original bedrock. As explained by Dickson and Scott 1997 that the dolerite tends to form dykes that weather readily, so that the soil is contaminated by transported material from adjacent radioelement-rich rocks (in this case sediments of the Beaufort and Stomberg groups). The XRD and Thin

section results indicate that the rocks are mostly composed of clay minerals such muscovite, montmorillonite, albite and calcian and the clay minerals are minerals form from weathering. The weathering in the dolerite sills and ring complexes is probably less than that of the dyke swarms due to a large volume of sills/ring complexes.

4.6 Conclusion

The gamma ray spectrometric maps interpretation lead to the conclusions that:

- The high radioelements concentrations values are associated with the Molteno Formation, Burgersdorp Formation and alluvium cover. These are exposed on the surface of the study area.
- The dykes have high concentrations of radioelements.
- The low radioelements concentrations in the study area are coinciding with the dolerite sills and ring complexes.
- The different spectrometric response of the dykes and sills or ring complexes could be due to weathering of dykes causing high radiometric concentrations as rock alteration can increase radioactivity due contamination of the transported material from adjacent radioelement-rich rocks [Dickson and Scott 1997].



CHAPTER 5: MAGNETIC METHOD

5.1 Magnetic method theory

The Earth is known to be made up of the core, mantle and crust. In the outer core, which is liquid rich in iron there are convection processes that give rise to a dipolar geomagnetic field that resembles that of a large bar magnet aligned approximately $11\frac{1}{2}^\circ$ to the west of the Earth's axis of rotation. The mantle plays insignificant role in the magnetism. The magnetic anomalies that are recorded during a detailed survey conducted close to the Earth's surface are produced by the interaction of the geomagnetic field with the rocks of the Earth's crust [Reeves, 2005].

The magnetic method involves measuring the Earth's magnetic field intensity that results from the magnetic properties of the underlying rocks. Different rocks have different magnetic susceptibility (content), rocks with high magnetic susceptibility result in strong magnetic field.



5.1.1 Magnetic units

University of Fort Hare
Together in Excellence

The magnetic field unit is defined in terms of the electric current flow needed in a coil to generate the field. The units for measuring magnetic field are volt-seconds per square metre or Weber/m² or Teslas (T). The Earth's magnetic field is only about 5×10^{-5} T. Thus a more convenient SI unit of measurement in geophysics is the nanoTeslas (nT = 10^{-9} T). The geomagnetic field “varies from less than 22000 nT in the southern Brazil to over 70 000 nT in Antarctica south of New Zealand’ [Reeves, 2005].

5.1.2 Geomagnetic field

The Earth's magnetic field can be visualised as radial lines around the Earth starting from the north magnetic pole and ending up on the south magnetic pole (see Figure 5.1). The magnetic field has its axis tilted at about $11\frac{1}{2}^\circ$ from the true north in a NW-SE direction [Reynolds, 1997]. Therefore, the magnetic north pole does not correspond with the true north and it is for

this reason that a compass direction at any location on the Earth's surface gives false directions and hence it must be corrected for to provide true directions.

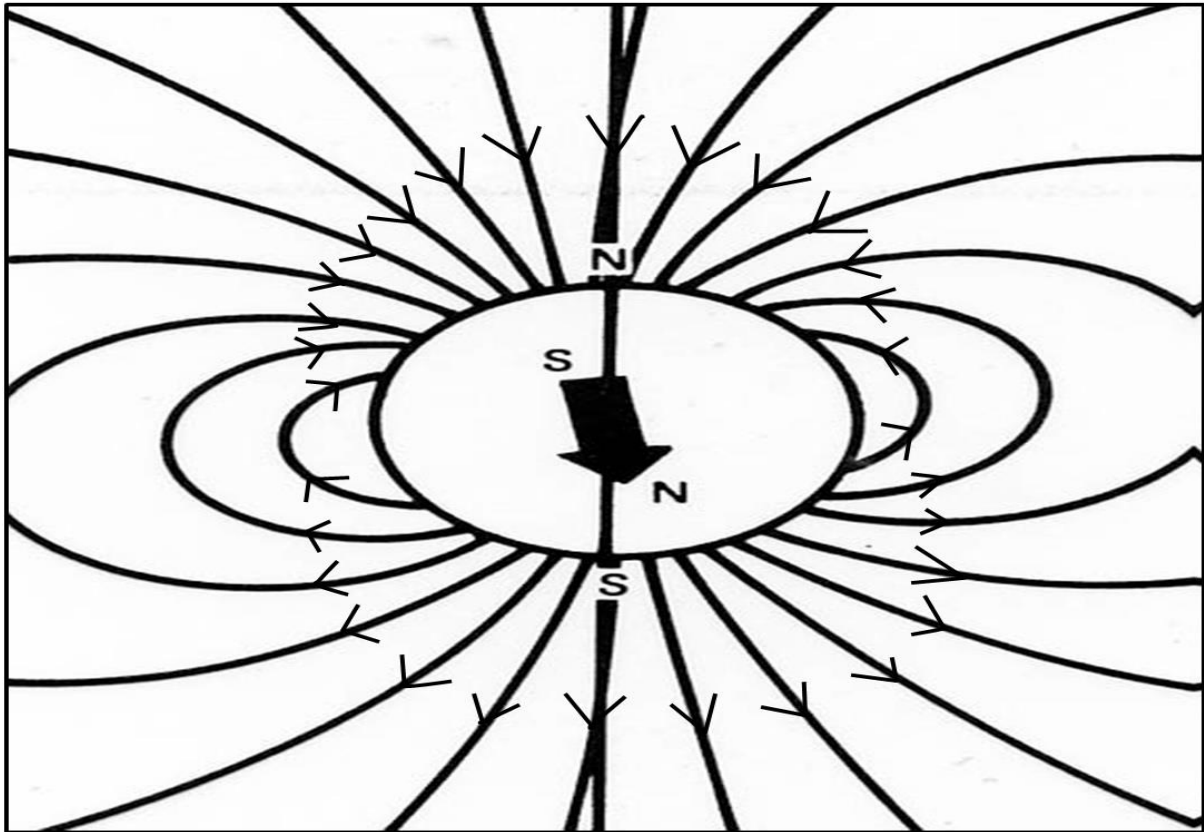


Figure 5. 1: The Earth's dipolar magnetic field. Note that the geomagnetic South Pole is a magnetic north pole and the geomagnetic North Pole is a magnetic south pole [Reeves, 2005].

The nature of the geomagnetic field is dipolar, which makes it essential to specify the field's direction. The field is orientated vertically downward at the north magnetic pole, horizontal (pointing north) at the equator and in the south magnetic pole it points vertically upwards (Figure 5.1).

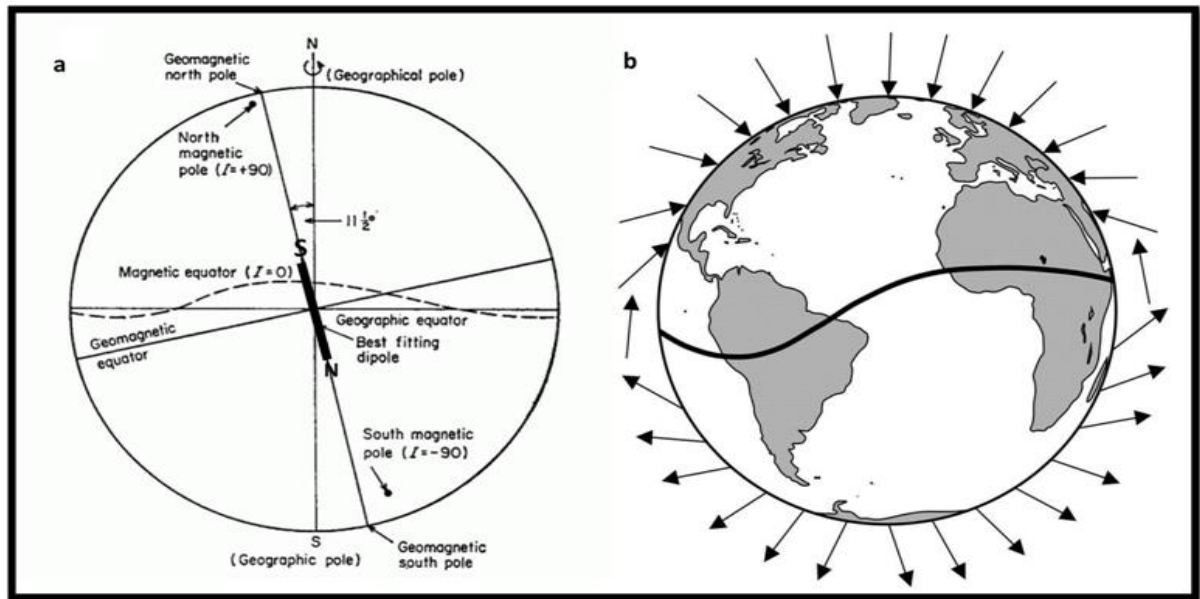


Figure 5. 2: The field due to an inclined geocentric dipole and the field lines [Reeves, 2005].

At random intervals over hundreds or thousands of years a pole reversal occurs about every 20 000 to 30 000 years and it has been more than that long since the last reversal occurred [Reynolds, 1997]. When the Earth's magnetic field reverses, it leaves a record in the rocks which is used for calculating the past movements of the continents and ocean floors which are due to tectonics [Reynolds, 1997]. The use of magnetic reversals to provide global chronometric of geological event is known as magnetostratigraphy [Sharma *et al.*, 2005].

5.1.3 Remanent and induced magnetization

Remanent magnetization is the magnetization in a rock that is present in the absence of an outside magnetic field usually the natural remanent magnetization, although some remanent magnetizations are produced using laboratory procedures. If a magnetic material with high susceptibilities or strong inducing field is placed under an inducing field, the magnetic material will remain with a portion of its induced magnetization even after the induced field is removed. The magnetic susceptibility of the rock depends on the alignment and shape of the magnetic grains scattered in the rock. This remaining magnetization is known as the remanent magnetization. Remanent magnetization is the part of the material's magnetization that is utilized to map the motion of continents and ocean basins that results from plate tectonics.

Natural remanent magnetization is mostly seen in volcanic rocks as they cool below the Curie temperature. At this temperature (between 550° and 600°C) rocks that possess magnetic properties begin to generate an induced magnetic field. In this case, the Earth's magnetic field is the inducing field and it changes with time resulting in the deflection or variation in the magnetic properties the rocks, although a portion of the induced field in the rock remains constant in a direction and strength, which indicates the Earth's magnetic field at the time the rock cooled through its Curie temperature. Remanent magnetization of the rock can be measured by taking the rock sample to the laboratory for analysis, which is time consuming and expensive.

5.1.4 Magnetic inclination and declination

The magnetic field (**F**) is a vector quantity that can be projected to the Earth's horizontal and vertical planes using its magnitude (**F**), the declination (**D**), inclination (**I**) (Figure 5.3)

Declination – The magnetic declination was first discovered by Christopher Coulomb in the year 1492 during his first voyage. In the second half of the 16th century, it was well known and measured at sea or in harbours [Lanza and Meloni, 2006]. According to Reeves [2005], the magnetic declination (**D**) is the angle between the vertical plane containing total field (**F**) and the geographic true north or the angle between true north and the horizontal component of the field measured east of the true north. Magnetic declination (**D**) is usually less than 15°, positive to the east and negative to the west [Figure 5.3].

Inclination – the angle that the Earth's magnetic field makes to the horizontal. In southern Africa the magnetic inclination is approximately -60°. At the magnetic equator the inclination is zero [Roux, 1980]. The discovery of inclination led to the correct drawing of the magnetic field lines of force, and therefore to a more complete description of the field [Lanza and Meloni, 2006].

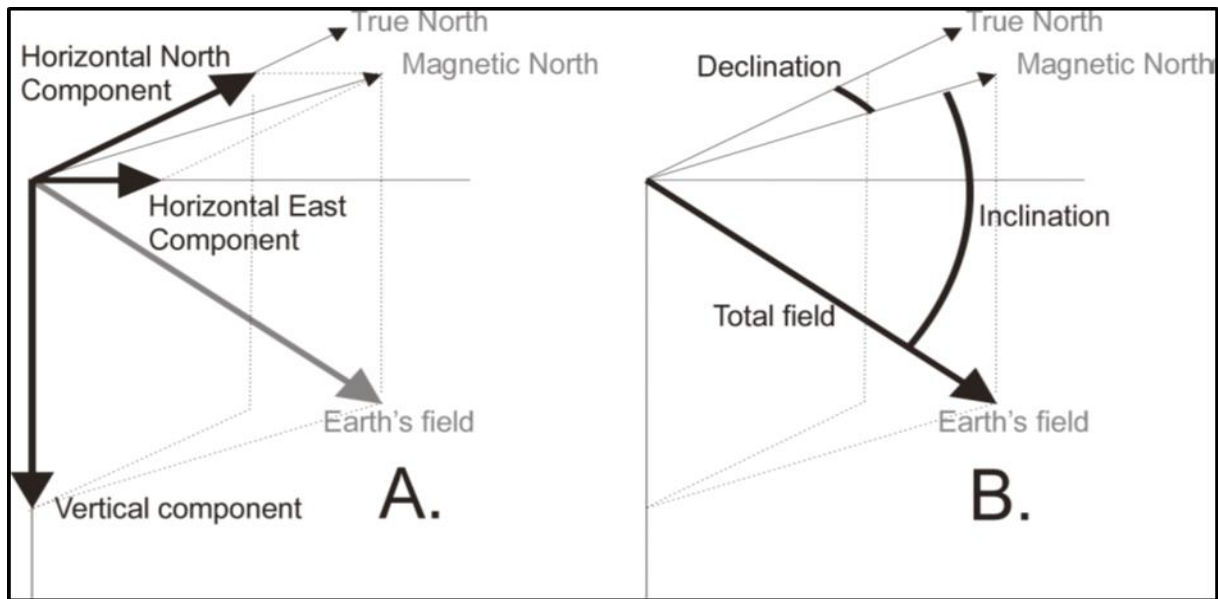
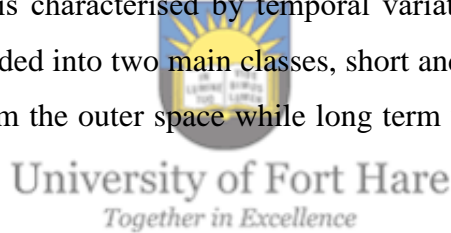


Figure 5. 3: The vector total magnetic field [Reeves, 2005].

5.1.5. Temporal variations of the Earth's magnetic field

The Earth's magnetic field is characterised by temporal variations. These variations have different origins and are divided into two main classes, short and long term variations. Short term variations originate from the outer space while long term variations are due to secular variations.



5.1.5.1 Secular variations

These are long-term (changes in the field that occur over the years) variations in the main magnetic field that are produced by fluid movement in the Earth's outer core. This variance will not complicate data reduction efforts, although it is important to correct for secular variations when carrying out a regional survey, but can be ignored for a local survey conducted over a short period of time.

5.1.5.2 Diurnal variations

These are fluctuations in the magnetic field that occur over the course of a day or several days, they cause changes in strength and direction of currents circulating in the ionosphere (Figure 5.4). These diurnal variations arise from the rotation of the Earth with respect to the sun. The 'solar wind' of charged particles emitted from the sun, even under normal or 'quiet sun'

conditions, tends to distort the outer regions of the Earth's magnetic field. The variation can be up to 20 to 30 nT per day and they are not predictable, but should be monitored and accounted for by using a base station magnetometer or a tie line method when conducting magnetic surveys.

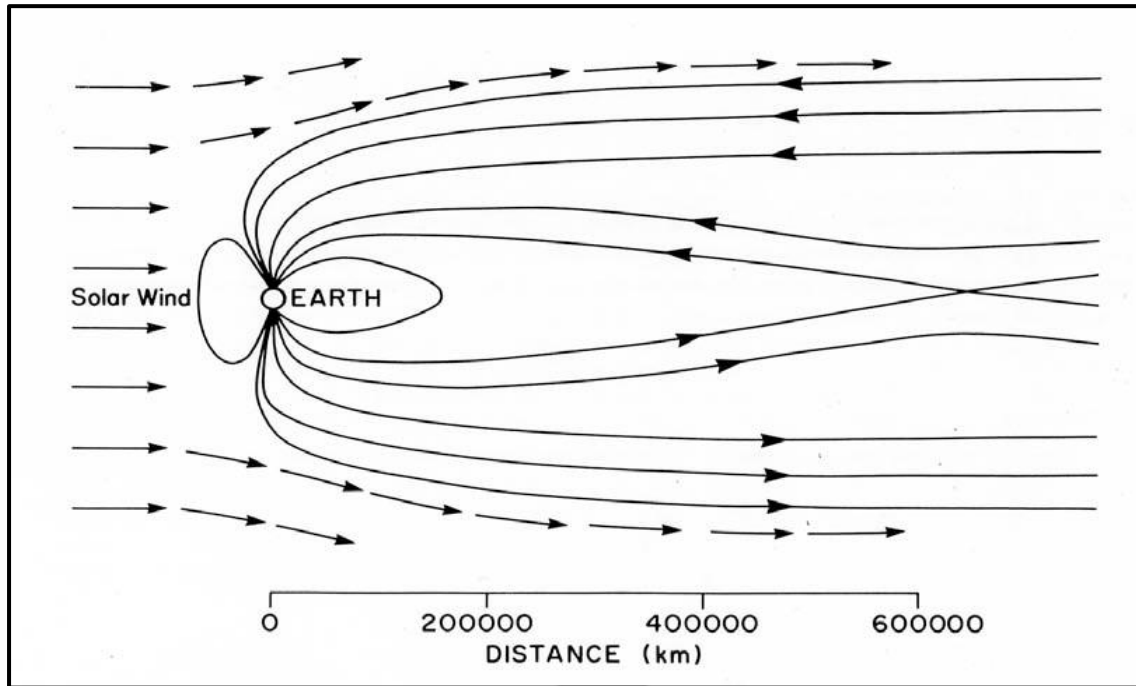


Figure 5. 4: The solar wind distorts the outer reaches of the Earth's magnetic field [Reeves, 2005].

5.1.5.3 Micropulsations

These are rapid or very short period variations of the Earth's magnetic field due to hydromagnetic disruption in the outermost exosphere, usually ranging from a fraction of a second to tens of minutes Reeves [2005] (Figure 5.5). Reeves [2005] stated that micropulsations are transitory variations of small amplitude of a few nanotesla and micropulsations sequence with shape varying from place to place over a few tens of kilometres. They leave no permanent effects on the field, but the effect measured in an aircraft or at a base station on the ground needs to be removed.

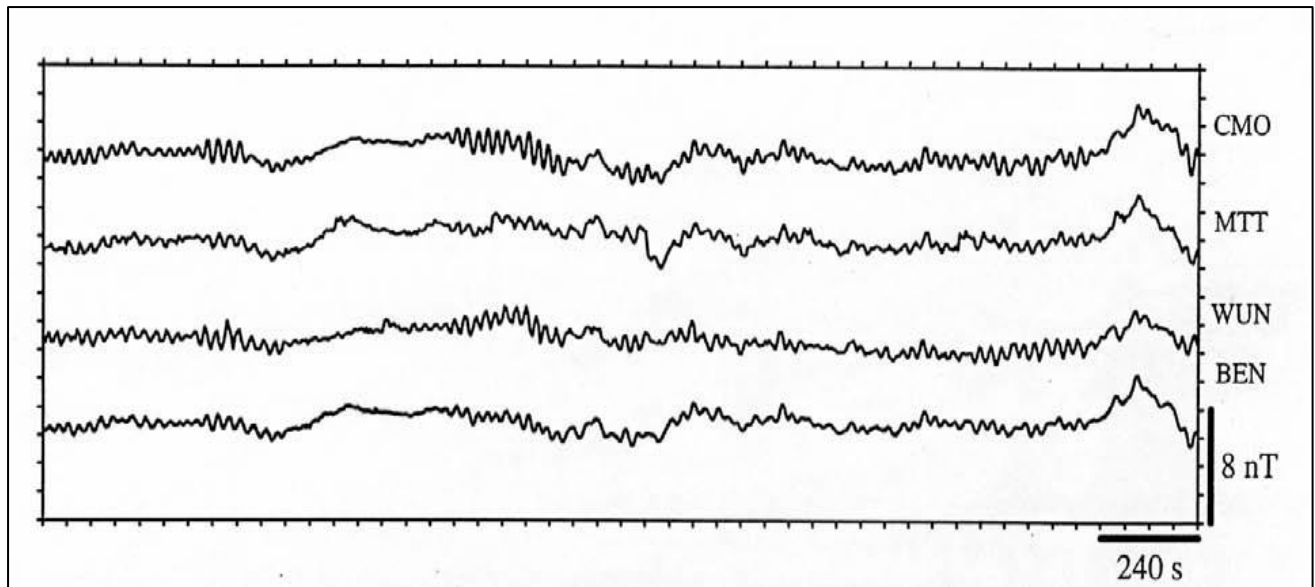


Figure 5. 5: Micropulsations recorded at stations few tens of kilometres apart [Reeves, 2005].

5.1.5.4 Magnetic storms

These are isolated points of higher degree of magnetic variation that occur occasionally. The magnetic activity in the ionosphere will suddenly increase due to magnetic storms which correlate with sunspot activity (Figure 5.6) [Reeves, 2005]. The magnetic field observed during such times is extremely irregular and unpredictable, sometimes start suddenly to a certain extent, having amplitudes as large as 1000 nT within an hour. Magnetic surveys should not be conducted during magnetic storms because they cannot be adjusted.

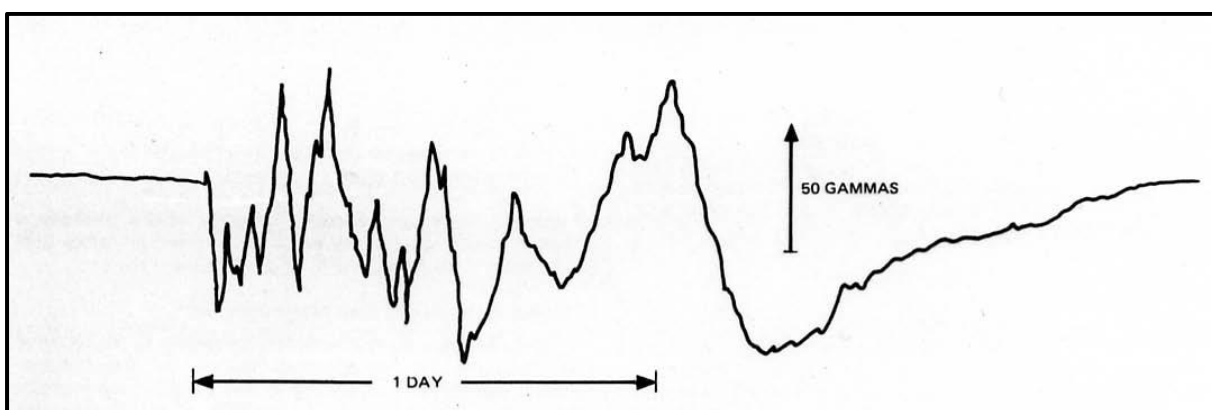


Figure 5. 6: A typical magnetic storm, as observed at a time of high solar activity [Reeves, 2005].

5.1.6 Magnetic instruments

According to Reynolds [1997] there are three types of magnetometers that can be used specifically for geophysical exploration and these are the torsion and balance, fluxgate and resonance types (which is subdivided into Proton or Overhauser and Alkali vapour absorption magnetometers).

Resonance types

Proton Magnetometer depends on the measurement of the free-precession frequency of protons that have been polarised in a direction approximately normal to the direction of the Earth's fields [Telford *et al.*, 1990]. It has a sensor which consists of a bottle containing a proton rich liquid usually water or kerosene, around which a coil is wrapped connected to the measuring apparatus. The protons act as small dipoles and normally align parallel to the ambient geomagnetic field. A current is passed through the coil to generate a magnetic field 50-100 times larger than the geomagnetic field, in a different direction, causing protons to realign in this new direction.

When the polarizing field is suddenly removed, the protons return to their original alignment by spiralling or precessing, in phase around the direction [Roux, 1980; Telford *et al.*, 1990; Kearey *et al.*, 2002].

Optical magnetometer

Optically pumped magnetometers are based on the precession of atomic spins about the magnetic field being measured.

Balance magnetometer –uses a small bar magnet which is suspended about its centre point by a horizontal quartz fibre. An external magnetic field will tilt the magnet in one or other direction. The amount of deflection will be related to the strength of the field and the direction relates to an increase or decrease of the field [Roux, 1980]. This type of magnetometer is the oldest form of magnetometers, it works no different than a compass used by early mariners [Zhdanov, 2009].

Fluxgate Magnetometer – originally the magnetometer was developed to detect submarines during the World War II, thereafter several designs for recording diurnal variation for airborne geomagnetics and as portable ground magnetometers [Reynolds, 2011]. The detector consists of cores of magnetic material, such as mu-metal or ferrite, which are wound coils through which alternating current can be passed. Variations in the electrical properties of the circuits with magnetisation of the cores can be converted into voltages proportional to the external

magnetic field along the core axes [Milsom, 2003]. Magnetic measurements are in the direction in which the sensor is pointed [Telford *et al.*, 1990; Milsom, 2003]. Portable magnetometers used for ground surveys consists of: a coil sensitive to magnetic field, an electronic oscillator and amplifier, a meter, and a- device for compensating the Earth's field [Roux, 1980]. Fluxgate magnetometers do not measure absolute fields and therefore require calibration [Milsom, 2003].

5.2 Data acquisition and data processing

The magnetic data were collected by Council for Geoscience using an aircraft Cessna 206 over the study area along north-south flight lines using two magnetometers, the first magnetometer for collection of airborne data and the second magnetometer a ground magnetometer for monitoring sunspot and for diurnal corrections. The lines were flown at a flight height of 80 m with lines spaced 200 m apart and measurements taken every 5 m station spacing. The ground speed of the aircraft was 200 km per hour.

The airborne magnetic data was levelled few times, first was pre-levelling which was done by subtraction of the base station magnetometer data from the airborne data to produce a new channel called basecor. A constant value which is the first value collected at the base station was added to the output to eliminate the negative numbers. MAGCOMP software checks for parallax problems and errors in the data and corrects them. The second levelling of magnetic data was done via the Intrepid software levelling tool. The normal method of levelling magnetic data is polynomial levelling which uses gradient sensitive weighting at the intersection. Loop levelling can produce good results if the data is very flat magnetically. Microlevelling is applied if there is a fine turning due to slight corrugation due to flight height and this produces the final channel which is magmicrolevel.

5.3 Data reduction

The total magnetic field which is observed in the field is given as:

$$F_{\text{observerd}} = F_{\text{main}} + F_{\text{temporal}} + F_{\text{crust}} \dots\dots\dots \mathbf{5.1}$$

where F_{observed} is the observed magnetic field, F_{main} is the Earth's main field, F_{temporal} is magnetic field due to temporal variations and F_{crust} is the crustal field associated with terrestrial crustal rocks.

The field which is due to crustal rocks (magnetic anomaly) is of interest in magnetic surveys,

thus: $F_{\text{crust}} = F_{\text{observed}} - F_{\text{main}} - F_{\text{Temporal}}$ **5.2**

The F_{main} is accurately estimated by International Geomagnetic Reference Field (IGF) model for the time of the survey, F_{Temporal} is monitored during the survey by a base station magnetometer and is removed.

5.4 Magnetic data enhancement

The gridded magnetic data from CGS was further processed by applying image enhancement, filtering, potential field transformation and spectral analysis. These processes which make the interpretation easier are presented in Appendix C. They include reduction to the pole, derivatives (vertical derivative, total horizontal derivative and analytical signal) and power spectrum.

5.5 Data presentation and interpretation



5.5.1 Geology map

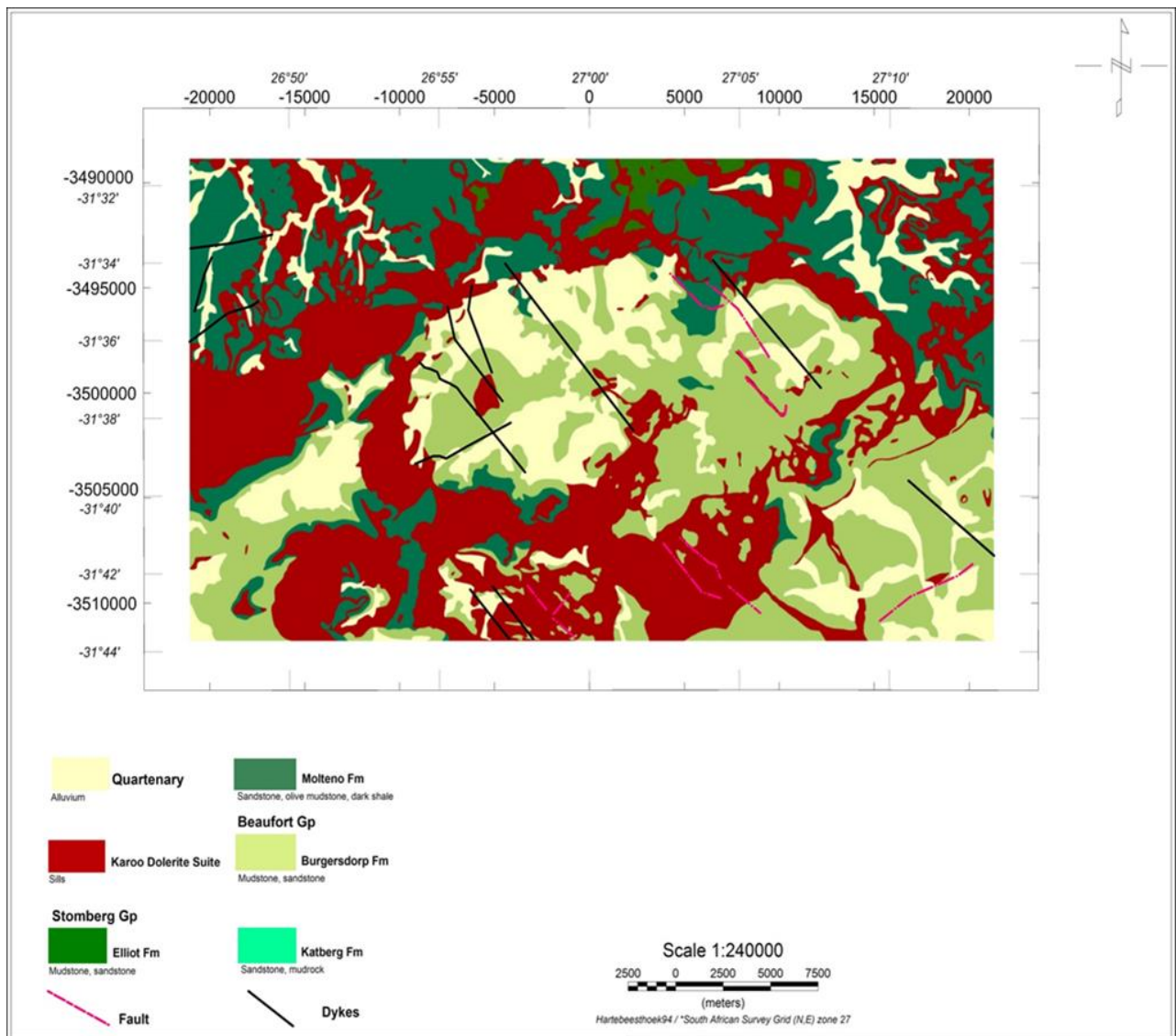


Figure 5. 7: Formations, simplified geology map of the study area from (Council for Geoscience, geology database accessed on 04/2017)

5.5.2 Reduced to pole map

Figure 5.8 is the reduced to pole of the total magnetic field overlain with the Karoo dolerite sills, dykes, ring complexes and faults digitized from the geology map of the study area in order to correlate magnetic signatures with geologic features. As explained in Appendix C, the reduction to pole transforms the dipolar magnetic field of a body to look like that of a body located at the poles. Hence it removed the effect of the magnetic inclination, to produce anomalies lying directly over the causative bodies.

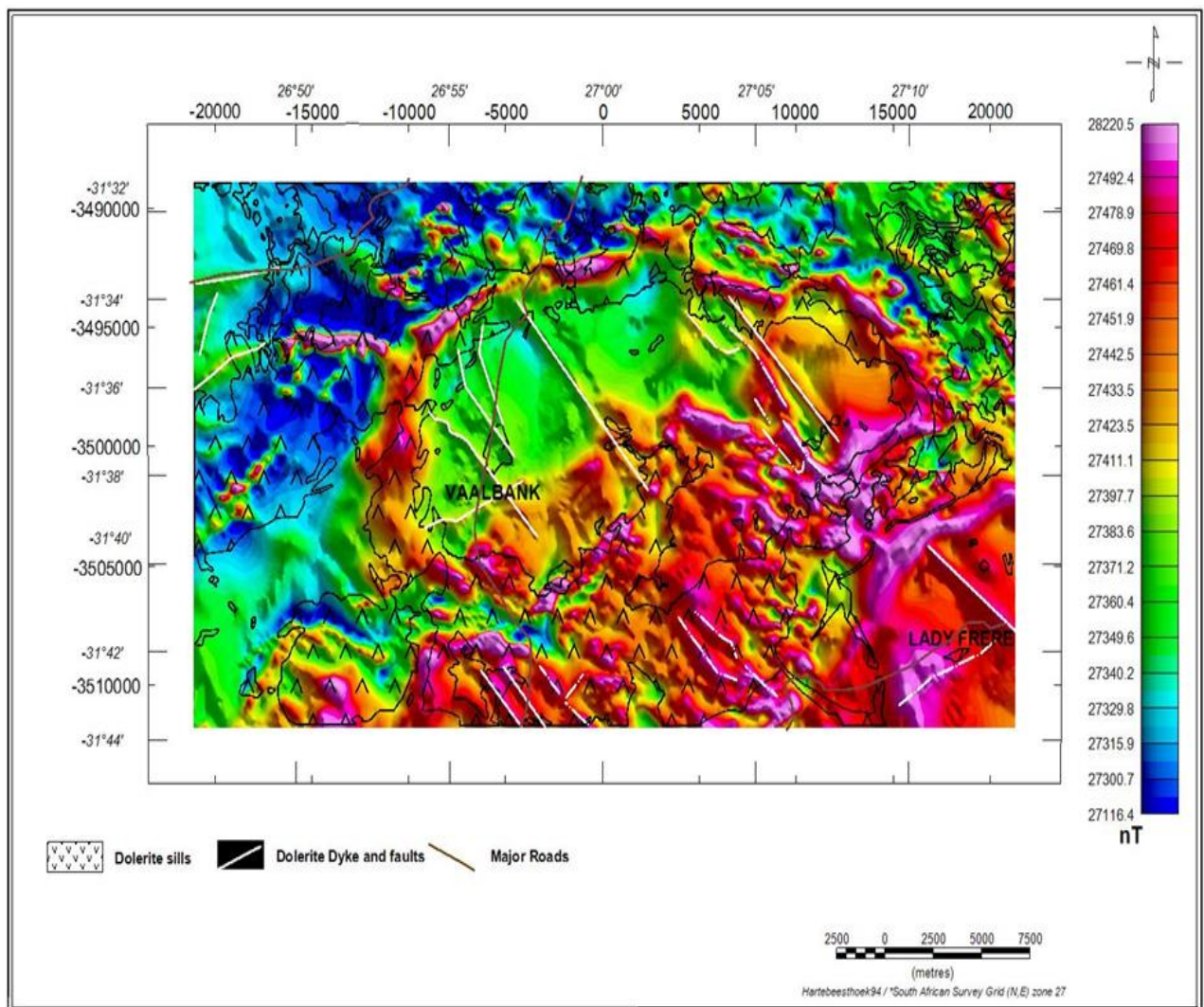


Figure 5. 8: Reduced to pole magnetic map overlain with the geology of the study area. The warm colours (red to purple) on the map represent high magnetic values whilst the cold colours (blue to deep blue) represent low magnetic values.

Figure 5.8 shows that the north western part of the map has low magnetic values compared to the rest of the map. There are numerous lineaments of high magnetic values trending predominantly in a NW-SE direction and a few that trend NE-SW. Magnetic highs forming a circular pattern are seen on the central part of the map. The highest magnetic anomalies correlate with the Karoo dolerite sills/ring complexes. There is a high magnetic anomaly in the south of Lady Frere and this could be due to deep magnetic bodies (e.g. sills). The mapped dykes and faults striking NW-SE are coincident with the magnetic high lineaments. However, there are more NW-SE magnetic high lineaments that are not shown on the geology map and these are inferred to be dykes and faults that come up close to the surface. These lineaments are part of the dyke swarms alluded to by Chevallier *et al.* [2001].



5.5.3 Vertical derivative magnetic map

Vertical derivative filters are enhancement techniques that aid in amplifying the shorter wavelength features relatively to those with larger wavelengths. The magnetic anomalies seen on the reduced to pole map (Figure 5.9) are broader than the extent of the magnetic bodies. The vertical derivative map narrows the anomalies and this helps in resolving the anomalies as well as suppressing the regional field. The vertical derivative map (Figure 5.9) clearly shows the linear anomalies due to NW-SE dykes and sills, and the broader, elongated magnetic high anomalies due to the dolerite sills.

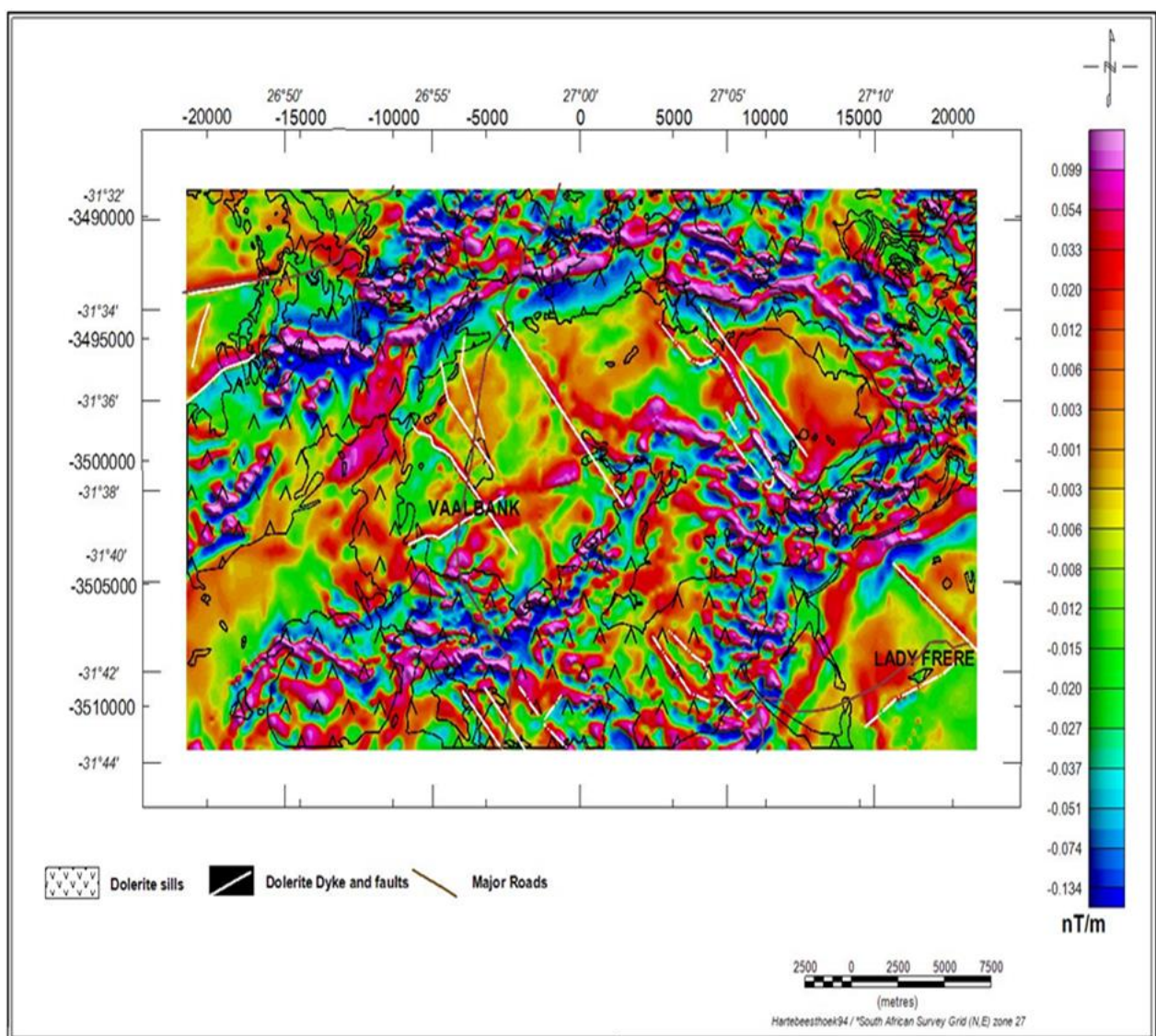


Figure 5. 9: Vertical derivative magnetic map superimposed geological features of the study area.

5.5.4 Total horizontal derivative magnetic map

A horizontal derivative is a tool used to resolve or separate anomalies that could be due to several magnetic bodies. The total horizontal derivative map (Figure 5.10) of the reduced to pole data shows highs whose peaks mark the edges of the magnetic bodies. Some of the highs trending NW-SE are associated with the dolerite dykes and faults, and others are coincident with circular patterns due to sills.

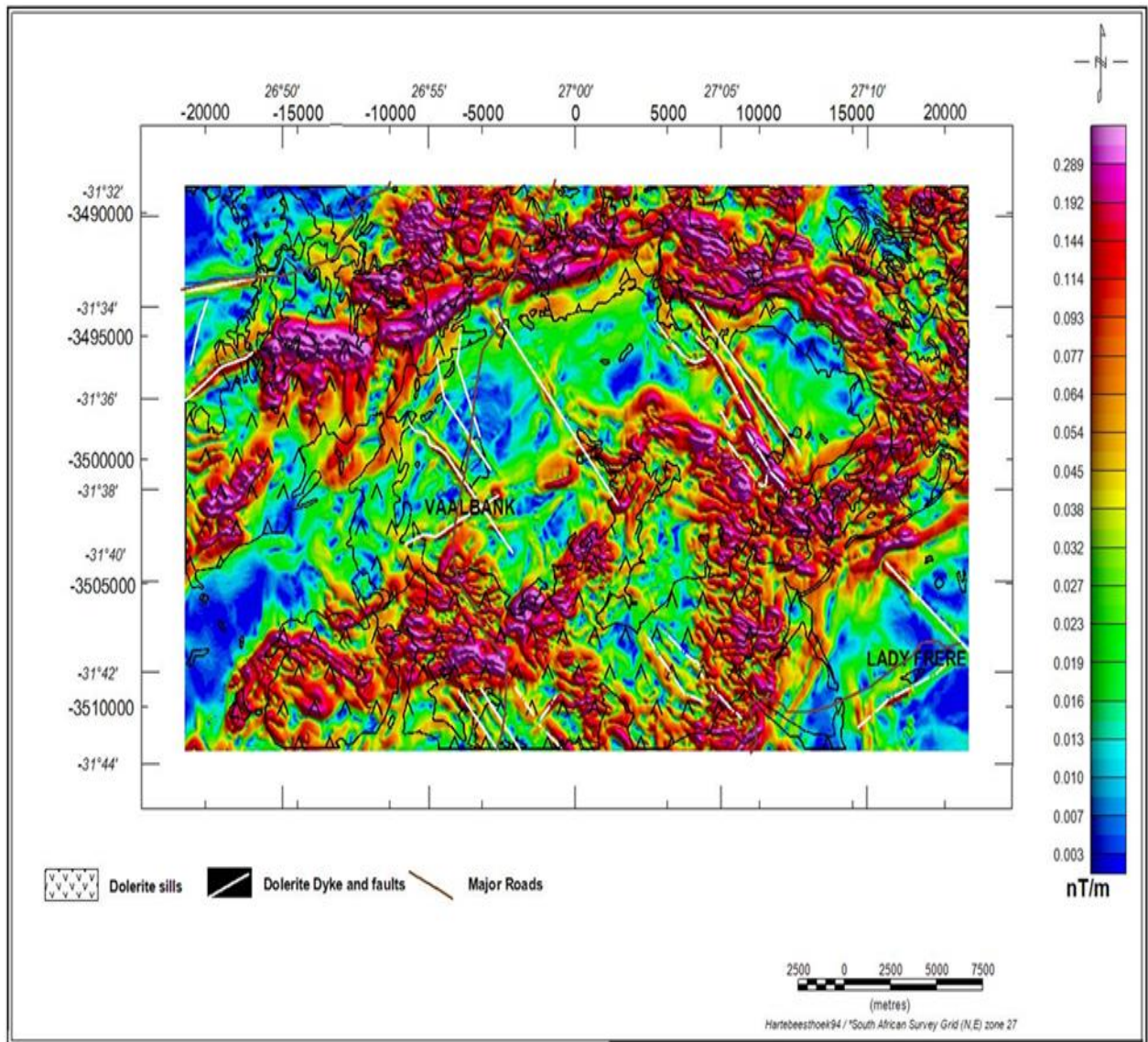


Figure 5. 10: Total horizontal derivative magnetic map superimposed geological features of the study area

5.5.5 Analytical signal magnetic map

The analytic signal magnetic map (Figure 5.11) was created by combining the total horizontal with vertical derivative as explained in Appendix C. The analytic signal peaks over the edges of the magnetic bodies. The map (Figure 5.11) shows broader highs that mainly fall within the area covered by dolerite sills. Further, there are magnetic highs lineaments that coincide with dolerite dykes and faults trending in the NW-SE direction.

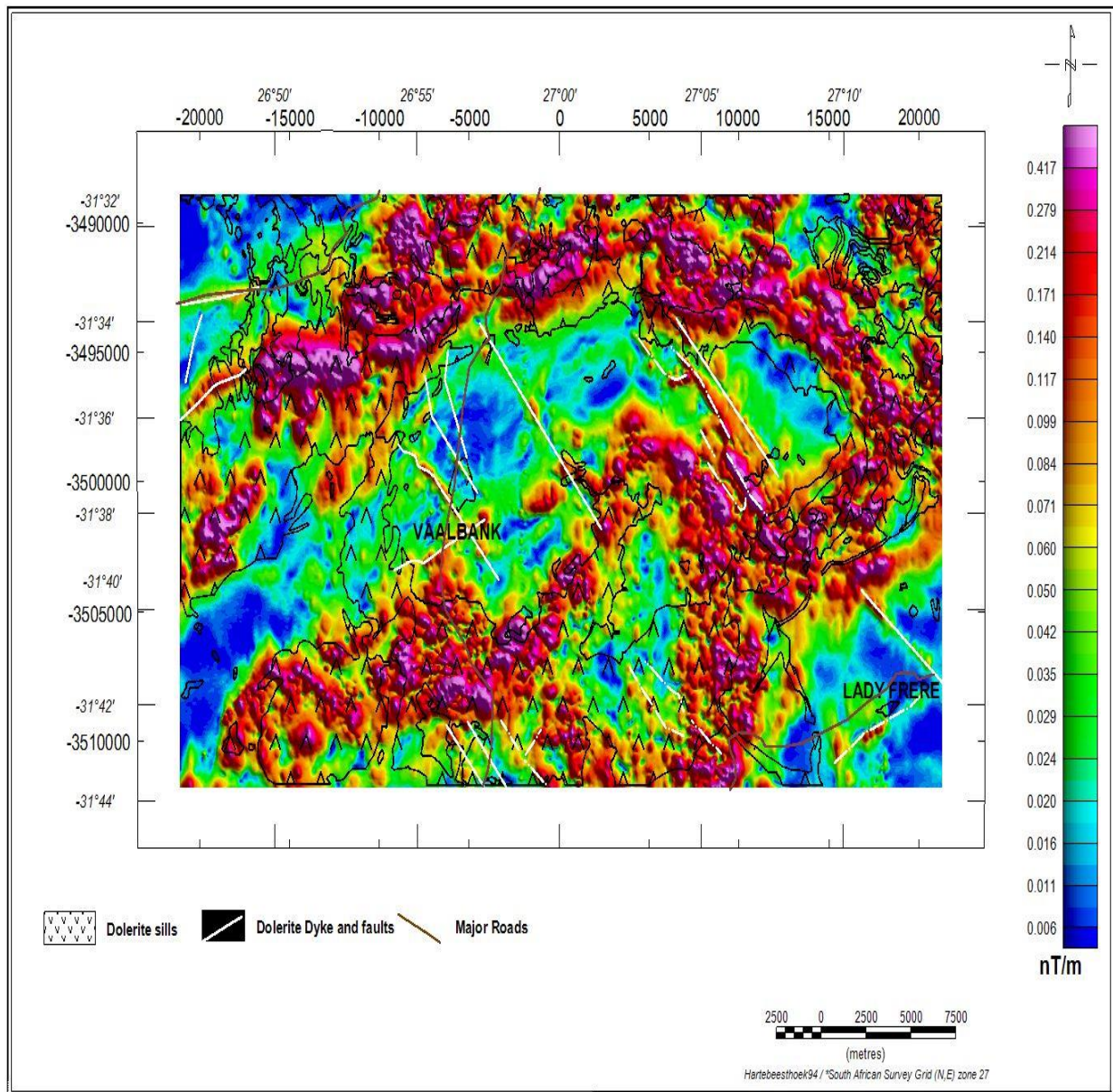


Figure 5. 11: Analytical signal magnetic map superimposed on geological features of the study area.

5.5.6 Radially averaged power spectrum and depth slicing

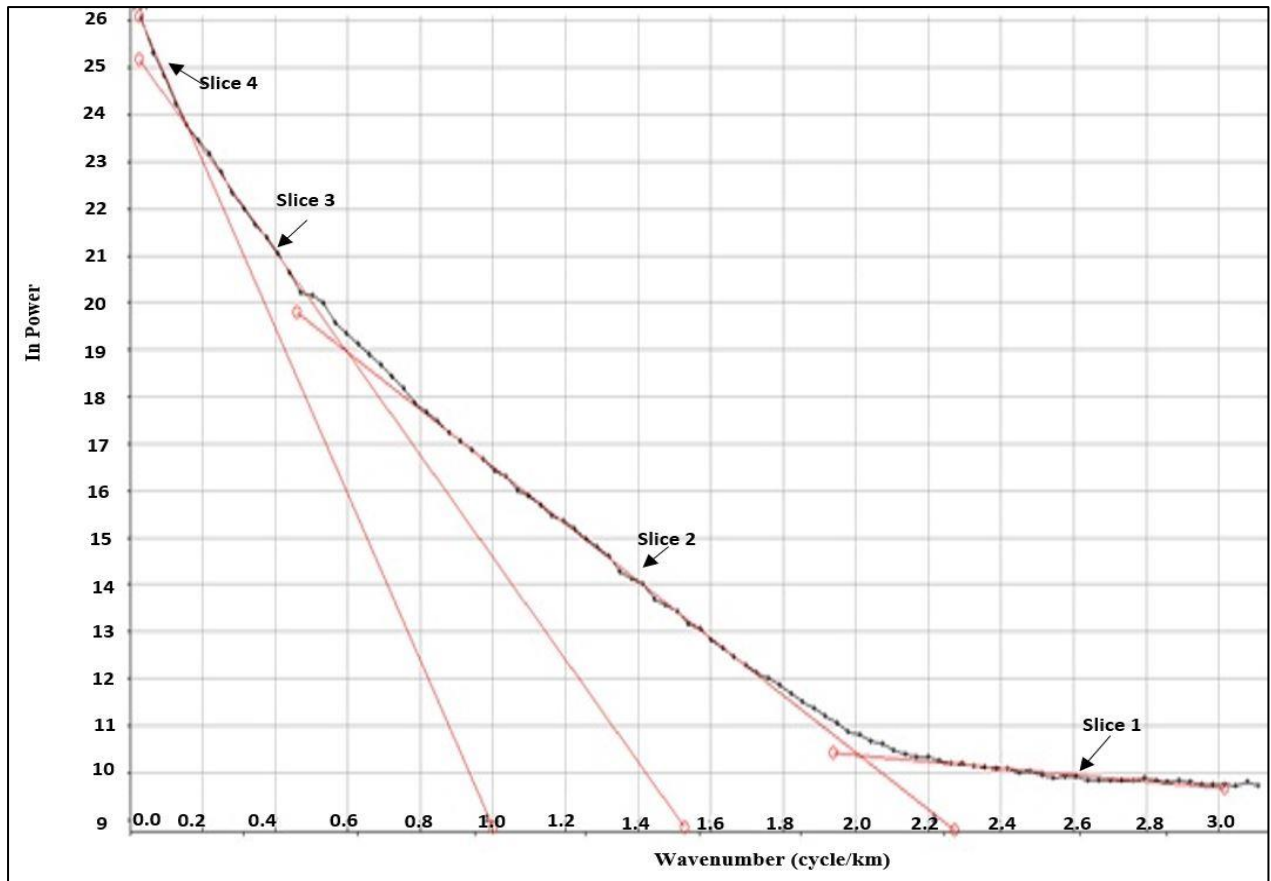


Figure 5. 12: Radially averaged power spectrum of magnetic data.

University of Fort Hare
Together in Excellence

The radially averaged power spectrum was introduced by Spector and Grant [1970] to estimate the average depth to a source directly from the slope of the radially averaged power spectrum. The depth h , is calculated from the slope as:

$$h = \frac{\text{Slope}}{-4\pi}$$

The steeper the slope, the deeper the magnetic depth to the source and, the gentler the slope the shallower the depth to the magnetic source.

Figure 5.12 is the radially averaged power spectrum of the magnetic data obtained using GETECH Resolve software. A total of four linear segments (depth slices 1-4) were fitted to the curve. The average depths to magnetic sources are 128 m, 1660 m, 2830 m and 12401 m for the four linear segments, respectively.

5.5.7 Depth slicing

The depth slices 1- 4 in Figure 5.13 were used to produce depth maps at depths of 110 m, 1660 m, 2830 and 12401 m, respectively. The depth slices 1 and 2 (at depths of 110 m and 1660 m) have several linear shaped anomalies as well as fewer ring shaped anomalies but both types of anomalies are weak. The depth slices 3-4 (Figure 5.13) have ring shaped anomalies that have a strong signature and the linear shaped anomalies have a weak response. The linear shaped anomalies are inferred to be due to dolerite dykes, while the ring anomalies are due to dolerite sills and ring complexes.

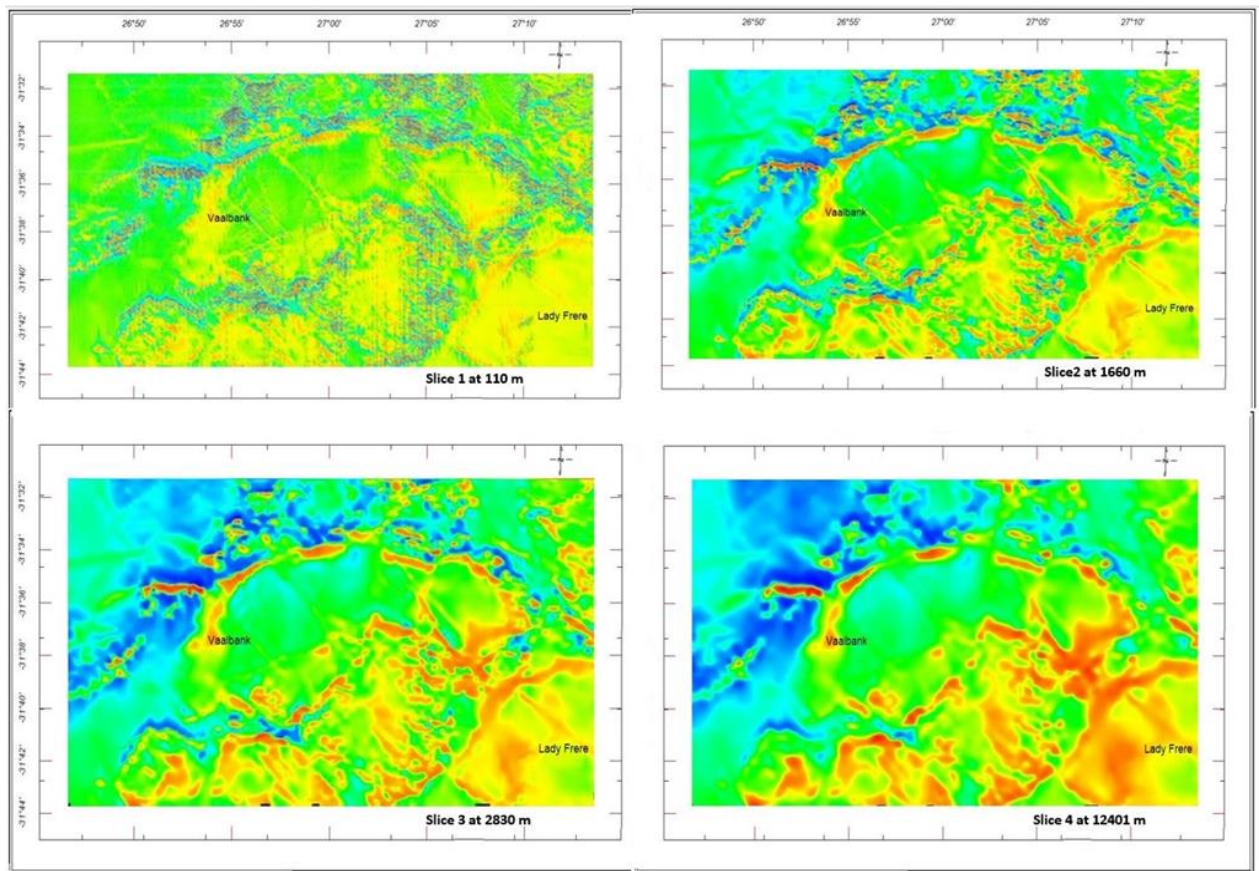


Figure 5. 13: Depth slice maps of the magnetic data showing changes in the magnetic anomalies with depth.

5.6 Discussion and summary of magnetic results

The various magnetic maps (Figures 5.8, 5.9, 5.10, 5.11) are characterised by magnetic high lineaments predominantly in a trending NW-SE direction and a few that are in NE-SW direction. A number of these lineaments coincide with mapped dolerite dykes and faults. Apart from the lineaments, there are several magnetic highs that are ring like shaped and are

of various diameters. These coincide in most places with the mapped dolerite sills/ring complexes. It is inferred that the magnetic high lineaments and the ring like patterns that are not mapped on the geology map, are due to dykes/faults and sills that do not outcrop but their tops are at shallow depths. The magnetic highs which coincide with the faults are caused by secondary magnetization produced by geochemical activities along the fault zone [Grauch *et al.* 2006].

Thin sections and XRD analyses confirmed that the dolerite samples obtained from the study area contain magnetite, which is the source of magnetic anomalies. The gamma ray spectrometry maps revealed the lineaments which are also revealed by magnetic maps and their depths are revealed by depths slices maps. Chevalier *et al.* [2001] and Woodford Chevallier [1997] have shown the presence of the lineaments (dykes and faults), and ring patterns (dolerite sills and ring complexes). The depth slices maps (Figure 5.13) show that the magnetic signatures extend from surface or shallow depths to at least 12.4 km depth.

5.7 Conclusion



The following conclusions can be made from the interpretation of the magnetic maps, radially averaged power spectrum and depths slices presented:

- The reduced to the pole magnetic field values vary from about 27116 nT to 28221 nT with low values in the northwestern part of the study area. Magnetic high values coincide with the dolerite intrusions (i.e. sill/ring complexes and dykes). The ring shaped magnetic high anomalies are due to sills/ring complexes.
- Magnetic high lineaments are due to predominant trend in a NW-SE direction with few in a NE-SW direction due to dykes and faults. Some of the inferred dykes are not mapped on the geological map.
- The radially averaged power spectrum indicates average depths to magnetic sources of 128 m, 1660 m, 2830 m, 12401 m. The corresponding depth slices maps show that the magnetic sources extend from the surface or shallow depth to depths of up to 12.4 km.

CHAPTER 6: GRAVITY METHOD

6.1 Introduction

Gravity method is a technique used to measure the variations in the gravitational acceleration of the Earth. Measuring of gravitational acceleration provides information to infer densities of the subsurface rocks. The strength of the gravitational field increases with an increase of the density of the underground material [Mickus, 2014]. There is a wide range of densities among rock types, therefore geologists can make inference about the rock distribution. The gravity data can be presented in the form of gravity profiles and maps.

The gravity method is based on Newton's two laws namely Newton's Universal Law of Gravitation and Newton's second Law of motion. Newton's Universal Law of Gravitation states that "the force of attraction between two bodies of known masses is directly proportional to the product of the two masses and inversely proportional to the square of the distance between them". Thus the magnitude of the force (F) is given as:

$$F = G \frac{m_1 m_2}{r^2} \quad 6.1$$

where m_1 and m_2 are the masses of the two bodies, r is the distance separating the two masses, $G = 6.67 \times 10^{-11} \text{ Nm}^2\text{kg}^{-2}$ is the gravitational constant.

Newton's Second law of Motion states that "the force is equal to the product of mass (m) and acceleration due to gravity (g)

$$\vec{F} = m\vec{g} \quad \text{or} \quad F = |\vec{F}| = mg \quad 6.2$$

For a mass m , on the Earth's surface at a distance $r = R$ (radius of the Earth) and equating expressions 6.1 and 6.2, g is obtained as

$$g = \frac{GM}{R^2} \quad 6.3$$

The Earth's gravitational acceleration is referred as gravity (g) and this is generally quoted to be about 9.8 ms^{-2} . If the Earth was a perfect sphere with no lateral inhomogeneous and did not rotate, g would be the same everywhere on surface. This gravity (g) is directly proportional to the mass (M) of the Earth and inversely proportional to the square of the Earth's radius (R). The mass (M) is a function of the density of subsurface rocks in the area of the measuring station. This implies that the Earth's gravitational field variations are due to differences in the density of the underground rocks and the distance to these rocks from the gravimeter.

6.1.1 Units for gravity

Gravity measurements were initiated by Galilei Galileo and the gravity units were given as Gal (1 cm/s^2) in honour of Galileo. However, the gravimeters were designed such that they are very sensitive and can measure signals less than a mGal (about ten parts per million).

In exploration the gravity variations are very small and hence a smaller unit the milliGal (mGal) is used. Further, a corresponding SI unit, the gravity unit (g.u) is the modern unit and is related to the milliGals as follows:

$$1 \text{ mGal} = 10 \text{ g.u and } 1 \text{ g.u} = 1 \times 10^{-6} \text{ m s}^{-2}$$

6.2 Gravity instrumentation

The instrument used to measure gravitational field of Earth at specific locations is called a gravity meter or gravimeter. The instrument works on the principle of measuring constant downward acceleration of gravity. According to Haldar [2018] There are two types of gravimeters i.e. the absolute and relative.

Absolute gravimeters measure the local gravity in absolute units (Gal). Absolute gravimeters are compact (Autograv CG-5 model) and used in the field. They work by directly measuring the acceleration of a mass during freefall in a vacuum. An accelerometer is rigidly attached to the ground.

Relative changes in gravity between two points or locations are measured in exploration using a relative gravimeter. There are different types of gravimeters used for relative measurements ranging from stable to unstable gravimeters depending on the purpose of the survey either for mineral or hydrocarbon exploration or regional geological studies. The stable gravimeter has a sensing system which returns to its original position when it is disturbed (e.g. Askania, Boliden and Gulf gravimeters). The unstable gravimeter has a system which moves farther away from its original position when it is disturbed (e.g. Lacoste-Romberg, Worden and Sodin gravimeters).

In a survey where relative gravity values are measured, they can be converted to absolute gravity values by tying a base station in the survey area to an International Gravity Standardisation Net 1971 (IGSN 71) network and thus all the acquired relative gravity values at all stations can be reduced to absolute gravity values.

6.3 Data acquisition and processing

The gravity data were supplied by the Council for Geoscience. The following corrections done by the Council for Geoscience on the gravity data include;

- i. Tidal correction
- ii. Instruments drift correction
- iii. Latitude correction
- iv. Free air correction
- v. Bouguer slab correction
- vi. Terrain correction

6.4 Data presentation and interpretation



6.4.1 Bouguer gravity map

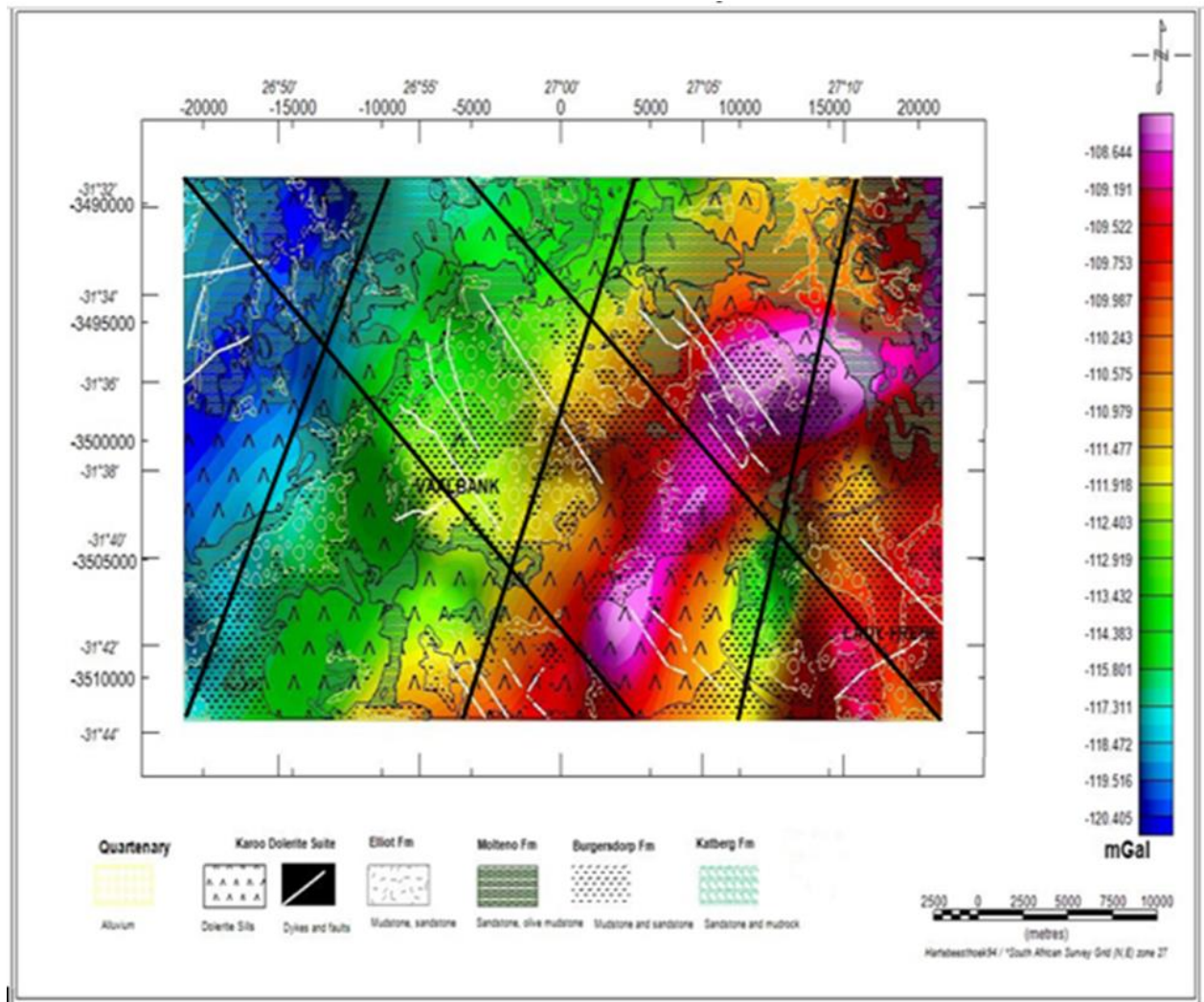


Figure 6. 1: Bouguer gravity map overlain with the geology. *Note: 1mGal= 10.g.u.* Pink-Yellow areas represent high gravity values while deep blue areas have low gravity values.

The Bouguer gravity map (Figure 6.1) shows variations in gravity over the study area. The Bouguer gravity values are negative with the lowest values (about -120.4 mGal) in the northwestern part of the map and highest values in the southeastern to eastern part of the map (Figure 6.1). Hence the gravity increases in a NW-SE direction and has a long wavelength component, which is probably due to crustal thinning from inland towards the coastal areas in the southeast outside the study area. There is a noticeable broad zone of a gravity high trending in a SW-NE direction. There is a circular gravity high anomaly that occurs in the south-eastern corner of the map.

6.4.2 Trended gravity map

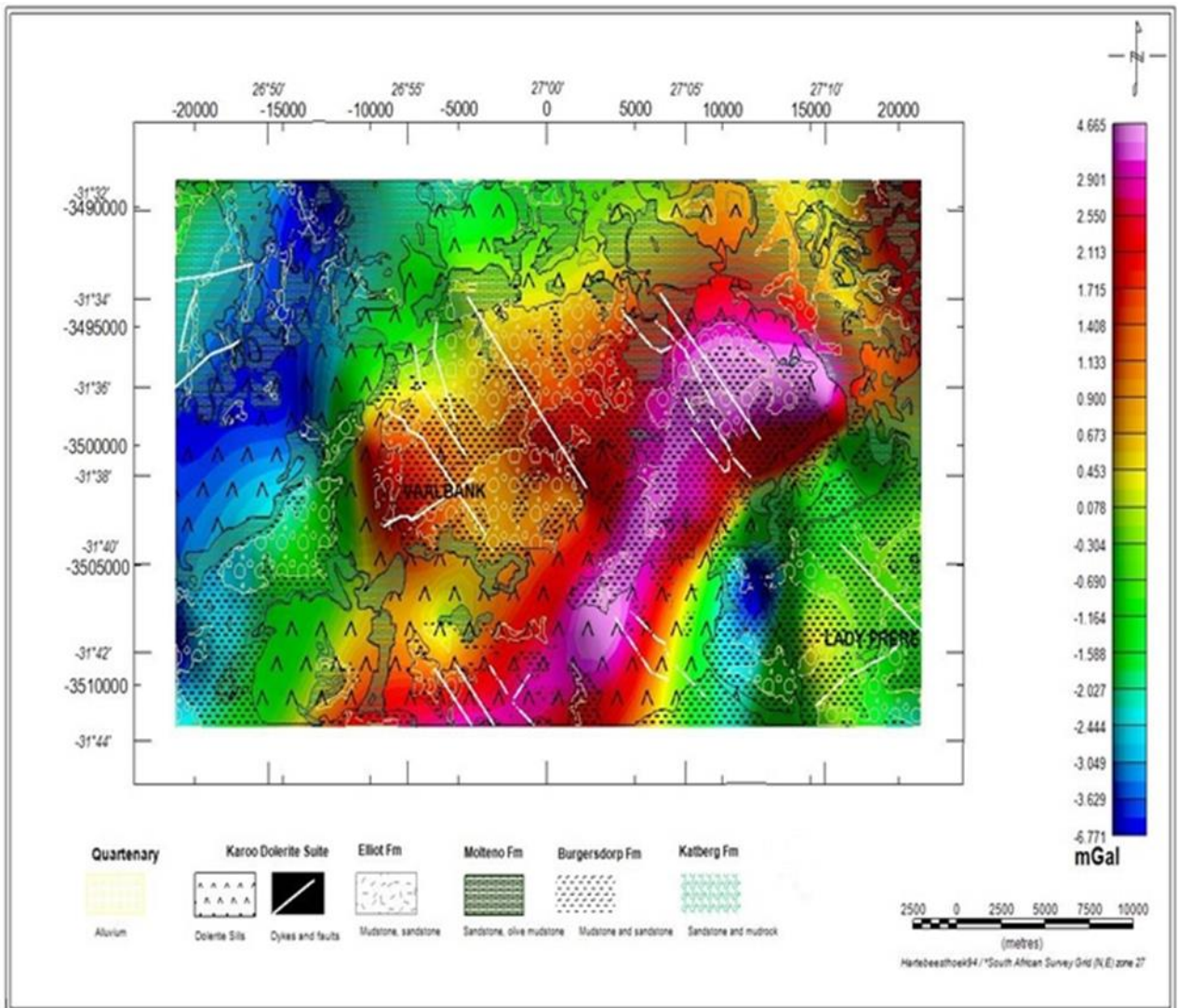


Figure 6. 2: Trended gravity map overlain with the geology of the study area

Figure 6.2 shows the trended Bouguer gravity map overlain with the geology of the study area. This trended map was obtained by removing a first order trend from Bouguer gravity map to leave the residual or local anomalies. Hence the local anomalies are emphasized. These residual anomalies have values that range from -4.771 to 4.665 mGal. A broad gravity high zone striking in a NE-SW direction coincides with the Burgersdorp Formation, alluvial cover and dolerite intrusions.

6.4.3 Gravity power spectrum

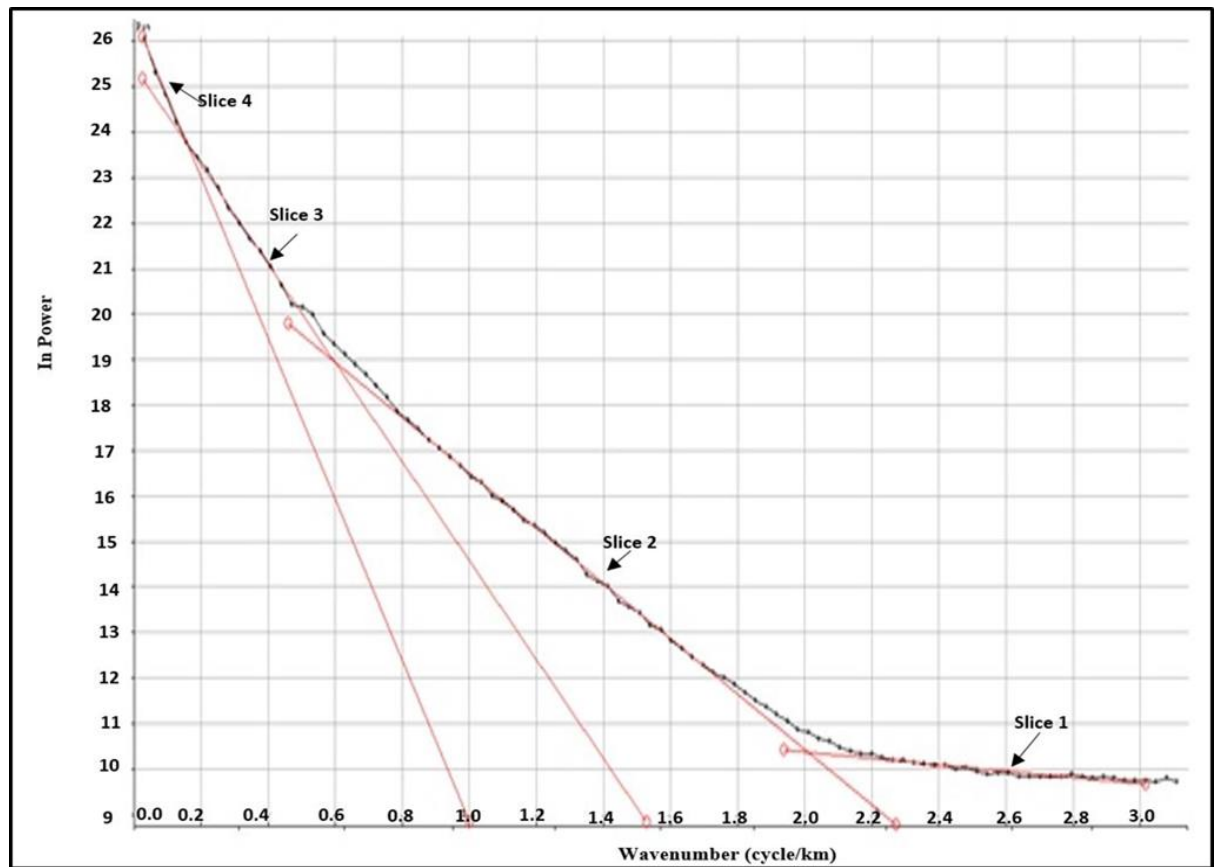


Figure 6. 3: Gravity radially averaged power spectrum

Figure 6.3 is the radially averaged power spectrum of the gravity data obtained using GETECH Resolve software. A total of four linear segments (depth slices 1-4) were fitted to the curve. The average depths to sources are 1230 m, 2720 m, 4400 m and 10100 m for the four linear segments, respectively. The steeper the line the deeper the source, the gentler the slope the shallower the source.

6.4.4 Gravity slice maps

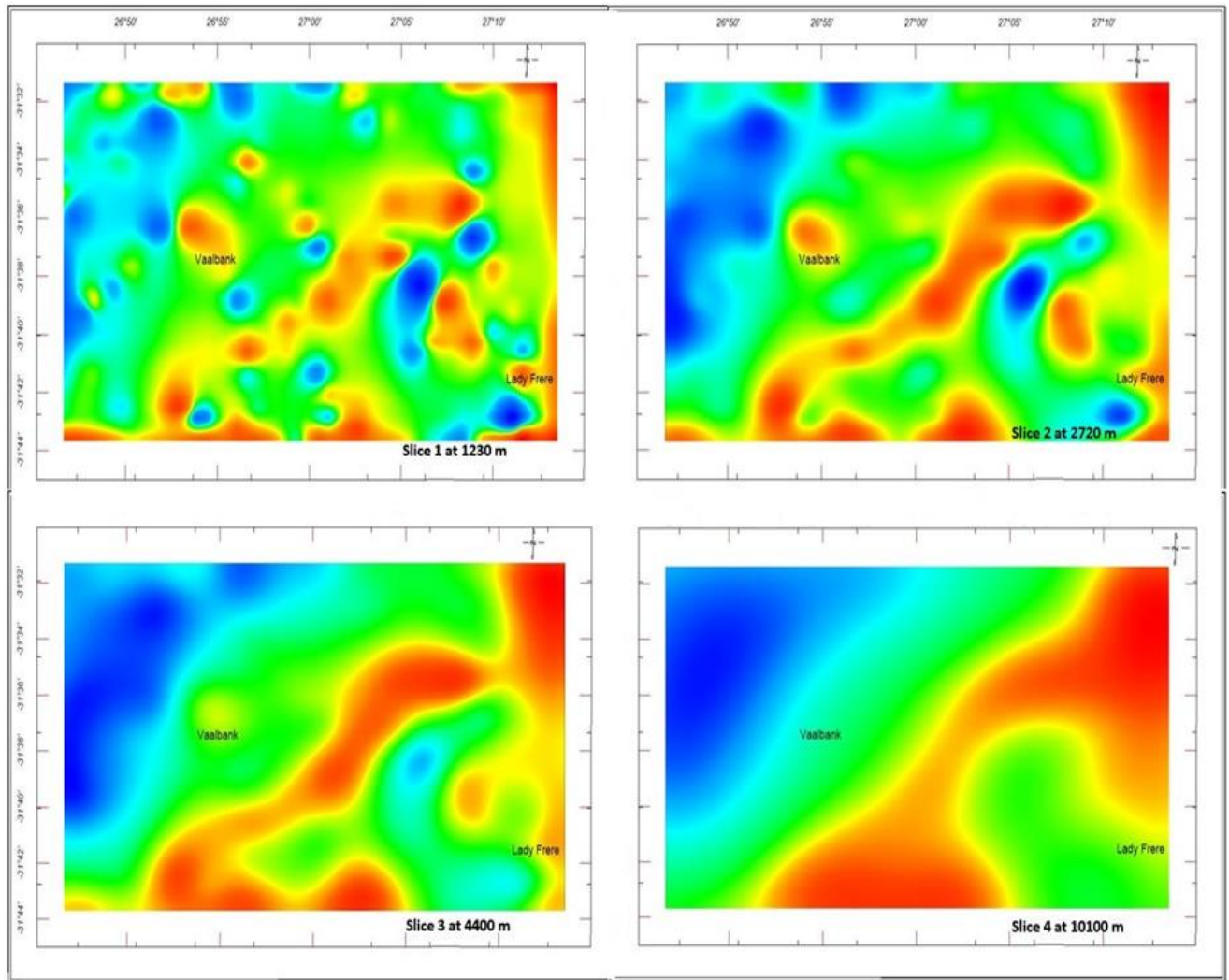


Figure 6. 4: Gravity slice maps of the study area at different depths.

The depth slices 1-4 in Figure 6.5 were produced using the average depths obtained from the gravity power spectrum (Figure 6.4). All the four depths slices show gravity high that trends from NE-SW direction and this anomaly gets stronger with depth.

6.5 Discussion of the gravity results

The gravity maps (Figures 6.1 and 6.2) show a high gravity zone trending in the NE-SW directions. These anomalies coincide with mapped dolerite sills, Burgersdorp Formation and alluvial cover. The measured dry density of the Burgersdorp Formation and dolerite intrusions are 2.458 kg m^{-3} and 2.771 kg m^{-3} , respectively (see Table 3.1). The depth slices maps reveal gravity high zone which is more intense with depth up to 10.1 km depth. It is therefore inferred

that the gravity high zone that trend in a NE-SW direction is due to the dolerite intrusions which are of high density material.

6.6 Conclusion

It can be deduced from interpretation of the gravity maps that:

- The long wavelength gravity anomaly that increases in NW-SE direction is possibly due to a deep source and this will be investigated through a 2½ D modelling in chapter 7.
- The gravity high zones of residual anomalies trending in a NE-SW direction coincident with Karoo dolerite, Burgersdorp Formation and alluvium cover is inferred to be due to the dolerite intrusions.
- The low Bouguer anomalies are mostly correlating with the Molteno Formation which has the least rock density and it has weathered sandstones which consist of less quartz compared to the sandstones of the Burgersdorp Formation.



University of Fort Hare
Together in Excellence

CHAPTER 7: 2 ½D GRAVITY MODELLING

7.1 Introduction to gravity modelling

In this chapter geological models were constructed to model the subsurface of the study area. A geological model is a spatial representation of the distribution of sediments and rocks in the subsurface. The model is usually presented by 2D cross-sections, but increasingly visualised as digital 3D models [Artimo et al., 2003; Kassenaar et al., 2003; Hinsby and Abatzis, 2004].

In forward modelling, the gravity effect of the constructed model is calculated and compared to that of the observed gravity along a profile. Gravity models are not unique as there are a number of possible models for the same data. The chosen models should be geologically reasonable to represent the actual geology.

7.1.1. Gravity profile modelling

The gravity profiles were modelled using GM-SYS. GM-SYS is a program that calculates the gravity and magnetic response from a geologic model. GM-SYS provides an interface that makes it easy to create and manipulate models to fit the observed gravity and magnetic responses from 2D, 2½ D and 2¾ D models.

GM-SYS version 9.5.1 was used to produce the models from selected five profile lines (A-E) that traverse through the study area (Figure 7.1). The profiles were selected in such a way that they cover most of the features of interest on the geology map (e.g. dolerite intrusions). The width of outcrop of the various geological formations were measured from the geology map of South Africa by Visser [1989]. Lines A-A' and B-B' run from NW-SE direction and lines C-C', D-D' and E-E' run in a NE-SW direction across the geology map (see Figure 7.1).

For each selected gravity profile, 3 models were generated, with the first model using the average measured densities, a second model was constructed based on the minimum measured density for each geological block and a third model that used the maximum measured density for each geological block. Hence, a total of 15 models were obtained for the five profiles. Densities of the formations of the Beaufort Group were measured in the laboratory while other densities of the formations that do not outcrop in the study area were taken from Baiyegunhi

[2015], Chima [2017] and Nxantsiya [2017]. The gravity data with the digital terrain data were used for modelling. The dry densities of rocks of the upper mantle (below the Moho) were taken from literature [Hynes and Snyder, 1995; Cook *et al.*, 2010; Mjelde *et al.*, 2013; Thybo and Artemieva, 2014; Baiyegunhi, 2015; Nxantsiya, 2017] since there is no access to measure these densities and the density values range from 3.140-3.400 g/cm³. The highest, lowest and average dry density values that were used in the models for the geologic groups are presented in Table 7.1

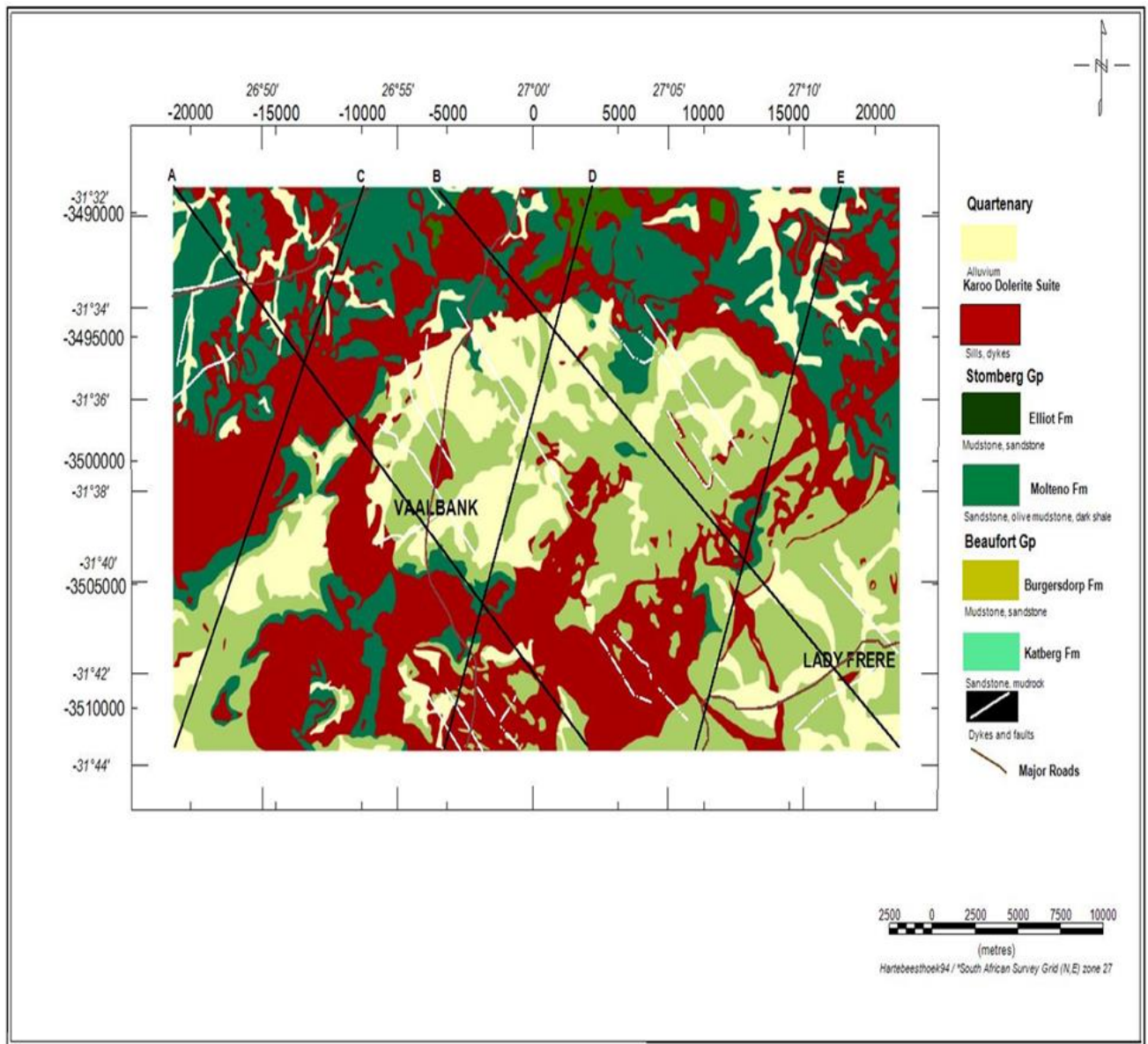


Figure 7. 1: Geology map of the study area with profile lines A-E.

Table 7. 1 Rock density values used for gravity profile modelling. Units are in g/cm³.

:

	Karoo Dolerite	Elliot Formation	Molteno Formation	Burgersdorp Formation	Adelaide Subgroup	Ecca Group	Dwyka Group	Cape Supergroup	Basement	Upper Mantle
Lowest density	2.624	2.494	1.557	2.192	2.674	2.349	2.585	2.630	2.723	3.140
Average density	2.771	2.507	2.595	2.458	2.723	2.565	2.662	2.675	2.772	3.270
Highest Density	2.941	2.519	2.672	2.654	2.772	2.781	2.678	2.719	2.820	3.400

7.2 Gravity modelling results

The models comprise of the upper mantle block (3.27 g/cm^3), overlain by the basement (2.77 g/cm^3), on top of the basement are the Cape Supergroup rock units (2.67 g/cm^3) overlain by the Karoo Supergroup. In the models the Karoo Supergroup is divided into groups, namely Dwyka Group (2.66 g/cm^3), Ecca Group (2.56 g/cm^3) and the Beaufort Group. The Beaufort Group is subdivided into the Adelaide Subgroup (2.72 g/cm^3) and the Tarkastad Subgroup. The Tarkastad Subgroup is subdivided into the Burgersdorp Formation (2.46 g/cm^3) and Katberg Formation, overlaying the Burgersdorp Formation are the Molteno (2.59 g/cm^3) and Elliot formations (2.507 g/cm^3) of the Stomberg Group. Cutting through the rocks of the Cape Supergroup and Karoo Supergroup are dolerite intrusions (2.776 g/cm^3). The Beaufort Group was broken into subdivisions in the models and this was necessary for a detailed interpretation of the study area. There is no density contrast between the dolerite intrusions and the basement. Although the dolerite intrusion bodies in the models appear to stop at the basement, in reality they continue further downwards and are indistinguishable from the basement due to having no density contrast.

The models were prepared by assigning names, rock densities, the length of blocks in +y and -y strike directions representing various rock units. The GM-SYS modelling software assumes that the Earth has no curvature and that the layers can be extended to infinity to avoid undesirable edge effects. Baiyegunhi [2015], Juliana et al. [2016] and Nxantsiya [2017], used this approach.

The inversion was applied to automatically minimize the root mean square (RMS) misfit between calculated and observed gravity. The geologic bodies had their geometry changed until the calculated gravity fitted the observed gravity data within an acceptable RMS error. Models using the average densities are presented in this chapter and the other models generated using the minimum and maximum densities are presented in Appendix E.

7.2.1 Modelling results for Profile A-A'

The profile runs from the NW-SE direction cutting through rocks of the Karoo Supergroup and that of the Cape Supergroup. The gravity ranges from -122 mGal at the beginning of the profile to -110 mGal at its end. The oldest to youngest geological units are from the bottom

to the top of the model. Figure 7.2 shows the starting model with a crustal block that extends to large distance (+550 km) beyond the ends of the profile. The starting model was created for profile A-A' using average densities of the sediments of the Karoo Supergroup and Cape Supergroup. The Moho depth was left to vary from a depth of 40-50 km. In the starting model there is a large misfit between the calculated and observed gravity with root mean square error (RMS) of 17.217. The inversion was ran to get a best fitting model shown in Figure 7.3 with error of 0.602. It was observed that the Moho was horizontal and at a depth of 47 km in the study area and was at a shallower depth of 45 km near the coastal areas. The depth of the Moho remained the same in the study area for all the models. Hence the final models are shown up to a depth of 15 km in order to clearly see the shallow structures in this depth range.

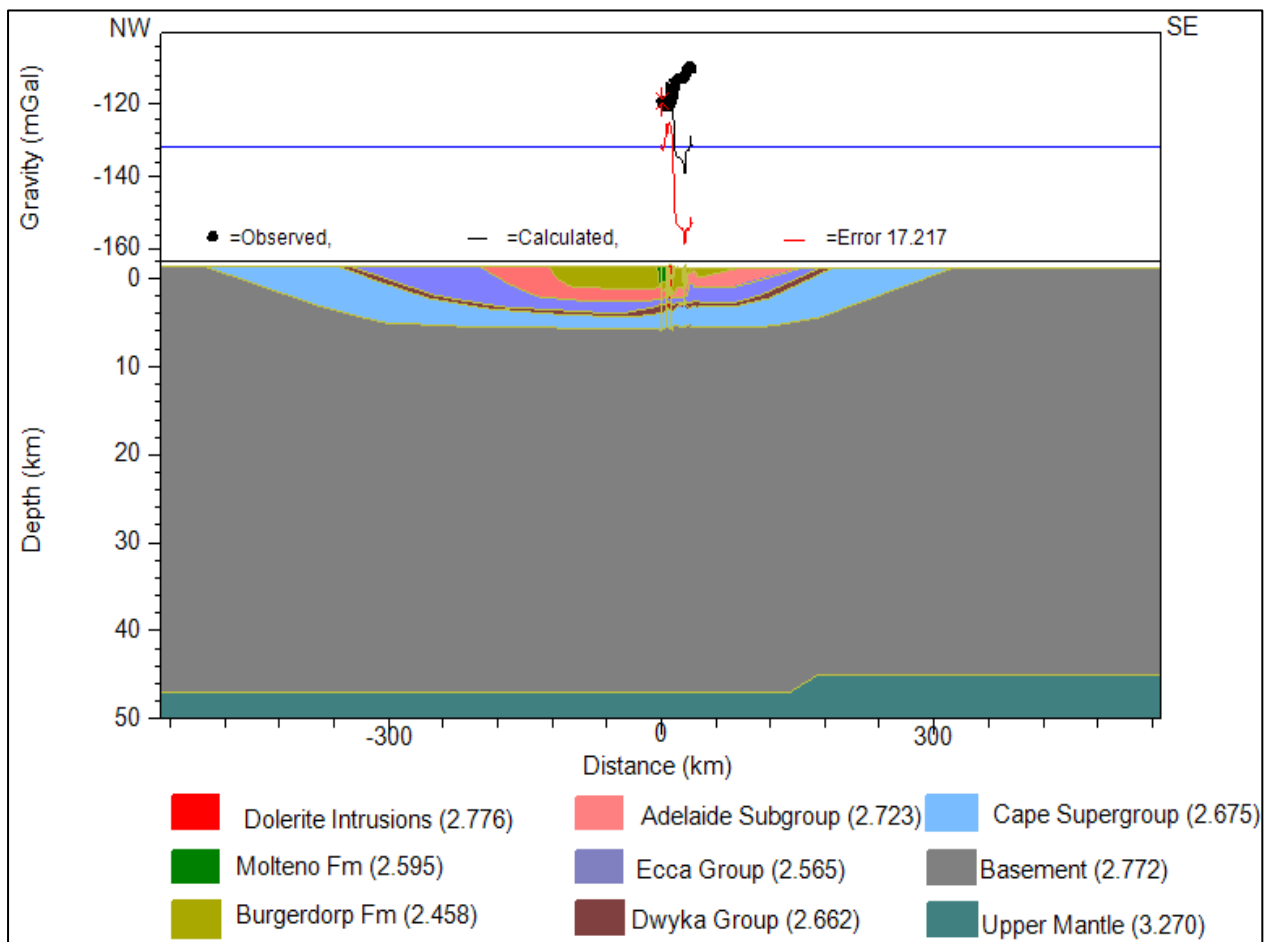


Figure 7. 2: A starting geological subsurface model for A-A'. Note: The Moho was left to vary within a depth range of 40-50 km. Note that the model block extends far away from the ends of the profile, i.e. to ± 550 km, vertical exaggeration (VE)=9.760 and RMS error=17.217

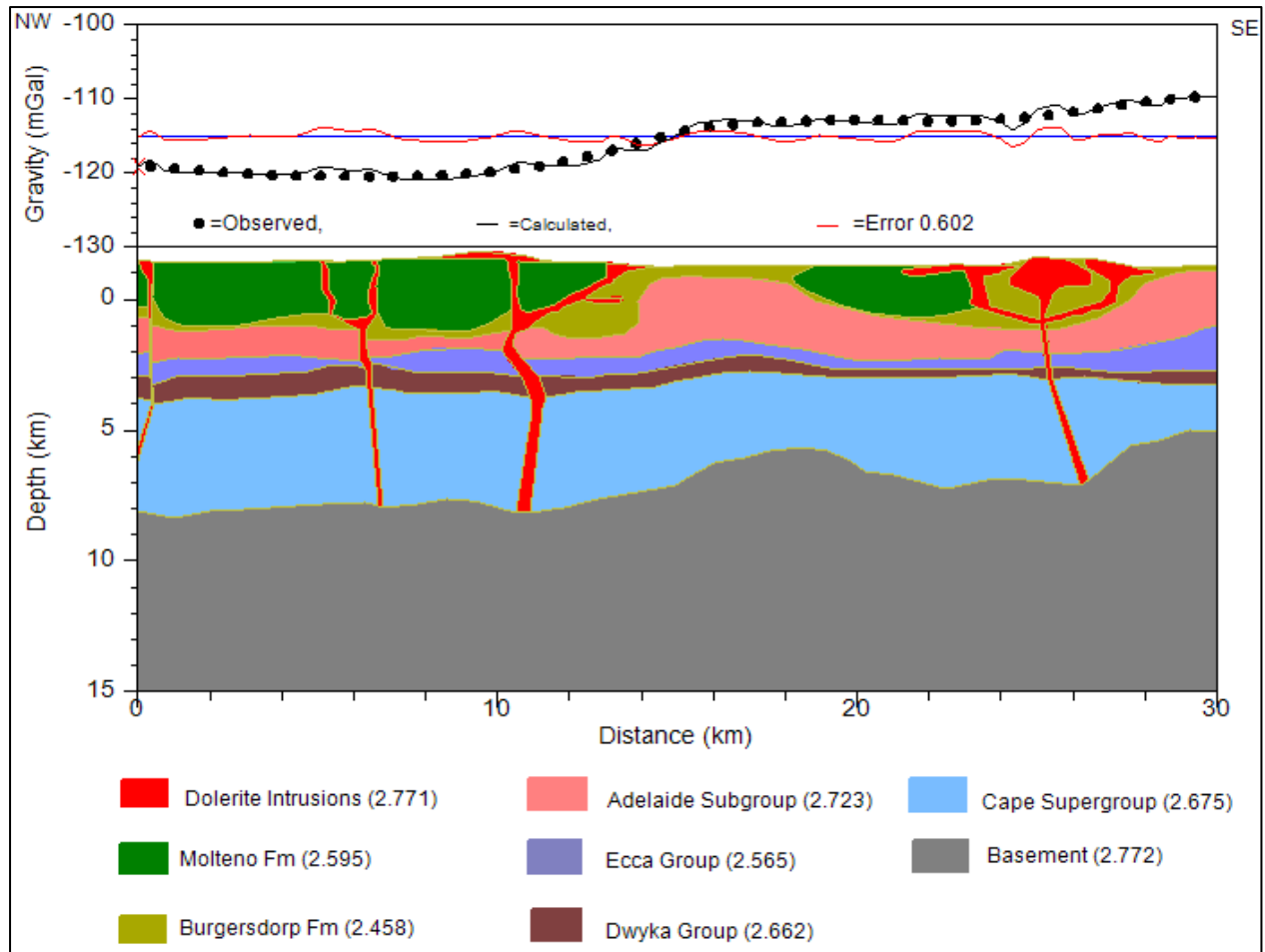


Figure 7. 3: A geological subsurface model for profile A-A'. VE=1, Initial RMS error=17.217 (Figure 7.2) and final RMS error=0.602. Note: The Moho is horizontal and at a depth of 47 km.

Figure 7.3 shows the final model along profile A-A'. The profile extends for a distance of 30km in a NW-SE direction. The gravity ranges from -120 mGal at the beginning of the profile to -110 mGal at its end. The region has dolerite intrusions (sills and dykes) cutting through sediments of the Karoo and the underlying Cape Supergroup. These dolerite sills are interconnected and some share a single feeder dyke. The Cape Supergroup extends from about 3.5-8.5 km depth with a thickness of about 5 km on the NW part of the profile NW end whilst on the SE end of the profile it extends from a depth of about 3-5.5 km with a thickness of about 2.5 km. The Dwyka Group occurs in the depth range of 3-4 km with a varying thickness of about 1 km on the NW end of the profile and about 0.5 km on the SE end of the profile. The Eccca Group is between a depth range of 1.5-3 km with a variable thickness from 0.5-1 km for most of the profile, except on the SE end where it thickens to a maximum value of

about 1.5 km. The Adelaide Subgroup has a maximum thickness of about 3 km at a distance of 14–18 km along the profile and has a minimum thickness of about 0.5 km between 6 -10 km distance along the profile. The Molteno Formation is about 2.5 km thick from 0 -10 km along the profile and about 1.5 km thick between 19–24 km distance along the profile. The Burgersdorp Formation underlies the Molteno Formation and has an average thickness of about 0.5 km except at distances from 11-14 km and 24 -28 km where it thickens to about 2 km. The Moho remained horizontal at 47 km depth for this profile.

7.2.2 Modelling results for Profile B-B'

Figure 7.4 shows the final model along profile B-B'. The profile is 36 km long and is in a NW-SE direction. The gravity values range from -118 mGal at the beginning of the profile to -110 mGal at its end. The region has dolerite intrusions (sills and dykes), cutting through sediments of the Karoo Supergroup and the underlying Cape Supergroup. The Cape Supergroup occurs at a depth between 3-5.5 km with a variable thickness that ranges from 1-2 km. The Dwyka occurs at a depth between 3-4 km and its thickness ranges from 250-500m. The Eccu Group is between a depth of 1-4 km and has thickness that ranges from 0.5-1 km for most of the profile except on the SE end where it thickens to 3.5 km. The Adelaide Subgroup occurs at a depth range between 1-3 km with a minimum thickness of 0.5 km and a maximum of 3.5 km. The Burgersdorp Formation, which is approximately 1 km thick, underlies the Molteno Formation from a distance of 0-10 km and thereafter it outcrops all the way to the end of the profile. The Molteno Formation outcrops from the beginning of the profile up to about 11 km along the profile and has a maximum thickness of about 2 km. The Moho remained horizontal at 47 km depth for this profile.

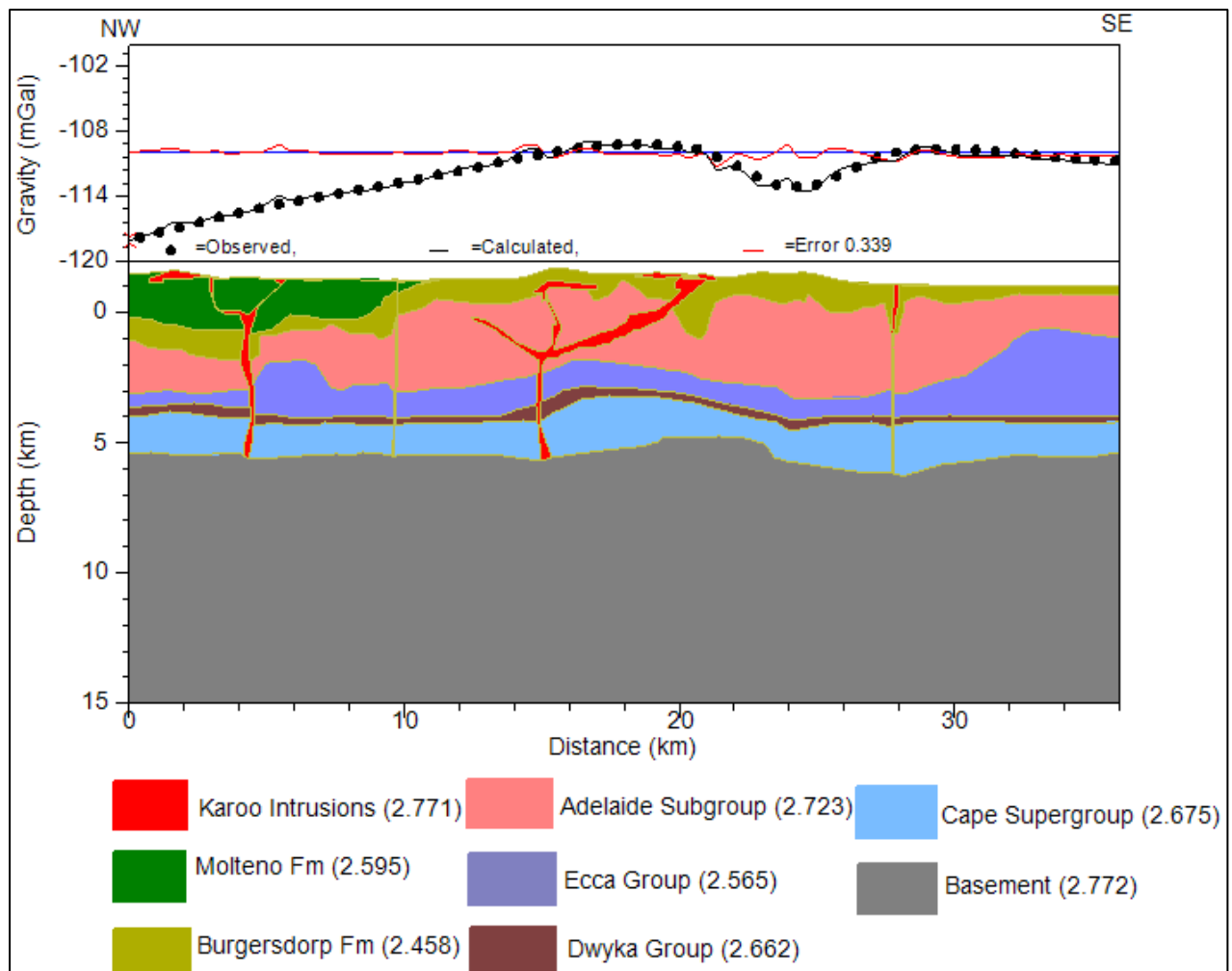


Figure 7. 4: A geological subsurface model along profile B-B'. VE=1, initial RMS error=3.889 and final RMS error=0.329

7.2.3 Modelling results for Profile C-C'

Figure 7.5 shows the final model along the profile C-C' which is 26 km long and runs in a NE-SW direction. The gravity ranges from -120 mGal at the beginning of the profile to - 118 mGal. The profile shows Cape Supergroup and the Karoo Supergroup rock sequences intruded by dolerite intrusions (dykes, ring complexes). The Cape Supergroup is between a depth range of 4-8.5 km with a thickness of 4.5 km on the NE part of the profile. On the SW part the thickness is 6.5 km of the Cape Supergroup at a depth between 3- 9.5 km. The Dwyka Group occurs at a depth range between 3-4 km with a thickness of 1km on the profile. The Ecca Group occurs at a depth range between 0.5-3 km with thickness of 2.5 km on the NE part of the profile while on the SW end of the profile depth is between 2-4.5 km with a

thickness of about 1.5 km. The Adelaide Subgroup occurs at a depth range between 1 to 2 km with a thickness of 1 km on the NE end of the profile but gets thicker towards the SW part of the profile at a depth between 1-3 km with a varying thickness from 2 km up to 3 km. The Burgersdorp Formation outcrops on the SW end of the profile and has a thickness that varies from 0.5 -1.5 km. The Molteno Formation outcrops from a distance of 0-21 km along the profile and has a thickness that ranges from 2-2.5 km. The dolerite sills outcrop on the surface. These dolerite sills share the dyke and are wider on this profile.

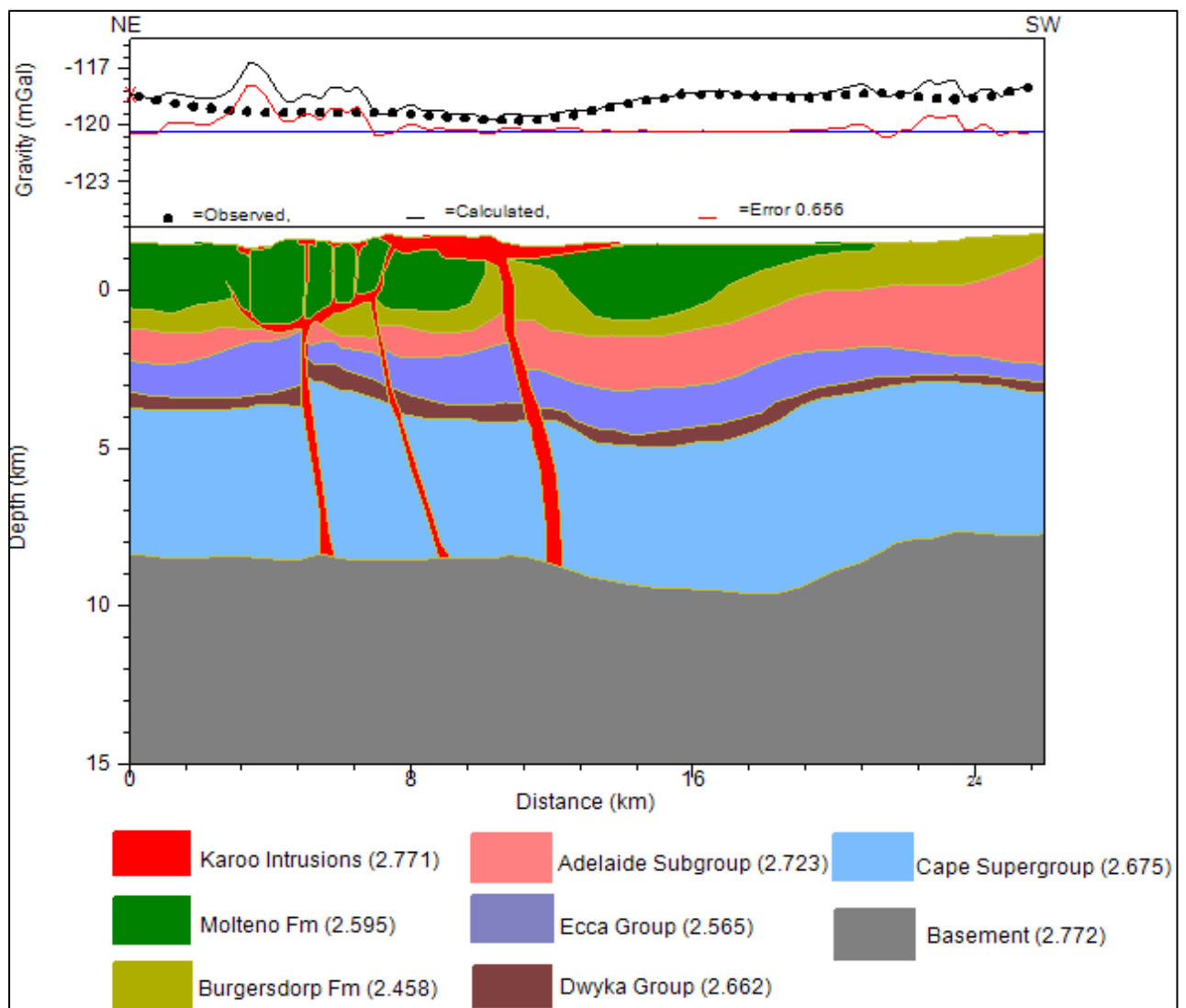


Figure 7.5: A geological subsurface model along profile C-C'. VE=1, initial RMS error=6.07 and final RMS error=0.656.

7.2.4 Modelling results for Profile D-D'

Figure 7.6 shows the model along profile D-D' which runs in the NE-SW direction and is 25 km long. The gravity ranges from -115 mGal at the beginning of the profile to -110 at its end. The Cape Supergroup occurs at a depth range of 3-6 km on the NE part of the profile with a thickness of 3 km whilst the central part occurs at a depth of 2-7 km with a thickness of 4.5 km and on the SE the depth ranges from 3.5-7 km with a thickness of 3.5 km. The Dwyka Group extends at a depth range of 1.5-3 km and its thickness varies from 200 m to 600 m. The Ecca Group occurs at a depth range between 1-2 km in the NE of the profile with a thickness of 1 km whilst on the SW it is in the depth range of 1.5-3.5 km. The Adelaide Subgroup occurs at a depth between 1-2 km with a thickness varying from 0.5-2 km. On the NE part of the profile there are outcrops of Elliot, Molteno and Burgersdorp formations. The Burgersdorp Formation has minimum and maximum thickness of 0.5 km to 2 km, respectively. The Molteno Formation has a minimum thickness of 0.5 km and a maximum thickness of 1.5 km. The Elliot Formation occurs on the NE part of the profile with a minimum thickness of 1 km and a maximum thickness of 2 km at a distance of 4 km. These formations are intruded by dolerite dykes and sills.



University of Fort Hare
Together in Excellence

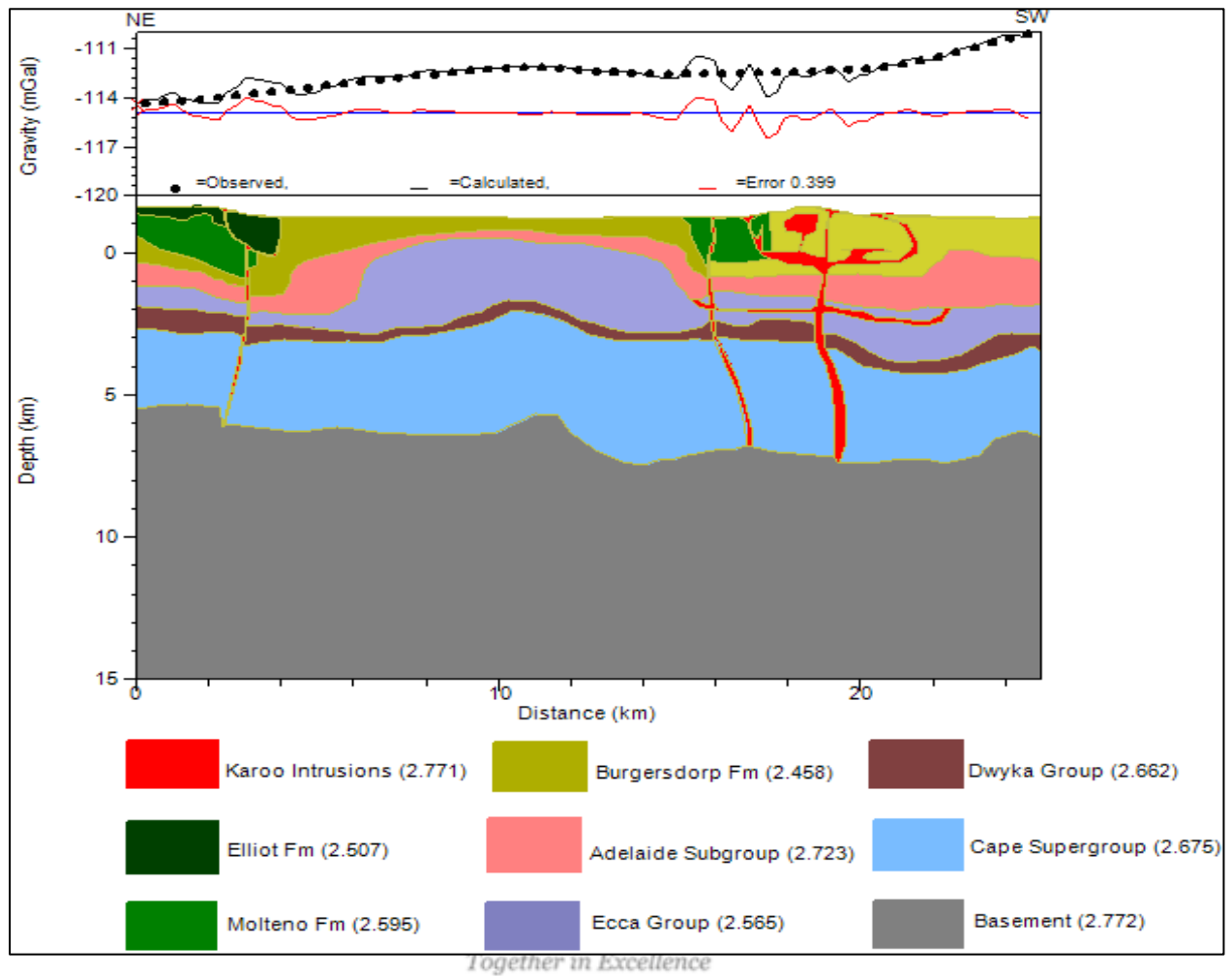


Figure 7. 6: A geological subsurface model along profile D-D'. VE =1, initial RMS error = 8.925 and final RMS error = 0.399.

7.2.5 Modelling results for Profile E-E'

Figure 7.7 shows the final model along profile E-E' which runs in the NE-SW direction and is 24 km long. The gravity values range from -112 mGal at the beginning of the profile to -110 mGal at its end. The Cape Supergroup occurs at a depth range between 5-9 km with a variable thickness from 1 km to 4 km. The Dwyka Group occurs at a depth between 5-5.5 km with a thickness of 0.5 km on the NE part of the profile whilst on the SW part of the profile the thickness is about 1 km at a depth range between 5-6 km. The Ecca Group occurs at a depth of 3-5.5 km on the NE part of the profile with a thickness varying from 1.5-2 km. The Adelaide Subgroup has minimum thickness of 1 km and maximum thickness of 2 km. The Burgersdorp Formation occurs on the surface from a distance of 8.5 km to the end of the

profile and extends to a maximum depth of 5 km. It has a minimum thickness of 2 km and maximum thickness of 6 km. The Molteno Formation outcrops on the surface with a minimum thickness of 1 km and maximum of 2 km. The dolerite sills are interconnected at depth sharing feeder dykes.

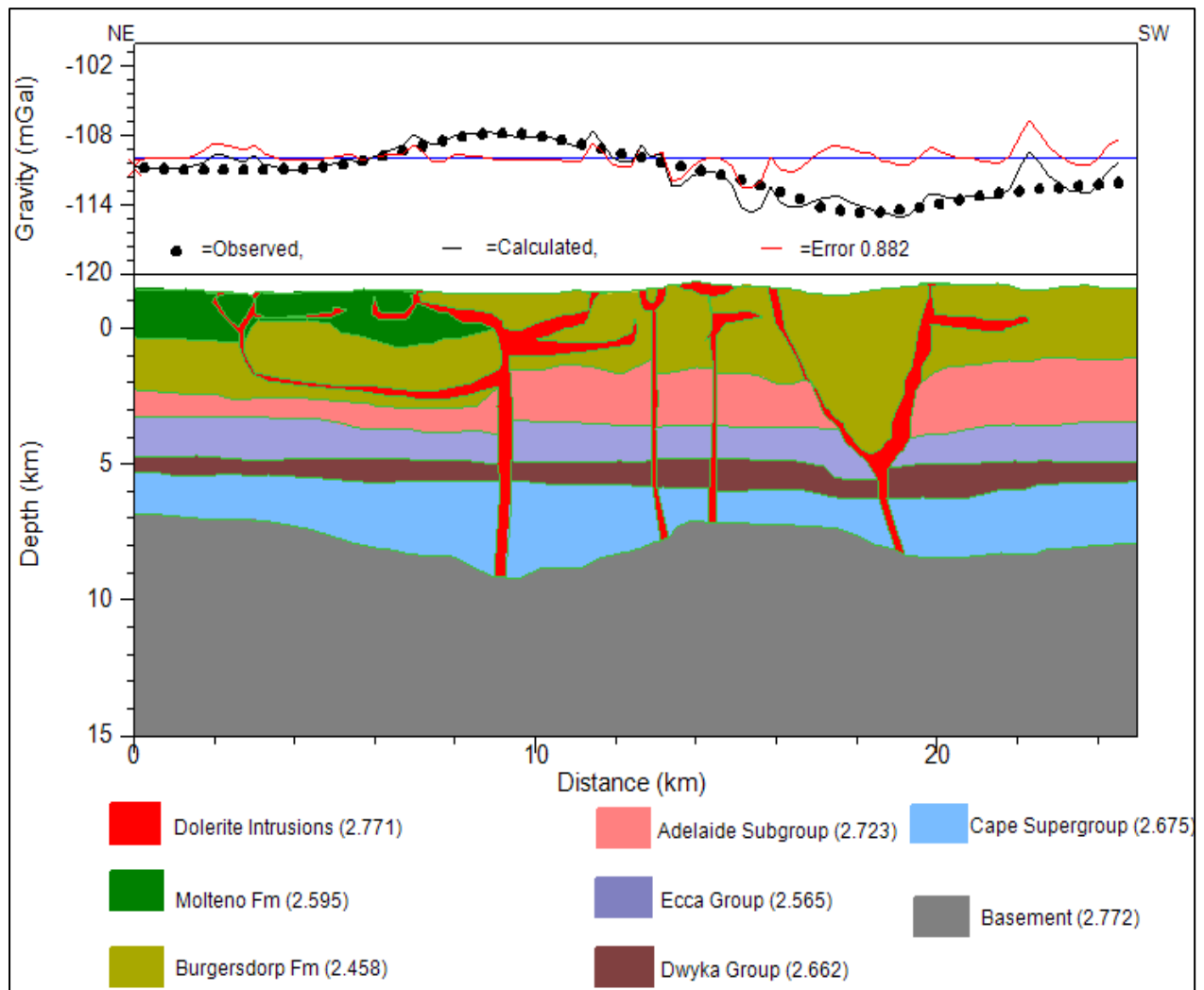


Figure 7. 7: A geological subsurface model along profile E-E'. VE = 1, initial RMS error = 11.956 and final = 0.882

7.3 Discussion of the gravity models

The sediment thicknesses were determined by subtracting the depth of the bottom surface from the depth of the top manually in GMSYS. The thicknesses of the sediments of the Karoo and Cape Supergroup vary along the profiles. Below are the minimum thicknesses and the

maximum thicknesses of the Karoo Supergroup sediments (Table 7.2 and Table 7.3, respectively).

Table 7. 2: Minimum thicknesses of the Karoo Supergroup sediments along different profiles.

Group/ Formation	Profile A-A' (km)	Profile B-B' (km)	Profile C-C' (km)	Profile D- D'(km)	Profile E-E' (km)	Minimum Thickness (km)
Elliot					1	1
Molteno	1.5	2	2	0.5	1	0.5
Burgersdorp	0.5	1	0.5	0.5	2	0.5
Adelaide	0.5	0.5	2	0.5	1	0.5
Ecca	0.5	0.5	2.5	1	1.5	0.5
Dwyka	1	0.25	1	0.2	0.5	0.2

University of Fort Hare
Together in Excellence

Table 7. 3: Maximum thicknesses of the Karoo Supergroup sediments along different profiles.

Group/ Formation	Profile A-A' (km)	Profile B-B' (km)	Profile C-C' (km)	Profile D- D'(km)	Profile E-E' (km)	Maximum Thickness (km)
Elliot					2	2
Molteno	2.5	2	2.5	1.5	2	2.5
Burgersdorp	2	1	1.5	2	6	6
Adelaide	3	3.5	3	2	2	3.5
Ecca	1	3.5	4.5	3.5	2	4.5
Dwyka	1	0.5	1	0.6	1	1

The Dwyka Group has a minimum thickness of 200 m and maximum thickness of 1 km. The Ecca Group has a minimum thickness of ½km and a maximum thickness of 4.5 km. The Beaufort Group (Elliot, Molteno and Burgersdorp formations and Adelaide Subgroup) has a minimum thickness of ½ km and a maximum thickness of about 6 km. The Entire Karoo Supergroup has a maximum thickness of 6½ km in the study area. These variations on the sediments are influenced by deformations that took place as a result of tectonic events

There are broader dolerite intrusions (sills, dykes and ring complexes) in the NE-SW trending profiles (Figure 7.5, 7.6 and 7.7) and fewer in the NW-SE trending profile direction. The dolerite intrusions coincide with the mapped intrusions. Some of these dolerite intrusions (sills, dykes and ring complexes) do not outcrop on the surface but they are at shallow depths. Magnetic and gravity maps confirmed that there are dolerite intrusions (sills, dykes, ring complexes) in the study area. The magnetic and gravity averaged power spectrums confirmed that some of the dolerite intrusions are at greater depths which means some are not exposed on the surface.

7.4 Conclusion



The interpretation of the gravity models led to the following conclusion:

- The sediments of the Karoo Supergroup has a maximum thickness of 6.5 km, with Beaufort Group (Elliot, Molteno and Burgersdorp formations and Adelaide Subgroup) being the thickest group with a thickness of 6 km.
- Some of the Karoo dolerite intrusions (sills and ring complexes) are interconnected below the surface and mostly share a feeder dyke (s)
- Small amplitude gravity highs of short wavelength correlate with dolerite intrusion (although some of dolerite intrusions do not outcrop)
- The broader, long wavelength gravity high which increases from -120 mGal in the northwestern area to -110 mGal in the southeastern area, is inferred to be due to a horizontal Moho at a depth of 47 km in the study area, which shallows outside of the study area near coastal regions

CHAPTER 8: SUMMARY OF FINDINGS, CONCLUSIONS AND RECOMMENDATIONS

8.1 Summary of findings

The study used field observations, rock samples collected in the field, existing airborne gamma ray spectrometry, magnetic and gravity data to reveal the subsurface geology of the Vaalbank and Lady Frere areas. The mineralogy and petrology studies were carried out using the collected rock samples to get the mineralogical composition of the sediments and dolerite intrusions. Geophysical (gamma ray spectrometry, magnetic and gravity) maps were generated and enhanced to show the subtle anomalies of the spatial data. Power spectra of magnetic and gravity data were computed to get depth estimates of the anomalous bodies. Five gravity profiles were selected and used to obtain $2^{1/2}$ D gravity models.

The literature review of the research has revealed that the study area belongs to the Beaufort Group and Stomberg Group sediments with some areas covered by quaternary alluvium [Cole and Cole, 2003]. The sediments are mostly composed of mudstone and sandstone of the Beaufort Group and mudstone, shale and sandstone of the Molteno Formation. These sediments were later intruded by Karoo dolerite and gabbro sills, dykes and ring complexes.

Petrographic investigation revealed that both the Molteno and Burgersdorp formations consist of sandstone that is mostly dominated by poorly to moderately sorted sub-angular to sub-round shaped quartz and feldspars with accessory minerals. The dominant minerals and accessory minerals are cemented by calcite, quartz and/or clay cement. The Karoo dolerites consists of coarse grained, euhedral structured minerals such as plagioclase, pyroxene, amphibole and magnetite.


The measured densities and porosities show that the Karoo dolerite suite has highest densities for dry, particle and wet/saturated densities, and lowest porosity values. The Burgersdorp Formation which mostly has quartz rich sandstone displays intermediate densities for dry, wet/saturated and particle densities, and intermediate porosities. The lowest densities are displayed in the Molteno Formation which consists of weathered sandstone and mudstone, and the formation has the highest porosity values.

The gamma ray spectrometry maps (Figures 4.2- 4.9) show high spectrometric values which correlate with the Burgersdorp Formation and alluvium cover. These high spectrometric values are up to 81% for K, 54 ppm for Th and 53.8 ppm for U. The low spectrometric values correlate with the Karoo dolerite sills and ring complexes, whereas the Karoo dyke swarms

have high spectrometric values. The K/U ratio map and the ternary map clearly outline the boundaries of the sills and ring complexes.

The magnetic maps (Figures 5.8 – 5.11) show the circular shaped features forming a chain that has high total magnetic values of up to 27504.5 nT and these correlate with the geologically mapped sills and ring complexes. The total horizontal derivative map (Figure 5.10) further reveals the chain of circular structures inferred to be sills and ring complexes and lineaments inferred to be dykes and faults. The inferred sills and ring complexes are more enhanced on the analytic signal map (Figure 5.11). The lineaments features seen trending NW-SE are predominantly dyke swarms and a few of them are faults.

The magnetic radially averaged power spectrum (Figure 5.12) consists of four linear segments corresponding to four average depths of the magnetic sources i.e. 0.128 km, 1.601 km, 2.830 km and 12.40 km. The magnetic depth slices maps (Figure 5.13) show that both the circular/ring-like and linear anomalies extend from shallow to deeper depths.



The Bouguer gravity map (Figure 6.1) has a long wavelength gravity anomaly with gravity values increasing in a NW-SE direction from about -120 mGals to -110 mGals. Results from 2½ D modelling (Figures 7.3 – 7.7) indicate that the long wavelength is due to a horizontal Moho at a depth of 47 km in the study area which shallows outside the study area on approaching the coastal areas. Superimposed on the long wavelength gravity anomaly are local anomalies due to low density sediments and high density Karoo dolerite intrusions. The 2½ D gravity models show sediments of the Karoo Supergroup that extend to a depth of about 5 km below sea level and the Cape Supergroup at varying depths. The radially averaged gravity power spectrum revealed more ring anomalies at shallow depth while at greater depths there is one broad anomaly.

8.2 Conclusions

8.2.1 Petrographic and geochemical investigations (XRD)

Petrography and mineralogy reveal that the quartz occur as the dominant mineral in sandstone and siltstone, followed by the feldspars and clay minerals as accessory minerals. The dominant mineral in dolerite is the plagioclase, with amphibole and magnetite. Hence the high magnetic values over the dolerite intrusions are due to magnetite.

8.2.2 Density and porosity investigations

The measured densities shows that the Molteno Formation has the lowest average density of 2.190 g/cm^3 and the highest average porosity of 14.5%, the Burgersdorp Formation has an average density of 2.458 g/cm^3 and porosity of 5.4 %, the Karoo dolerites have an average density of 2.771 g/cm^3 and the lowest porosity of 3.0 %.

8.2.3 Geophysical investigations

The magnetic maps show ring like magnetic high anomalies that largely coincide with the mapped Karoo dolerite sills and ring complexes. Numerous narrow linear magnetic high anomalies are clearly visible on the maps and some of these coincide with the few mapped dykes and faults. Some inferred dykes are not mapped on the geological map and this could be due to the dykes having no outcrop but they come close to the surface. All the dykes form collectively a dyke swarm. The magnetic depth slices reveal that the magnetic bodies extend from the surface or shallow depth to deeper depths of about 12.4 km.



The high gamma spectrometric values associated with Burgersdorp Formation of the Beaufort Group are as a result of sandstones that are sedimentary products of weathering, erosion, deposition and cementation as this lithology is dominant in the Burgersdorp Formation. These sandstones seldom have a high content of radioactive minerals when deposited. They are much more porous and permeable and often host uranium and thorium minerals deposited by groundwater. The sandstones of the Beaufort Group acted as fluid pathways for mineralising fluids.

There are high Bouguer anomaly values which correlate with Karoo dolerites that have high density and Burgersdorp Formation which is dominated by sandstone rocks. Sandstones from the Burgersdorp Formation are mostly rich in quartz and these sandstones are fresh and compacted, this may be the cause of their high density compared to the Molteno Formation. The low Bouguer anomalies are mostly correlating with the Molteno Formation which has the least rock density and it has weathered sandstones which consist of less quartz compared to the sandstones of the Burgersdorp Formation.

8.2.4 2 ½ D gravity modelling

A long wavelength gravity anomaly that increases from about -120 mGals in the NW end of the profiles to about -110 mGals in the SE of the profiles is due to a horizontal Moho at a depth of about 47 km inland which shallows towards the coastal areas. The sediments of the Karoo Supergroup extend up to a depth 5 km below sea level and attain a maximum thickness of about 6½ km. Most of the dolerite intrusions are interconnected below the surface.

8.3 Previous work done

Chevallier *et al.*, [2001] completed a study using 3D terrain modelling, map compilation, remote sensing, aeromagnetic, detailed geological cross sections and mechanical stress simulation to assess the occurrence of groundwater associated with Karoo dolerite sills and ring complexes. In their study the aim was to understand the structure of the large scale intrusions (i.e. their morphology, geometry, shape, size, fracturing, tectonics and mechanism of emplacement) and also to establish the occurrences of groundwater associated with the intrusions. Chevallier *et al.* [2001] concluded that the study resulted in the compilation of hydro-morphology that highlights zones of potential open fracturing which is associated with emplacement of dolerite sills and ring complexes.

Nhleko [2008] conducted a study where the aim was to investigate the groundwater flow dynamics of various fractured rock aquifers (deep and shallow) associated with Karoo dolerite ring complexes in the Qoqodala area (northeast of Queenstown in the Eastern Cape Province). The objectives of his study were to carry out structural analysis of a pilot site across a specific dolerite ring (using field mapping, satellite image interpretation, fracture mapping, exploration drilling, borehole logging, geophysical profiling, and geological cross-sections across the intrusion) and assessment of the groundwater flow dynamics of the fractured-rock aquifer associated with dolerite intrusion (using video camera, geophysical logging, the results of pump tests and injection tests). In his study high permeability of the fractures was established during pump testing where high transmissivity values were obtained. The high average storability and transmissivity values confirm the sustainability of the aquifers. Nhleko [2008] concluded that the fractured medium of the aquifer systems served as a conduit for groundwater flow as well as storage.

8.4 Contribution of the study

The three geophysical data sets have complemented each other in revealing the locations, depth and extent of the ubiquitous dolerite intrusions which may be interconnected at depth. These dolerite intrusions, consisting of an intricate relationship between the dykes and sill/ring complexes are associated with groundwater specifically in many fractures that propagated into the host rocks during intrusion and at contacts between the feeder dykes with the sills [Chevallier et al., 2001]. Hence knowing their locations on surface and at depth is useful for defining potential targets for groundwater. It is further inferred from the pervasiveness of the dolerite intrusions that the study area is highly unlikely to host significant shale gas reserves as the high temperature of the intrusions would have burnt or driven off the shale gas.

8.5 Recommendations

The gravity data used in the study is too sparse and does not give detailed information to accurately model the numerous, narrow dykes identified by the airborne gamma ray spectrometry and magnetic data. A more detailed gravity survey of closely spaced measurements (station space of 30 m apart) is recommended to be carried out in the entire study area. The gravity data could be modelled jointly with the aeromagnetic data to reveal the intricate, interconnected feeder dykes and the sills/ring complexes. The models could be used to select targets for detailed ground follow up using magnetic gradiometer survey to accurately locate the edges of dolerite intrusions, electrical resistivity tomography to map the shallow aquifers and time domain electromagnetic measurements to check for deep aquifers.

REFERENCES

- Akulga, C. [2013].** Investigating Gold Mineralization Potentials in Part of the Kibi-Winneba Belt of Ghana Using Airborne Magnetic and Radiometric Data, Unpublished Master of Philosophy (Geophysics), Kwame Nkrumah University of Science and Technology, Ghana, 116 pp.
- Artimo, A., Makinen, J., Berg ,R.C., Abert, C.C., and Salonen, V.P. [2003].** Three-dimensional geologic modeling and visualization of the Virttaankangas aquifer, southwestern Finland. – Hydrogeology Journal, 11(3), 378–386.
- Baiyegunhi, C. [2015].** Geological and Geophysical Investigation of the Southeastern Karoo Basin, South Africa. Unpublished MSc dissertation, University of Fort Hare, South Africa, 294 pp
- Bamford, M.K. [2004].** Diversity of woody vegetation of Gondwanan southern Africa. Gondwana Research, 7, 153-164
- Botha, J. F., Verwey, J. P., Van der Voort, I., Vivier, J. J. P., Colliston, W. P. and Loock, J. C.[1998].** Karoo Aquifers. Their Geology, Geometry and Physical Behaviour. WRC Report No 487/1/98.
- Bumby, A.J., Guiraud, R. [2005].** The geodynamic setting of the Phanerozoic basins of North Africa: Journal of African Earth Science., 43, 1-12
- Brime, C. [1985].** The accuracy of X-ray diffraction method for determining mineral mixtures, Mineralogical Magazine. 49, 531-538
- Burger, C.A.J., Hodgson F.D.I. & Van der Linde P.J. [1981].** Hidrouliese eienskappe van akwifere in die Suid-Vrystaat. Die ontwikkeling en evaluering van tegnieke vir die bepaling van die ontginningspotensiaal van grondwaterbronne in die Suid-Vrystaat en in Noord-Kaapland, Volume 2, Instituut vir Grondwaterstudies, Oranje Vrystaat Universiteit
- Catuneanu, O., Hancox, P. J. and Rubidge, B.S. [1998].** Reciprocal flexural behaviour and contrasting stratigraphies: a new basin development model for the Karoo retroarc foreland system, South Africa. Basin Research, 10, 417-439
- Catuneanu, O., Wopfner, H., Eriksson, P.G., Cairncross, B., Rubidge, B.S., Smith, R.M.H. and Hancox, P.J. [2005].** The Karoo basins of south-central Africa. Journal of African Earth Sciences, 43, 211-253.

Catuneanu, O and Elango, H. N. [2001]. Tectonic control on fluvial styles: The Balfour Formation of the Karoo Basin, South Africa. *Sedimentary Geology*, 140, 291-313.

Chevallier, L. and Woodford, A.C. [1999]. Morpho-tectonics and mechanism of emplacement of the dolerite rings and sills of the western Karoo, South Africa. *South African Journal of Geology*, 102, 43–54.

Chevallier, L., Goedhart, M & Woodford, A. [2001]. The influence of dolerite sill and ring complexes on the occurrence of groundwater in Karoo fractured aquifers: a morpho-tectonic approach. Water Research Commission Report No.937/1/01, Pretoria, 145 pp.

Chevallier, L. and Woodford, A. [2002]. Regional characterization and mapping of Karoo fractured aquifer systems. An integrated approach using a Geographical Information System and digital Image processing. Water Research Commission Report 653/1/02, 220 pp.

Chima, P. [2017]. Sedimentological and Geophysical Studies on the Molteno, Elliot and Clarens Formations of the Karoo Supergroup in the Eastern Cape, South Africa. Unpublished MSc dissertation, University of Fort Hare, South Africa, 253 pp.

Cole, D.I. [1992]. Evolution and Development of the Karoo Basin. In: de Wit, M.J. and Ransome, I.G.D., (Ed.), *Inversion Tectonics of the Cape Fold Belt, Karoo and Cretaceous Basins of Southern Africa*. Balkema, Rotterdam, Netherland, 87-100.

Cole, J. and Cole, P. [2003]. High resolution airborne geophysical survey for sheets 3126DB Vaalbank and 3127CA Lady Frere: Survey specifications and preliminary interpretation, Council for Geoscience, Pretoria, South Africa.

Cole, D.I. and Smith, R.M.H. [2008]. Fluvial architecture of the Late Permian Beaufort Group deposits, S.W. Karoo Basin: Point bars, crevasse splays, palaeosols, vertebrate fossils and uranium. Field Excursion Guidebook, American Association of Petroleum Geologists International Conference, Cape Town, FT02, 1 - 110.

Cooke S.E., Corner, R.J., Gravoies, P.R. and Grealish, G.J. [1996]. Use of gamma radiometric data for soil mapping: *Australian Journal of Soil Research* 34, 183-194.

Cook, F. A., White, D. J., Jones, A. G., Eaton, D. W., Hall, J., and Clowes, R. M. [2010]. How the crust meets the mantle: Lithoprobe perspectives on the Mohorovicic' discontinuity and crust–mantle transition. *Canadian Journal of Earth Sciences*, 47, 315–351.

Cordell, L., and Grauch, V.J.S. [1985]. Mapping basement magnetization zones from aeromagnetic data in the San Juan basin, New Mexico, in Hinze, W.J., (ed), The utility of regional gravity and magnetic anomaly maps. SEG, 181-197.

Department of Environmental Affairs (DEA). [2018].
https://www.environment.gov.za/otherdocuments/reports/southafricas_secondnational_climatechange [accessed on 10/2018]

de Witt, M., Armstrong, R.A., de Ronde, C.E., Green, R.W., Treadoux, M., Perberdy, E. and Roering, C. [1992]. Formation of Archean Continent, *Nature*, 357, 53–562.

Duncan R.A., Hooper P.R., Ehacek J., Marsh J.S. and Duncan R.A. [1997]. The timing and duration of the Karoo igneous event, Southern Gondwana. *Journal of Geophysical Research*, 102. 18127 – 18138



Du Toit, A.L. [1905]. Geological survey of Glen Grey and parts of Queenstown and Woodehouse, including the Indwe area. Geological Commission of the Cape of Good Hope, tenth annual report 95-140.

Du Toit, A.L. [1920]. The Karoo Dolerites- a study in Hypabyssal Intrusion. *Transactions of the Geological Society of South Africa*, 23,1-42.

Elawadi, E., Ammar, A. and Elsirafy, A. [2004]. Mapping surface geology using airborne gamma-ray spectrometric survey data - A case study, *Proceedings of the 7th SEGJ International Symposium*, Japan.

Fitch, F.J. and Miller, J.A. [1984]. Dating Karoo igneous rocks by the conventional KAr and ⁴⁰Ar/³⁹Ar age spectrum methods. In: AJ. Eriank (Ed), *Petrogenesis of the volcanic rocks of the Karoo Province*. Geological Society of South Africa, Special Publication, 13,247-256.

Fuller, B.D. [1967]. Two-dimensional frequency analysis and design of grid operators, in

Hansen, D.A., Heinrichs, W.E., Holmer, R.C., MacDougall, R.E., Rogers, G.R., Sumner, J.S., and Ward, S.H., 1967, Society of Exploration Geophysicists' Mining Geophysics, 2, 658-708.

Galerne, C.Y., Galland, O., Neumann, E.R and Planke, S. [2011]. 3-D relationships between sills and their feeders: evidence from the Golden Valley Sill Complex (Karoo basin) and experimental modelling. *Journal of Volcanology and Geothermal Research*, 202, 189-199.

Grant, J.A. [1998]. Ten things the textbooks don't tell you about processing and archiving airborne gamma ray spectrometric data. In *Current Research 1998 D*. Geological Survey of Canada, Ottawa, 83-87.

Grauch, V.N.S., Minor, S.A, Hudson, M.R and Caine, J.S. [2008]. Sources of along-strike variation in magnetic anomalies related to intrasedimentary faults: A case study from the Rio Grande Rift, USA. *Exploration Geophysics*. DOI: 10.1071/EG06372

Gunn, P.J., [1972]. Application of Wiener filters to transformations of gravity and magnetic data: *Geophysical Prospecting*, 20, 860-871.

Haldar, S.K. [2018]. in *Mineral Exploration (Second Edition)*, 2018



Hälbich I.W. [1983]. A tectonogenesis of the Cape Fold Belt (CFB). In: Söhne, A.P.G., Hälbich, I.W. (Eds). *Geodynamics of the Cape Fold Belt*. Geological Society of South Africa, Special Publication, 12, 165–175.

Hancox, P.J. [1998]. Stratigraphic, sedimentological and palaeoenvironmental synthesis of the Beaufort-Molteno contact in the Karoo Basin. Unpublished PhD Thesis, University of the Witwatersrand, South Africa, 380pp.

Hinsby K and Abatzis, I. [2004]. Petroleum geology modelling tools of relevance to groundwater investigations. – *Geologisk Tidsskrift* 2004 2: 10–11 (in Danish).

Hynes, A., and Snyder, D. B. [1995]. Deep-crustal mineral assemblages and potential for crustal rocks below the Moho in the Scottish Caledonides. *Geophysical Journal International*, 123, 323-339.

Hovgaard, J., and Grasty, R. L., [1997]. Reducing statistical noise in airborne gamma-ray data through spectral component analysis, in Gubins, A. G., Ed., Proc. of Exploration 97: Fourth Decennial Conference on Mineral Exploration, 753–764

International Atomic Energy Agency (IAEA). [1991]. Airborne gamma ray spectrometer survey, Vienna Austria STI/DOC 10/323i, 94 pp

International Atomic Energy Agency (IAEA). [2013]. Advance in Airborne and Ground Geophysical Methods for uranium exploration, Vienna Austria, No.NF-T-1.5, 55pp

Johnson, M.R. [1991]. Sandstone petrography, provenance and plate tectonic setting in Gondwana context of the south-eastern Cape Karoo basin. South African Journal of Geology, 94, 137-154.

Johnson, M.R., van Vuuren, C.J., Hegenberger, W.F., Key, R. and Shoko, U. [1996]. Stratigraphy of the Karoo Supergroup in southern Africa: an overview. Journal of African Earth Sciences, 23, 3–15.



Johnson, M.R., van Vuuren, C.J., Visser, J.N.J., Cole, D.I., Wickens H. de V., Christie, A.D.M., Roberts, D.L and Brandl, G. [2006]. Sedimentary Rocks of the Karoo Supergroup. In: Johnson, M.R., Anhaeusser, C.R. and Thomas, R.L. (Eds.). The Geology of South Africa. Geological Society of South Africa, Johannesburg /Council for Geoscience, Pretoria. 461-499.

Juliana, G.D., David, L.D.C., Samir, N.C. and Zorano, S. S. [2016]. Magnetic and gravity modeling of a Paleogene diabase plug in Northeast Brazil. Journal of Applied Geophysics, 136 (2017), 219–230.

Kassenaar ,D., Holysh, S., and Gerber, R. [2003]. An integrated 3D Hydrostratigraphic Interpretation Methodology for Complex Aquifer Systems. – In: Poeter, Zheng, Hill and Doherty (eds.): Proceedings, MODFLOW and More, understanding through modelling, Colorado School of Mines, Golden CO, 16–19 September, 2003, 661–665.

Kearey, P., Brooks, M. and Hill, I. [2002]. An Introduction to Geophysical Exploration. 3rd Edition. London: Blackwell Science Ltd.(Chapter 6)

Kent, L. E. [1980]. Stratigraphy of South Africa. In Geologic Survey of South Africa Handbook (1–680).

Keyser, A.W. and Smith, R.M.H., [1977/78]. Vertebrate biozonation of the Beaufort Group with special reference to the western Karoo Basin. Annals of Geological Survey of South Africa 12, 1–36.

Lanza, R. and Meloni, A. [2006]. The Earth's Magnetism, An Introduction for Geologists. Berlin-Heidelberg: Springer-Verlag.

Killeen, P.G. [1979]. Gamma ray spectrometric methods in uranium exploration – application and interpretation. In Geophysics and Geochemistry in the Search for Metallic Ores, edited by P.J. Hood, Geological Survey of Canada Economic Geology Report 31, 163-230.

Linol, B., Chere, N., Muedi, T., Nemgovhela, V. and de Wit, M. J., [2016]. Deep borehole lithostratigraphy and basin structure of the southern Karoo Basin re-visited. In Linol, B. and de Wit, M.J. (2016) (Eds). Origin and Evolution of the Cape Mountains and Karoo Basin Regional Geology Reviews, DOI 10.1007/978-3-319-40859-0_18

Lock, B.E., [1978]. The Cape Fold Belt of South Africa; tectonic control of sedimentation. Geological Association of London. Proceeding, 89, 263-281.

Lock, B.E., [1980]. Flat-plate subduction and the Cape Fold Belt of South Africa. South Africa Journal of Geology, 8, 35-39.

Low, A.B. and Rebelo, A.G. [1996]. Vegetation of South Africa, Lesotho and Swaziland. Department of Environmental Affairs and Tourism, Pretoria.

Madi, K. [2014]. Targeting and characterizing potentially high yield aquifers in the neotectonic zones in the Eastern Cape Province in South Africa. Unpublished PhD Thesis, University of Fort Hare, South Africa, 254 pp

MacDonald, I., Boyce, A.J., Butler, I.J., Herrington, R.J. and Polya, D.A. [2005] Mineral Deposits and Earth Evolution. London. The Geological Society of London, 269 pp.

Malthe-Sørenssen, A., Planke, S., Svensen, H. and Jamtveit, B. [2004]. Formation of saucer –shaped sills. In: Breitzkreuz., Petford, N. (Eds), Physical geology of high level magmatic systems. Geological Society, London, Special publication ,234,215-227.

McCarthy, T. and Rubidge, B. [2005]. The Story of Earth and Life—A South African Perspective on a 4.6 Billion Year Journey. Cape Town: Struik, 209-211, 262-264

McKinnon, M. [2014]. Density of the geological material. Fluid and dynamic disaster, geophysics and fieldwork <http://geomika.com/blog/2014/03/13/density-materials/>

Mickus, K. [2014]. Gravity method: environmental and engineering applications, Department of Geosciences, Southwest Missouri State University, Springfield, 13 pp.

Milsom, J. [2003]. Field Geophysics, 3rd ed. Third, The geological field guide series. Third. Chichester: John Wiley & Sons Ltd. doi: 10.1002/9780470972311.

Minty, B.R.S. [1991]. Simple micro-levelling for aeromagnetic data. Exploration Geophysics, 22, 591-592.

Mjelde, R., Goncharov, A., and Müller, R. D. [2013]. The Moho: Boundary above upper mantle peridotites or lower crustal eclogites? A global review and new interpretations for passive margins. Tectonophysics, 609, 636–650.

Musset, A.E. and Khan, M.A. [2000]. Looking Into the Earth. Cambridge University Press, New York, USA, 470 pp.

Nhleko, L.O. [2008]. Implication of geological structure of the Qoqodala Dolerite ring complex for groundwater dynamics, unpublished MSc dissertation, University of the Western Cape, South Africa, 91 pp.

Nxantsiya, Z. [2017]. A study of the southwestern Karoo basin in South Africa using magnetic and gravity data, unpublished MSc dissertation, University of Fort Hare, South Africa, 213 pp

Polteau, S., Ferré, E.C., Planke, S., Neumann, E.R. and Chevallier, L. [2008]. How are saucer-shaped sills emplaced? Constraints from the Golden Valley Sills, South Africa. *Journal of Geophysical Research: Solid Earth*, 113, BB12104, doi:10.29/2008JB005620

Reeves, C. [2005]. Aeromagnetic Surveys, Principles, Practice & Interpretation. Published by Geosoft, 146 pp.

Reynolds, J.M. [1997]. An Introduction to Applied and Environmental Geophysics, John Wiley and Sons, NY, 806p.

Richardson S.H. [1984]. Sr, Nd and O isotope variation in an extensive Karoo dolerite sheet, Southern Namibia. In: A.J. Eriank (Ed), Petrogenesis of the volcanic rocks of the Karoo Province. Geological Society of South Africa. Special Publication, No 13, 289-293.

Robb, L. J. and Meyer, F. M. [1995]. The Witwatersrand Basin, South Africa: Geological framework and mineralization processes', *Ore Geology Reviews*, 10, 67–94.

Roux, A. [1980]. The magnetic method in the South Africa Geophysics Association Manual. Geophysics division of the national physical research laboratory of CSIR, Pretoria

Rust, I.C. [1975]. Tectonic and sedimentary framework of Gondwana basins in southern Africa. In: Campbell, K.S.W. (Ed.), *Gondwana Geology* (3rd Gondwana Symposium). Australian National University Press, Canberra, pp. 537–564.

SACS (South African Committee for Stratigraphy). [1980]. Lithostratigraphy of the Republic of South Africa.

Sharma, S.R., Poornachandra Rao, G.V.S., and Rao, V.K. [2005]. Heat flow, Curie depth and composition of lower crust beneath the India shield. Singapore, Proceedings of 2nd Asia Oceania Geosciences Society International Symposium (AOGS), 1-6.

Smart, M. C., [1998]. An explanation of the 1:500000 General Hydrogeological Map Queenstown 3126. Pretoria: Department of Water Affairs.

Smith, R.M.H., [1995]. Changing fluvial environments across the Permian-Triassic boundary in the Karoo Basin, South Africa and possible causes of tetrapod extinctions. *Palaeogeography. Palaeoclimatology. Palaeoecology*. 117, 81–104.

Smith, R.M.H., Eriksson, P.G. and Botha, W.J. [1993]. A review of the stratigraphy and sedimentary environments of the Karoo-aged Basins of southern Africa. *Journal of African Earth Sciences*. 16 (1/2), p.143-169

Spector, A. and Grant, F.S. [1970]. Statistical models for interpreting aeromagnetic data. *Geophysics*, **35**, 293-302.

Stevenson, D. S., Doherty, R. M., Sanderson, M. G., Collins, W. J., Johnson, C. E., and Derwent R. G., [2004]. Radiative forcing from aircraft NO_x emissions: Mechanisms and seasonal dependence, *Journal of Geophysical Research.*, 109, D17307, doi:10.1029/2004JD004759

Svensen, H., Planke, S., Chevallier, L., Malthe-Sorensen, A., Corfu, F. and Jamtveit, B. [2007]. Hydrothermal venting of greenhouse gases triggering Early Jurassic global warming. *Earth and Planetary Science Letters*. 256 (3–4), 554–566.

Telford, W., Geldart, L. and Sheriff, R. [1990]. *Applied Geophysics*. 2nd Ed. New York: Cambridge University Press.



Thybo, H., and Artemieva, I.M. [2014]. Moho and magmatic underplating in continental lithosphere. *Tectonophysics*, 609, 605-619.

Toerien, D.K. and Hill, R.S. [1989]. The geology of the Port Elizabeth area. Explanation to 1:250 000 geology sheet 3324 Port Elizabeth, Council for Geoscience, Pretoria, 35 pp.

Turner, B.R. [1975]. The stratigraphy and sedimentary history of the Molteno Formation in the Main Karoo Basin of South Africa and Lesotho. Unpublished PhD, University of Witwatersrand, 314 pp.

Turner, B.R. [1984]. Palaeogeographic implications of braid bar deposition in the Triassic Molteno Formation of the eastern Karoo Basin, South Africa. *Palaeontology Africa*, **25**, 29-38.

Vandoolaeghe, M.A.C. [1980]. Queenstown geohydrological investigation, Main report

Department of Water Affairs Unpublished Technical report Gh 3153, Pretoria. 26 pp.

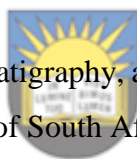
Visser, J.N.J. and Botha, B.J.V. [1980]. Meander belt, point bar, crevasse splay and aeolian deposits from the Elliot Formation in Barkly Pass, north **83**, 55-62.

Visser, D.J.L. [1989]. The geology of the republics of South Africa, Transkei, Bophutatswana, Venda and Ciskei and The kingdoms of Lesotho and Swaziland. Explanation of 1: 1000 000 geological map. Geological Survey of South Africa. Pretoria.

White R.S. [1997]. Mantle plume origin for the Karoo and Ventersdorp flood basalts, South Africa. South African Journal of Geology, 100 (4), 271 - 282.

Wilford, J.R., Bierwirth, P.N and Craig, M.A. [1997]. Application of airborne gamma ray-spectrometry in soil/regolith mapping and applied geomorphology. Journal of Australian geology and geophysics, 17(2), 201-216.

Winter, H. de LA R. [1984]. Tectonostratigraphy, as applied to the analysis of South African Phanerozoic basins. Geological Society of South Africa, 87, 169-179.



University of Fort Hare
Truth in Excellence

Woodford A.C. and Chevallier, L. [1996]. Regional characterization of Karoo Aquifer systems - An integrated approach using a geographical information system and satellite image processing. Water Research Commission project progress report, 22pp.

Woodford A.C. and Chevallier L. [2001]. Regional characterization of Karoo Aquifer systems - An integrated approach using a geographical information system and satellite image processing. Water Research Commission project K&653.

Woodford, A.C and Chevallier, L. [2002]. Hydrogeology of the main Karoo Basin: Current Knowledge and Future research needs. Water Research Commission Report No TT 179/02, 466pp.

Woodford, A. and Chevallier, L. [2002b]. Regional characterization and mapping of Karoo fractured aquifer systems. An integrated approach using a Geographical Information System and digital Image processing. Water Research Commission Report 653/1/02, 220 pp.

Zhdanov, M. [2009]. Geophysical Electromagnetic Theory and Methods. Amsterdam: Elsevier B.V, 868 pp.



University of Fort Hare
Together in Excellence

APPENDIX A

A.1 XRD results and Patterns

A qualitative x-ray diffraction analysis was conducted on 10 samples at Council for Geoscience laboratory. Below are the results of the analysis.

Table A. 1: X-Ray diffraction results of the selected rock samples from Burgersdorp, Molteno Formation and Karoo Dolerite

Sample ID	Calcite	Clino-pyroxene	Plagioclase	Quartz	Kaolinite / Clinocl ore	Amphibole	Mica	I/S Interstratification
BFX1	-	-	35	51	-	-	12	2
BFX2	-	-	9	70	-	-	18	3
BFX3	-	-	24	70	-	-	4	2
BFX4	-	-	32	61	-	-	7	Tc
BFX5	9	-	29	59	3	-	tc	-
MFx1	-	-	16	77	-	-	5	2
MFx2	-	-	26	55	9	-	10	-
MFx3	-	-	5	95	-	-	tc	Tc
MFx4	-	-	29	59	6	-	6	-
KDX1	-	25	53	5	8	9	-	-

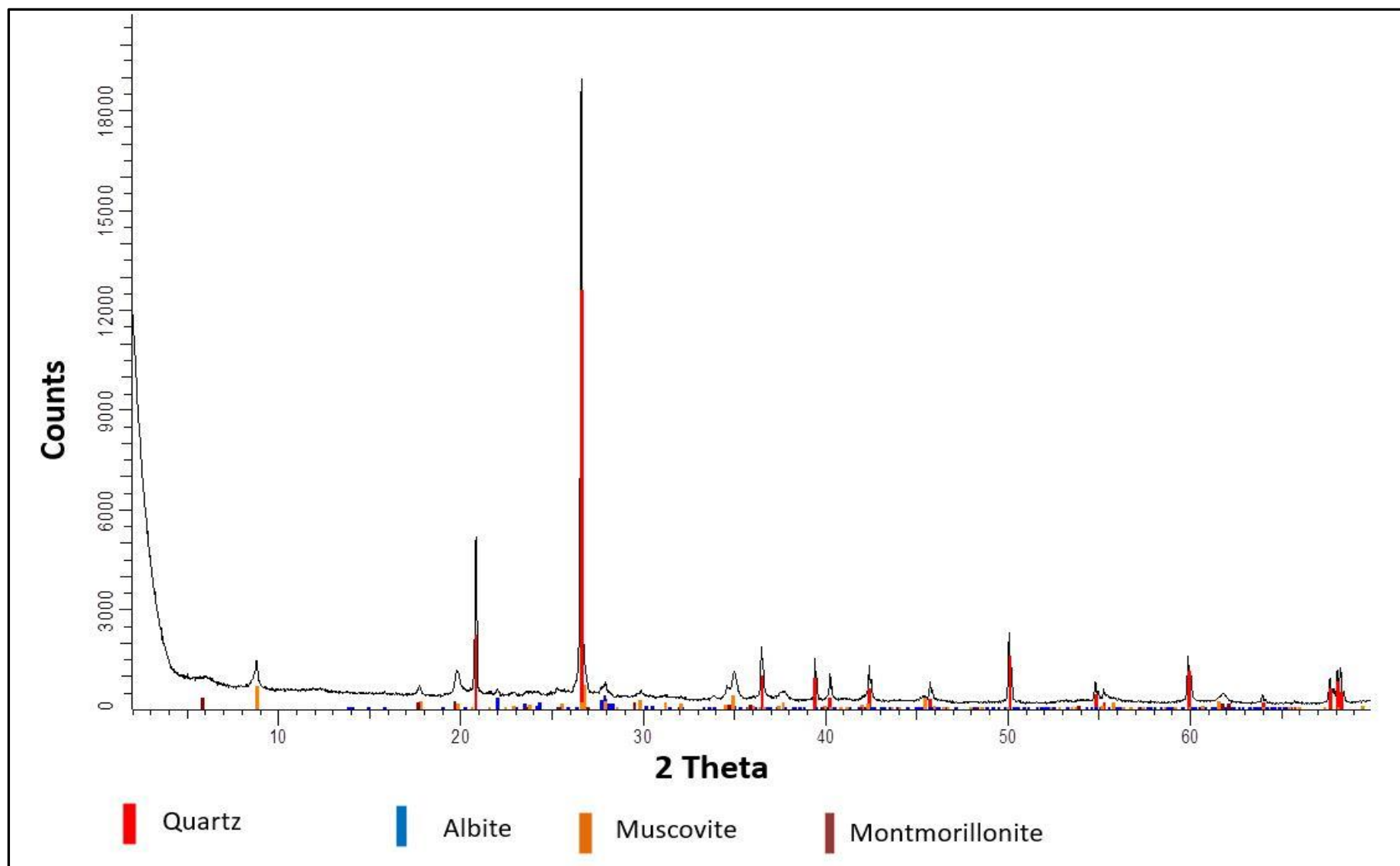


Figure A. 1: XRD pattern for Burgersdorp Formation sandstone

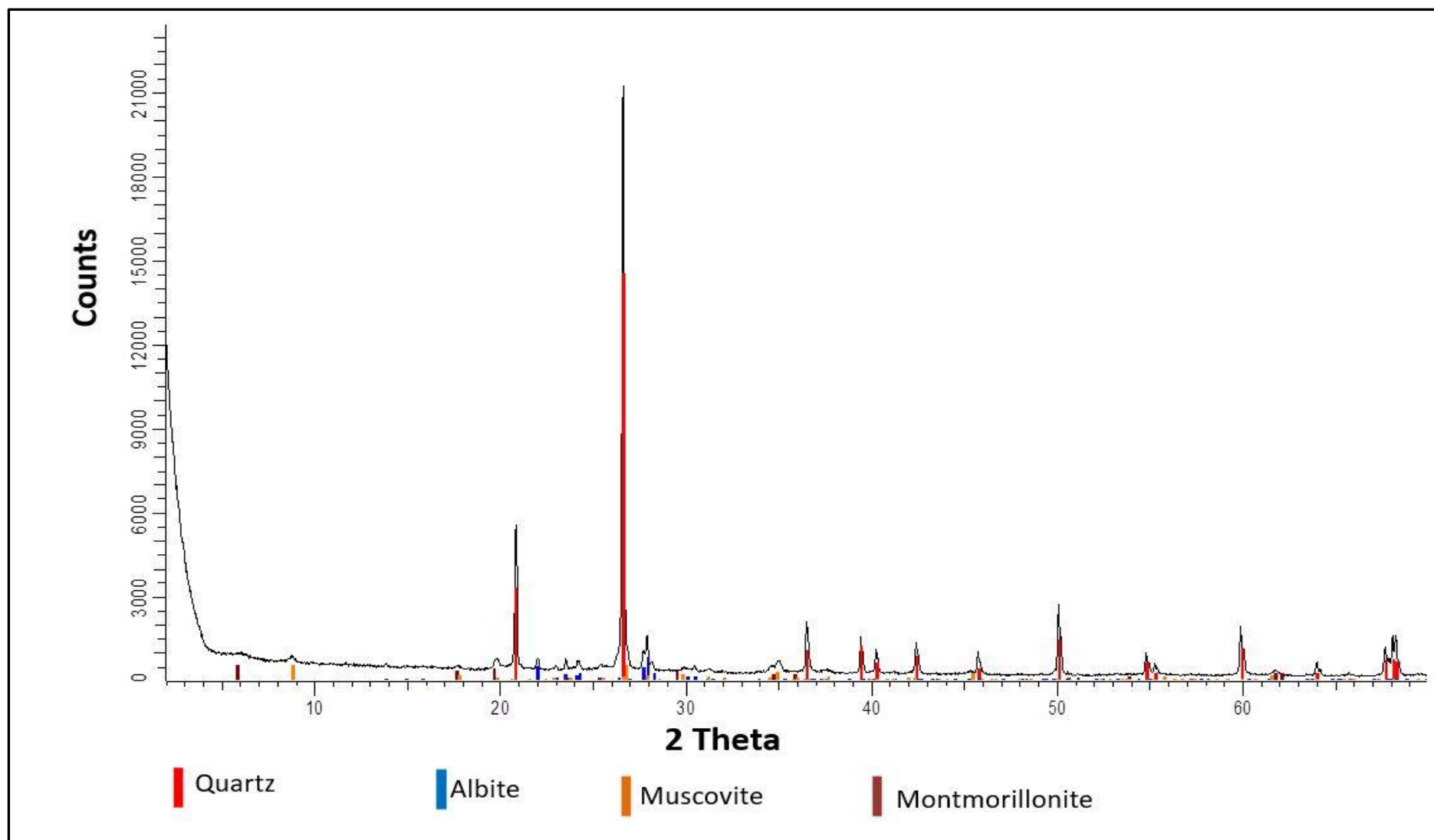


Figure A. 2. XRD pattern for Burgersdorp Formation sandstone

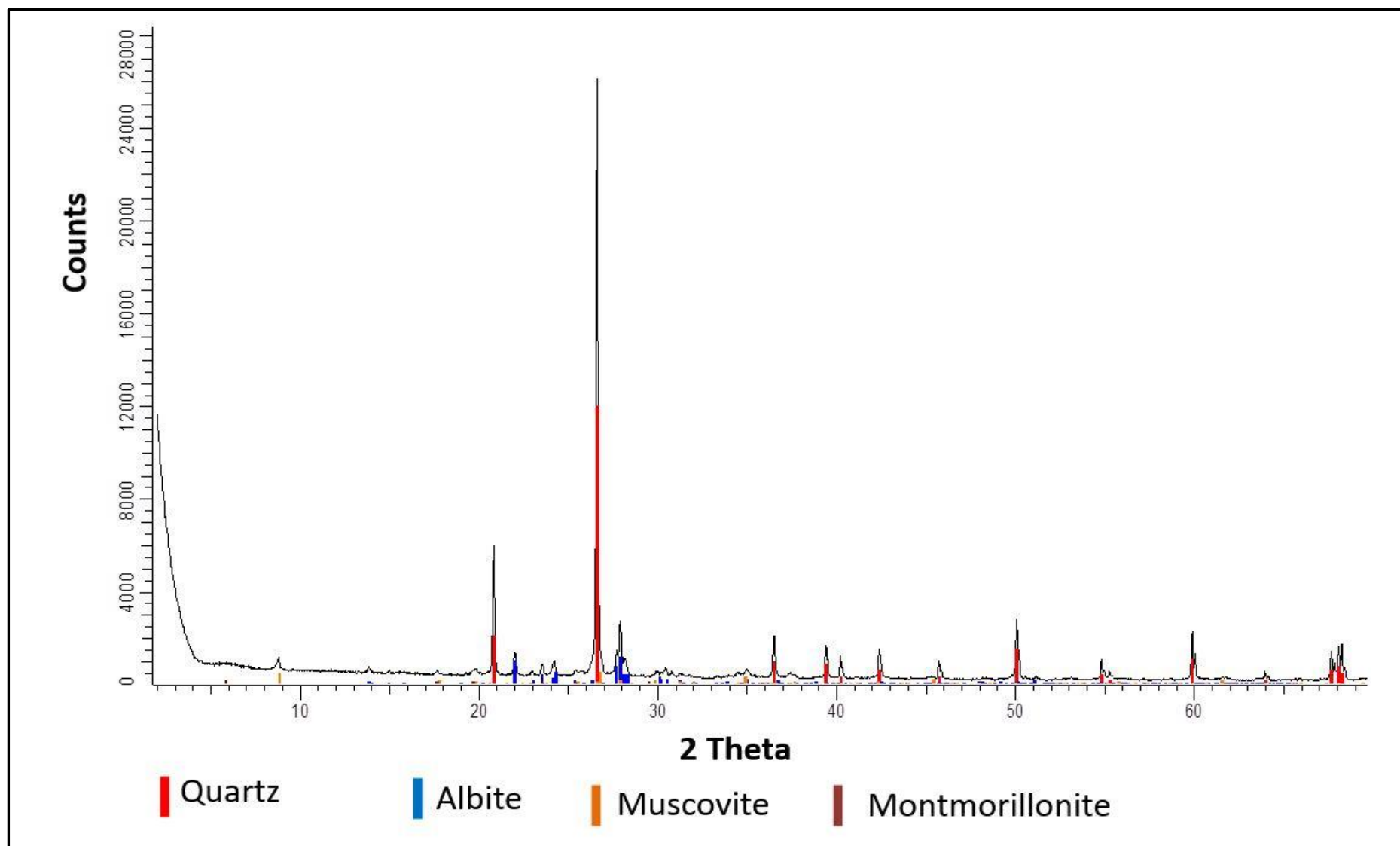


Figure A. 3 XRD pattern for Burgersdorp Formation sandstone

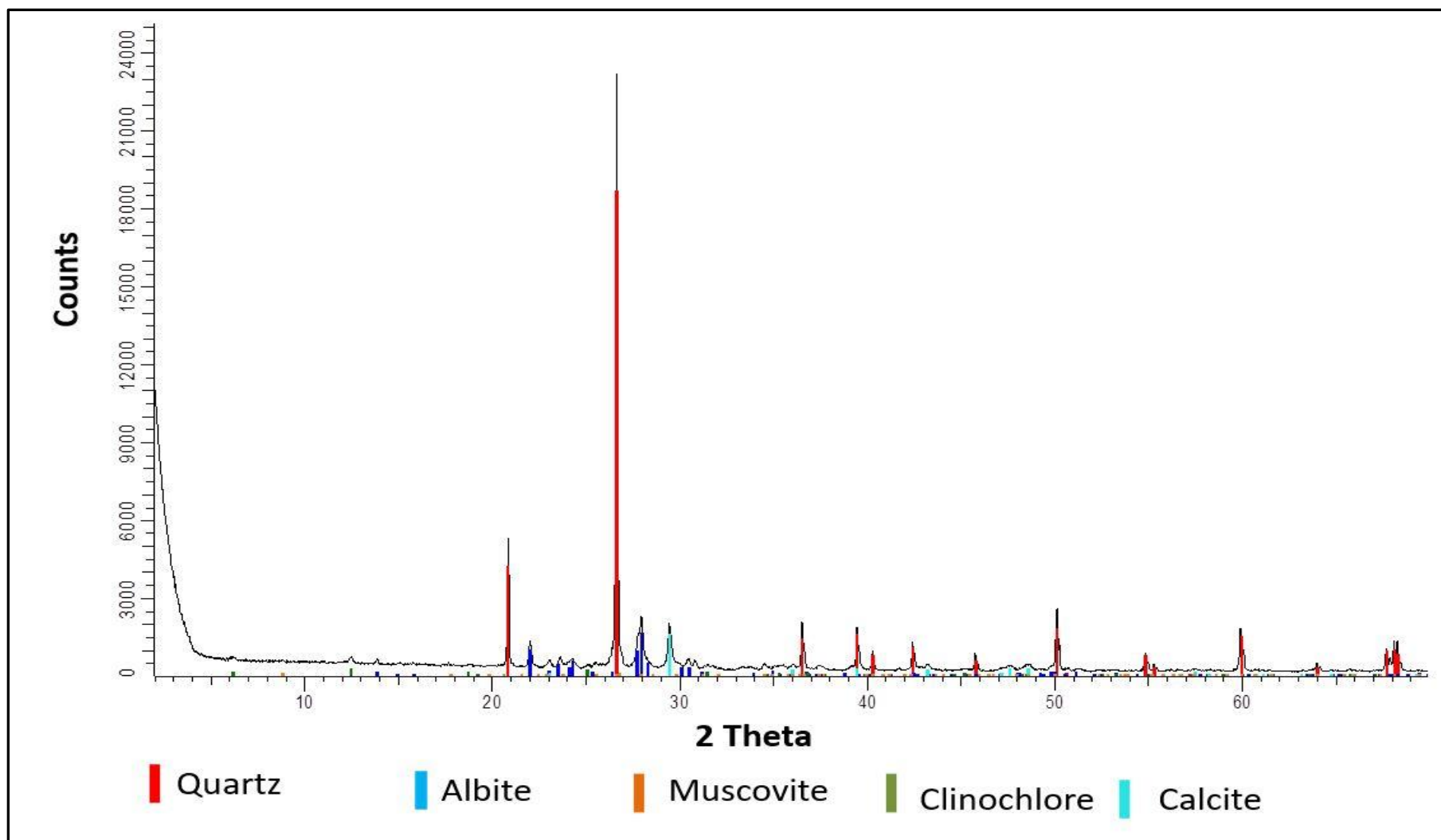


Figure A. 4: XRD pattern for Burgersdorp Formation sandstone

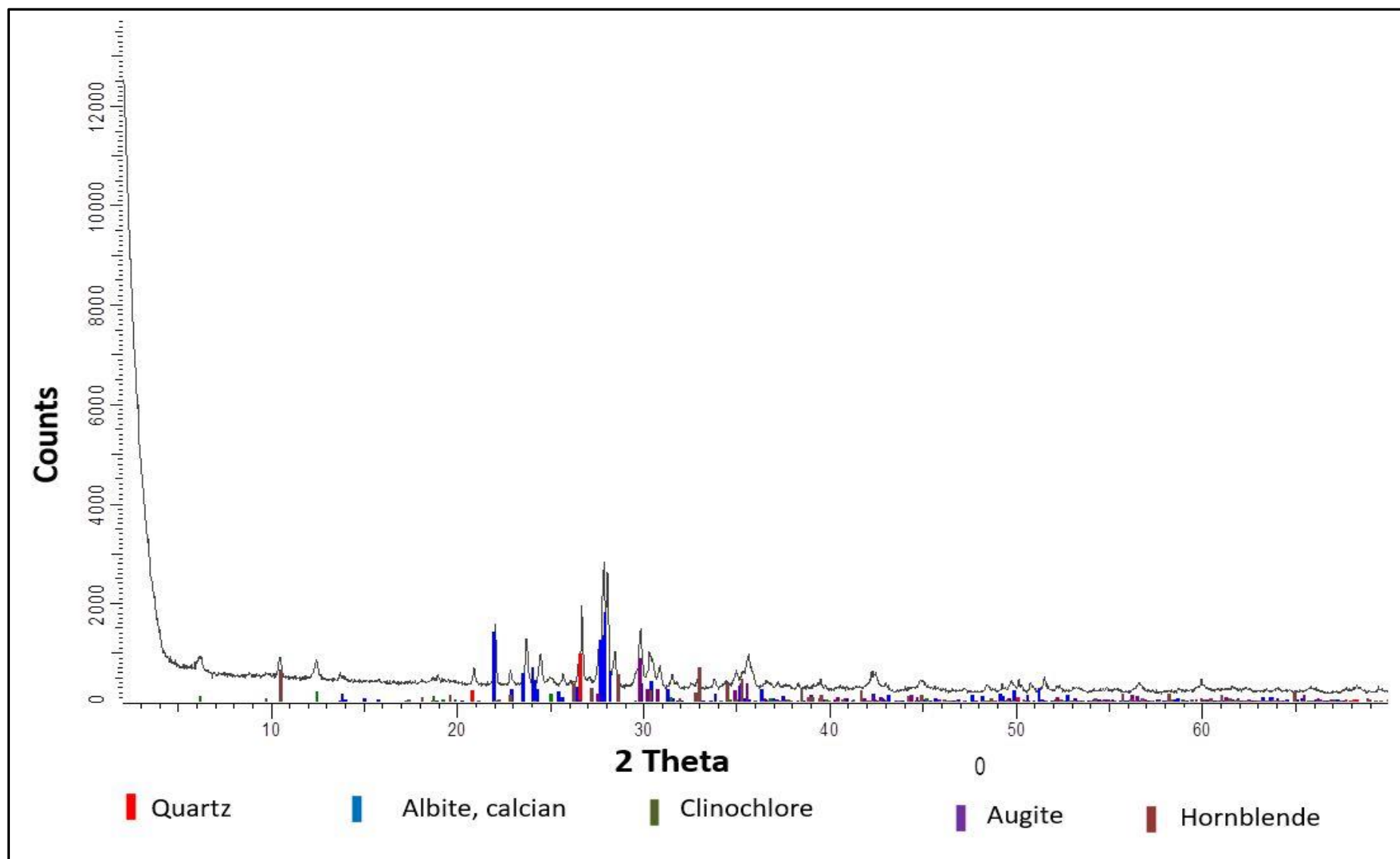


Figure A. 5: XRD pattern for Dolerite of the Karoo Suite

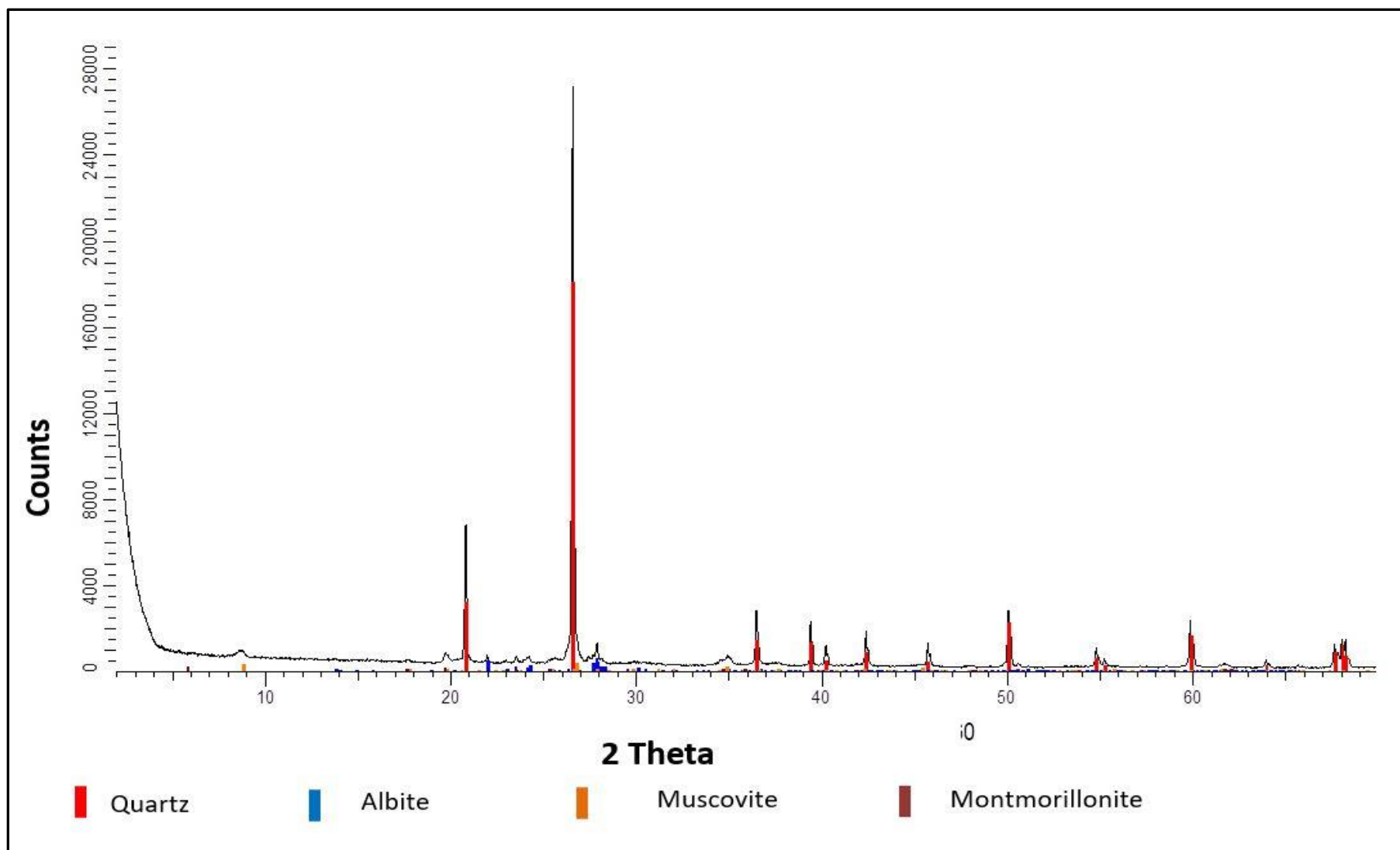


Figure A. 6: XRD pattern for Sandstone of the Molteno Formation

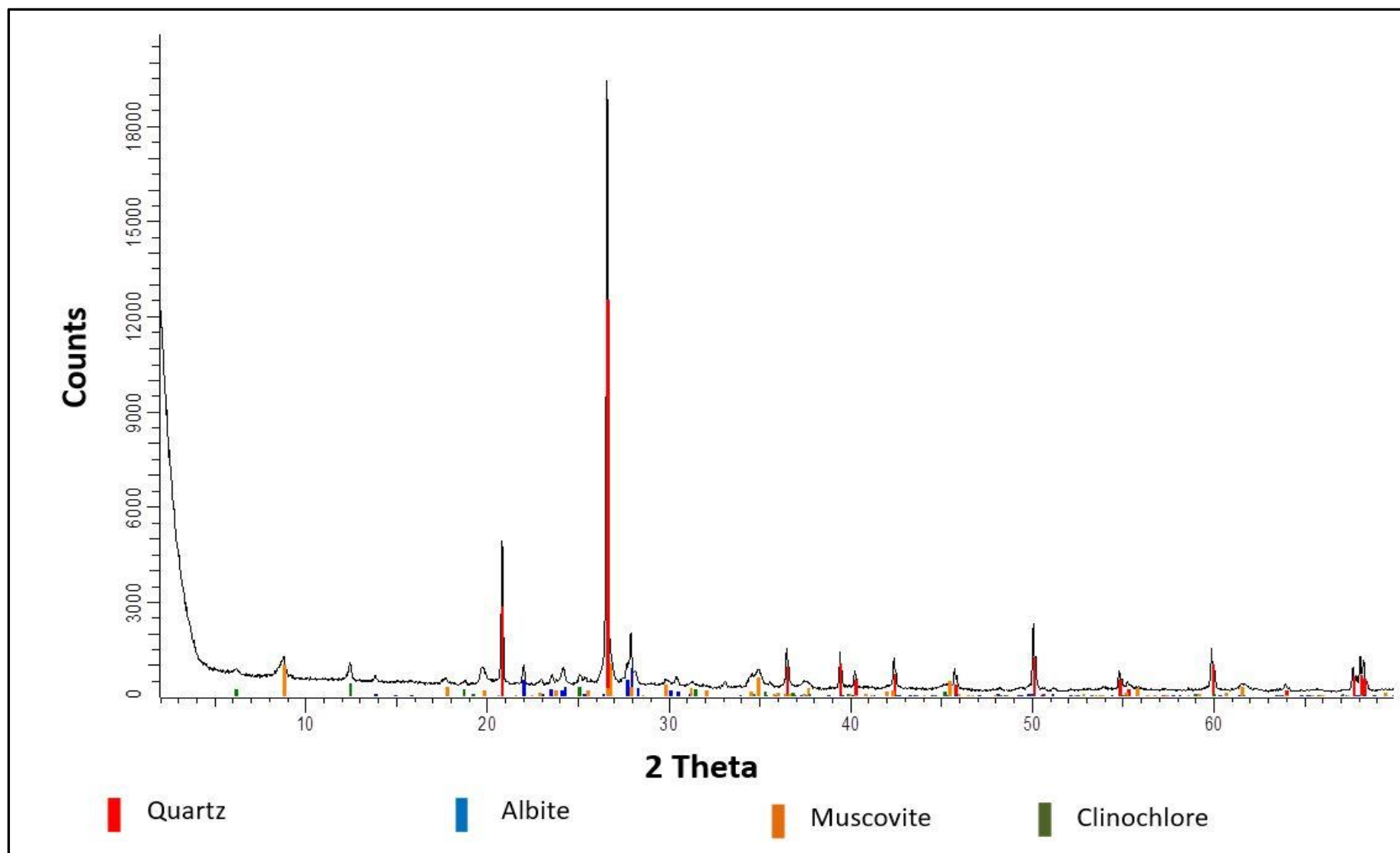


Figure A. 7: XRD pattern for Sandstone of the Molteno Formation

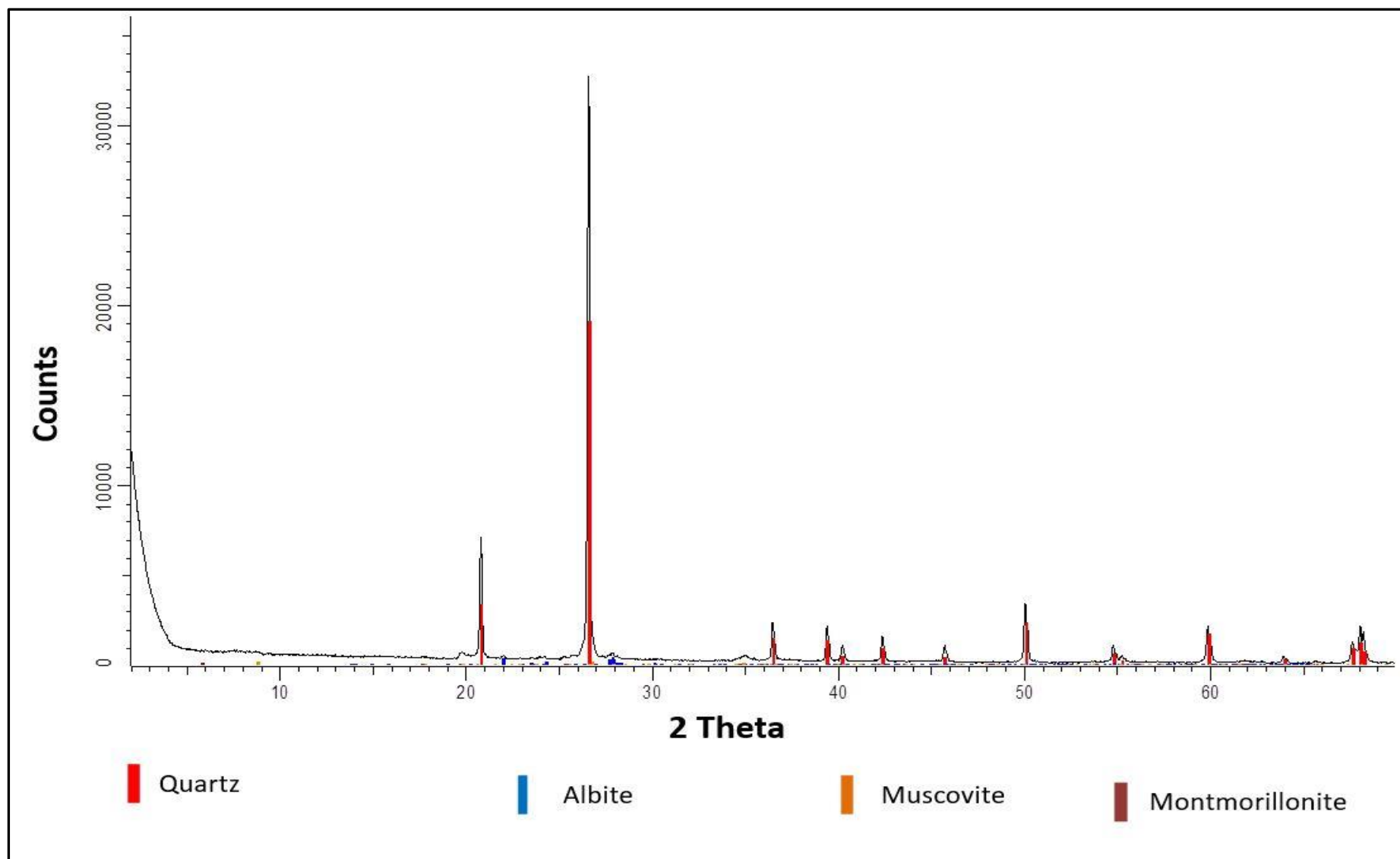


Figure A. 8: XRD pattern for Sandstone of the Molteno Formation

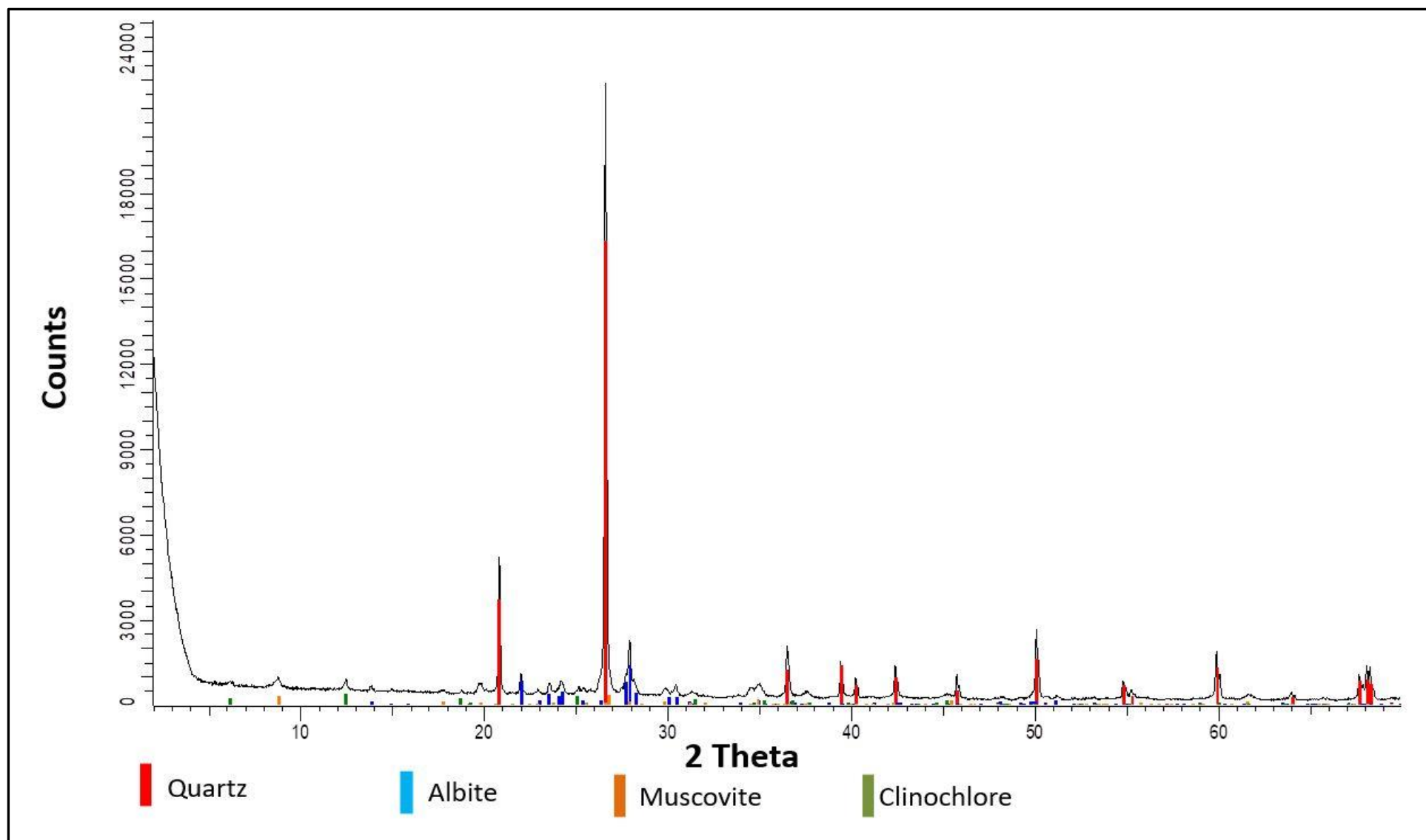


Figure A. 9: XRD pattern for Molteno Formation sandstone.

APPENDIX B:

B.1. Gamma ray spectrometry Processing and corrections

B.1.1 Deadtime

Spectrometers require a finite time to process each pulse from the detector. Any pulse that arrives while another is being processed is automatically rejected, and the total counting time available is thus reduced by the time taken to process all pulses detected. A typical dead time would be of the order of 5-15 μ s/pulse, and can be corrected for as follows:

$$N = \frac{n}{1 - nt} \quad \text{B.1}$$

Where N = corrected count rate (count/sec)

n = observed count rate (count/sec)

t = the total dead time in seconds for this one second sample intervals.

This calibration procedure is based on the assumption that the total dead time is nt, where n is the total number of counts recorded.



B.1.2 Energy Calibration

University of Fort Hare
Together in Excellence

This is due to changes in the gain of the photomultiplier tubes because of the drift in the high voltage supply and changes in temperature. Lovborg [1984] simulated the effect of the drift on the stripping ratios for portable spectrometers. He used synthetic spectra to a drift or just 2% changes stripping ratios by several per cent. The old airborne spectrometers could drift up to 2-3 channels during the course of a day and spectrometer drift is thus the significant source of the error with the old spectrometer. Modern spectrometers have built-in self-stabilising features and the total drift is less than 1 channel. Multichannel airborne spectrometer data can be corrected for energy drift as long as all the crystal photo multiplier assemblages in the detector drift sympathetically.

The estimation of photopeak positions for energy calibration requires good-quality spectra. One approach is to sum the spectra along each line over at least 600 s and determine the peak positions from this total spectrum. These are then used to calibrate the energy of each individual 1 s spectrum used in the summation. A simple method of calibrating multichannel

spectra is that used by the Geological Survey of Canada. The energy of at least two prominent photo peaks is determined as the maximum value of a quadratic fitted in the vicinity of each photopeak. A linear function is then fitted to the photopeak positions (channel number vs energy) to obtain the energy at channel 1 and the gain (keV per channel). These parameters are then used to correct each 1 spectrum within the integration period by resampling each channel to its correct energy range.

B.1.3 Cosmic correction

This arises from reaction of the primary cosmic radiation with atoms and molecules in the upper atmosphere. This creates a complex secondary radiation, which reacts with air, aircraft and the detectors to produce the measured cosmic spectrum. The cosmic spectrum in the lower atmosphere is near constant shape and its amplitude decreases with altitude. At energies greater than 3 MeV, all radiation is cosmic in origin and airborne spectrometers monitor a cosmic window to estimate cosmic background.



Aircraft and cosmic background spectra are estimated as the following $N_i = a_i + b_i N_{cos}$

Where N_i = aircraft + aircraft background count rate in the channel

N_{cos} = cosmomic window count rate, a_i = aircraft background in the i^{th} channel and b_i = cosmic background in the i^{th} channel normalised to unit counts in the cosmic window.

The aircraft and cosmic background spectra are subtracted from dead time corrected from energy calibrated observed spectra.

B.1.4 Radon correction

Radon gas (^{222}Rn) is very mobile and can escape into the atmosphere from soils and rock fissures in response to the pumping action of changing temperature and pressure. The Rn component of background is due to atmospheric ^{222}Rn and its daughters. This is a major contributor to background radiation. Up to 50 per cent of the U window count rate can arise from Rn daughter products in the atmosphere. A serious problem associated with the removal of Rn background is that it is not evenly distributed through the lower atmosphere. For example, under early morning still-air conditions Rn and its daughters can be trapped close to the ground in temperature inversion layers. The spectrum of airborne Rn and its daughters has

a very similar shape to that of U and its daughter products in the ground. This is because the most prominent gamma-ray emitter (^{14}Bi) occurs below ^{222}Rn in the ^{238}U decay chain, and only the relative height of photopeaks distinguishes the two spectra.

There are two procedures that can be used to remove Rn background namely: the spectra ratio and the upward-looking detector method. The spectra ratio method use U series photopeaks to determine the contribution to the spectrum of U in the ground and Rn in the air. This method requires multichannel spectra that have dead time, energy calibrated and aircraft and cosmic background removed.

The second method of removing Rn background is by using the upward looking detector which only requires window data.

B.1.5 Noise Adjusted Singular Value Decomposition (NASVD)

The NASVD method [Hovgaard and Grasty, 1997] transforms the observed spectra into orthogonal spectral components that are ordered according to the degree to which each component contributes to the shape of the observed spectra. Since the signal correlates between channels, this ends up in the lower-order components. The random noise, on the other hand, does not correlate from one channel to the next, and tends to be evenly represented in all of the components. The noise is removed by reconstructing the spectra using the lower-order (signal-rich) components only. The NASVD method differs from the principal component method in two important respects. First, the spectra are normalized to unit variance in each channel prior to analysis using an *a priori* model of the noise. Second, the singular value decomposition method is used to extract the spectral components.

B.1.7 Compton stripping of K, Th, U channels

This correction, also known as the channel interaction correction, is used to correct K, U and Th window count rates for gamma rays not originating from the radioelement or decay series being monitored. For example, Th series gamma rays appear in both the U and K windows, and U series gamma rays appear in the K window.

B.1.6 Height attenuation correction

Airborne gamma-ray spectrometric data need to be corrected to a nominal survey height to remove the effect of variation in the height of the detector. The attenuation of gamma rays with elevation above the ground depends on the geometry of the source as well as the energy of the radiation. Thus, radiation from narrow sources attenuates more rapidly with distance than that from broad sources, and low-energy radiation falls off more rapidly with distance than high-energy radiation. A gross correction for height can be obtained by considering an exponential fall-off of radiation as a function of the instantaneous height of the detector:

$$N = N_0 e^{-\mu(H-h)}$$

where μ = the empirically derived height attenuation coefficient for any particular energy interval and a particular source type;

N_0 the observed count rate at the STP height, h , and

N = the corrected count rate for the nominal survey height H .

This algorithm is adequate for subdued topography and heights in the range 50-250 m. Attenuation coefficients for broad sources are universally used as this is the most common source type in the geological environment.



B.1.8 Conversion to ground concentration

University of Fort Hare
Together in Excellence

Gamma ray spectrometric data are usually in counts per unit time (count rates). This is undesirable because the count rates are dependent not only on the ground radioelement concentrations, but also on the equipment used and the nominal height of the particular survey. Crystal volume, detector efficiency, and window widths all affect the observed count rate and make it difficult to compare results from two different surveys. Measuring units should have a direct geological significance and be independent of instrument and survey parameters. Airborne count rates should, therefore, be converted to mean-ground-level abundances of the radioelements. The conversion is usually performed by dividing each of the corrected three channel count rates by a 'sensitivity' coefficient.

B.1.9 Levelling and Microlevelling of ground correction.

A. Levelling

Changes in soil moisture, vegetation thickness and Rn content of rocks and soils during the course of an airborne survey cause variations in the radiation output of the Earth and result in unwanted changes in the measured radiation both along and between lines. The effect is particularly severe for radiation from U. Also, all the data-correction procedures involve assumptions about source geometry that may not always be valid. These, combined with the errors in the calibration constants, can result in long-wavelength 'level shift' errors in the processed data. One or more of three methods are usually used to correct the data.

B. Microlevelling

Minty [1991] described a simple method for removing residual levelling errors from located aeromagnetic data, which is just as applicable to airborne gamma-ray spectrometric data. The errors are removed from a grid of the data by a directional grid filtering technique, and the filtered grid is then used to correct the located data. The method must be used selectively, since it is not rigorous, and real elongate anomalies in the flight-line direction are removed just as easily as levelling errors.



B.2 Radiometric Filters

University of Fort Hare
Together in Excellence

A. Band ratios

Any arithmetic combination of radioelement grids can be represented as grey-scale images. One of the more useful arithmetic combinations is the ratio of two radioelement grids. The ratio of the K and Th grids, for example, is computed as: $r_{(K/Th)} = \frac{K}{Th}$

The effect of environmental factors on radiometric response, such as soil moisture, vegetation, and topography, are less evident on band ratios. The ratios therefore often correlate more highly with geological units. Also, since there is usually a high correlation between bands, the ratios often show subtle features that are not apparent on the original grids. In theory, the ratio values range from zero to infinity. A more uniform scaling can be achieved by computing the ratio as:

$$r_{(K/Th)} = \tan^{-1} \frac{K}{Th}$$

Grant [1998] recommends a method to compute ratios above a pre-defined minimum noise level for both radioelement profiles and grids. The technique was motivated by the

observation that low count rates in either the numerator or denominator yield large fluctuations in the computed ratios. Adjacent samples are summed until numerator and denominator thresholds are reached. The thresholds depend on the precision of the concentration estimates. Negative concentrations are excluded, and over-water samples are masked using a threshold on the K channel.



APPENDIX C

C.1 Magnetic corrections and Filters

C.1.1 Filters

These are the enhancements that were applied to the magnetic field data. These are Upward and downward continuation, reduction to the pole and derivative (full horizontal, first vertical and analytic signal) filters. These are described below.

A. Upward and downward continuation

Upward and downward continuations are mathematical methods that are adopted in geophysics to separate the regional field from the residual anomaly. These filters are applied in magnetic field data to obtain magnetic field intensity which would be observed if survey measurements were taken at a greater (upward continuation) or lesser height (downward continuation), than were actually taken. For the purpose of this study, the upward continuation filter was applied in order to smoothen out near surface effects. In Musset and Khan [2000] it is described that upward continuation is used to decrease the relative size of anomalies that arise from shallow, near surface bodies, as well as to enhance signatures arising from deep seated anomalous bodies.

Telford et al. [1990] describe the upward continuation using a mathematical expression given

$$\text{by; } F(x, y+h) = \frac{h}{2\pi} \iint_{-\infty}^{\infty} \frac{F(x-y, 0) dx dy}{\{(x-x')^2 + (y-y')^2 + h^2\}^{1/2}}$$

where $F(x, y, +h)$ is the total field at point $P(x', y', +h)$ above the surface at which $F(x, y, 0)$ is known and h represent the elevation above the surface. The upward continuation filter in the wavenumber domain is $(r) = e^{-hr}$, where h is the continuation height and r is the radial wavenumber. Similarly, the downward continuation filter is expressed in the form of this equation $(r) = e^{hr}$, where h is the distance to be continued downwards [Keary and Brooks, 1991]. In this study this filter was applied using Geosoft Oasis Montaj to accentuate on anomalies arising from shallow near surface bodies.

B. Reduction to Pole (RTP)

Quite often the magnetic field anomalies are dipolar i.e. an anomaly will have a positive and a negative lobe. For the purpose of this study, the magnetic gridded data have been reduced to the pole to remove its dependence on the angle of magnetic inclination. Generally, reduction to the pole filter is applied on magnetic data to remove the effects of inclined magnetic field and to get the field intensity similar to one which would be observed if the Earth's magnetic field had been vertical not inclined during the survey. This effect causes anomalies to be seen directly above causative bodies rather than being shifted or tilted aside due inclination effect.

Reduction to pole filter is described as: $L(\theta) = \frac{1}{[\sin(Ia) + \cos(I) \cos(D - \theta)]}$

I= geomagnetic inclination

Ia = inclination for amplitude correction,

D= geomagnetic inclination

C. Vertical Derivative (VD)



This filter emphasizes anomalies that are due to near surface features. It enhances shallow magnetic sources and tends to sharpen the boundaries of their anomalies. Vertical derivative has been applied in observed field magnetic data to delineate edges of short wavelength features. Its filter is given by: $L(r) = rn$, with n being the order of the vertical derivative.

D. The total horizontal derivative (THD)

The total horizontal derivative (THD) enhances high frequencies and outlines the edges or boundaries of the sources. Thus its peaks lie directly over the edges or boundaries of broad bodies. The filter calculates the nth horizontal derivatives in x and y directions. The THD varies with inclination, gives a clearer or sharper image and produces a better anomaly peak centred over the edges of the body. Cordell and Grauch [1985] stated that THD is suitable for edge detection and can be expressed as: $THD = \sqrt{\left[\frac{dF}{dx}\right]^2 + \left[\frac{dF}{dy}\right]^2}$ where F is the magnetic field and are the two orthogonal horizontal derivatives of the magnetic field (**F**).

E. Analytical signal

This filter integrates HD and VD to produce magnetic features that are independent of the direction of remanent magnetization of the source with amplitudes that are related to the magnetic body. The analytical signal is commonly applied to delineate the magnetic contacts and give approximate estimates of their depth.

The analytical signal is given by; $A(x, y) = \sqrt{\left[\frac{dM}{dx}\right]^2 + \left[\frac{dM}{dy}\right]^2 + \left[\frac{dM}{dz}\right]^2}$

with A representing an amplitude of the analytical signal and M the magnetic field.

F. Depth slicing

Depth to sources is connected to wavelength or frequency of the potential field data. The depth slices highlight specific interval of spatial frequencies (wavelength) that matches with the calculated or estimated depth in the subsurface by generating separate magnetic maps for a sequence of horizons with increasing depth. It aids comparison of amplitude response, thus the appearance and disappearance of a magnetic unit at different depth is recognised. Depth slicing works on the principle of Wiener filtering, which assumes that potential field signals (e.g. magnetic and gravity) results from two or more uncorrelated arbitrary processes [Fuller, 1967]. Fuller ([1967] stated that the various components of the data can be separated by highlighting the effects of shallow sources from deeper sources. Most magnetic anomalies at the surface, usually originate at shallow depth while obscure magnetic anomalies usually originate from a deeper depth [Gunn, 1972].

APPENDIX D

D.1 Gravity Corrections

The gravity data of this study were supplied by the Council for Geoscience. The following corrections done by the Council for Geoscience on the gravity data include;

- i. Tidal corrections
- ii. Instruments drift correction
- iii. Latitude correction
- iv. Free air correction
- v. Bouguer slab correction
- vi. Terrain correction

D.1.1 Tidal correction

The tidal correction is necessary for;

- Ultra-accurate surveys where it is not sufficiently accurate to absorb the effect of the sun and moon in the drift correction, and
- If gravimeter drift is low and the base station tie backs were made with a similar period as the tides.

Tides occur both in the solid Earth and the sea. The latter is important for marine surveys.

The period of the tides is about 12 hrs. The amplitude of the gravitational effect of the solid Earth tides is up to ~ 0.3 mGal throughout the day at a fixed point on Earth [Kearey *et.al*, .2002]. It can be corrected by using a computer program or published tidal gravity correction tables.

To correct for tidal effect, the tidal value is subtracted from the observed gravity value as shown in equation below;

$$\Delta g = g_{obs} - ID - TD$$

D.1.2 Instrument drift

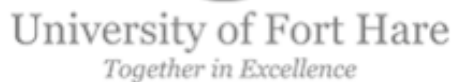
This drift is related to gravimeter that is used during the gravity survey. The gravimeter is affected by temperature changes causing elastic creep in the springs. The changes can be corrected by repeating measurements at the base station throughout the day and plot the gravity measurements against time to form a drift curve.

D.1.3 Latitude correction

Gravity values measured at the Earth's surface changes with latitude. This is caused by the Earth which is not a perfect sphere and thus gravity increases from the equator towards the poles [Robinson and Coruh, 1998]. An International Gravity Formula (IGF) is adopted to correct for the effect of the latitude from the measure gravity data during survey and is expressed by;

$$g_0 = 9780326.7714 \left(\frac{1 + 0.00193185138639 \sin^2 \varphi}{\sqrt{1 - 0.00669437999013 \sin^2 \varphi}} \right) g.u$$

The IGF give theoretical sea level gravity value, therefore subtracting this value from the observed gravity gives the corrected gravity value which is free of latitude effects.



D.1.4 Free air correction

The free-air correction accounts for the decrease in magnitude of gravity due to increase in elevation (height) above the datum (e.g. sea level) without considering the mass of the rock underneath. Reynolds [1997] expressed the free-air correction as $3.086h$ g.u. which is the difference between the measured gravity at sea level and at an elevation (h) above the datum, assuming there is no rock in between.

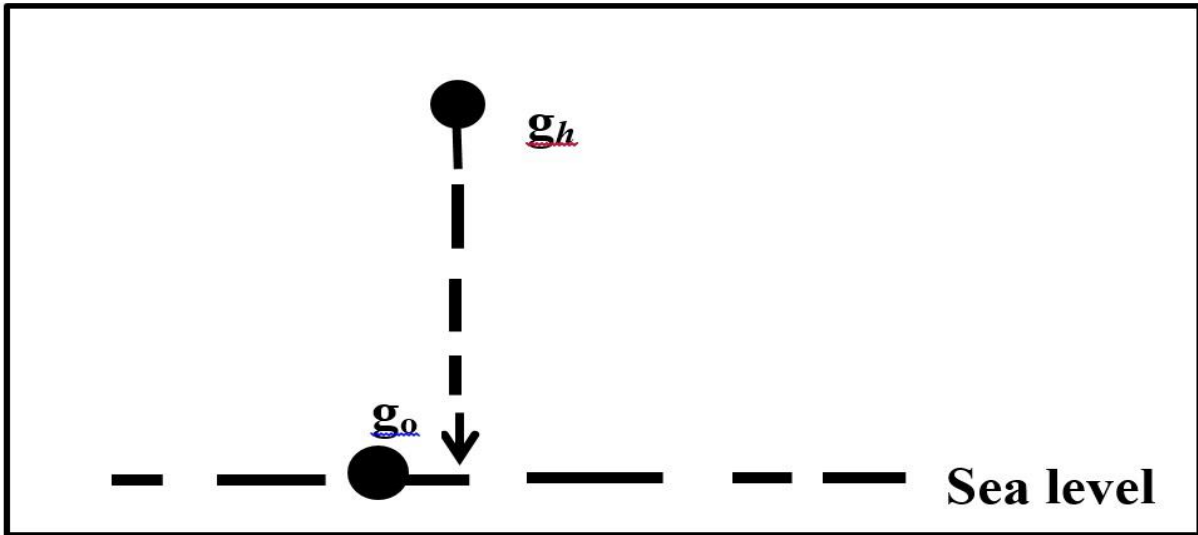


Figure D. 1: Schematic representation of free-air correction [Reeves, 2005].

The free-air correction is added to the observed absolute gravity in order to remove the effect of the height or elevation above the datum. Given that $\partial g_F = 3.086h$ g.u., the free air anomaly can be expressed as:

$$\Delta g_{FAA} = g_{obs} - TD - ID - g + 3.086h \text{ g.u.}$$

D.1.5 Bouguer correction

This accounts for the mass of rock between the station and sea level. It has the effect of increasing g at the station, and thus it is subtracted. The formula for the Bouguer correction on land is expressed:

$$\Delta g = 2\pi G \rho h$$

where ρ is the density of the slab, h is the height (m) above the datum and $G = 6.672 \times 10^{-11} \text{ N m}^2 \text{ Kg}^{-2}$.

The simple Bouguer anomaly is given as:

$$g = g_{obs} - TD - ID - g_0 + [3.086 - 2\pi G \rho h]g.u.$$

It is common to use a Bouguer reduction density = 2670 kg m^{-3} and the above expression becomes:

$$g = g_{obs} - TD - ID - g_0 (3.086 - 0.49 \times 10^{-3} \rho h)g.u.$$

The term in brackets is known as the combined elevation factor which reduces to g.u. for = 2670 kg m^{-3} . The expression above (equation 5) is used in geologic interpretation.

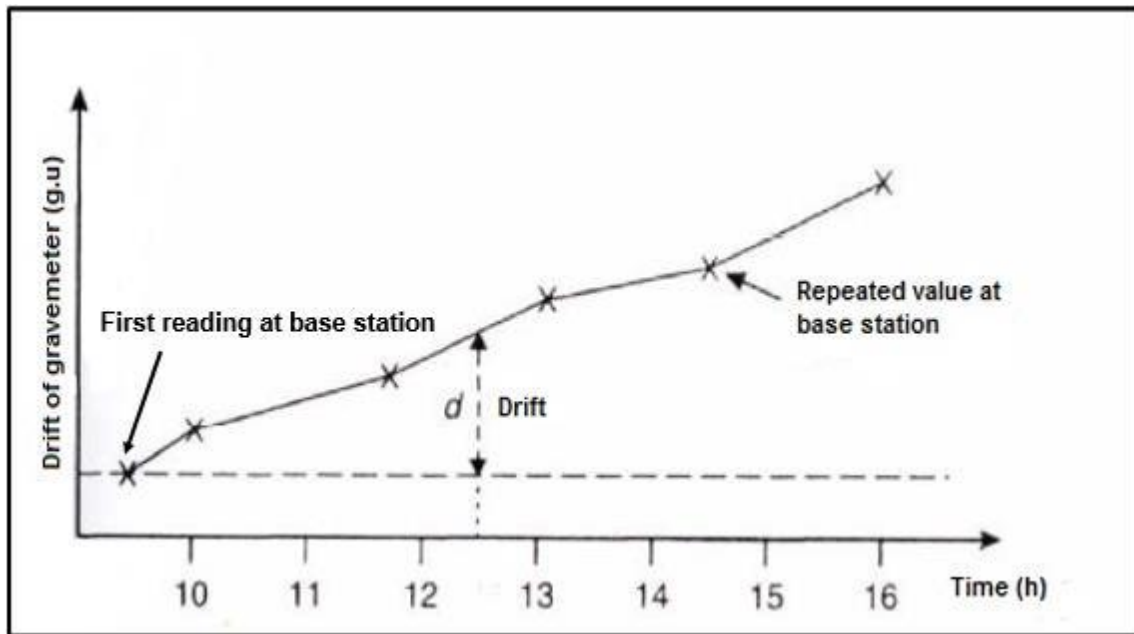


Figure D. 2: A gravimeter drift curve [adapted from Reynolds, 1997].

D.1.6 Terrain correction



The terrain correction accounts for the assumption in Bouguer correction that the station rests on an infinite slab with a thickness equal to the difference in elevation between the station and the datum [Telford *et al.*, 1990]. The terrain T is added to get the complete Bouguer anomaly CBA given by $CBA = g_{obs} - TD - ID + 3.086h - 2\pi G\rho h + T$

APPENDIX E

E.1 Minimum and maximum density gravity models

The minimum, average and maximum density values were obtained in the by measuring rock densities of the study area. For each profile (A-E) three models (minimum, average and maximum density gravity) were generated. The average density values models were used in chapter 7. This section presents the models for minimum and maximum density values. These models are geologically reasonable.

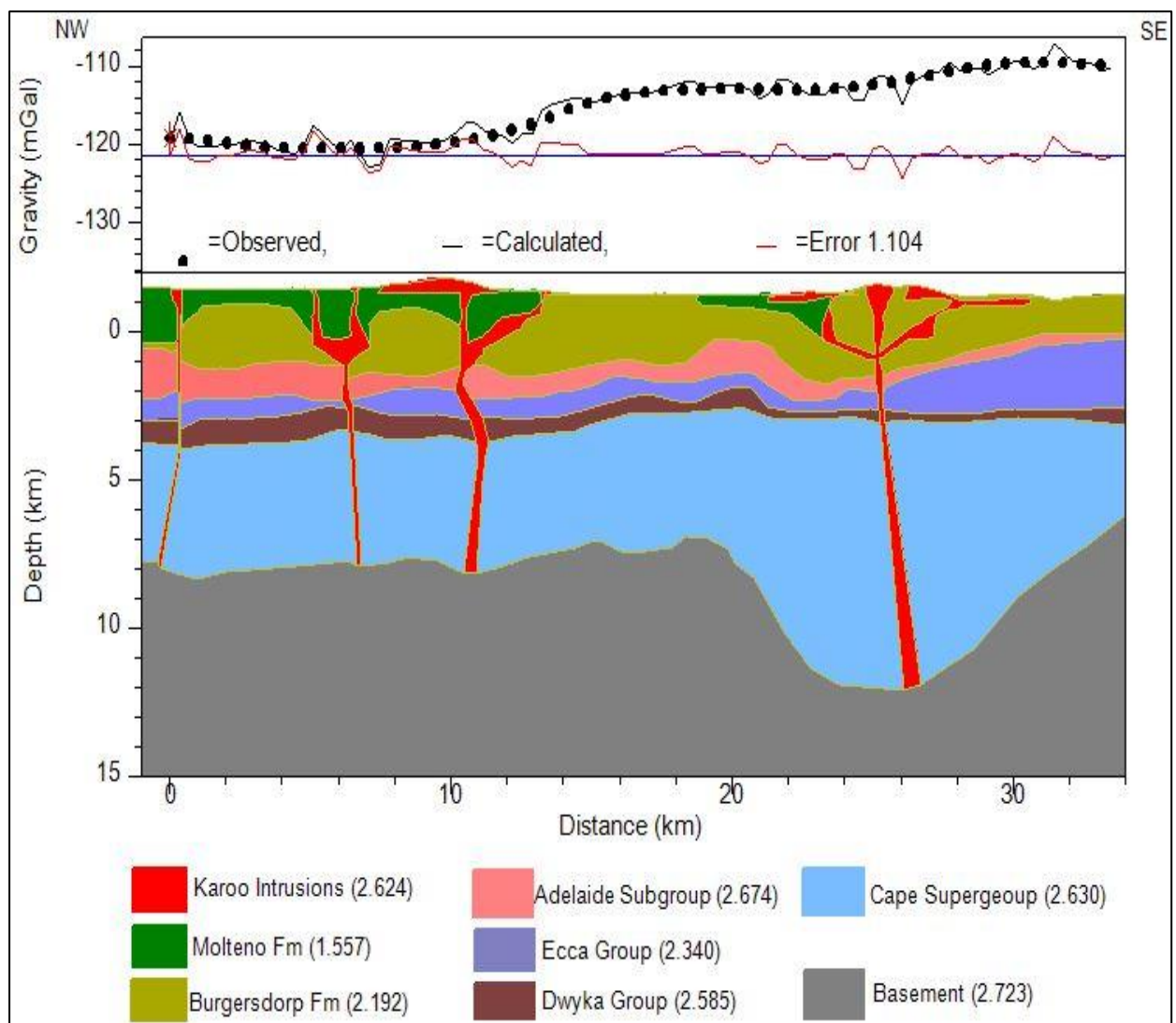


Figure E. 1: Profile A-A' gravity model for minimum density values.

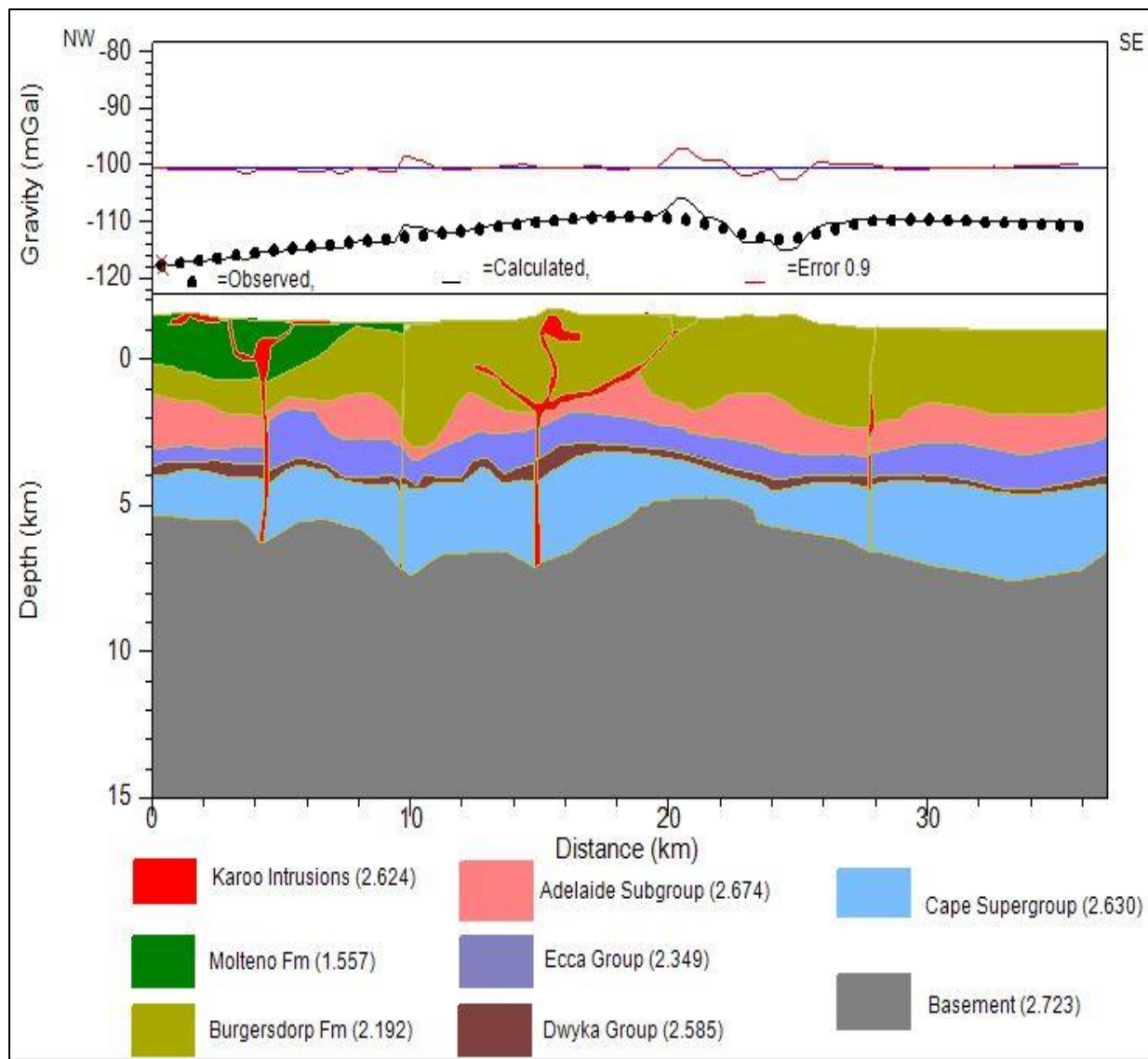


Figure E. 2: Profile B-B' gravity models for minimum density values

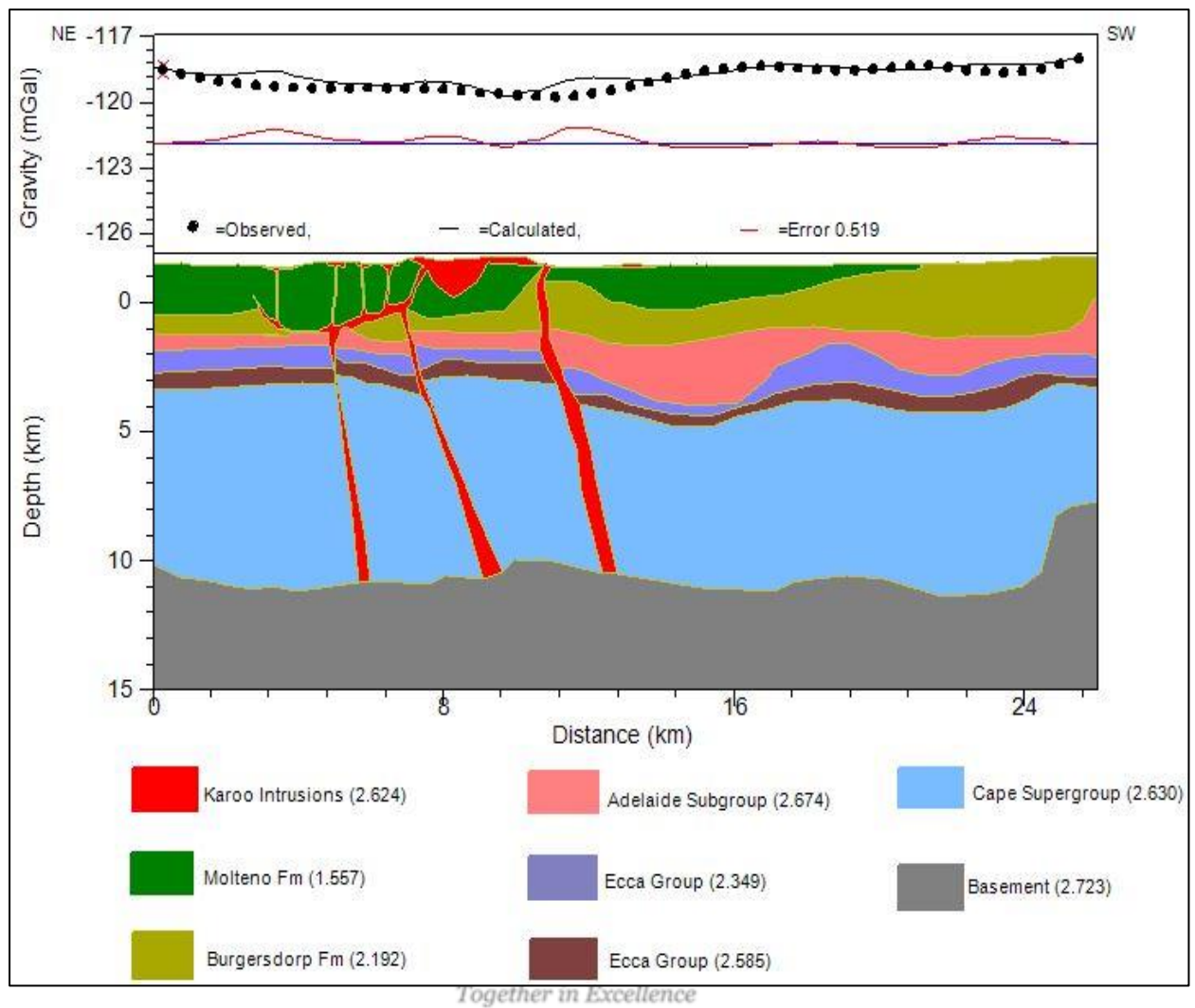


Figure E. 3: Profile C-C' gravity model for minimum density values

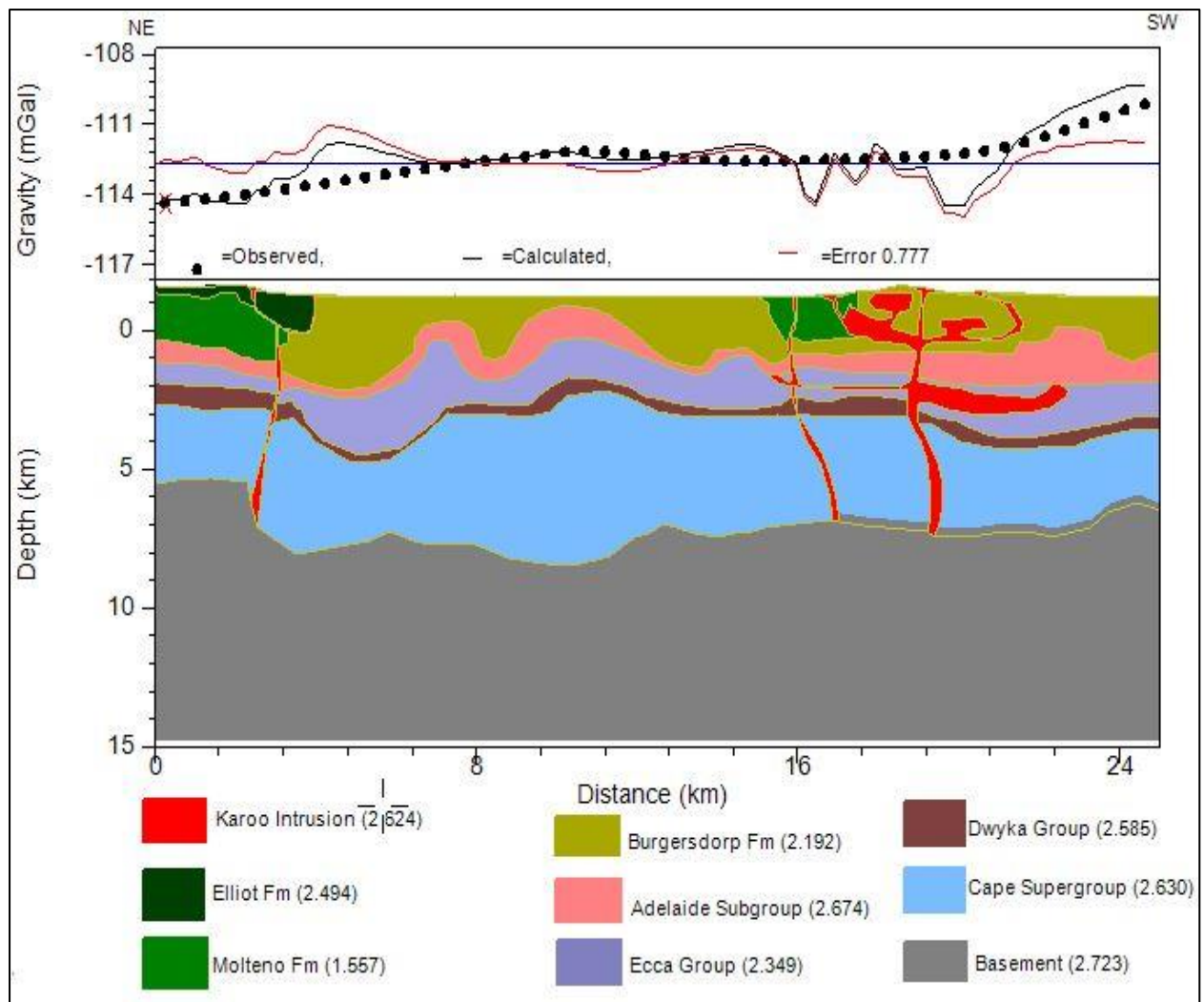


Figure E. 4: Profile D-D' gravity model for minimum density values

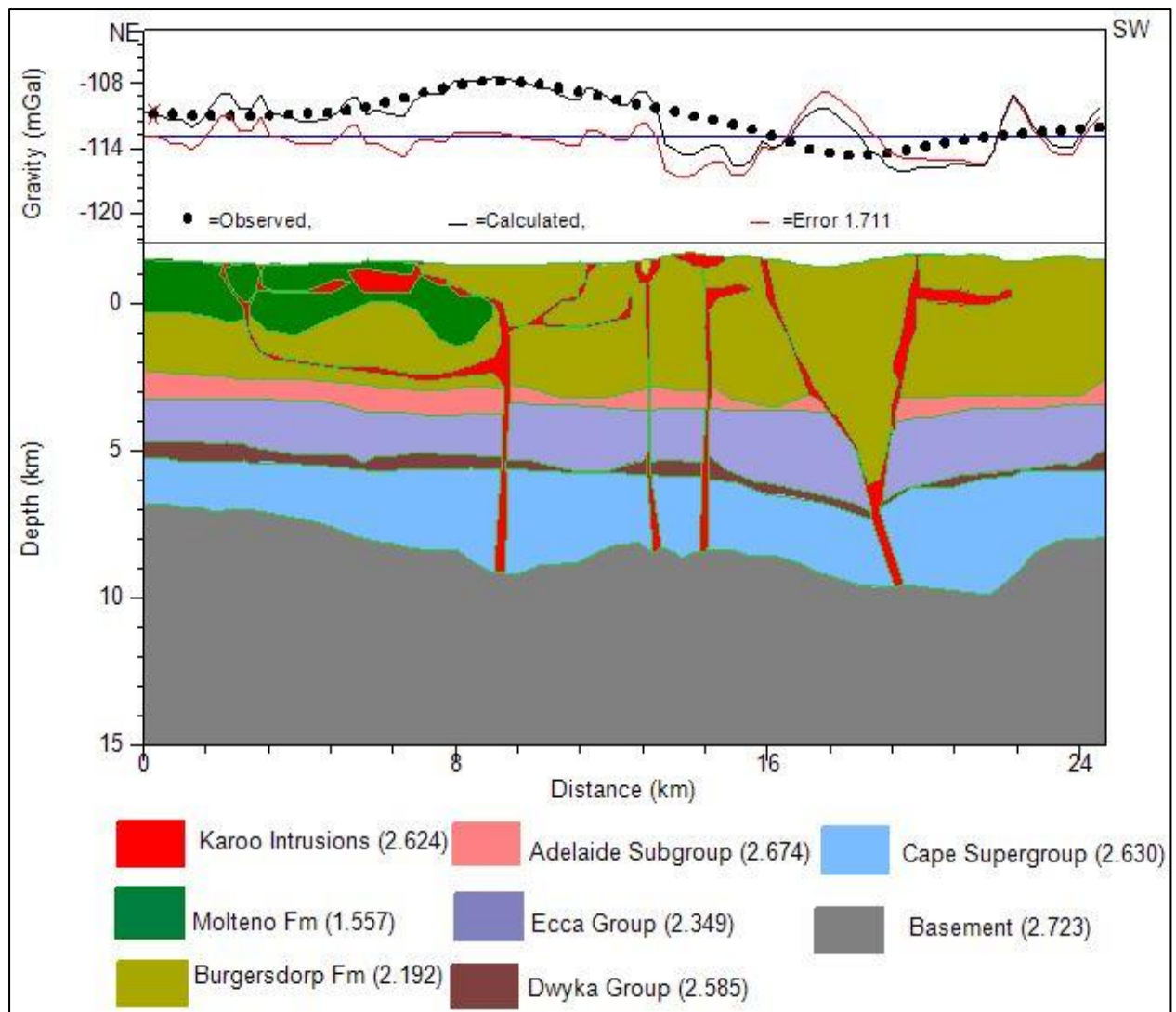


Figure E. 5: Profile E-E' gravity model for minimum density values.

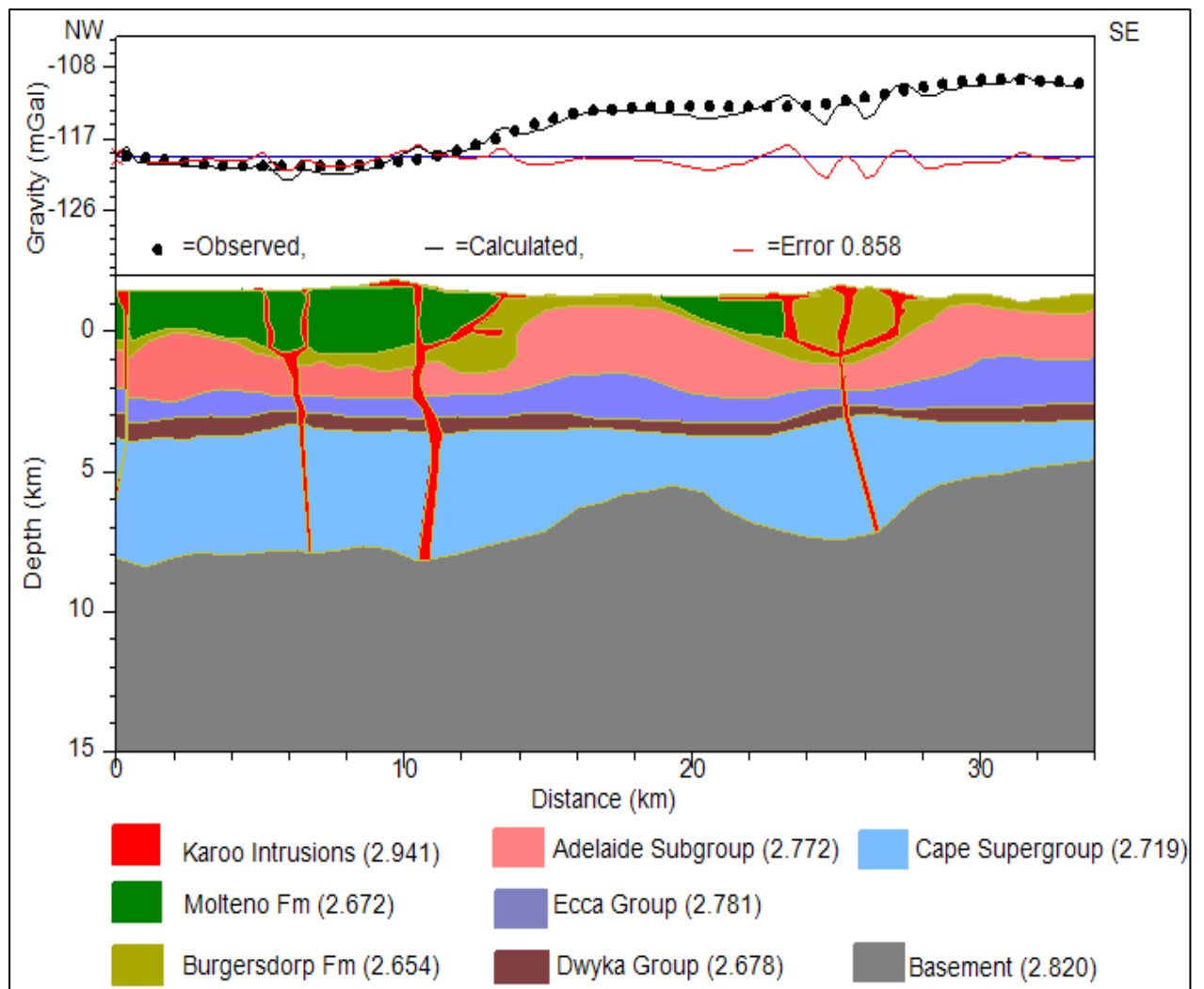


Figure E. 6: Profile A-A' gravity model for maximum density values.

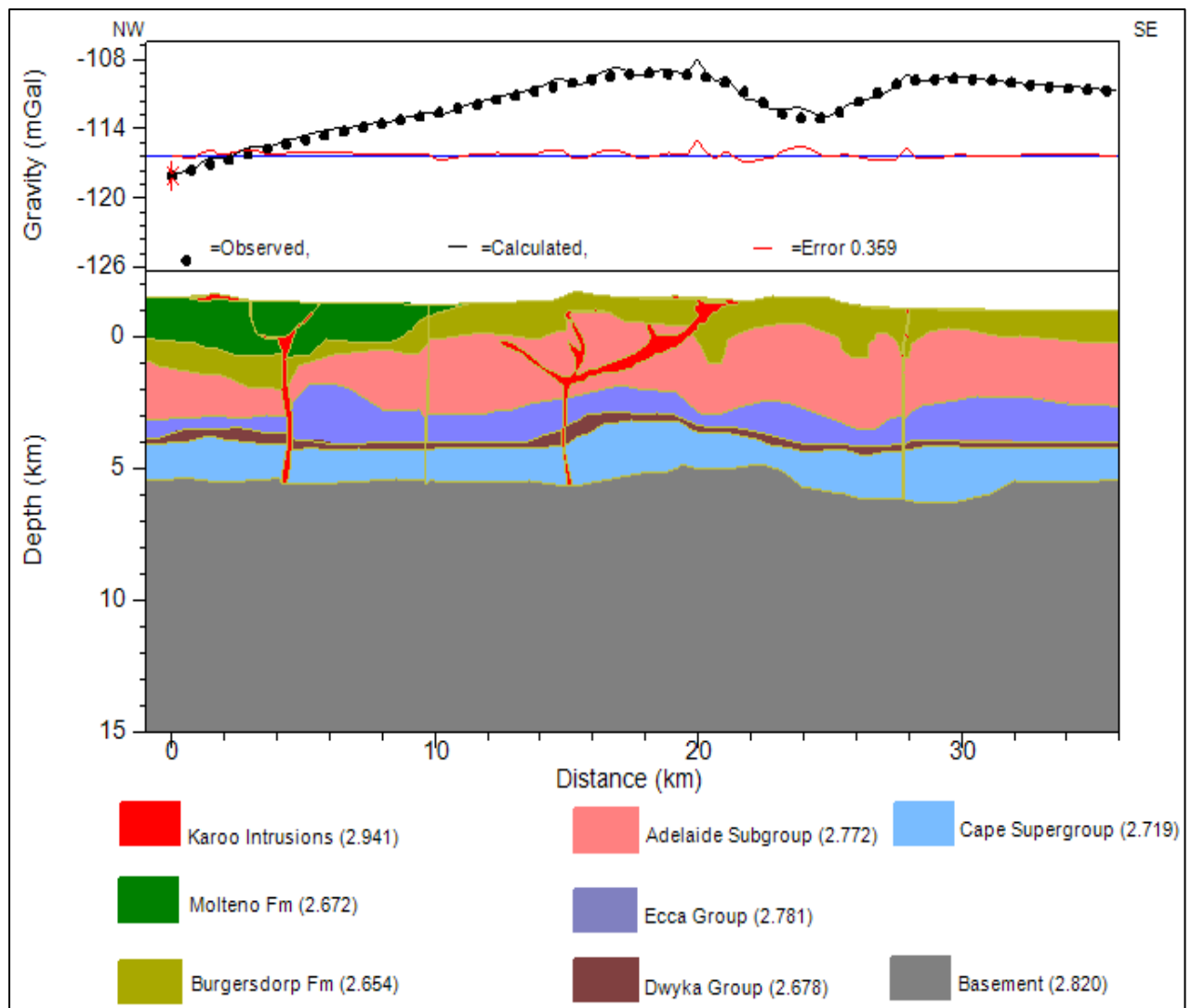


Figure E. 7: Profile B-B' gravity model for maximum density values.

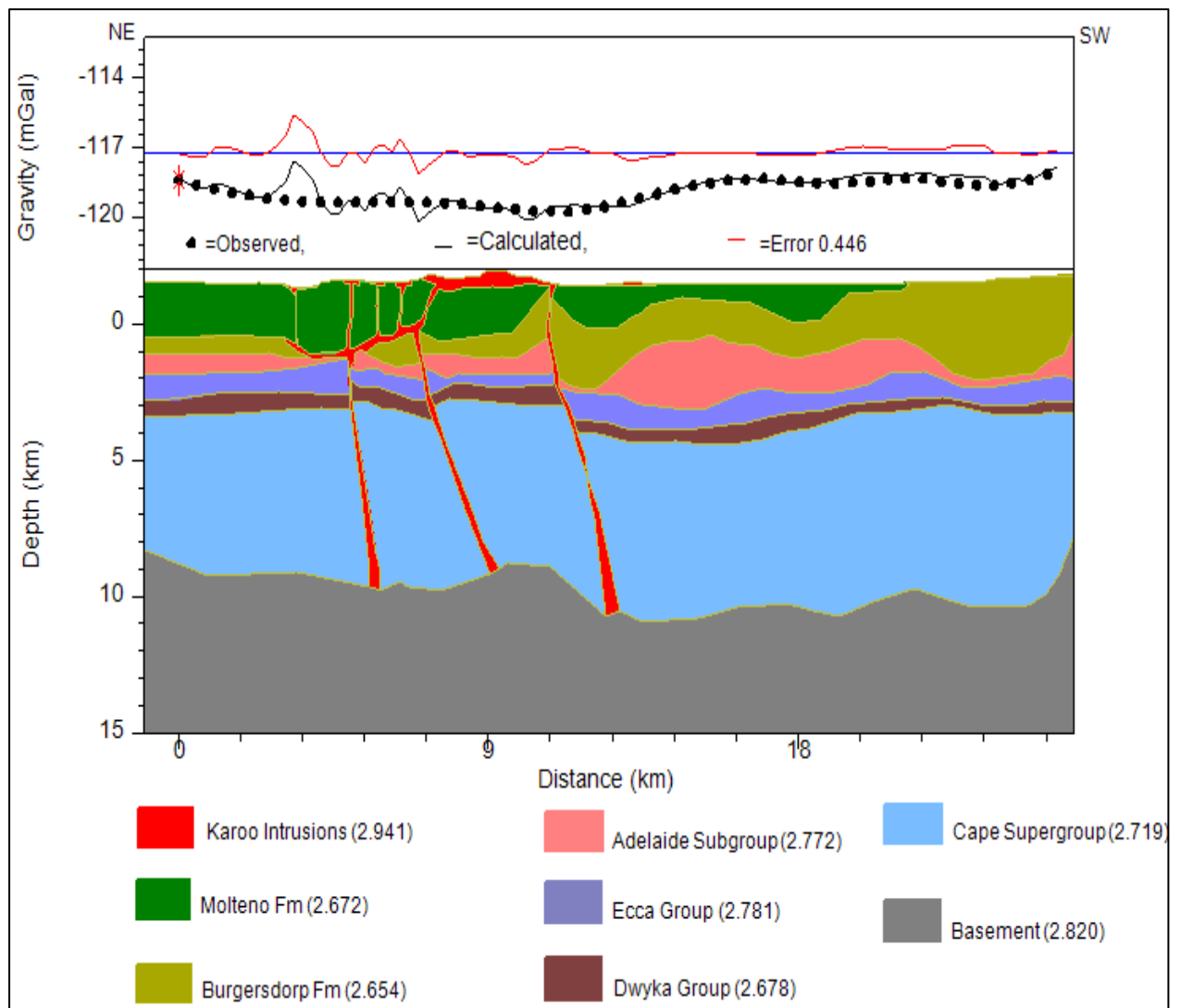


Figure E. 8: Profile C-C' gravity model for maximum density values.

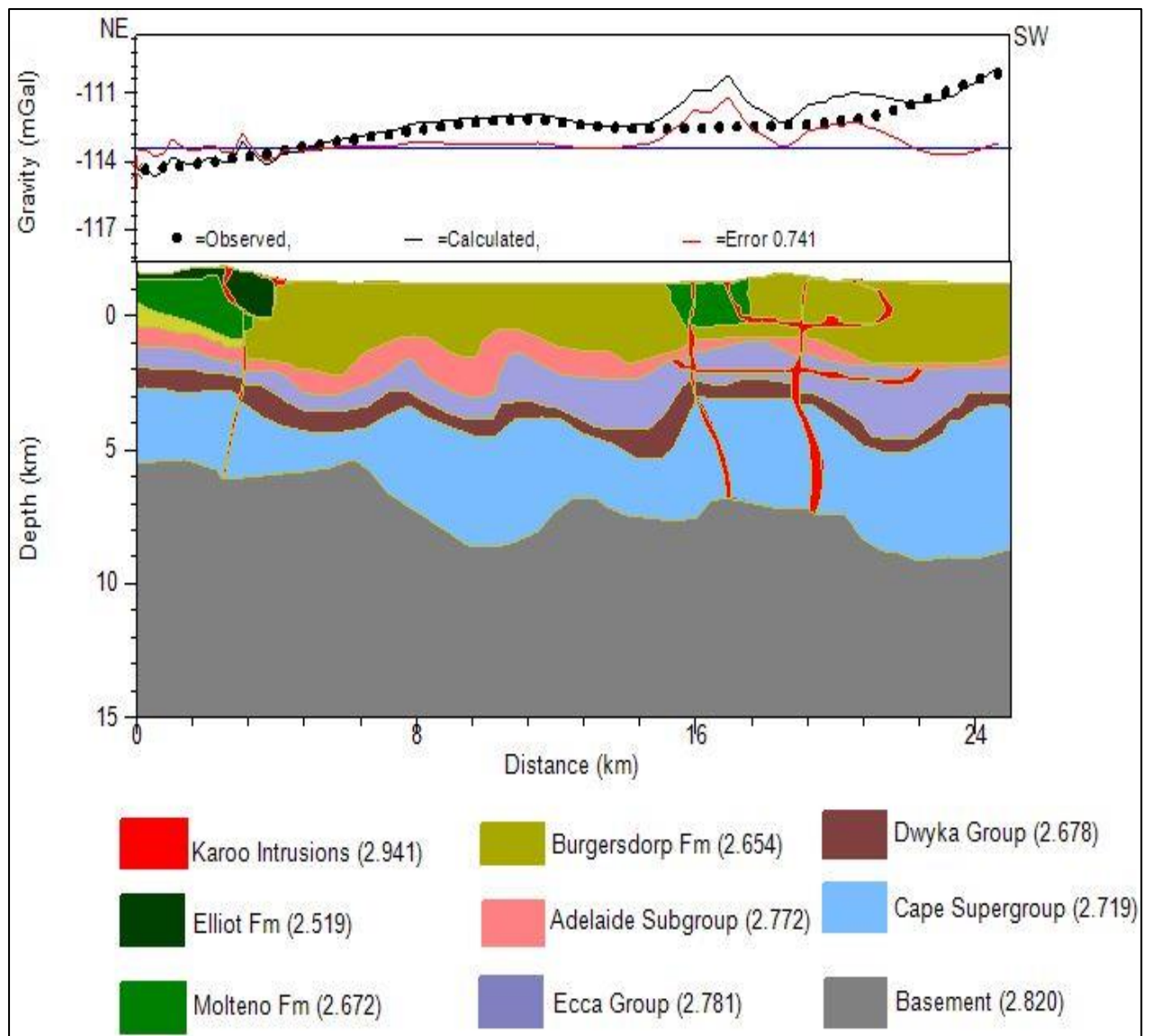


Figure E. 9: Profile D-D' gravity model for maximum density values.

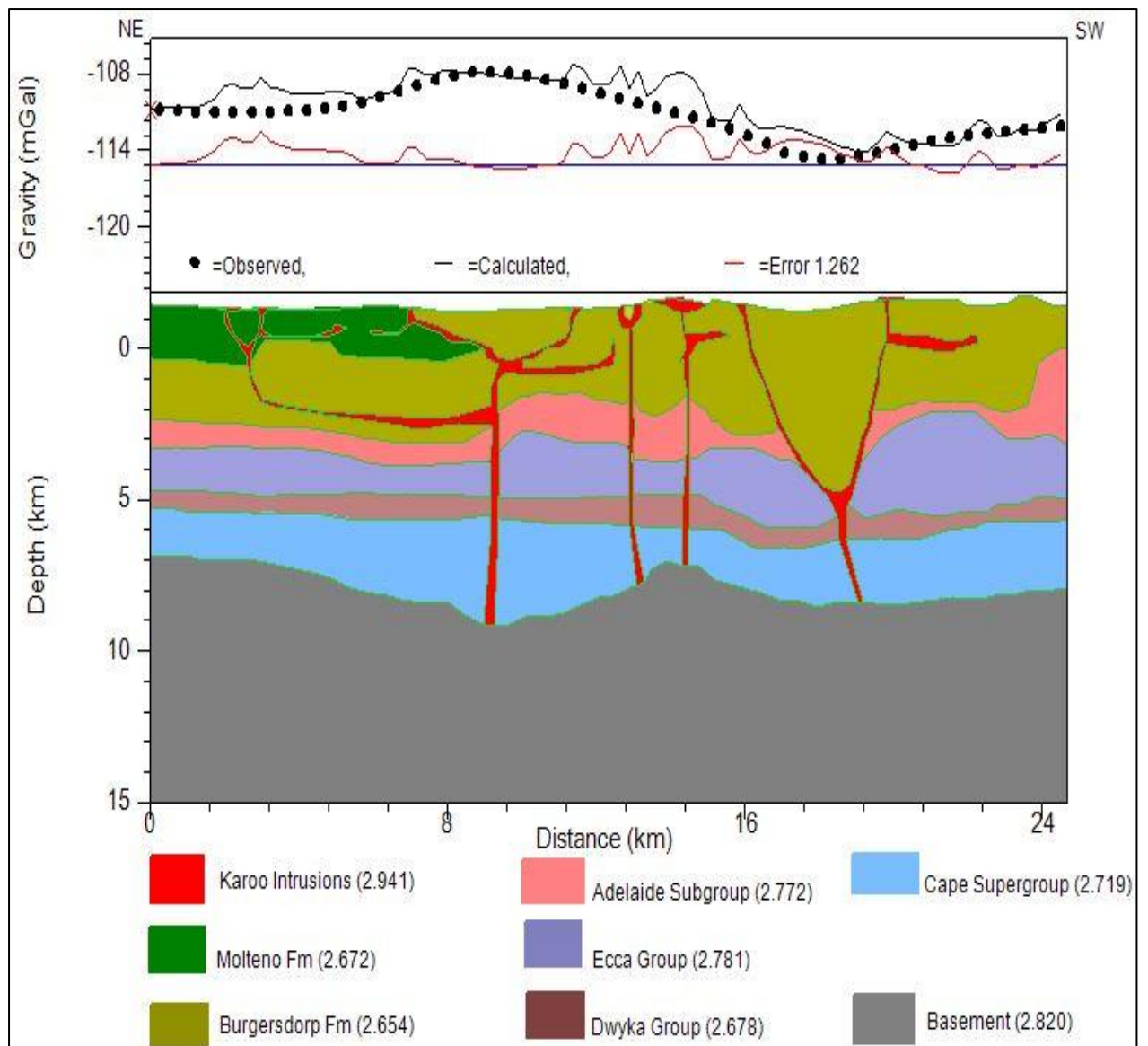


Figure E. 10: Profile E-E' gravity model for maximum density values.